Impacts of anthropogenic aerosols on the terrestrial carbon cycle

Yuan Zhang

THESE DE DOCTORAT DE

SORBONNE UNIVERSITÉ

ÉCOLE DOCTORALE N°129

Sciences de l'environnement d'Ile-de-France

Yuan ZHANG

Impacts of anthropogenic aerosols on the terrestrial carbon cycle

LMD/LSCE/IPSL

soutenue le 16 mars 2020

Jury:

Présidente : **Agnès Ducharne**, CNRS, METIS/IPSL
Directeur de thèse : **Olivier Boucher**, CNRS, IPSL
Co-directeur de thèse : **Philippe Ciais**, CEA, LSCE/IPSL
Rapporteur: **Stephen Sitch**, University of Exeter
Rapporteur: **Sönke Zaehle**, Max Planck Institute
Examinateur: **Roland Séférian**, CNRM, Météo-France/CNRS
Examinatrice: **Lingli Liu**, Chinese Academy of Sciences
Invité : **Laurent Li**, CNRS, LMD/IPSL

Acknowledgements

The three years' time as a PhD student in Paris passed very fast. Finally, I get my thesis finished. It is an achievement earned with the help of a lot of people. Here I would like to thank all the people who helped me with my study and my life. First, I would like to thank my supervisors, Olivier Boucher, Philippe Ciais and Laurent Li, for the opportunities they provided me to do this study and the chances they gave me to communicate with other researchers during conferences, and also for their help with my study and my life. It is a great honor to work with them. Before I came to France, I had no experience working with models and knew little about aerosols. Olivier's guidance helped me to quickly enter this field. Discussing with him gave me many new perspectives and helped a lot solving problems in my study. Besides his help in my study, he also helped significantly with my life at Paris. Without his help, I would not survive so easily. Philippe gave me lots of help on my study from the perspective of carbon cycle. I would specially thank him for organizing meetings to discuss my work every month. Every time talking with him I learn something new. His passion in science also inspires me. Laurent also helped me a lot with my work. As a new modeler, I had many troubles with the code when I began my work. Laurent's patient explanations on the processes and on the code helped me to learn the modeling tools fast. Also, he helped me a lot with my life here.

I would thank all my colleagues who helped with my study. I would give my special thanks to Daniel Goll, Ana Bastos and Fabienne Maignan. They spent time to discuss my work every week and helped significantly on all the main chapters of the thesis. I also thank Yves Balkanski, Nicolas Viovy, Shilong Piao, Nicolas Vuichard, Philippe Peylin, Alessandro Cescatti, Josefine Ghattas, Thibaut Lurton, Vladislav Bastrikov, Dan Zhu and Thomas Gasser, who gave me help and technical supports on my PhD work. I would thank colleagues from Australia, US and UK, as well as the flux network for kindly providing the data to finish the works presented in this thesis. I would thank all the coauthors and reviewers of the chapters

for their help in improving the manuscript. I also thank all the jury members for their agreement to join in and their time to review the work presented in this thesis.

During the three years, I harvested not only my thesis but also a lot of great colleagues and friends, at LMD, LSCE and from other labs and schools. Maxence Lefèvre, Binta Diallo, Alexandre Boissinot, Xiaoyi Shi, Vladimir Zakharov, Max Popp, Margaux Vals, Yanfeng Zhao, Addisu Semie, Yue Li, Wei Li, Xuhui Wang, Yan Sun, Dan Zhu, Yilong Wang, Bo Zheng, Zun Yin, KanKan Qin, Yao Zheng, Wei Zhang, Shiya Chen, Binhua Ma, Lin Zhang, Guanzheng Zhuang, Chao Yue, Karine Marquois, Anna-Lea Albright, Ludovic Touze-Peiffer, Jan Vatant d'Ollone, Friederike Hemmer, Roland Young, Flo Lemonnier, Kevin Olsen, Martin Turbet, Jinghui Lian, Itziar Garate-Lopez, Fuxing Wang, Xin Lin, Shan Li, Hui Yang, Can Zhao and many many. The list is very long, and I would give my thanks to all of them. The enjoyable time with them made my life in a foreign country easier and more colorful.

Finally, I would thank my parents and grandparents. Their supports gave me the courage to overcome hard times. I owe them a lot.

List of main acronyms:

AA: Anthropogenic aerosols

CCAA: Climate Change from Anthropogenic Aerosols

CMIP: Coupled Model Intercomparison Project

CRU: Climatic Research Unit

ESM: Earth System Model

Fdf: Fraction of diffuse radiation

GPP: Gross Primary Production

JRA: Japanese reanalysis

LAI: Leaf Area Index

LSM: Land Surface Model

LUE: Light Use Efficiency

NBP: Net Biome Production

NCEP: National Centers for Environmental Prediction

ORCHIDEE: Organizing Carbon and Hydrology In Dynamic Ecosystems

PAR: Photosynthetically Active Radiation

PFT: Plant Functional Type

TER: Total Ecosystem Respiration

VPD: water Vapor Pressure Deficit

Titre: Impacts des aérosols anthropiques sur le cycle du carbone terrestre

Mots clés: changement climatique, aérosols, le cycle du carbone terrestre, fertilisation par rayonnement diffus, modélisation

Résumé: Il est reconnu que les aérosols atmosphériques d'origine anthropique ont eu un impact significatif sur le système climatique au cours des dernières décennies via leurs interactions avec le rayonnement et les nuages. Outre ces processus physiques bien connus mais mal compris, des études récentes ont fait état de fortes influences des aérosols sur le cycle du carbone, en particulier sur sa composante terrestre. Les changements du cycle du carbone vont alors modifier le climat par le biais de la rétroaction climat-carbone. On ne sait toujours pas bien dans quelle mesure les aérosols anthropiques perturbent le cycle du carbone terrestre. Cette thèse vise à quantifier et à attribuer les impacts des aérosols anthropiques sur le cycle terrestre en utilisant une approche de modélisation.

Au chapitre 2, un ensemble de simulations « hors ligne » utilisant le modèle de surfaces continentales ORCHIDEE forcé par les champs climatiques de différents modèles climatiques de la génération CMIP5 ont été réalisées pour étudier les impacts des aérosols anthropiques sur le cycle du carbone terrestre au travers de leurs impacts sur le climat. Les résultats indiquent une augmentation du puits de carbone terrestre de 11,6 à 41,8 PgC cumulé entre 1850 et 2005 en raison des aérosols anthropiques. L'augmentation de la production nette du biome (net biome production, NBP) se situe principalement dans les tropiques et les latitudes moyennes de l'hémisphère nord. Le refroidissement induit par les aérosols est le principal facteur à l'origine de cette évolution de la NBP. Aux hautes latitudes, le refroidissement induit par les aérosols a provoqué une diminution plus forte de la production primaire brute (gross primary production, GPP) que de la respiration totale de l'écosystème (total ecosystem respiration, TER), ce qui a entraîné une baisse de la NBP. Aux latitudes moyennes, la diminution de la TER due au refroidissement est plus forte que celle de la GPP, ce qui entraîne une augmentation nette de la NBP. Aux basses latitudes, la NBP a également augmenté en raison de l'augmentation de la GPP due au refroidissement, mais la diminution des précipitations régionales en réponse aux

émissions d'aérosols anthropiques peut annuler l'effet de la température. Comme les modèles de climat sont actuellement en désaccord sur la manière dont les émissions d'aérosols affectent les précipitations tropicales, la modification des précipitations en réponse aux aérosols devient la principale source d'incertitude dans les changements de flux de C causés par les aérosols. Les résultats suggèrent qu'une meilleure compréhension et simulation de la manière dont les aérosols anthropiques affectent les précipitations dans les modèles de climat est nécessaire pour une attribution plus précise des effets des aérosols sur le cycle du carbone terrestre.

Le chapitre 3 présente le développement et l'évaluation d'une nouvelle version du modèle ORCHIDEE appelé ORCHIDEE_DF. Par rapport à la version standard d'ORCHIDEE, ORCHIDEE_DF comprend un nouveau module de partitionnement de la lumière pour séparer le rayonnement solaire descendant en ses composantes directe et diffuse, ainsi qu'un nouveau module de transfert radiatif pour simuler la transmission du rayonnement diffus et direct dans la canopée, et différentier l'absorption de la lumière par les feuilles éclairées et ombragées. Le nouveau modèle ORCHIDEE_DF a été évalué à l'aide d'observations de flux par la méthode « eddy covariance » provenant de 159 sites de mesures sur le globe. Par rapport au modèle standard, ORCHIDEE_DF améliore la simulation des GPP dans des conditions ensoleillées et simule bien la photosynthèse supérieure observée dans des conditions plus nuageuses pour la plupart des types fonctionnels de plantes (plant functional types, PFT). Les résultats d'ORCHIDEE_DF et de la version standard d'ORCHIDEE pris ensemble indiquent que la GPP plus importante dans des conditions nuageuses par rapport aux conditions ensoleillées est principalement due à l'augmentation de la lumière diffuse le matin et l'après-midi, et à la diminution du déficit en pression de vapeur d'eau (water vapor pressure deficit, VPD) et de la température de l'air à midi. Les effets positifs les plus importants de la lumière diffuse sur la photosynthèse se situent dans la plage de 5 à 20 °C et des VPD inférieures à 1 kPa. On constate que cet effet diminue lorsque les VPD deviennent trop importantes ou que la température tombe en dehors de cette plage, probablement parce que la conductance stomatale prend le contrôle de la photosynthèse. ORCHIDEE_DF sous-estime l'effet de la lumière diffuse à basse température dans toutes les PFT et surestime cet effet à haute température et à un VPD élevé

dans les prairies et les terres cultivées. Ce biais est probablement dû à la paramétrisation du modèle standard. Le nouveau modèle permet de mieux étudier l'impact des changements d'aérosols à grande échelle sur le bilan du carbone terrestre, à la fois dans la période historique et dans le contexte des futures politiques de qualité de l'air et/ou de l'ingénierie climatique.

Le chapitre 4 présente deux séries de simulations basées sur sur le modèle ORCHIDEE_DF forcé par l'ensemble de données climatiques CRUJRA, et les champs climatiques des simulations IPSL-CM6A-LR et vise à étudier systématiquement les impacts des changements induits par les aérosols sur le rayonnement diffus et des autres facteurs. Les deux séries de simulations montrent une augmentation du puits de carbone terrestre cumulatif de 6,8 PgC (données climatiques du CRUJRA) et de 15,9 PgC (données climatiques de l'IPSL-CM6A-LR) en réponse aux changements de la fraction de rayonnement diffus causé par les aérosols anthropiques au cours de la période historique, et cette augmentation se produit principalement après les années 1950. La série de simulations factorielles forcées par le climat IPSL montre que globalement, l'augmentation du puits de carbone terrestre anthropique causé par les aérosols est principalement due à l'effet de fertilisation diffuse par la lumière mais aussi à l'effet de refroidissement. En outre, une comparaison des différentes méthodes de reconstruction du champ de rayonnement diffus dans un scénario sans aérosol anthropique indique qu'il est essentiel de prendre en compte correctement la variabilité de la fraction de rayonnement diffus pour obtenir des flux de carbone non biaisés.

Bien que cette thèse ait permis d'acquérir une compréhension assez holistique des impacts des aérosols sur les écosystèmes terrestres, il subsiste des incertitudes dues aux limites des outils de modélisation et des plans d'expérience actuels. Pour réduire ces incertitudes, les travaux futurs doivent inclure les mécanismes manquants (par exemple, le dépôt de nutriments associé aux aérosols) dans les modèles de surface terrestre, recueillir davantage d'observations pertinentes pour l'étalonnage et concevoir des expériences pour étudier les impacts des aérosols dans des simulations entièrement couplées. Grâce à des scénarios futurs fiables d'émissions d'aérosols (tels que ceux du jeu de données SSP-RCP), les nouveaux outils de modélisation

devraient permettre de mieux évaluer et orienter l'élaboration des politiques de qualité de l'air relatives aux aérosols.

Title: Impacts of anthropogenic aerosols on the terrestrial carbon cycle

Key words: climate change, aerosols, terrestrial carbon cycle, diffuse light fertilization, modeling

Abstract: Anthropogenic atmospheric aerosols have been recognized to have significantly affected the climate system through their interactions with radiation and cloud during the last decades. Besides these well-known but poorly-understood physical processes in the atmosphere, recent studies reported strong influences of aerosols on the carbon cycle, especially its terrestrial component. The changes in carbon cycle will further alter the climate through the climate-carbon feedback. It remains uncertain how much anthropogenic aerosols perturb the land carbon cycle. This thesis aims to quantify and attribute the impacts of anthropogenic aerosols on the terrestrial cycle using a modeling approach.

In Chapter 2, a set of offline simulations using the ORCHIDEE land surface model driven by climate fields from different CMIP5 generation climate models were performed to investigate the impacts of anthropogenic aerosols on the land C cycle through their impacts on climate. The results indicate an increased cumulative land C sink of 11.6-41.8 PgC during 1850-2005 due to anthropogenic aerosols. The increase in net biome production (NBP) is mainly found in the tropics and northern mid latitudes. Aerosol-induced cooling is the main factor driving this NBP changes. At high latitudes, aerosol-induced cooling caused a stronger decrease in gross primary production (GPP) than in total ecosystem respiration (TER), leading to lower NBP. At mid latitudes, cooling-induced decrease in TER is stronger than for GPP, resulting in a net NBP increase. At low latitudes, NBP was also enhanced due to the cooling-induced GPP increase, but regional precipitation decline in response to anthropogenic aerosol emissions may negate the effect of temperature. As climate models currently disagree on how aerosol emissions affect tropical precipitation, the precipitation change in response to aerosols becomes the main source of uncertainty in aerosol-caused C flux changes. The results suggest that better understanding and simulation of how anthropogenic aerosols affect precipitation in climate

models is required for a more accurate attribution of aerosol effects on the terrestrial carbon cycle.

Chapter 3 presents the development and evaluation of a new version of ORCHIDEE model named ORCHIDEE_DF. Compared with the standard ORCHIDEE model (ORCHIDEE trunk), ORCHIDEE_DF includes a new light partitioning module to separate the downward shortwave radiation into direct and diffuse components, as well as a new canopy radiative transmission module to simulate the transmission of diffuse and direct radiation, and the light absorption of sunlit and shaded leaves separately. The new model ORCHIDEE_DF was evaluated using flux observations from 159 eddy covariance sites over the globe. Compared with the original model, ORCHIDEE_DF improves the GPP simulation under sunny conditions and captures the observed higher photosynthesis under cloudier conditions for most plant functional types (PFTs). The results from ORCHIDEE_DF and standard ORCHIDEE together indicate that the larger GPP under cloudy conditions compared to sunny conditions is mainly driven by increased diffuse light in the morning and in the afternoon, and by the decreased water vapor pressure deficit (VPD) and air temperature at midday. The strongest positive effects of diffuse light on photosynthesis are found in the range 5-20 °C and VPD<1 kPa. This effect is found to decrease when VPD becomes too large, or temperature falls outside that range, likely because stomatal conductance takes control of photosynthesis. ORCHIDEE_DF underestimates the diffuse light effect at low temperature in all PFTs and overestimates this effect at high temperature and high VPD in grasslands and croplands. This bias is likely due to the parameterization in the original model. The new model has the potential to better investigate the impact of large-scale aerosol changes on the terrestrial carbon budget, both in the historical period and in the context of future air quality policies and/or climate engineering.

Using empirically tuned ORCHIDEE_DF, Chapter 4 performed two sets of simulations based on the observation-based CRUJRA climate dataset, and the climate fields from IPSL-CM6A-LR simulations to systematically investigate the impacts of aerosol-induced changes in diffuse radiation and other factors. The two sets of simulations find an enhanced cumulative land C sink of 6.8 PgC (CRUJRA climate) and 15.9 PgC (IPSL-CM6A-LR climate) in response

to the anthropogenic aerosol-caused diffuse radiation fraction changes during the historical period and this enhancement mainly occurs after the 1950s.A series of factorial simulations driven by IPSL climate show that globally, the anthropogenic aerosol-induced land C sink increase is mainly due to the diffuse light fertilization effect but there is also a contribution from the cooling effect. Furthermore, a comparison of different methods reconstructing the diffuse radiation field under no anthropogenic aerosol scenario indicates that correctly considering the variability of diffuse radiation fraction is essential to obtain unbiased carbon fluxes.

Although this thesis gained a relatively systematic understanding in aerosol impacts on terrestrial ecosystems, there remain uncertainties due to the limit of current modeling tools and experimental designs. To reduce these uncertainties, future work needs to include representation of currently missing mechanisms (e.g., deposition of nutrients associated with aerosols) into land surface models, collect more relevant observations for calibration, and design experiments to investigate aerosol impacts in fully coupled simulations. With the help of reliable future scenarios in aerosol emissions (such as those from the SSP-RCP dataset), improved modeling tools are expected to better evaluate the aerosol-related air quality policies.

Table of contents

CHAPTER 1. GENERAL INTRODUCTION 1

1.1 THE TERRESTRIAL CARBON CYCLE 2

1.1.1 Main processes in the terrestrial carbon cycle 2

1.1.2 Factors affecting the terrestrial C cycle 3

1.1.3 Climate-Carbon feedback 6

1.2 ATMOSPHERIC AEROSOLS 7

1.2.1 A brief introduction to atmospheric aerosols 7

1.2.2 Aerosol-radiation interactions and aerosol-cloud interactions 9

1.2.3 Impacts of aerosols on terrestrial C cycle 11

1.3 METHODS INVESTIGATING AEROSOL IMPACTS. 13

1.4 THE OBJECTIVES OF THE THESIS 15

CHAPTER 2. IMPACTS OF ANTHROPOGENIC AEROSOLS ON LAND C FLUXES THROUGH CHANGING CLIMATE 16

SUMMARY 16

CHAPTER 3. MODELLING THE IMPACTS OF DIFFUSE LIGHT FRACTION ON PHOTOSYNTHESIS 48

SUMMARY 48

3.1 INTRODUCTION 49

3.2 DATA AND METHOD 51

3.2.1 Model description 51

3.2.2 Flux data and site level simulations 61

3.2.3 Analyses 62

3.3 RESULTS 65

3.3.1 Diffuse light fraction 65

3.3.2 General model performance 65

3.3.3 Effects of diffuse light on GPP and LUE 68

3.3.4 Interactions between diffuse light and environmental factors 71

3.4 DISCUSSION 76

3.4.1 Improvement of ORCHIDEE_DF 76

3.4.2 Factors affecting diffuse light effect on GPP 77

3.4.3 Uncertainties and Limitations 78

3.5 CONCLUSION 79

SUPPORTING INFORMATION FOR CHAPTER 3 81

CHAPTER 4. AEROSOL IMPACTS ON THE LAND CARBON CYCLE THROUGH CHANGING DIFFUSE RADIATION 89

SUMMARY 89

4.1 INTRODUCTION 89

4.2 DATA AND METHODS 91

4.2.1 ORCHIDEE_DF model 91

4.2.2 Forcing data and Experimental design 94

4.3 RESULTS 99

4.3.1 CRUJRA simulations 99

4.3.2 IPSL simulations 104

4.4 DISCUSSION 117

4.4.1 Fdf response to anthropogenic aerosols 117

4.4.2 Methods to reconstruct NoAA Fdf 118

4.4.3 Global impacts of diffuse radiation on C fluxes 119

4.4.4 The impacts of Radiation quality vs Radiation quantity 119

4.4.5 The main factors causing C flux changes 120

4.4.6 The impacts of volcanoes 122

4.4.7 Uncertainties 123

4.5 CONCLUSION 124

CHAPTER 5. CONCLUSION AND PERSPECTIVES 126

REFERENCES 132

Chapter 1. General introduction

The climate system has been being strongly affected by the increasingly intensive anthropogenic activities since the industrial revolution in the 18th century. During the last century, evidences have shown significant changes in the atmosphere composition, increase in, the Earth's surface air temperature, melting rate of glaciers, elevation of sea level, etc. (Stocker *et al.*, 2013). These changes have impacted both natural and human systems, and will likely affect human well-being more strongly and challenge the sustainability of human societies in the future.

A good understanding of the climate system is the basis to project future climate and to face the associated challenges. There is a wide consensus in the scientific community that global warming is primarily driven by the increasing concentration of greenhouse gases in the atmosphere, especially CO_2 (Stocker *et al.*, 2013), whose concentration has increased by about 100 ppm, or near one third since 1958. This increase in atmospheric CO_2 can be attributed to anthropogenic emissions through fossil fuel burning and land use changes (Friedlingstein *et al.*, 2019), but there remain uncertainties on current carbon budget and its projections because the biosphere may also release or absorb CO_2 when the atmospheric CO_2 concentration and climate changes. It has been suggested that the natural terrestrial ecosystem is a C sink of 160 ±90 PgC in response to the changes in CO_2 concentration and climate since 1750 (Ciais *et al.*, 2013). This C sink in turn affect the atmospheric CO_2 concentration and consequently the climate. This feedback, referred to as climate-carbon feedback, is still poorly understood (Friedlingstein *et al.*, 2006). Apart from greenhouse gases, anthropogenic aerosols are also thought to have a considerable impact on climate as they alter the radiation budget at land surface (Heywood and Boucher, 2000). This climate change from anthropogenic aerosols will also affect the climate-carbon feedback (Jones *et al.*, 2003). Moreover, recent studies have found that the terrestrial ecosystems are also affected by the aerosol-caused changes in diffuse radiation (Gu *et al.*, 2003; Mercado *et al.*, 2009) and nutrients deposition (Magnani *et al.*, 2007; Wang *et al.* 2017). However, there remains no study systematically investigating the impacts of anthropogenic aerosols on carbon cycle. This gap of understanding on how much do anthropogenic aerosols affect the C cycle of ecosystems may cause large uncertainty in

future climate projections and will increase the risks in making aerosol emission policies.

1.1 The terrestrial carbon cycle

1.1.1 Main processes in the terrestrial carbon cycle

The carbon cycle is influenced by all carbon (C) exchanges at the Earth's surface among the atmosphere, the biosphere, the hydrosphere, the geosphere and the lithosphere. The terrestrial ecosystems have the largest active C pools in this system. The total C stored in biomass and soil is 2000-3000 PgC, which is 4-6 times of the amount in the atmosphere (Ciais *et al.*, 2013). Also, the gross C exchanges between atmosphere and the terrestrial ecosystems due to photosynthesis and respirations are the largest C fluxes in and out of the atmospheric C pool. Therefore, this thesis will focus on the C fluxes of the terrestrial ecosystems.

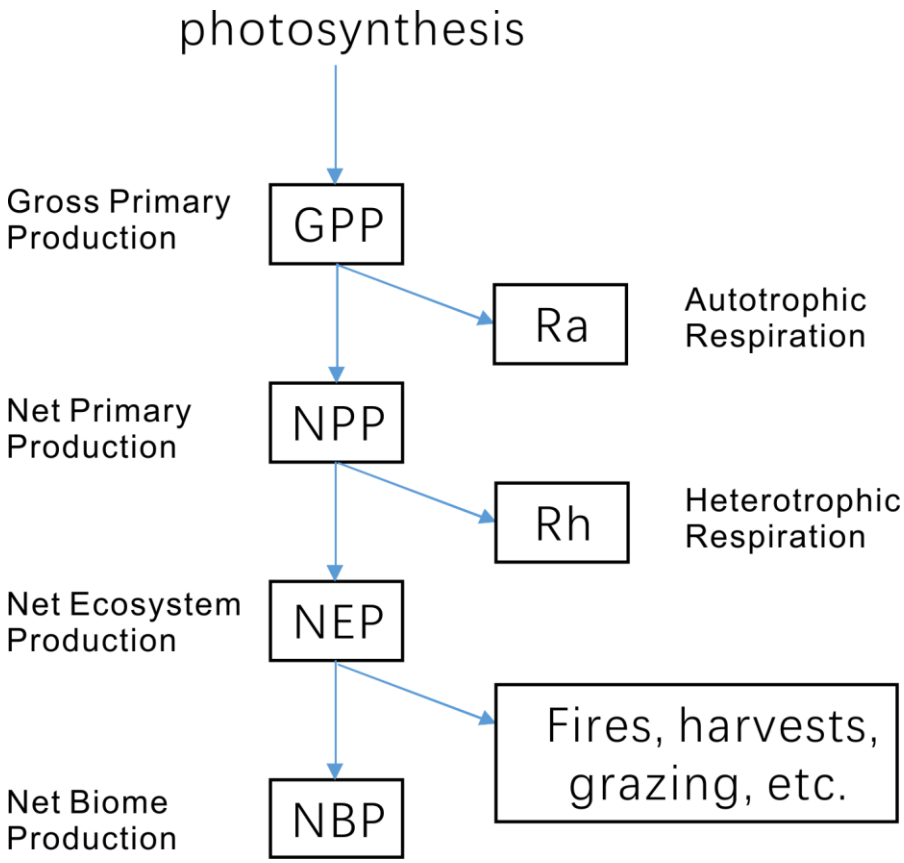

Figure 1.1 A Schematic of the main C fluxes in land C cycle

Plant photosynthesis is almost the only way through which atmospheric CO_2 get can fixed by terrestrial ecosystems. The total C fixed by photosynthesis of an ecosystem is called gross primary production, or GPP, which was estimated to be 109-175 PgC yr^{-1} as a global total (Zhao *et al.*, 2005; Beer *et al.*, 2010; Jung *et al.*, 2011; Welp *et al.*, 2011; Piao *et al.*, 2013).

Because the plants need energy to grow and to maintain their lives, a large proportion of the photosynthesis products is used through respiration by the plants themselves, and the C in these products is released as CO_2 to the atmosphere. This C loss due to plant respiration is referred to as autotrophic respiration, or Ra. The C flux associated with the remaining products is called net primary production, or NPP. The global NPP is estimated about 44-70 PgC yr^{-1} (Cramer *et al.*, 1999; Zhao *et al.*, 2005; Yu *et al.*, 2017).

Most of the NPP will go to litter and soil C pools after the death of plants and leaf shedding. These organic C will be decomposed by microbes through their respirations. This respiration is called heterotrophic respiration, or Rh. The remaining C left in the ecosystem is referred to as net ecosystem production, or NEP. The sum of Ra and Rh is often defined as the total ecosystem respiration (TER). Global TER is comparable but slightly smaller than GPP in magnitude.

Apart from respirations, C stored in ecosystems may also get released through other processes, such as fire, harvest or grazing. These C fluxes are small compared to respirations but important for C balance. The difference between GPP and all the effluxes (fluxes which release C from the ecosystem) is called net biome production, or NBP. In other words, NBP represents the C gain or loss of land ecosystems. Ecosystems with positive NBP absorb C from atmosphere and act as C sink. While those with negative NBP release C to atmosphere and act as C source.

1.1.2 Factors affecting the terrestrial C cycle

The main C fluxes introduced above are contributed by photosynthesis and respiration of organisms. Due to the dependence of the biochemical reactions involved in the C cycle to environmental factors, the terrestrial C fluxes are strongly affected by climate.

Temperature is one of the most important factors affecting both photosynthesis and respiration. The photosynthesis has been found to be maximum under an optimal temperature. Whenever temperature increases or decreases around that optimal temperature, the photosynthesis rate declines (Berry and Bjorkman, 1980). This optimal temperature may vary spatially and temporally at different scales (Huang *et al.*, 2019; Yamori *et al.*, 2013; Smith and Dukes, 2017), in order to acclimate (temporal trait changes within lifetime, often reversible) or adapt (permanent trait changes over generations, not reversible) to the various environmental temperature. However, there are limits on how plants (and therefore ecosystems) can acclimate their optimal temperature. When temperature is too high or too low, plants may get irreversible damage. Because of the complex mechanisms how the photosynthesis acclimates to temperature at different time scales, as well as the large variety of this acclimation among species, the quantitative understanding on photosynthesis acclimation at large scale remains poor (Kattge and Knorr, 2007; Smith and Dukes, 2013; Mercado *et al.*, 2018).

Apart from affecting photosynthesis rate, temperature variations also affect the length of the growing season. For example, the multi-daily cumulative temperature in degree above a threshold (growing degree day), is found to be a good indicator of the start of the growing season for many plant species in temperature-limited regions. For some boreal species, some period of cold weather (chilling) during their dormancy in winter is required before the start of growing season (Yu *et al.*, 2010). Besides the chilling requirements, observations at flux sites also found that warmer spring advanced the start of the growing season and increased the annual GPP (Barr *et al.*, 2002; Niemand *et al.*, 2005). A 7 to 14-day earlier start of the growing season is observed by remote sensing since the 1980s at different regions in northern mid to high latitudes and is thought to be mainly the response to a warming climate (Piao *et al.*, 2019).

Temperature is also an important factor affecting respiration, especially for soil respiration that builds on a large soil C pool. A plenty of studies have used an exponentially increase of soil respiration rates with soil temperature (Lloyd and Taylor, 1994; Davidson *et al.*, 1998; Peng *et al.*, 2009) following the theory of van't Hoff (1899). Similarly, the maintenance respiration (plant respiration to maintain the living biomass, an important fraction of Ra) also shows an exponential relationship with temperature. Under the background of global warming, the ecosystem respirations are

also expected to increase, which will accelerate the turnover of C pools in ecosystems, and consequently play a considerable role in climate-carbon feedback.

Precipitation is another crucial factor regulating C fluxes. Water is one of the reactants in photosynthetic reaction. The light-dependent reactions in photosynthesis will not happen without the participation of water. Also, water availability also affects stomatal conductance of CO_2. When plant is water stressed, the stomata will close to prevent water loss, which simultaneously prevents CO_2 from entering leaf tissues and hinder the photosynthesis (Schippers *et al.*, 2015). Persistent severe drought may cause mortality of plants due to C starvation, hydraulic failure etc. (Mencuccini *et al.*, 2015). At larger scale, drought may increase the probability and intensity of fires (Brando *et al.*, 2014).

Respiration is found to be affected by soil moisture, which is strongly affected by precipitation. In situ observations from different ecosystems have shown that soil respiration can be inhibited by drought (Suseela *et al.*, 2012; Yuste *et al.*, 2003; Saleska *et al.*, 2003). This inhibition can be explained by the reduced substrate diffusion and the lowered intracellular water potential under dry conditions (Stark & Firestone, 1995). Inversely, when precipitation is too high, soil respiration may also decrease due to the inhibition of oxygen diffusion in wet soil (Suseela *et al.*, 2012).

Solar radiation at 400-700 nm (photosynthetically active radiation, or PAR) provides energy for photosynthesis. Therefore, it determines the potential GPP when other factors are not limiting photosynthesis. A light addition experiment in tropical forests during cloudy period found that increase PAR will result in higher CO_2 uptake in this system, indicating that radiation is the factor limiting CO2 uptake during rainy season (Graham *et al.*, 2003). Observations also show that some tropical forests tend to have higher GPP during sunnier dry seasons compared with cloud season (Saleska *et al.*, 2003). A global study suggested that in most tropical and subtropical forests, radiation is the main limiting factor for NPP (Nemani *et al.*, 2003). A recent study found that whether the ecosystem is radiation-limited depends on the annual precipitation received by the system (Guan *et al.*, 2015).

It should be noted that the directional property of solar radiation is also an important factor regulating photosynthesis. For a given radiation level, diffuse radiation often results in higher GPP than direct radiation. This is because direct radiation

distributes more photons on sunlit leaves, which are often light saturated, whereas diffuse radiation is more evenly distributed in canopy and can significantly enhance the photosynthesis of shaded leaves (Gu *et al.*, 2003; Mercado *et al.*, 2009; Wang *et al.*, 2018).

Apart from climate factors, ambient CO_2 concentration also plays an important role. The majority of Free-air CO_2 Enrichment (FACE) experiments suggested that increasing CO_2 concentration can increase water use efficiency and light use efficiency, resulting in higher production (Norby *et al.*, 2005; Ainsworth and Long, 2004; Nowak *et al.*, 2004). This CO_2 fertilization effect differs among different ecosystems and depends on the magnitude of CO_2 enrichment (Ainsworth and Long, 2004; Nowak *et al.*, 2004).

Mineral nutrients play essential roles in the construction of plant tissues and they participate to plant and microbe metabolism. For instance, nitrogen (N) is one of the core element needed for the enzymes involved in both photosynthesis and respiration. Therefore, C fluxes in ecosystems may also get limited by nutrient availability besides climate factors. Nitrogen addition experiments have shown that N deposition could enhance NPP in many ecosystems across the world (LeBauer *et al.*, 2008). Experiments suggested that N limitation may weaken the expected NPP increase under elevated CO_2 concentration (i.e. modulation of CO_2 fertilization effect by N availability) (Norby *et al.*, 2010). The deposition of N also affects respiration (Sun *et al.*, 2014). A meta-analysis suggested that N deposition may decrease soil respiration by reducing underground C allocation, changing soil microbe community or stabilizing soil organic matters (Janssens *et al.*, 2010). Besides N, phosphorus (P) is also suggested to limit C fixation in tropical regions (Sun *et al.*, 2017).

1.1.3 Climate-Carbon feedback

As introduced in Section 1.1.2, terrestrial C fluxes are regulated by climate and atmospheric CO_2 concentration, meanwhile the interannual variation of atmospheric CO_2 concentration is strongly affected by net C fluxes of terrestrial ecosystems (Friedlingstein *et al.*, 2019), which could be further explained by the variation of climate. Therefore, there exist a range of feedbacks between climate and the C cycle.

To investigate these feedbacks, the Coupled Climate–Carbon Cycle Model Intercomparison Project (C4MIP) experiments were designed, which use fully and partly coupled simulations to evaluate the contribution of climate-carbon feedbacks to the carbon cycle and to climate changes (Jones *et al.*, 2016). Under this framework, Friedlingstein *et al.* (2006) showed a positive climate-carbon feedback (i.e., the feedback will cause higher atmospheric CO_2 concentration and stronger warming) at the end of the 21st century using simulations from 11 Earth System Models (ESMs). However, the magnitude of the warming contributed by climate-carbon feedback remains very uncertain. Also, there is no consensus on whether the observed changes in land C fluxes are mainly attributable to primary production or to respiration.

1.2 Atmospheric aerosols

1.2.1 A brief introduction to atmospheric aerosols

In general, an aerosol refers to a suspension of solid or liquid particles in air. In climate sciences, cloud particles are often differentiated from other particles, hence "aerosols" is often used to represent the suspensions of solid or liquid particles except the hydrometeors (Boucher, 2015). This definition is hereafter used in this thesis.

Atmospheric aerosols can be classified into primary aerosols and secondary aerosols according to whether the aerosols are emitted as particles directly (primary aerosols) or come from condensation of atmospheric gas-phase species during chemical processes (secondary aerosols). These gas-phase species are called aerosol precursors.

According to their source, atmospheric aerosols can be divided into natural aerosols and anthropogenic aerosols. Natural aerosols mainly include biogenic (organic) aerosols derived from volatile organic compounds emitted by terrestrial plants and marine algae, dust lifted by winds, sea spray aerosols, black carbon from wildfires. Apart from the above ones, volcanic eruptions can also emit a large quantity of sulphate aerosol precursors into the atmosphere including in the stratospheres into higher atmosphere. Anthropogenic aerosols are emitted from anthropogenic activities such as fossil fuel burning, mining, agriculture and land use change. These activities can result in emissions of precursors of sulphate, nitrate and organic aerosols, but also primary black carbon and organic aerosols. Fly ash and industrial dust are other types of

anthropogenic aerosols. In natural conditions, atmospheric aerosols are often a mixture of different chemicals. These mixtures can be of different particles with pure chemical composition each (external mixture), or of particles composed by well mixed chemicals (internal mixture). The mixing can strongly affect the particle physics and lead to different aerosol properties (Boucher, 2015).

The various source and types, as well as complex mixture of aerosols result in a heterogeneous spatiotemporal distribution of aerosols (Figure 1.2). Industrialized regions such as East Asia, Europe and North America generally have higher aerosol concentration than other regions, as the intense human activities strongly increase the emission of anthropogenic aerosols and their precursors. Besides these regions, deserts such as Sahal also have high aerosol concentration. This is because that the non-vegetated ground in deserts can easily become a source of dust aerosols when wind is strong. Tropical forest regions may also have high aerosol concentrations because of the large production of organic aerosol precursors in these forests. In addition, wild fires can occasionally cause high concentration of black carbon aerosols near the burned regions.

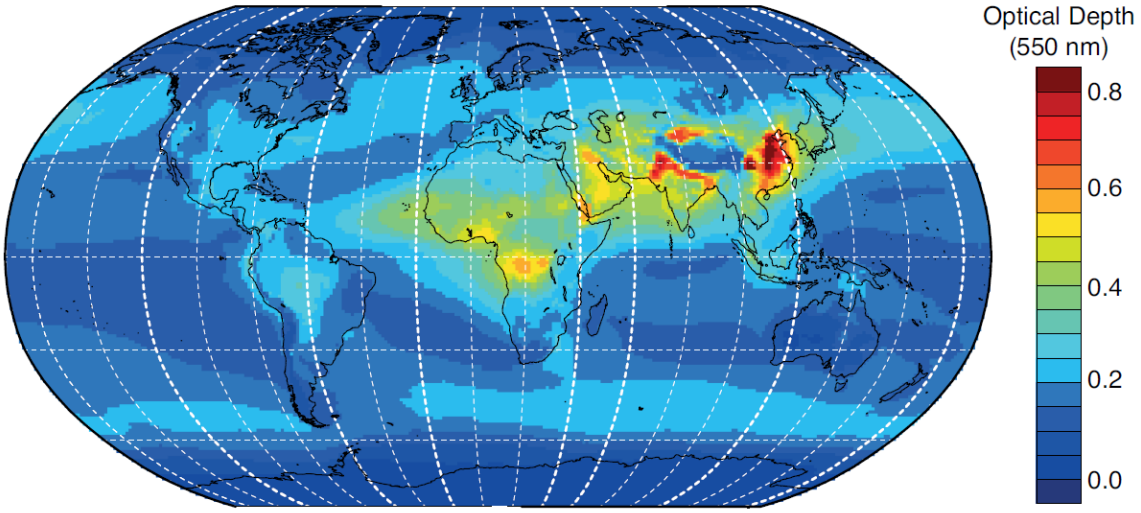

Figure 1.2 The spatial distribution of 550 nm aerosol optical depth during 2003-2010 from the European Centre for Medium Range Weather Forecasts (ECMWF) Integrated Forecast System model with assimilation of Moderate Resolution Imaging Spectrometer (MODIS) aerosol optical depth. (adapted from Boucher et al., 2013)

1.2.2 Aerosol-radiation interactions and aerosol-cloud interactions

The most known and studied mechanisms how aerosols affect climate system are aerosol-radiation interactions and aerosol-cloud interactions (Heywood & Boucher 2000). Aerosol-radiation interactions happen through the scattering and absorption of (essentially solar) radiation by aerosols. Because part of the irradiance is absorbed or scattered back to outer space during this process, aerosol-radiation interaction often causes a cooler surface and lead to a cooler climate. An exception occurs if the aerosol is very absorbing (e.g. black carbon) and/or the land surface is covered by snow or ice, resulting in a high albedo. In such case, the absorption of this aerosol may warm the climate system although locally it may still cool the surface because levels of solar radiation at the surface decreases. Globally, aerosol-radiation interactions are suggested to cause a radiative forcing of –0.45 (–0.95 to +0.05) W m^{-2} (Boucher *et al.*, 2013).

Aerosol-cloud interactions occur because the formation of clouds can be affected by aerosols (Figure 1.3). Aerosols as a suspension of particles often serve as cloud

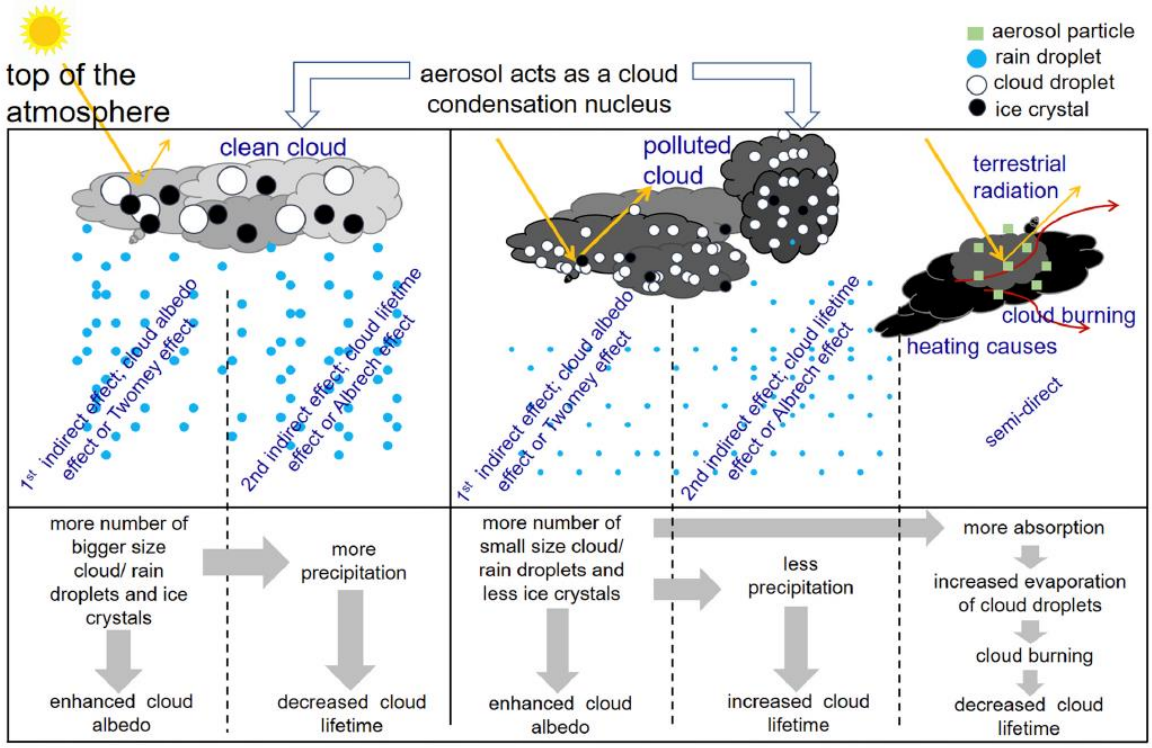

Figure 1.3. A Schematic of aerosol-cloud interactions. (from Kuniyal and Guleria, 2019)

condensation nuclei (CCN), so the presence of anthropogenic aerosols result in an increase in cloud condensation nuclei concentration. This increase in CCN further changes the size distribution of cloud droplets, and in turn alters the distribution, reflectance and life time of clouds. For a given cloud water content, more and smaller droplets leads to higher cloud reflectance. Aerosol-cloud interactions are estimated to cause a radiatve forcing of –0.45 (–1.2 to 0.0) W m^{-2} globally (Boucher *et al.*, 2013).

The aerosol radiative forcing is highly heterogeneous (Figure 1.4). Generally, the regions with strong negative aerosol radiative forcing (<−1 W m^{-2}) are mainly distributed in East and South Asia, Europe, East US, where intense anthropogenic activities emitted large amount of sulphate and nitrate aerosols and aerosol precursors.

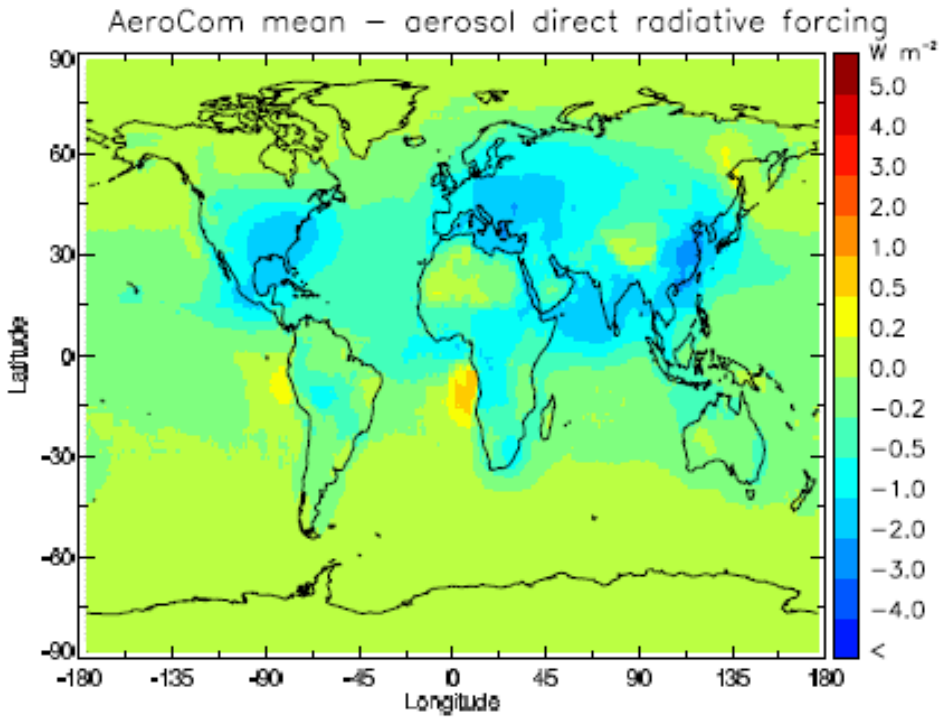

Figure 1.4 The spatial distribution of anthropogenic aerosol radiative forcing at the top of the atmosphere at 2000 according to simulations on 9 AeroCom models. (adapted from Schulz et al., 2006)

1.2.3 Impacts of aerosols on terrestrial C cycle

Aerosols can affect the terrestrial C cycle in multiple ways (Figure 1.5). The first way is through their contribution to changing climate. Generally, the negative radiative forcing caused by aerosols results in lower temperature and a weaker solar irradiance at land surface. The precipitation changes in response to aerosol emissions remain poorly understood. These changes in climate in turn alter the C fluxes. This impact is implicitly included in previous fully coupled simulations using earth system models, however, rarely quantified.

Jones *et al.* (2003) investigated the impacts of sulphate aerosols on the C cycle by comparing coupled simulations with and without sulphate aerosol forcing on HadCM3L. Their study considered the aerosol-radiation interaction and the aerosol impacts on cloud albedo, but omitted the impacts of aerosols on cloud lifetime. The results suggested that sulphate aerosols can increase global C sink through their cooling effect, which suppressed the increasing soil respiration under a warming climate. A similar study was performed by Mahowald *et al.* (2011) using the Community Climate System Model (CCSM3.1) model. However, their study showed a relatively small impact of aerosols on global C cycle and attributed it to the weaker climate-carbon feedback in their model. There is no consensus on the impacts of aerosol-induced climate change on the land C cycle.

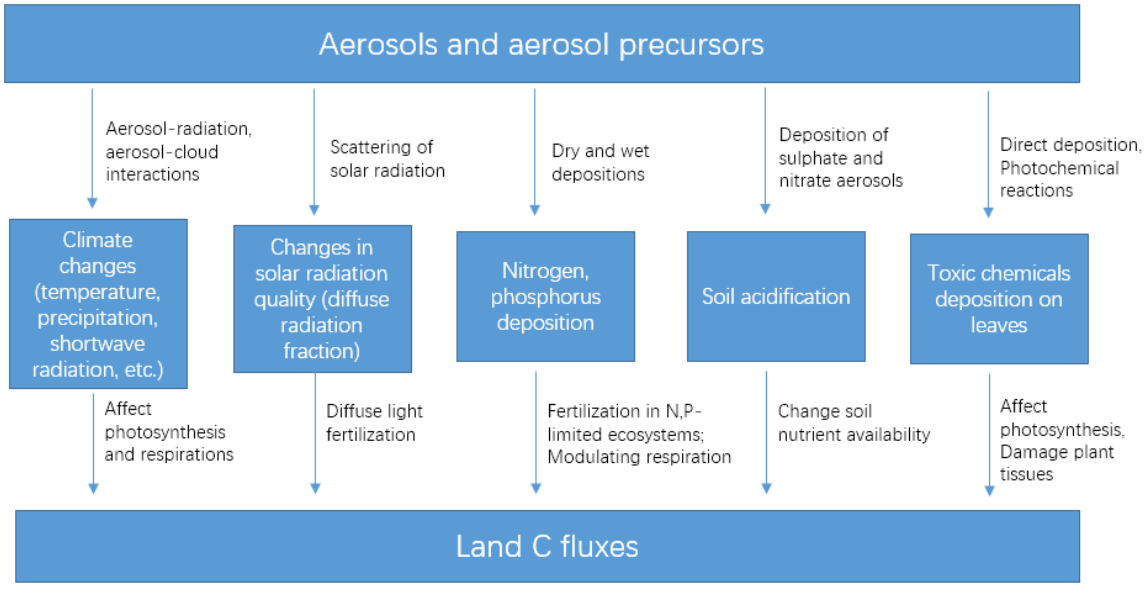

Figure 1.5 The main pathways how aerosols affect the terrestrial C cycle

Besides changing climate, aerosols can also alter the land C fluxes through a pathway named diffuse light fertilization. As atmospheric aerosols scatter solar radiation before it reaches the vegetation canopy, the solar radiation reaching the surface often show a more homogeneous directional distribution (higher diffuse radiation fraction) when aerosol concentration is high. This in turn affects GPP due to the different light use efficiency of diffuse and direct solar radiation. A site level study using eddy flux observations has shown that the increase of diffuse radiation after the eruption of the Mount Pinatubo increased the noontime photosynthesis by over 20% (Gu *et al.*, 2003). Several other studies also reported enhanced photosynthesis under conditions with more diffuse radiation for a given level of total solar irradiance (Gu *et al.*, 2002; Niyogi *et al.*, 2004; Alton *et al.*, 2007). At the global scale, Mercado *et al.* (2009) used the JULES land surface model to assess the impacts of changes in diffuse light fraction. Their study found that the changes of diffuse light fraction enhanced the global land C sink by about one quarter during 1960-1999. The robustness of this result remains difficult to test due to the lack of such processes in other land surface models.

Apart from their impacts on climate and radiation quality, some aerosols can deposit nutrients into terrestrial ecosystems through their deposition. Since many terrestrial ecosystems are nitrogen or phosphorus limited, the deposition of the aerosols containing N and P elements can fertilize the ecosystems and enhance C fixation. The impacts of N deposition have been investigated by several studies using various methods. For instance, based on C:N ratio, Schindler and Bayley (1993) estimated a global C sink of 1.0 PgC yr^{-1} to 2.3 PgC yr^{-1} due to N deposition using N budget estimations in 1980s. Based on CENTURY model, Townsend *et al.* (1996) and Holland *et al.* (1997) estimated a global N deposition-induced C sink from 0.3 PgC yr^{-1} to 2.0 PgC yr^{-1} around 1990. Liu and Greaver (2009) analysed the results from over a hundred of N addition experiments and suggested that the global C sink stimulated by N is 0.35 PgC yr^{-1} to 0.58 PgC yr^{-1} using N deposition from mid 1990s and agricultural N use in 2000s. Using stoichiometry of different part of plants, Wang *et al.* (2017) estimated the N deposition induced C sink in forests during 1997-2013 as 0.14 Pg C yr^{-1} to 0.4 Pg C yr^{-1}. Recently, the impacts of N in ecosystems has been added implicitly or explicitly to a number of land surface models (Zaehle and Dalmonech, 2011). Model simulations suggested increased global C sink due to N deposition from 0.2 PgC yr^{-1} to 0.5 PgC yr^{-1} in 1990s (Zaehle and Dalmonech, 2011).

In contrast to N deposition, the impact of P deposition remains poorly understood. This is because the lack of P deposition data. Wang *et al.* (2017) estimated global P deposition and assessed the impact of P deposition on forest C balance. Their results showed that P deposition increased forest C sink by −0.05 PgC yr^{-1} to 0.15 PgC yr^{-1} during 1997-2013.

Besides the mechanisms above, the sulphate and nitrate aerosols/precursors (mainly anthropogenic) can interact with clouds and reduce the pH of rainwater (Rodhe *et al.*, 2002). This acidification of rain may cause plant tissue damage and will lead to a decreased soil pH (i.e. increase hydrogen ions, or H^+). Acid soil solutions can dissolve metal ions that are bound in soil and cause a leaching of these nutrients, which can affect plant physiology and consequently the C fluxes.

Finally, sulphate aerosols can damage photosynthesis tissues (Eliseev, 2015). Also, some aerosols can participate in photochemical reactions and produce near surface ozone, which also damage leaf tissues and inhibit photosynthesis (Sitch *et al.*, 2007).

1.3 Methods investigating aerosol impacts.

Intensive measurements of C fluxes in field were not available before the appearance of eddy covariance technique. Using this technique, a network of C flux sites was built across the world (Baldocchi *et al.*, 2001). These measurements have provided and continue to provide valuable information understanding the responses of ecosystems to different environmental factors including atmospheric aerosols. For instance, using in situ flux observations, Gu *et al.* (1999, 2002, 2003) investigated the response of land ecosystems to changing diffuse radiation, and found that volcanic aerosols from the eruption of Mount Pinatubo can enhance the C fixation in a temperate deciduous forest. Some studies applied statistical methods or modeling tools to flux site observations to separate the effects of aerosol or cloud-caused diffuse radiation change and water vapor deficit change (Knohl and Baldocchi, 2008; Cheng *et al.*, 2014). However, it remains very difficult to fully understand the aerosol impacts from such observations alone because of the high complexity of land ecosystems and the multiple interactions among processes related to aerosols.

Apart from eddy covariance technique, some other tools were also developed to measure C fluxes directly at smaller scale (e.g. leaf level). There measurements give

limited information on the entire ecosystem, but can be used to monitor the response of leaves to a single impact of aerosols under more controlled conditions. These data can give a deeper insight into the mechanisms of how aerosols affect photosynthesis. For example, Li *et al.* (2014) used measurements in greenhouse to investigate how diffuse radiation changes the distribution of light and the photosynthesis rate in canopy. Using leaf-level measurements, Wang *et al.* (2018) found different mechanism how sunlit and shaded leaves respond to diffuse radiation changes.

One limit of such observation is that they are difficult to scale up from single sites or even networks to the large scale because of the complex interactions among aerosol-induced environmental factor changes and the large spatiotemporal heterogeneity of ecosystems and aerosols. One possible way to learn more on these processes is through the use of mechanism-based vegetation models. These models can be further embedded into land surface models or earth system models and be used to assess the impacts of aerosol at regional to global scales. Furthermore, since it is much easier to control environmental conditions in simulation experiments, these models are able to be used to separate aerosol impacts from other factors. Current global estimations of aerosol impacts are mostly based on model simulations (Jones *et al.*, 2003; Mercado *et al.*, 2009; Mahowald *et al.*, 2011). However, due to the limited understanding of some processes and a number of assumptions in models, the modelling approach always suffers from large uncertainties. Simulations performed using different models can thus give different aerosol impacts, e.g. Jones *et al.* (2003) and Mahowald *et al.* (2011). One way to understand the uncertainty and make more confident estimation and attribution of aerosol impacts is to use multiple models to simulate the evolution of the system under a standard framework with well-designed experiments, and analyze the results from different models together. Current multi-model comparison projects (MIPs) provide opportunities to understand and maybe reduce the uncertainty from climate field when investigating large scale aerosol impacts. Another problem the modelling approach is that some processes are not well represented or not represented at all in the current generation of current models. There is a limited number of land surface models that include the differential canopy light transmission of direct and diffuse radiation (Dai *et al.*, 2004, Mercado *et al.*, 2009). Most existing ones uses oversimplified parameterizations in a single-layer canopy and cannot represent the vertical heterogeneity of leaf traits (Dai *et al.*, 2004). In terms of nutrient, only a few number

of models have incompletely considered the N-related processes (Zaehle and Dalmonech, 2011), and fewer models considered phosphorus (Goll *et al.*, 2017; Wang *et al.*, 2010; Wang *et al.*, 2018). The soil pH impact remains poorly understood and absent in land surface models. For toxic chemical impacts, Sitch *et al.* (2007) and Chen (2013) have considered the impacts of ozone in large scale models, while most other chemicals remain absent. To fully understand the aerosol impacts, these missing processes are needed to be added to current land surface models.

1.4 The objectives of the thesis

Anthropogenic aerosols are known to play an important role in the climate system through aerosol-radiative and aerosol-cloud interactions. However, the impacts of aerosols on the global carbon cycle are not well understood. This thesis aims to investigate the impacts of anthropogenic aerosols on terrestrial ecosystems during the "historical" period since the industrial revolution through different pathways. In Chapter 2, the ORCHIDEE land surface model is driven by different climate fields from CMIP5 experiments to assess the impacts of climate change induced by anthropogenic aerosols (CCAA) on global land C budget and to identify why there are large uncertainties in current estimates. Chapter 3 will introduce a new version of land surface model, labelled ORCHIDEE_DF, that distinguishes direct and diffuse radiation in canopy. Observations from flux sites and simulations from the model will be used to investigate the spatiotemporal variation of the impacts of the diffuse radiation fraction on photosynthesis. Chapter 4 will use ORCHIDEE_DF to quantify the impacts of aerosols on land C fluxes and investigate the global impacts from aerosol-induced diffuse radiation changes. Finally, Chapter 5 will summarize the main conclusions of this thesis and discuss about the future directions on studies of aerosol-carbon interactions.

Chapter 2. Impacts of anthropogenic aerosols on land C fluxes through changing climate

Summary

Anthropogenic aerosols have contributed to historical climate change through their interactions with radiation and clouds. In turn, climate change due to aerosols has impacted the C cycle. It remains uncertain how large this impact is and existing studies on single models show different results. Here we use a set of offline simulations made with the ORCHIDEE Land Surface Model (LSM) driven by bias-corrected climate fields from simulations of three CMIP5 Earth System Models (ESM) (IPSL-CM5A-LR, CSIRO-Mk3.6.0 and GISS-E2-R) to quantify the climate-related impacts of aerosols on land carbon fluxes during 1860-2005. We found that Climate Change from Anthropogenic Aerosols (CCAA) globally cooled the climate, and increased land carbon storage, or cumulative Net Biome Production (NBP), by 11.6-41.8 PgC between 1860 and 2005. The increase in NBP from CCAA mainly occurs in the tropics and northern mid latitudes, primarily due to aerosol-induced cooling. At high latitudes, cooling caused stronger decrease in gross primary production (GPP) than total ecosystem respiration (TER), leading to a lower NBP. At mid latitudes, cooling-induced decrease in TER is stronger than that of GPP, resulting in NBP increase. At low latitudes, NBP was also enhanced due to the cooling-induced GPP increase, but precipitation decline from CCAA may negate the effect of temperature. The three ESMs show large divergence in low-latitude CCAA precipitation response to aerosols, which results in considerable uncertainties in regional estimations of CCAA effects on carbon fluxes. Our results suggest that better understanding and simulation of how anthropogenic aerosols affect precipitation in ESMs is required for a more accurate attribution of aerosol effects on the terrestrial carbon cycle. This chapter has been published as Zhang, Y., Goll, D., Bastos, A., Balkanski, Y., Boucher, O., Cescatti, A., Collier, M., Gasser, T., Ghattas, J., Li., L., Piao, S., Viovy., N., Zhu, D., and Ciais, P. (2019), Increased global land carbon sink due to aerosol-induced cooling, *Global Biogeochemical Cycles*, *33*(3), 439-457. In this paper, I performed all the simulations and analyses, also wrote the first version of the manuscript.

Global Biogeochemical Cycles

RESEARCH ARTICLE
10.1029/2018GB006051

Increased Global Land Carbon Sink Due to Aerosol-Induced Cooling

Yuan Zhang[1,2], Daniel Goll[1], Ana Bastos[1], Yves Balkanski[1], Olivier Boucher[2], Alessandro Cescatti[3], Mark Collier[4], Thomas Gasser[5], Josefine Ghattas[2], Laurent Li[2], Shilong Piao[6], Nicolas Viovy[1], Dan Zhu[1], and Philippe Ciais[1]

[1]Laboratoire des Sciences du Climat et de l'Environnement (LSCE), IPSL, CEA/CNRS/UVSQ, Gif sur Yvette, France, [2]Laboratoire de Météorologie Dynamique, IPSL, Sorbonne Université/CNRS, Paris, France, [3]Institute for Environment and Sustainability, Joint Research Centre, European Commission, Ispra, Italy, [4]CSIRO Oceans and Atmosphere, Aspendale, Victoria, Australia, [5]International Institute for Applied Systems Analysis, Laxenburg, Austria, [6]Sino-French Institute for Earth System Science, College of Urban and Environmental Sciences, Peking University, Beijing, China

Abstract Anthropogenic aerosols have contributed to historical climate change through their interactions with radiation and clouds. In turn, climate change due to aerosols has impacted the C cycle. Here we use a set of offline simulations made with the Organising Carbon and Hydrology In Dynamic Ecosystems (ORCHIDEE) land surface model driven by bias-corrected climatefields from simulations of three Coupled Model Intercomparison Project Phase 5 (CMIP5) Earth system models (ESMs; IPSL-CM5A-LR, CSIRO-Mk3.6.0, and GISS-E2-R) to quantify the climate-related impacts of aerosols on land carbonfluxes during 1860–2005. We found that climate change from anthropogenic aerosols (CCAA) globally cooled the climate, and increased land carbon storage, or cumulative net biome production (NBP), by 11.6–41.8 PgC between 1860 and 2005. The increase in NBP from CCAA mainly occurs in the tropics and northern midlatitudes, primarily due to aerosol-induced cooling. At high latitudes, cooling caused stronger decrease in gross primary production (GPP) than in total ecosystem respiration (TER), leading to lower NBP. At midlatitudes, cooling-induced decrease in TER is stronger than that of GPP, resulting in NBP increase. At low latitudes, NBP was also enhanced due to the cooling-induced GPP increase, but precipitation decline from CCAA may negate the effect of temperature. The three ESMs show large divergence in low-latitude CCAA precipitation response to aerosols, which results in considerable uncertainties in regional estimations of CCAA effects on carbonfluxes. Our results suggest that better understanding and simulation of how anthropogenic aerosols affect precipitation in ESMs is required for a more accurate attribution of aerosol effects on the terrestrial carbon cycle.

Key Points:
- Offline simulations on the ORCHIDEE model are used to investigate land Cfluxes under different aerosol scenarios using CMIP5 climate
- Anthropogenic aerosols have increased global land NBP by 11.6–41.8 PgC between 1860 and 2005, mainly through their cooling effects
- Poor understandings in low-latitude precipitation response to aerosols lead to large uncertainties on aerosol impacts on NBP

Supporting Information:
- Supporting Information S1

Correspondence to:
Y. Zhang,
yuan.zhang@lmd.jussieu.fr

Citation:
Zhang, Y., Goll, D., Bastos, A., Balkanski, Y., Boucher, O., Cescatti, A., et al. (2019). Increased global land carbon sink due to aerosol-induced cooling.*Global Biogeochemical Cycles*, *33*. https://doi.org/10.1029/2018GB006051

Received 8 AUG 2018
Accepted 30 JAN 2019
Accepted article online 7 FEB 2019

1. Introduction

Aerosols have considerable impacts on climate through their direct impact on radiation transfer, as well as through aerosol-cloud interactions (Bellouin et al., 2011; Haywood & Boucher, 2000). According to the Fifth Assessment Report of Intergovernmental Panel on Climate Change (IPCC AR5), aerosols emitted by human activities caused a−0.9 (−1.9 to−0.1) W/m ^{2} radiative forcing, partly offsetting the global warming due to anthropogenic greenhouse gases (Boucher et al., 2013). Because terrestrial ecosystems are sensitive to climate, the climate change from anthropogenic aerosols (hereafter CCAA) will affect land surface carbon (C)fluxes, which will in turn alter the climate through the climate-carbon cycle feedbacks (Jones et al., 2003; Mahowald, 2011). The effect of CCAA on terrestrial and oceanic carbon storage is implicitly included in Earth system model (ESM) fully coupled simulations but rarely isolated from other effects, nor are its mechanisms well understood. This low level of understanding hinders our ability to assess the full impact of aerosol emissions on the climate system and therefore the indirect implications of reduced aerosol emissions, in particular in relation to air quality improvement policies that will likely reduce aerosols in the near future.

Anthropogenic aerosols (AA) perturb the terrestrial C balance through several mechanisms. First, terrestrial ecosystems respond to CCAA caused by aerosol-radiation and aerosol-cloud interactions (Jones et al., 2003; Mahowald, 2011). Second, aerosols change the quality of radiation with increased scattering and a higher fraction of diffuse light, which can penetrate deeper into vegetation canopies than can direct light. Upper

levels of canopy are often light saturated; thus, ecosystems with deep canopies respond with higher gross primary production (GPP) to more diffuse light (Gu et al., 2003; Mercado et al., 2009). Third, some aerosols contain nutrients such as nitrogen (N) or phosphorus in forms that can be utilized by plants. Deposition of these nutrients has been suggested to have fertilized current ecosystems and change the C balance (Magnani et al., 2007; Mahowald et al., 2017; Wang et al., 2017) and to partly alleviate N limitations (Luo et al., 2004; Norby et al., 2010). Additionally, aerosols decrease soil pH through N and sulfur (S) deposition, which may accelerate leaching and reduce the availability of nutrients to plants, leading to C loss (Bowman et al., 2008). Furthermore, sulfate aerosols can oxidize photosynthesis tissues (Eliseev, 2015), and other aerosols affect the photochemical processes producing near-surface ozone (Xing et al., 2017), which impairs stomatal conductance and photosynthesis (Sitch et al., 2007).

Due to the complexity of terrestrial ecosystems and the interactions between processes related to AA, separating the impacts of AA from other factors on historical changes in the land C balance using observations and statistical methods is almost impossible. Process-based models provide a way to estimate the effects of AA on the terrestrial C cycle through factorial simulation experiments. Currently, most land surface models (LSMs) do not simulate nutrient cycling or diffuse light effects on the canopy; thus, they cannot be used to investigate the full impacts of aerosols on the terrestrial C cycle. Previous studies reached contradictory conclusions about the response of the terrestrial C sink to aerosols. Using the HadCM3L ESM, Jones et al. (2003) showed that CCAA have triggered a large C sink, which was explained by suppressed soil respiration under cooler climate. Using the Community Climate System Model, CCSM3.1, Mahowald et al. (2011) found a very small global Cflux response to CCAA. This discrepancy may relate to uncertainties both in how climate models simulate CCAA and in how the LSMs represent the carbon cycle processes responding to CCAA.

A well-known set of climate model simulation experiments is from the Coupled Model Intercomparison Project Phase 5 (CMIP5; Taylor et al., 2012). One of the core experiments of CMIP5 is the historical experiment (*hist*), which simulates the evolution of the Earth system driven over the historical period (1850–2005) by all natural and anthropogenic forcings. Two of the CMIP5 ESMs, IPSL-CM5A-LR and CSIRO-MK3.6.0 (hereafter referred to as IPSL and CSIRO) further provided experiments similar to*hist*with the exception that the radiative effects of AA were omitted (hereafter referred to as*NoAA*). The comparison of the*hist* and*NoAA*experiments allows investigating the climate effects of AA on terrestrial Cfluxes. The GISS-E2-R ESM (hereafter referred to as GISS) provided an experiment without the radiative effect of all aerosols (hereafter referred to as*NoA*). Considering that the effects of AA and all aerosols on climate are similar (see section 3.1), in order to include more ESMs and assess the uncertainties, the GISS model is also considered. For the sake of simplicity, we hereafter refer to CCAA and AA for all three ESMs, even though it does not strictly apply to GISS.

Using the climate simulations from the*hist*and*NoAA*/*NoA*scenarios from the three CMIP5 ESMs, we aim to estimate the terrestrial Cflux change caused by CCAA during the period 1860–2005 using a single process-based LSM, Organising Carbon and Hydrology In Dynamic Ecosystems (ORCHIDEE). The main objectives of this study are (1) to quantify the impacts of CCAA on land Cfluxes, as modeled by ORCHIDEE, at global and regional scales; (2) to evaluate how uncertainty in CCAA simulated by ESMs translates into uncertainty in Cfluxes in ORCHIDEE; and (3) to understand the mechanisms behind these impacts and uncertainties.

2. Data and Methods

2.1. ORCHIDEE Model

The ORCHIDEE model is the LSM component of the Institute Pierre-Simon Laplace (IPSL) ESM. ORCHIDEE represents key energy, water, and biogeochemical processes in terrestrial ecosystems (Krinner et al., 2005) and is mainly based on three components: the Surface-vegetation-atmosphere transfer SECHIBA (Schématisation des Echanges Hydriques à l'Interface entre la Biosphère et l'Atmosphère) model, dealing with energy and hydrological processes (De Rosnay & Polcher, 1998; Ducoudré et al., 1993); the Lund-Potsdam-Jena dynamic global vegetation model, LPJ, which simulates the dynamics of natural vegetation (Sitch et al., 2003); and the STOMATE (Saclay Toulouse Orsay Model for the Analysis of Terrestrial Ecosystems) model, which models the main biogeochemical and related processes (e.g., photosynthesis, carbon allocation, respiration, and phenology; Krinner et al., 2005). Detailed descriptions of the parameterizations of the main processes in ORCHIDEE can be found in Krinner et al. (2005) and Piao et al. (2009).

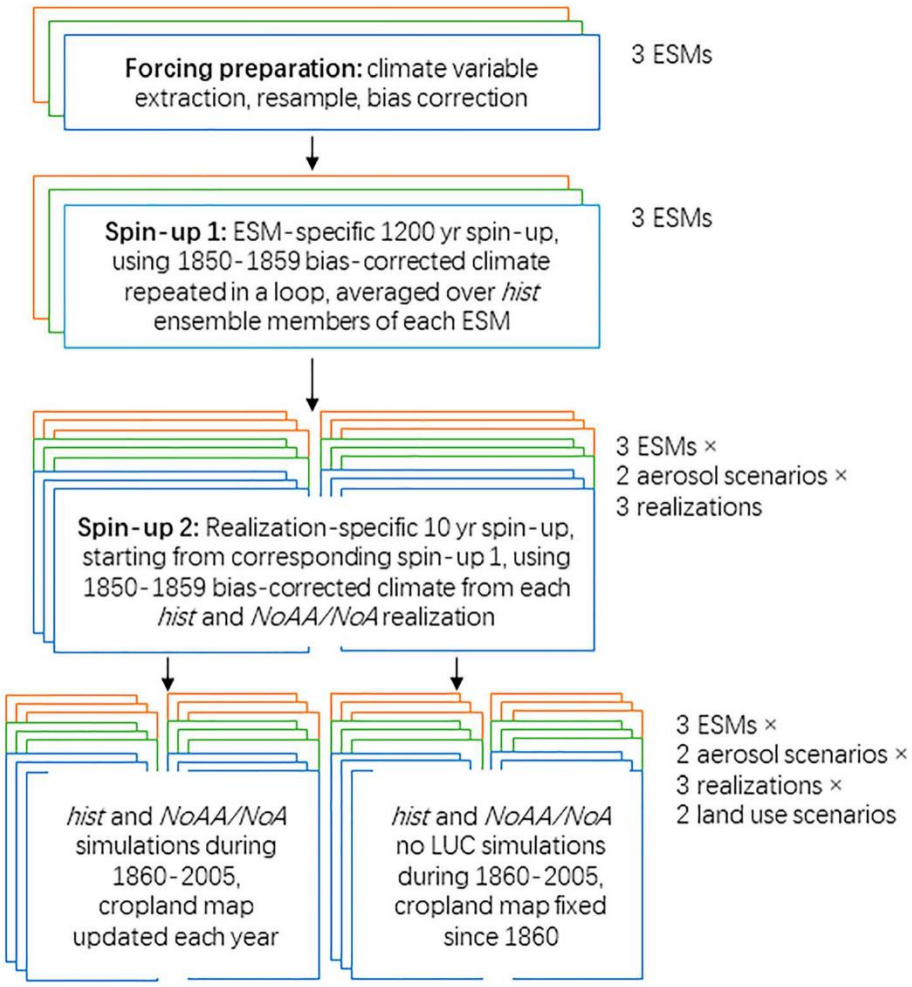

Figure 1. Schematic of the spin-up and simulations. ESM = Earth system model.

ORCHIDEE has been tested at various spatial-temporal scales using in situ measurements from different plant functional types and satellite observations (Ciais et al., 2005; Krinner et al., 2005; Piao et al., 2006; Traore et al., 2014) and has been widely applied to estimate global and regional C budgets (Le Quéré et al., 2017; Piao et al., 2009) and to investigate the biogeochemical consequences of climate trends and extremes (Ciais et al., 2005; Piao, Ciais, et al., 2009; Reichstein et al., 2007).

Here we use ORCHIDEE version v4220 in offline mode (i.e., the model output does not affect climate forcing), with the setup configurations described in the next section and in Figure 1. It should be noted that the differential direct and diffuse light transmission scheme remains unavailable for the current ORCHIDEE version, nor does the model simulate effects of nutrient deposition.

2.2. Forcing Data and Experiments Setup

2.2.1. ESM Simulations

Climate data used to drive ORCHIDEE are derived from simulations of three CMIP5 ESMs that documented separately climate change with and without AA/aerosols (*hist*and*NoAA*/*NoA*), including the IPSL ESM (IPSL-CM5A-LR; Dufresne et al., 2013), the CSIRO ESM (CSIRO-Mk3.6.0; Jeffrey et al., 2013; Rotstayn et al., 2012), and the GISS ESM (GISS-E2-R; Miller et al., 2014; Schmidt et al., 2014). Furthermore, three realizations (i.e., perturbed initial conditions) of the*hist*and*NoAA*/*NoA*experiments of each ESM are used (Table S1). Under the CMIP5 protocol, the*hist*experiment uses simulations driven by all observation-based natural and anthropogenic forcings, including AA emissions. While for*NoAA*/*NoA*simulations, the forcings

remain the same as those for*hist*simulations except that aerosol emissions are prescribed at the preindustrial level (AA for*NoAA*, whereas all aerosol emissions for*NoA*in GISS). All ESMs simulate the radiative effects of aerosol species including dust, sea salt, sulfate, black carbon, and organic carbon. The GISS model additionally considered nitrate aerosols. All ESMs include the direct radiative effect (i.e., light absorption and scattering) on climate and the indirect effect of aerosols on climate by changing cloud albedo. The CSIRO model also includes aerosols' impact of a reduction of cloud droplet size on the precipitation efficiency.

The climate variables required to drive ORCHIDEE are daily or higher-frequency air temperature maximum (*Tmax*) and minimum (*Tmin*), precipitation (*Precip*), downward surface shortwave radiation (*SWdown*), downward surface longwave radiation (*LWdown*), near-surface specific humidity (*Qair*), air pressure (*Ps*), and near-surface (10 m) zonal (*Wind_E*) and meridional (*Wind_N*) wind components. These climate variables are further interpolated to 30-min time steps in ORCHIDEE forflux simulations. We obtained the climate variables at daily resolution from IPSL and CSIRO output under*hist*and*NoAA*scenarios from the Earth System Grid Federation node (https://esgf-node.ipsl.upmc.fr/projects/esgf-ipsl/) or directly from the modeling centers. For GISS, daily output since 1850 is available from only one*hist*realization (CMIP5 GISS-E2-R r6i1p3), while the other*hist*and*NoA*realizations only provide monthly data. Here we calculated the daily climate anomalies in each month using GISS r6i1p3 data and added them to the monthly data of the other*hist*and*NoA*realizations. All data are regridded to 2° × 2°. Apart from climate, global annual atmospheric CO_2 concentration is also required as an input ORCHIDEE, and is taken from an ice core and National Oceanic and Atmospheric Administration monitoring station data (https://www.esrl.noaa.gov/gmd/ccgg/trends/).

2.2.2. Bias Correction

The response of terrestrial ecosystems to climate change depends on background climate (Ahlström et al., 2017; Sitch et al., 2008; Wang et al., 2014). Since ESMs have bias in their simulated climate compared with observations (Flato et al., 2013), systematic errors in simulated Cfluxes with ORCHIDEE could be introduced if the ESM output is not corrected for its biases. The impact of such bias in ESM climate on Cfluxes and pools was nicely illustrated in Ahlström et al. (2017) for precipitation over the Amazon, for instance. Therefore, we corrected biases in ESM preindustrial climate at a pixel level using the observation-based reanalysis data set CRU-NCEP (Climatic Research Unit-National Centers for Environmental Prediction; version 7.2) at 2° × 2° resolution and 6-hourly time steps for the period 1901–2016 (available online at: https://vesg.ipsl.upmc.fr/thredds/catalog/store/p529viov/cruncep/V72_1901_2016/catalog.html). For each ESM simulation,*Tmax*,*Tmin*,*Wind_N*,*Wind_E*, and*Ps*are corrected as follows:

$$V_{\mathrm{corr}}(t,m) = V_{\mathrm{mod}}(t,m) - \Delta V(m) \tag{1}$$

$$\Delta V(m) = V_{\mathrm{base},hist}(m) - V_{\mathrm{base,obs}}(m) \tag{2}$$

while*Precip*,*SWdown*,*LWdown*, and*Qair*are corrected as follows:

$$V_{\mathrm{corr}}(t,m) = V_{\mathrm{mod}}(t,m) / \Delta V(m) \tag{3}$$

$$\Delta V(m) = V_{\mathrm{base},hist}(m) / V_{\mathrm{base,obs}}(m) \tag{4}$$

where$V_{\mathrm{corr}}(t,m)$ is the corrected climate variable at day*t*of month*m*,$V_{\mathrm{mod}}(t,m)$ is the CMIP5 climate output at time*t*of month*m*, and$V_{\mathrm{base,obs}}(m)$ is the climate baseline from observations (here CRU-NCEP data) in month*m*, calculated as the average climate in month*m*during thefirst 10 years of this data set (1901–1910).$V_{\mathrm{base},hist}(m)$ is the modeled climate baseline of month*m*, which is ESM dependent and calculated during 1850–1859 using the average climate across the three ensemble members of*hist*simulations. Here we correct the ESM baseline from 1850 to 1859 using CRU-NCEP data from 1901 to 1910. This mismatch in the baseline period is unavoidable because the CRU-NCEP data set begins in 1901. Nevertheless, it should not cause large errors because the simulated climate change between the two periods is small (<0.19 °C in surface temperature or*Tair*, <10 mm in*Precip*, and <1.2 W/m^2 in*SWdown*) compared with that during the entire study period of 1850–2005 (Figure 2). This is due to relatively low anthropogenic forcing level prior to 1900.

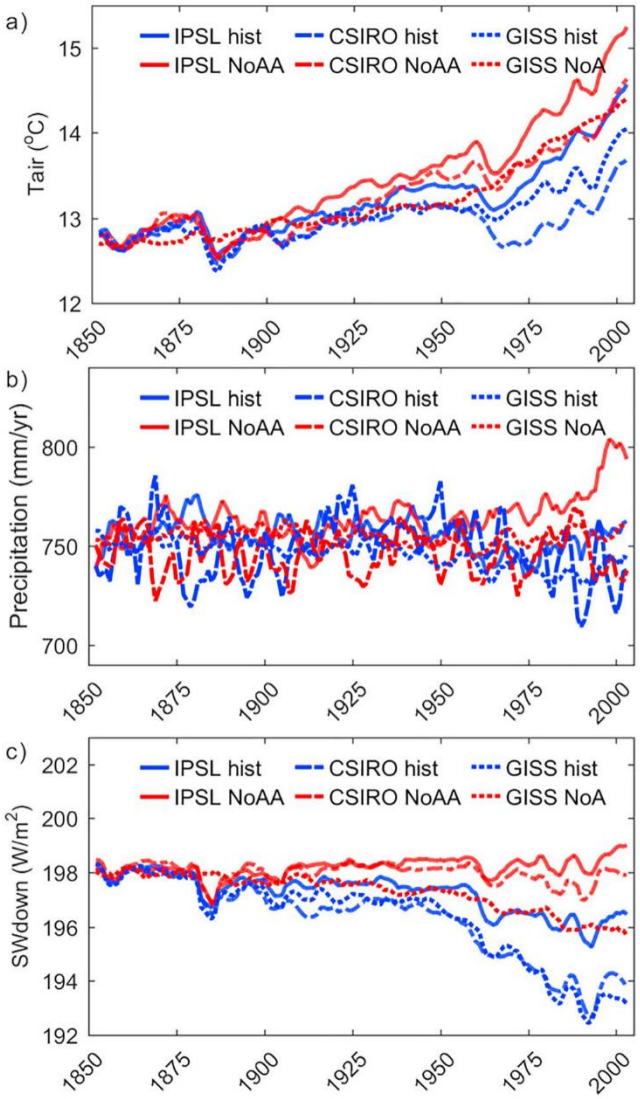

Figure 2. Global average bias-corrected terrestrial (a) air temperature, (b) precipitation and (c) incoming shortwave radiation (*SWdown*) under the *hist* (blue) and *NoAA/NoA* (red) scenarios for IPSL (solid lines), CSIRO (dashed lines), and GISS (dotted lines). Five-year moving average was applied to all variables.

2.2.3. Experimental Design

Because of the high computational demand of the LSM to equilibrate land carbon cycle to the initial climate state (1850–1859), and the rather small differences in the initial climate between the bias-corrected ensemble members and between the *hist* and *NoAA/NoA* scenarios (Figure 2), we used a two-step spin-up scheme to equilibrate the carbon cycle (Figure 1). First, for each ESM, a long spin-up of 1,200 years was performed with ORCHIDEE driven by a 10-year climate sequence (1850–1859) repeated in a loop to bring all C pools to equilibrium. To construct this 10-year climate, we averaged the bias-corrected ESM climate over *hist* ensemble members from each ESM. We have checked that the 10-year period has no anomalous decadal variability (Figure 2). Then, a 10-year short spin-up starting from the end of the first spin-up using 1850–1859 climate from each *hist* or *NoAA/NoA* ensemble member was used to adjust the C pools with fast turnover (e.g., leaf and litter C pools) to the corresponding climate. Since AA emissions remain small during this period, the initial C pools from the *NoAA/NoA* simulations are not significantly different from the *hist* simulations (Figure S1).

After the two-step spin-up, two simulations with ORCHIDEE for the period 1860–2005 were performed with the bias-corrected climatic forcing and different land use scenarios (Figure 1). One simulation used a cropland distribution updated each year according to LUH2v2h (Land Use Harmonization)-based LC_CCI (The ESA Land Cover Climate Change Initiative) plant functional type (Hurtt et al., 2011; Poulter et al., 2015), while the other simulationfixed the cropland distribution to the one of 1860 (natural vegetation being simulated by the dynamic global vegetation model module). By comparing results from the two simulations, we can quantify the Cflux caused by land use change (land use emissions) and by climate and CO_2 changes (natural sink). Altogether, 3 ESMs × 2 aerosol scenarios × 3 ESM ensemble members × 2 land use scenarios were considered, making a total of 36 different ORCHIDEE runs. A detailed experiment setup is shown in Table 1.

2.3. Analyses

The analysis is based on Cfluxes averaged among the three realizations to represent each experiment in Table 1. To investigate how the Cfluxes are affected by different climate variables and atmospheric CO_2, a multiple regression approach was used to decompose the Cflux time series to the effects of different climate factors, following the method of Piao et al. (2013):

$$Y = a \times Tair + b \times Precip + c \times SWdown + d \times CO_2 + e + \varepsilon \quad (5)$$

where Y is the Cfluxes and a, b, c, and d are the sensitivities of target Cflux to temperature, precipitation, shortwave radiation, and CO_2 concentration, respectively.

Then, the contribution of climate variable V to Cflux (Y) can be written as

$$\Delta Y_V = S \times \Delta V \quad (6)$$

where ΔY_V is the contribution of a given climatic factor V to the difference in Cflux between the end (1996–2005) and beginning (1860–1869) of the study period. S is the sensitivity of the corresponding factor calculated in equation (5), and ΔV is the change of the climate factor during the same period. The Cflux

Table 1
The Climate and Land Use Scenarios for Each Experiment

Experiment name	Number of realizations	Climate scenario	Cropland map
IPSL*hist*	3	IPSL historical[a]	Time varying
IPSL*hist NoLUC*	3	IPSL historical	Fixed at 1860
IPSL*NoAA*	3	IPSL historicalNoAA[b]	Time varying
IPSL*NoAA NoLUC*	3	IPSL historicalNoAA	Fixed at 1860
CSIRO*hist*	3	CSIRO historical	Time varying
CSIRO*hist NoLUC*	3	CSIRO historical	Fixed at 1860
CSIRO*NoAA*	3	CSIRO historicalNoAA	Time varying
CSIRO*NoAA NoLUC*	3	CSIRO historicalNoAA	Fixed at 1860
GISS*hist*	3	GISS historical	Time varying
GISS hist*NoLUC*	3	GISS historical	Fixed at 1860
GISS*NoA*	3	GISS historicalNoA[c]	Time varying
GISS*NoA NoLUC*	3	GISS historicalNoA	Fixed at 1860

[a](Climate from simulations driven by all natural and anthropogenic forcings). [b](Same as historical, but anthropogenic aerosol emissions are prescribed at the preindustrial level). [c]Same as historical, but all aerosol emissions are prescribed at the preindustrial level.

change caused by AA through changes in climate factor*V*at the end of the study period,$\Delta Y_{V,\,\mathrm{aero}}$ can be diagnosed as

$$\Delta Y_{V,\mathrm{aero}} = \Delta Y_{V,hist} - \Delta Y_{V,NoAA/NoA} \tag{7}$$

This decomposition scheme is not perfect because it assumes a linear response of Cfluxes to climate variables, while terrestrial ecosystems do not always behave linearly. In addition, there might be interactions between different climate factors. Nevertheless, at the interannual time scale, this simple approach has been shown to be useful to estimate the effects of different climate factors (Jung et al., 2017; Piao et al., 2013).

3. Results

3.1. Impacts of Aerosols on Climate

The evolution of the bias-corrected global climate (for convenience, all climates hereafter indicate the climate after bias correction) under the*hist*and*NoAA/NoA*scenarios is shown in Figure 2. Due to the bias correction, the climate states of*hist*and*NoAA/NoA*from different ESMs are similar in the 1850s.

Simulated*Tair*presents increasing trends under all the scenarios during the study period, especially after the 1960s (Figure 2a). This temperature increase is more pronounced for the*NoAA/NoA*scenarios than for the *hist*scenarios for each ESM, indicating a cooling effect of aerosols. In spite of the consistency in the sign of the AA-induced temperature change, the three ESMs show different magnitudes of the CCAA cooling effect, with the strongest land surface cooling found in CSIRO (0.75 °C in 2005), followed by IPSL (0.64 °C in 2005) and GISS (0.37 °C in 2005). Because GISS*NoA*excluded the effects of both natural aerosols (including volcanic aerosols) and AA, the difference in interannual climate variations between GISS*hist*and GISS*NoA*is larger than that between*hist*and*NoAA*from other ESMs.

In contrast to temperature, precipitation generally shows no trend in most of the simulations (Figure 2b), except that the IPSL*NoAA*ensemble average exhibits an increasing global precipitation trend after the 1960s. This trend leads to a 40-mm/year precipitation difference between IPSL*hist*and IPSL*NoAA*in the 2000s. In CSIRO and GISS, the global mean precipitation under the *hist* and *NoAA/NoA* scenarios are similar.

In terms of*SWdown*, all the three ESMs show remarkable decreasing trends after the 1960s under the*hist* scenario, while*SWdown*under the*NoAA/NoA*scenarios either remains relatively constant (IPSL*NoAA* and CSIRO*NoAA*) or decreases only slightly (GISS*NoA*; Figure 2c). These differences indicate a diming effect of aerosols. Similar to the cooling effect, the diming is stronger in CSIRO (4.8 W/m^2 in 2005) than in IPSL and GISS (both 2.7 W/m^2 in 2005).

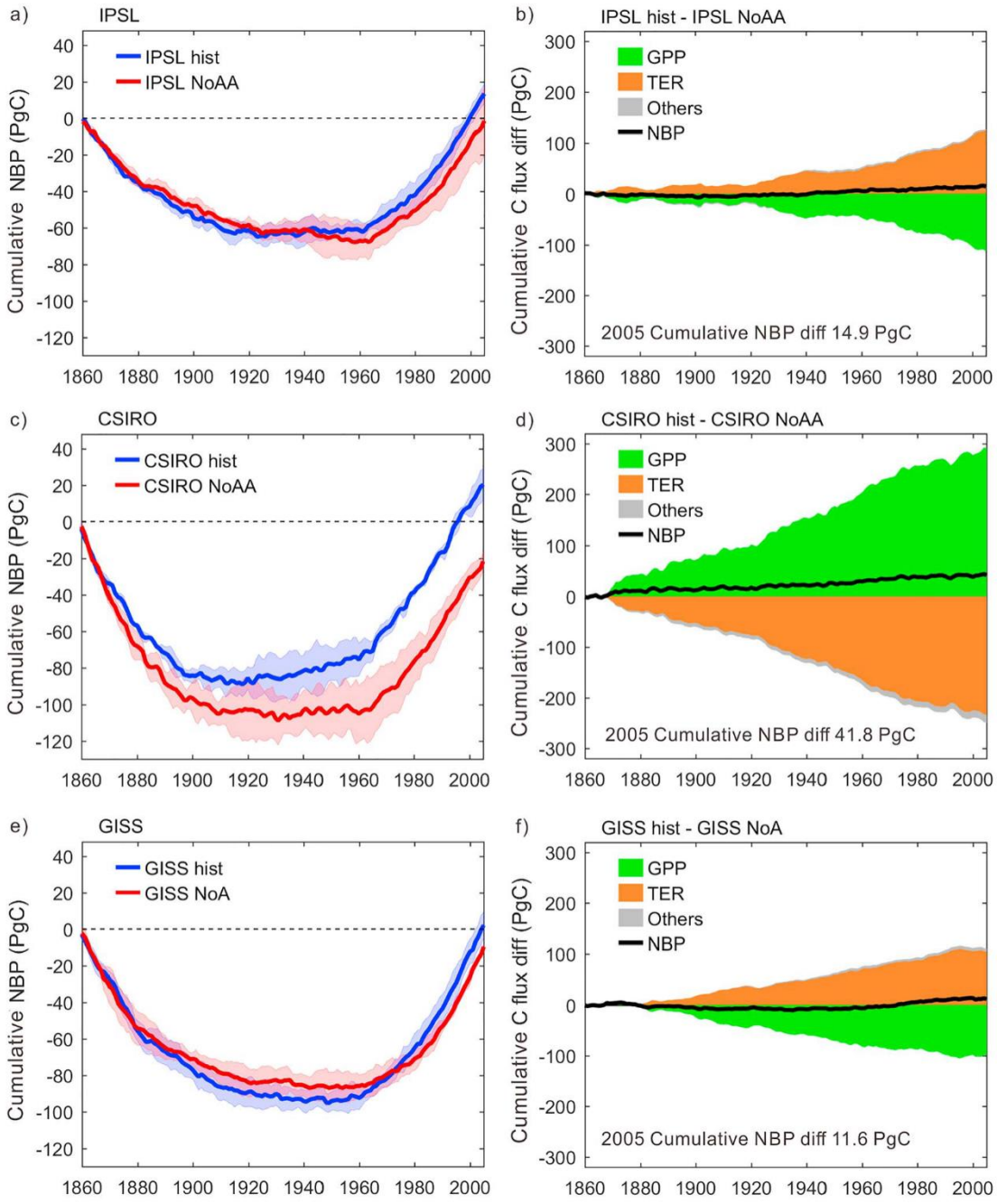

Figure 3. Cumulative terrestrial Cfluxes under the*hist*and*NoAA/NoA*scenarios and their difference. (a) The cumulative terrestrial net biome production (NBP) since 1860 from the IPSL simulations. The shaded area indicates standard deviation among ensemble members. (b) The cumulative difference in gross primary production (GPP), total ecosystem respiration (TER), other Cfluxes (i.e.,fire and harvest), and NBP between IPSL*hist*and IPSL*NoAA*. (c, e) The same as (a) but for the CSIRO and GISS simulations, respectively. (d, f) The same as (b) but for the CSIRO and GISS simulations, respectively. Positiveflux indicatesflux from atmosphere to terrestrial ecosystems.

3.2. Responses of C Fluxes at the Global Scale

The global cumulative land net biome production (NBP; defined as the netflux of CO_2 from atmosphere to land) since 1860 under the*hist*and*NoAA/NoA*scenarios is shown in Figures 3a, 3c, and 3e. All the*hist*simulations show persistent land C losses before 1900 and C gains after the 1960s. At the end of the study period, a positive cumulated NBP is found (13.4 PgC for IPSL*hist*, 20.3 PgC for CSIRO*hist*, and 2.1 PgC for GISS*hist*). The magnitude of this C uptake is within the range of that assessed in IPCC AR5 (Ciais et al., 2013).

The cumulative NBP in the*NoAA/NoA*simulations showed a U-shape curve similar to that in the*hist*simulations (Figures 3a, 3c, and 3e). However, at the end of the study period, the cumulative*NoAA/NoA*NBP is negative, that is, a net loss of CO_2 from the land to the atmosphere (−1.5 PgC for IPSL*NoAA*,−21.5 PgC for CSIRO*NoAA*, and−9.4 PgC for GISS*NoA*). The difference between*hist*and*NoAA/NoA*on cumulative NBP is mainly due to a weaker C sink in*NoAA/NoA*after the 1960s. For CSIRO, there is also a more pronounced C loss in the*NoAA*than*hist*scenario before 1960.

Differences in gross Cfluxes of GPP and total ecosystem respiration (TER) during 1860–2005 between the *hist*and*NoAA*simulations, that is, CCAA-induced changes in thesefluxes, are illustrated in Figures 3b, 3d, and 3f. For the IPSL and GISS models, CCAA cause a small decrease in both GPP and TER (Figures 3b and 3f). The GPP decrease (0.77 PgC/year for IPSL and 0.68 PgC/year for GISS) is smaller than the decrease in TER and other emissions (e.g.,fires, harvest, or direct C loss from land use change; 0.87 PgC/ year for IPSL and 0.76 PgC/year for GISS), leading to an NBP increase, that is, a larger sink due to CCAA (0.10 PgC/year for IPSL and 0.08 PgC/year for GISS). In contrast, the CCAA of the CSIRO model cause a positive response of GPP and TER and other emissions (Figure 3d). However, due to a larger increase in GPP (on average 1.99 PgC/year) than in TER and other emissions (on average 1.71 PgC/year), NBP increases due to CCAA in the CSIRO model as well (0.29 PgC/year). Bear in mind that these results depend on the response of ORCHIDEE to CCAA and could be qualitatively and quantitatively different with another LSM.

3.3. Responses of C Fluxes at Different Latitudes

To identify the regions that compose the above global difference in CCAA-induced GPP and TER changes among the three ESMs, we analyze changes in different latitude bands during 1966–2005 in Figure 4. This period was selected because it shows the strongest CCAA (Figure 2).

At southern midlatitudes (30–60°S; Figure 4), IPSL and CSIRO show positive impacts of CCAA on GPP and TER. Due to the larger increase in GPP than in TER, CCAA triggered an increase of NBP of 46 TgC/year for IPSL and 23 TgC/year for CSIRO during 1966–2005. However, for GISS, both GPP and TER decreased slightly, and a 1 TgC/year NBP increase is found in response to CCAA during 1966–2005. An investigation of CCAA during the same period shows that aerosols caused an increase in precipitation in IPSL and CSIRO but a small decrease in precipitation in GISS (Figure S11).

The largest differences among ESMs are found at low latitudes (30°S–30°N; Figure 4). For IPSL, CCAA caused declines in both GPP and TER (Figure 4a), while for CSIRO and GISS, CCAA increased GPP and TER (Figures 4b and 4c). For the CSIRO model, the increase of GPP and TER simulated by ORCHIDEE is 5 times larger than for GISS. Although the GPP and TER responses to CCAA diverge among ESMs, all the simulations indicate a positive NBP response to CCAA in the low latitudes during 1966–2005 (42 TgC/year for IPSL, 353 TgC/year for CSIRO, and 369 TgC/year for GISS). The magnitude of the NBP response at low latitudes is 1 order of magnitude larger than in the other latitude bands for CSIRO and GISS, while it is comparable for IPSL.

At northern middle (30–60°N) and high (60–90°N) latitudes (Figure 4), the CCAA from all the three ESMs result in declines in both GPP and TER. These GPP and TER responses to CCAA are opposite to those in southern midlatitudes for IPSL and CSIRO, which might be due to the opposite response of precipitation to aerosols in the two latitudinal bands (Figure S11). At northern midlatitudes, TER decreases more than GPP, leading to a small increase in NBP (123 TgC/year for IPSL, 2 TgC/ year for CSIRO, and 25 TgC/ year for GISS), while at northern highlatitudes, GPP decreases more than TER, causing a small NBP decrease of 31, 101, and 47 TgC/year, respectively.

Using simulations withfixed cropland maps, we decomposed the total NBP into“natural sink”and“land use emissions.”The impacts of CCAA on bothfluxes are also shown in Figure 4. All ESMs in all latitudes agree that the CCAA-induced difference in the natural sink (“NoLUC”in Figure 4) is similar but slightly larger compared with the total NBP change. In contrast, the land use emissions (i.e., the difference between the total NBP and the natural sink, referred to as“LUC effect”in Figure 4) is almost insensitive to CCAA.

3.4. Spatial Pattern of NBP Difference

The spatial pattern of CCAA-caused NBP change during 1966–2005 is shown in Figures 5a, 5c, and 5e. All the ESMs generally show patterns of NBP increases at middle to low latitudes in response to CCAA,

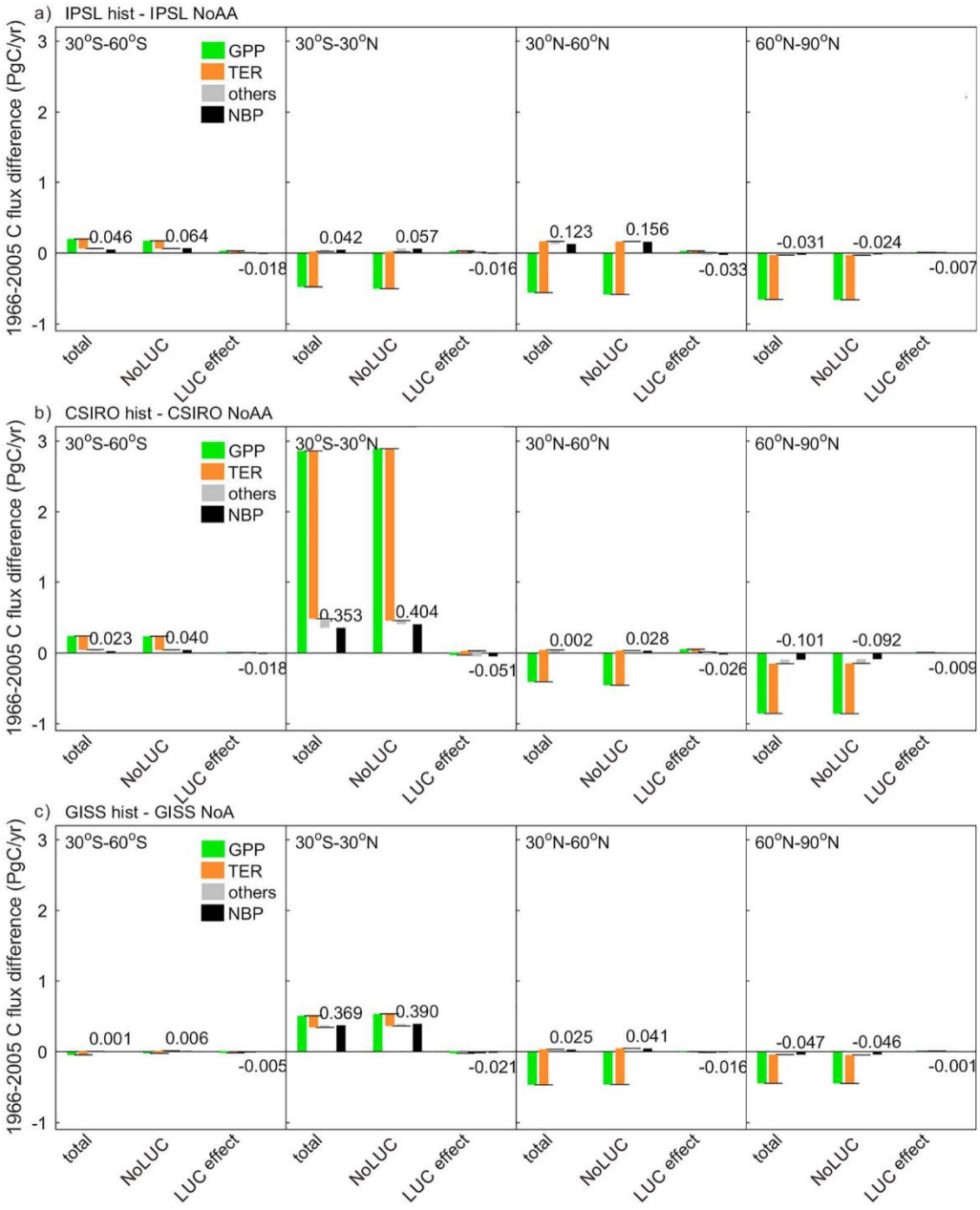

Figure 4. Difference in gross primary production (GPP), total ecosystem respiration (TER), other Cfluxes (i.e.,fire and harvest), and net biome production (NBP) under the*hist*and*NoAA*/*NoA*scenarios during 1966–2005 in different latitudes. (a) Cflux difference from the IPSL simulations; (b) Cflux difference from CSIRO simulations; and (c) Cflux difference from the GISS simulations."Total"indicates simulations with cropland map updated each year;"NoLUC"indicates simulations withfixed cropland map, indicating"natural sink"(see methods);"LUC effect"is the difference between"total"and"NoLUC,"indicating the"land use emissions."The baseline of respiration and other Cflux bars are indicated as short black horizontal lines. The numbers indicate the average NBP difference during 1966–2005. Positiveflux indicate increase in GPP or decrease in C release (respiration and otherfluxes) due to anthropogenic aerosols.

except over the eastern Amazon for IPSL and small regions in the Amazon for CSIRO. The spatial pattern of NBP change at northern high latitudes from CCAA is less consistent among ESMs. Nevertheless, all the ESMs agree that in this region more areas show negative impacts of CCAA on NBP, that is, a decreased sink or an increased source. Globally, CCAA cause NBP to increase in 55–60% of the land area and to decrease in 37–43% of the area.

To investigate which climate variables control the CCAA-induced NBP difference patterns, we show the temperature and an aridity index (precipitation-potential evapotranspiration, P-PET) changes due to

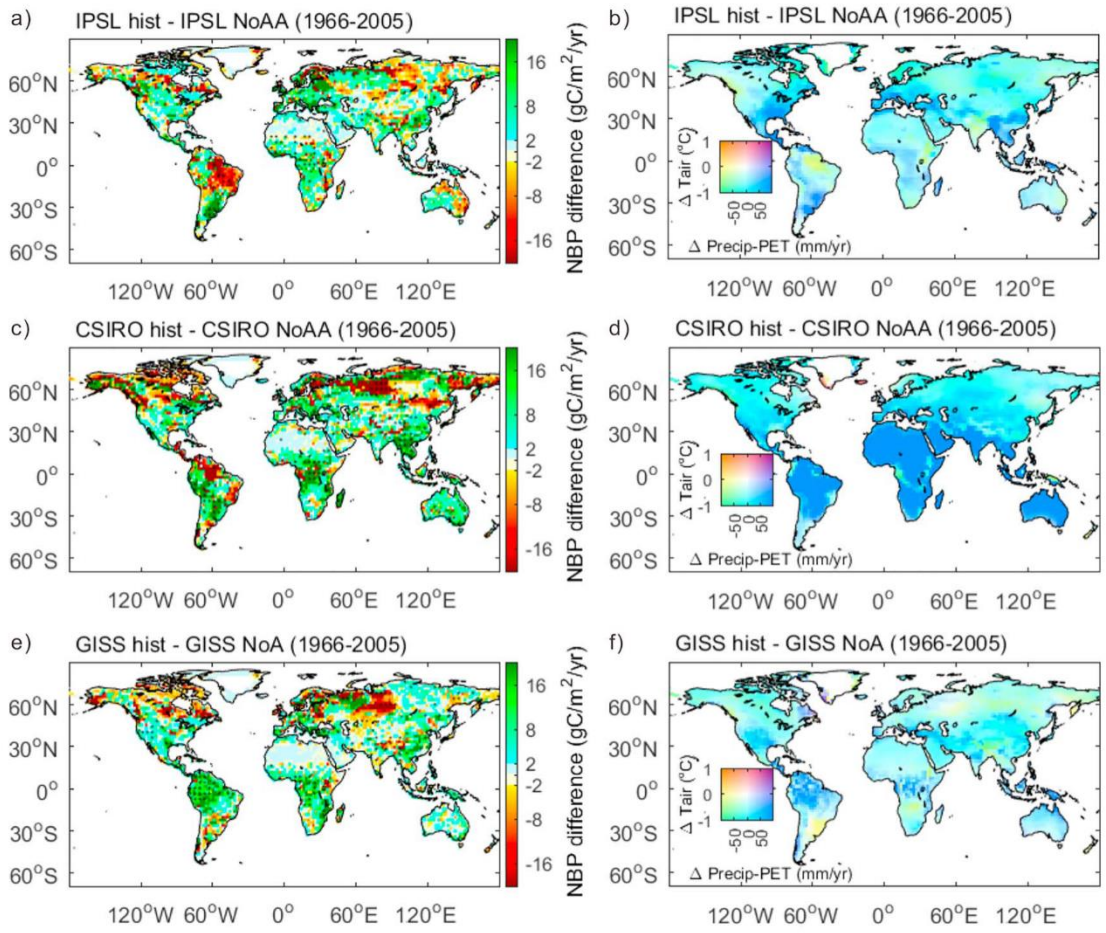

Figure 5. Spatial patterns of differences in net biome production (NBP) and climate between *hist* and *NoAA/NoA* during 1966–2005. (a) NBP difference between IPSL*hist* and IPSL*NoAA*. (b) Air temperature and precipitation-potential evapotranspiration (P-PET) differences between IPSL*hist* and IPSL*NoAA*. (c, e) The same as (a) but for CSIRO and GISS, respectively. (d, f) The same as (b) but for CSIRO and GISS, respectively. The PET is calculated following Thornthwaite (1948). Dotted areas in (a), (c), and (e) indicate significant difference between the *hist* and *NoAA/NoA* ensembles.

CCAA in Figures 5b, 5d, and 5f (*SWdown* is not shown because its contribution to CCAA is similar to temperature change). For all ESMs, a cooler temperature is the globalfingerprint of CCAA. However, the response of P-PET to AA is remarkably different among ESMs. For IPSL, AA caused wetter climate in eastern North America, western South America, Argentina, central Africa, and south China, whereas it induced drier climate in eastern South America and east Australia (Figure 5b), which coincide with the mid-latitude and low-latitude NBP-increase and NBP-decrease areas from CCAA (Figure 5a). For CSIRO and GISS, P-PET decrease also matches most of the NBP-decrease regions at low latitudes (e.g., East Brazil and west equatorial Africa for CSIRO and Argentina for GISS).

In Figure 6, we investigated whether the impacts of CCAA on NBP operate mainly through changes on GPP or TER. Simulations from all the ESMs agree that in most pixels CCAA affect NBP mainly through changing GPP, regardless of whether the change is positive or negative (Figure 6). The area dominated by the GPP response accounts for 62–68% of the land area, while the area dominated by the TER response is only 28–35%. These TER-dominated areas are mainly found in east North America, as well as east Europe and central South America for IPSL.

3.5. Sensitivities of C Fluxes to Climate Factors

To understand how CCAA quantitatively affect Cfluxes as simulated by ORCHIDEE, we present the sensitivities of NBP and GPP to *Tair*, *Precip*, and *SWdown* in Figures 7 and S5–S9. Similar sensitivity patterns are found between the *hist* and *NoAA/NoA* simulations and among ESMs, so that the impact of CCAA is not

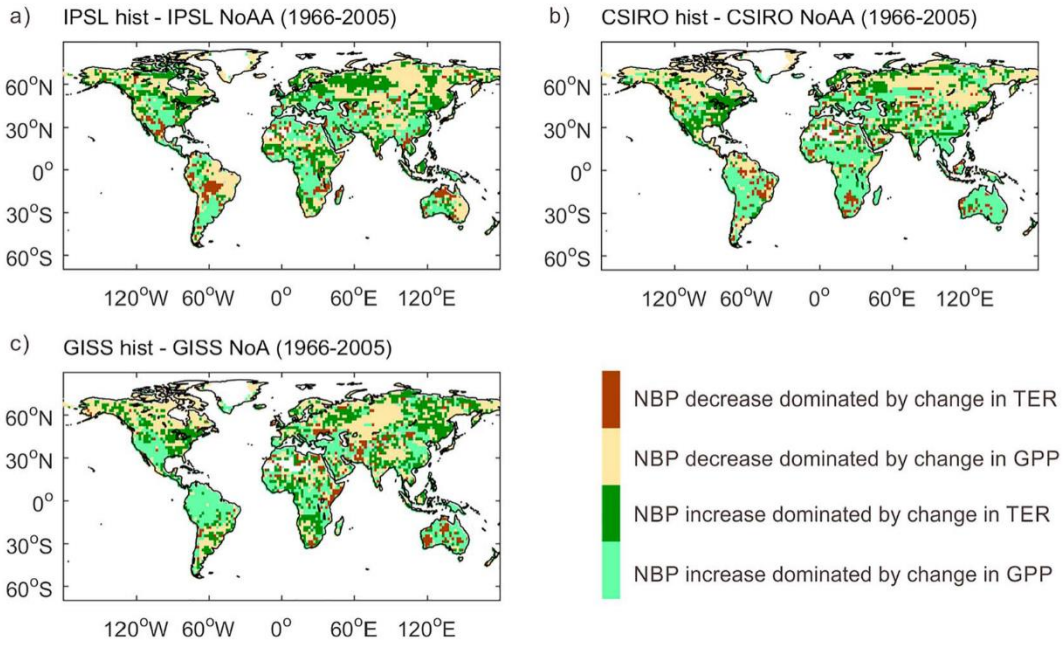

Figure 6. Spatial patterns of the main contributors (gross primary production [GPP] or total ecosystem respiration [TER]) to the net biome production (NBP) difference caused by anthropogenic aerosols during 1966–2005. (a) The main contributors for the IPSL simulations. (b, c) the same as (a) but for the CSIRO and GISS simulations, respectively. The green and red indicate NBP increase or decrease in response to aerosols. The light and dark colors indicate if theNBP difference is mainly caused by GPP or TER.

because the terrestrial C cycle sensitivity is changed but because of regional changes in *Tair*, *Precip*, and*SWdown*.

The NBP sensitivity to temperature shows a strong meridional gradient (Figure 7a). At low latitudes, NBP has strong negative sensitivity to temperature, with a magnitude of−80 gC·m $^{-2}$·year^{-1}·°C^{-1}, while at high latitudes, NBP slightly increases with temperature (10 gC·m^{-2}·year^{-1}·°C^{-1}).

Opposite to temperature, the NBP sensitivity to precipitation is generally positive in latitudes south than 60°N, whereas it becomes negative at latitudes north of 60°N (Figure 7c). The strongest positive NBP-precipitation sensitivity values are found in dry regions, such as Sahel, the central United States, middle Asia, Southern Africa, west Argentina, and Australia, with values over 6–8 gC·m^{-2}·year^{-1}·(10 mm/year)$^{-1}$. NBP is insensitive to precipitation in regions covered by rainforests along the equator.

In terms of NBP sensitivity to*SWdown*(Figure 7e), the ORCHIDEE simulations using the different ESM forcings generally agree that in most low-latitude regions, NBP decreases with radiation, except for rainforests in west Amazon, central Africa, and Indonesia, where light was thought to be the limiting factor of vegetation growth (Huete et al., 2006; Nemani et al., 2003; Zhang et al., 2016). In some semiarid regions (e.g., north Argentina), negative sensitivity of NBP to*SWdown*is detected, potentially because the increase in*SWdown* can increase evapotranspiration and decrease water availability. At high latitudes, the radiation sensitivity is less consistent among ESMs.

The GPP sensitivities to each climate factor show similar patterns to NBP sensitivities, but with much stronger magnitude (Figures 7b, 7d, and 7f). This similarity in sensitivity pattern is expected because GPP is found to be the dominantflux causing NBP change (Figure 6).

3.6. Dominant Climate Factors Causing NBP Change Due to AA

The decomposition shown in equations (5)–(7) allows us to investigate which climate factor contributes the most to the CCAA-induced NBP change (Figure 8). A robust meridional pattern of the main climate factors is found among ESMs.

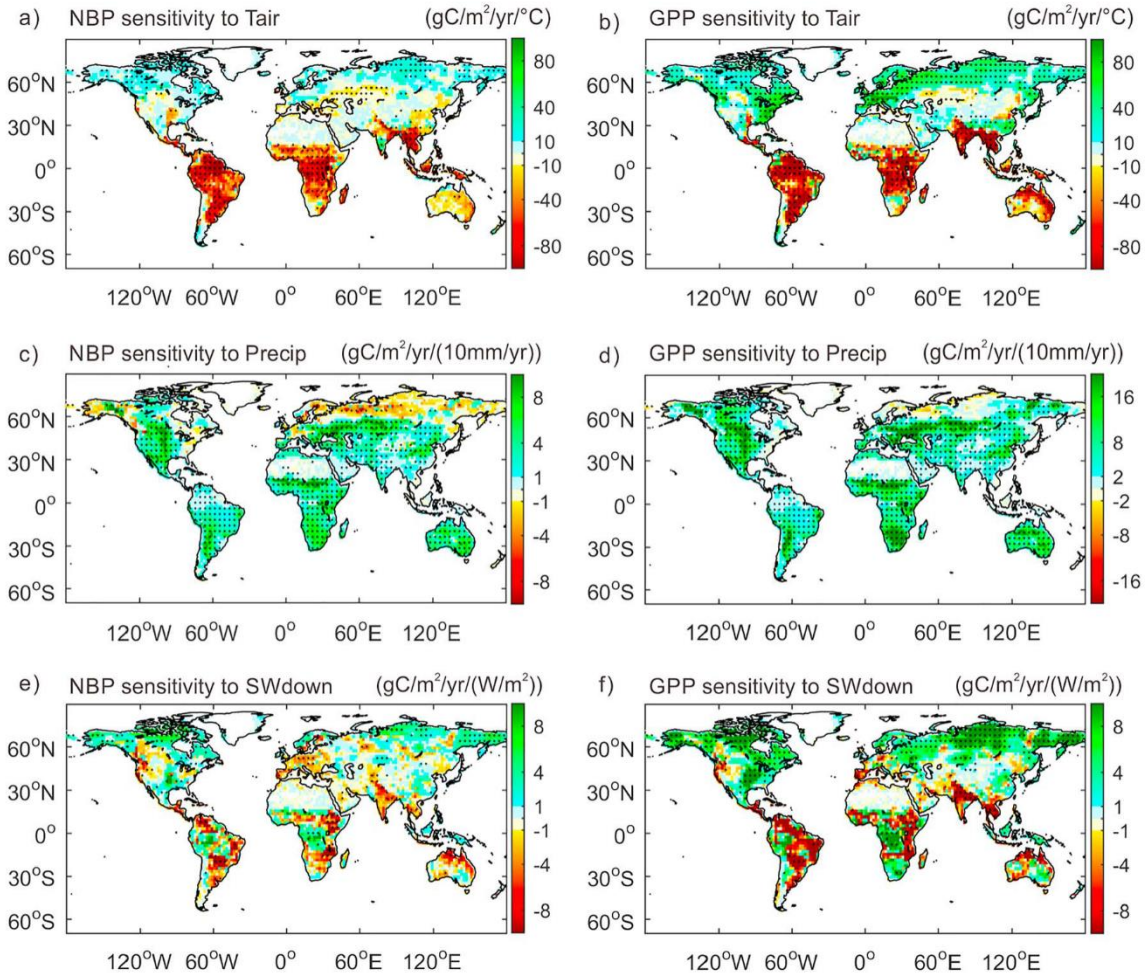

Figure 7. The sensitivity of net biome production (NBP) and gross primary production (GPP) to climate factors for IPSL*hist* simulations during 1860–2005. (a) NBP sensitivity to temperature. (b) GPP sensitivity to temperature. (c) NBP sensitivity to precipitation. (d) GPP sensitivity to precipitation. (e) NBP sensitivity to *SWdown*. (f) GPP sensitivity to *SWdown*. The dotted regions indicate where at least two of the three ensemble members detected a sensitivity significantly different from 0. The sensitivities for IPSL*NoAA* and other Earth system models are in Figures S5–S9.

At southern midlatitudes (30–60°S), the NBP change is mainly due to CCAA-related precipitation change (e.g., south Argentina and South Australia; Figures 8a, 8c, and 8e). The precipitation-dominated areas cover about 50% of this latitude band for all the three ESMs (Figures 8b, 8d, and 8f).

At low latitudes (30°S–30°N), positive and negative NBP changes cannot be attributed to a single climate factor (Figure 8). In 56–75% of the pixels with an increase in NBP, CCAA-induced temperature change (i.e., the cooling effect of AA) is the main factor. However, CCAA-induced precipitation decrease is found to be the main factor causing NBP decrease, covering 38–57% of the NBP-decrease area (Figures 5 and 8).

At northern midlatitudes (30–60°N; Figures 8a, 8c, and 8e), simulations for the three ESMs agree with a temperature-dominated NBP increase in East Asia and the southeast United States, as well as a precipitation-dominated NBP increase in the central United States. However, large discrepancies are found among ESMs in central Eurasia. The IPSL and CSIRO simulations imply an increase of NBP mainly due to precipitation and radiation, respectively, while the GISS leads to an NBP decline due to lower precipitation from CCAA.

In contrast to the other regions, the high northern latitudes (60–90°N) showed larger area of NBP decline than increase in response to CCAA (Figure 8). This decrease is largely caused by the cooling and diming effects of aerosols, over mainly temperature-or radiation-limited ecosystems. The two factors dominate 76–81% of the high-latitude NBP-decrease region.

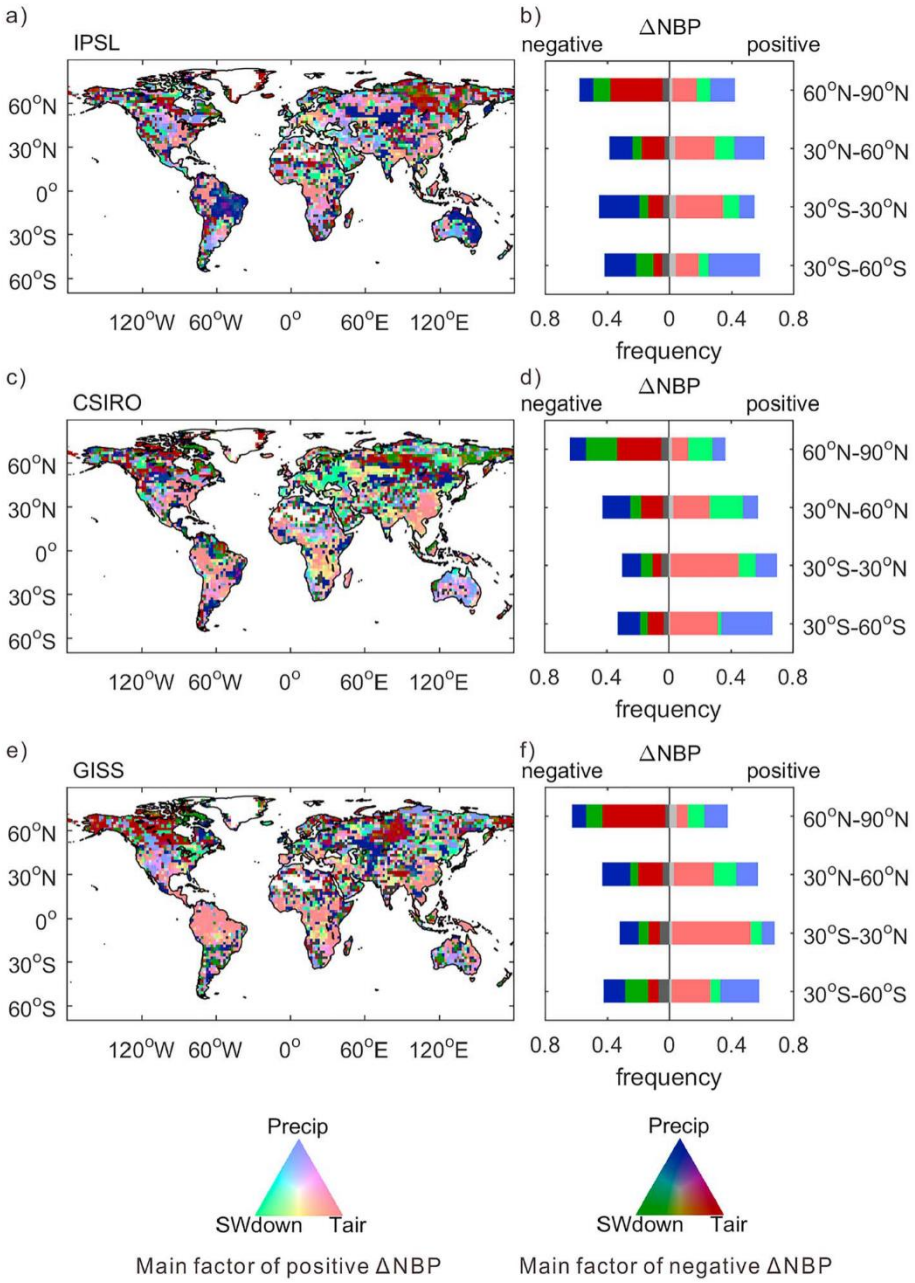

Figure 8. The spatial distribution of the main climate factors causing aerosol-induced net biome production (NBP) change. (a) The main factor for IPSL; the pixels where NBP difference is mainly contributed by*Tair*,*Precip*, and *SWdown*are presented in red, blue, and green, respectively. The bright colors indicate pixels with positive response of NBP to anthropogenic aerosols, while dark colors indicate negative response. Pixels where NBP difference cannot be explained by the three factors are shown in light gray (positive NBP response) and dark gray (negative NBP response). (b) The area statistics for the main factors (*Tair*,*Precip*,*SWdown*, and"no dominant factor"in red, blue, green, gray, respectively; positive and negative NBP responses showed in light and dark colors). (c, e) The same as (a) but for CSIRO and GISS, respectively. (d, f) The same as (b) but for CSIRO and GISS, respectively.

4. Discussion

4.1. Impacts of Aerosols on Climate

The best understood aerosol impacts on climate are through aerosol-radiation and aerosol-cloud interactions (Haywood & Boucher, 2000). Aerosol-radiation interaction occurs through the scattering and absorption of shortwave radiation. This effect often causes a negative radiative forcing because aerosols usually contribute

to enhance the Earth's albedo, except for absorbing aerosols (e.g., black carbon) in situation when the surface albedo is high (e.g., for snow or ice surfaces). The global integral of this effect results in−0.45 (−0.95 to +0.05) W/m^2 radiative forcing, although the uncertainty remains large (Boucher et al., 2013). Aerosol-cloud interactions indicate the pathways through which aerosols affect the distribution and radiative properties of clouds, mainly by acting as cloud nuclei and affecting cloud droplet size and phase (Boucher, 2015). The total radiative forcing of aerosol-cloud interactions is−0.45 (−1.2 to 0.0) W/m ^{2} (Boucher et al., 2013).

Both aerosol-radiation and aerosol-cloud interaction mechanisms have been incorporated in the three CMIP5 ESMs used in this study (for aerosol-cloud interaction, IPSL and GISS omitted the response of rainfall efficiency to cloud droplet size change). As a response to the aerosol-caused negative radiative forcing, cooling and diming effects are found in all of the modeled climate as expected (Figure 2). Although there is no direct observation under the*NoAA*/*No*Ascenario to validate the cooling and diming effects, such effects have been reported under high-aerosol-loading period after large volcano eruptions (Parker et al., 1996; Schwartz, 2005). However, due to different parameterizations in ESMs, the magnitudes of the cooling (0.37–0.65 °C) and diming (2.7–4.8 W/m^2) effects remain poorly constrained.

Compared with temperature and*SWdown*, precipitation has more complex responses to the radiative forcing from aerosols. At relatively short time scales, aerosols can alter precipitation by changing atmospheric radiative budget, but at longer time scales, they can meanwhile decrease precipitation by cooling the Earth's surface (Andrews et al., 2010). Here we found that all the three ESMs simulate a weak drying effect of aerosols at high latitudes (Figures 5 and S3), suggesting that the aerosol-caused surface cooling effect is predominant at this latitude. This effect is in line with Wu et al. (2013), who reported a weakened global hydrological cycle due to aerosols. At middle to low latitudes, the precipitation response to aerosols vary among ESMs, which is consistent with a recent multimodel comparison work (Samset et al., 2016). This is not surprising, because even under the same scenario (*hist*), CMIP5 ESMs already produce distinct precipitation pattern in the tropics (Ahlström et al., 2017; Mehran et al., 2014). For now, it remains difficult to say which ESM reproduced better aerosol impacts on precipitation, because no observation is available under the*NoAA*/*No*Ascenario, and any decomposition of observed climate change between several causes remains dependent on the underlying model used for the decomposition.

The climate responses discussed here are for all aerosols in GISS but only for AA for IPSL and CSIRO. The similar magnitude in the impacts from all aerosols in GISS and from AA in IPSL and CSIRO does not mean that the natural aerosols are negligible. A recent study has shown considerable feedbacks between natural aerosols and climate (Scott et al., 2018).

4.2. Response of C Fluxes

Using bias-corrected climate from CMIP5 historical experiments to force ORCHIDEE, we obtained a global C sink during 1860–2005 of 2.1–20.3 PgC, falling in the range of the IPCC AR5 estimates for the industrial period (30 ± 45 PgC; Ciais et al., 2013), which gives some confidence in the validity of this LSM to simulate historical changes in the C budget.

Compared with the positive cumulated NBP in the*hist*simulations, all the*NoAA/NoA*simulations indicate a net source during 1860–2005; that is, aerosols induce a net cumulative CO_2 sink since 1860. Similarly, Jones et al. (2003) reported that sulfate aerosols enhanced land C sink and even reversed land from C source to sink during the post-Pinatubo period. These results indicate that CCAA are an important factor for the net land C balance that may have mitigated the increase of atmospheric CO_2 concentration considerably by enhancing the terrestrial C sink. However, the magnitude of NBP increase due to CCAA remains quite uncertain (11.6–41.8 PgC during 1860–2005), which we attribute to the different aerosol treatments and climate parameterizations in the ESMs.

Despite the large range in aerosol-induced NBP increase, climate from all the ESMs leads to NBP increase mainly in the tropics and northern midlatitudes (Figure 4). This result is in line with previous studies, which showed that the interannual variation of global land C balance is mainly controlled by these regions (Cox et al., 2013; Wang et al., 2013).

A decomposition of the CCAA-caused NBP change to differentfluxes revealed different mechanisms in different latitudes, when NBP is simulated with ORCHIDEE. At northern middle to high latitudes, aerosols

decreased both GPP and TER. However, the different relative strengths of the GPP and TER declines caused opposite NBP response in the two regions (Figure 4). In contrast to the consistency at middle to high latitudes, the opposite mechanism of NBP increase is found in the tropics among simulations forced by different ESM climates. This divergence can only come from the discrepancy on the aerosol-caused climate change in this region among ESMs because all Cfluxes are calculated by the same LSM and the baseline difference in ESM climate has been removed (see section 2.2.2). Since the tropics contribute most to global land Cflux, the mechanisms for global NBP change in response to aerosols are thus distinct among ESMs (Figure 3).

Although different ESM forcings lead to different GPP and TER responses to aerosols, all simulations agreed that the GPP change is the driver of NBP change in most regions, regardless of its sign (Figure 6). This result is in line with Koven et al. (2015), who showed a prevalent GPP-driven NBP change in ESM simulations because the substrate for respiration is ultimately originating from GPP. Nevertheless, there remain middle-to high-latitude regions where CCAA-induced NBP change is driven by TER (Figure 6). This might be due to large soil C pools in this region, which can result in strong respiration sensitivity to temperature. It should also be noted that even though most pixels in the tropics showed a GPP-driven NBP change, a small portion of TER-driven pixels can dominate the totalflux at the regional scale (e.g., IPSL; Figure 4).

The net emission from land use (including instantaneous C change, long-term emissions from organic matter decomposition, and possible vegetation regrowth) is one of the most important components of land C fluxes. It determines the land C balance along with the natural C sink (C sink due to processes other than land use; Ciais et al., 2013). Our decomposition of NBP using two land use scenarios reveals that CCAA mainly affect the natural C sink, but much less land use emissions during 1966–2005. This result is robust if the period was extended to 1860–2005 (not shown). It is in line with the theoretical conclusions by Gasser and Ciais (2013). However, it is still early to draw the conclusions on how aerosols affect land use emissions because this work only includes the information on cropland extent, while land management in forests and grassland may also have considerable C consequence (Erb et al., 2018) and more impacts from CCAA.

4.3. Mechanisms of NBP Change

In this study, we found that the difference in CCAA-induced NBP change patterns at low latitudes is largely explained by aerosol-induced P-PET changes (Figure 5). For each ESM forcing, the resulting decline in NBP matches well the decrease of P-PET, indicating that C uptake is limited by water availability at middle to low latitudes. Similarly, Piao, Ciais, et al. (2009) found predominant precipitation limitation of NBP at middle to low latitudes.

How aerosols affect Cfluxes not only depends on how climate is affected but may also depend on the sensitivities of Cfluxes to each climate factor due to the aerosol-induced climate baseline change. Our analyses with ORCHIDEE suggest that C uptake increases in response to lower temperature and higher precipitation at low latitudes and behaves oppositely at high latitudes (Figure 7). This pattern shows high consistency among simulations using different ESM climates and between different aerosol scenarios (Figures 7 and S5–S9), indicating that aerosols do not remarkably alter the Cflux sensitivities to climate during the study period. The Cflux changes caused by aerosols are mainly controlled by the effect of aerosols on climate rather than on Cflux sensitivities.

It should be noted that the sensitivity is based on a multilinear regression (equation (5)). Although this method has been used in previous work (Piao et al., 2013), it may fail when factors are strongly correlated, especially when there exist long-term trends in variables such as temperature, radiation (Figure 2), and CO_2. To test whether the sensitivity detected by this method is an artifact, we repeated the*hist*simulation using bias-corrected IPSL-CM5A-LR r2i1p1 climate, but keeping the atmospheric CO_2 concentrationfixed at the preindustrial level. Using a similar decomposition as equation (5) but without the CO_2 term (Figure S10), we found very similar climate sensitivities as for the IPSL*hist*simulations (Figure 7), implying that the sensitivities detected by the multilinear regression is unlikely an artifact of the method.

Using the Cflux sensitivities to different climate factors given by ORCHIDEE, for thefirst time we were able to decompose the aerosol-caused Cflux change to different climate factors (Figure 8). Our results show that at middle to low latitudes, aerosol-caused cooling is responsible to most of the NBP increase, in line with previous studies showing strong sensitivity of tropical C to warming (Cox et al., 2013; Wang et al., 2013).

However, aerosols also triggered NBP decline in regions through decrease precipitation (Figure 8). The asymmetry in factors driving positive and negative NBP changes probably implies that current precipitation in some tropical regions (e.g., east Amazon) may be near or have already exceeded the threshold at which water availability begins to limit C sequestration.

Compared with those at low latitudes, the aerosol-induced NBP changes at high latitudes are more prevalently negative and can be mainly attributed to cooling and diming (Figure 8), in line with the energy limitation of C uptake in these regions (Nemani et al., 2003, Piao, Ciais, et al., 2009; Stine & Huybers, 2014). It also implies a higher temperature sensitivity of C assimilation than decomposition at high latitudes. However, C decomposition rate increases with temperature exponentially, so if temperature keeps rising, the sensitivity of TER to temperature could become stronger than that of GPP. In that case, the cooling from aerosols may cause stronger decrease in TER than in GPP and lead to positive NBP.

4.4. Advantages and Limitations of the Method

Previous studies that investigated the aerosol impacts on the C cycle also used simulations with and without aerosols (Jones et al., 2003; Mahowald et al., 2011). Using HadCM3L ESM, Jones et al. (2003) suggested a large C sink due to suppressed soil respiration in response to the cooling from CCAA. However, with CCSM3.1 ESM, Mahowald et al. (2011) gave only a small aerosol impact on global Cflux. This difference implies a high sensitivity of the CCAA effect on Cfluxes to the choice of one ESM forcing. In this study, we use climate data from three different ESMs, and use ensembles with three members each to further reduce the uncertainties and solidity of our results. The simulations forced by different ESMs show robust Cflux response to aerosols at middle to high latitudes. However, in the tropics, there remains large divergence in CCAA-induced Cflux changes among ESMs due to distinct precipitation response to aerosols. Therefore, tropical precipitation modeling is likely responsible for the different aerosol impacts found in the previous studies (Jones et al., 2003; Mahowald et al., 2011). Currently, the most efficient way to reduce the uncertainty in aerosol impacts on the C cycle should be to improve the simulation of precipitation patterns in ESMs and gain confidence on their changes in response to climate forcings (Ahlström et al., 2017).

Apart from these advantages, the current method still presents some limitations. First, the simulations in this study are all based on a single LSM, which limited the investigation of LSM-source uncertainty in aerosol impacts. Similar simulations using different LSMs are needed to test the robustness of our results. Second, besides changing climate, aerosols are able to alter the land C cycle through other pathways, such as changing light quality (Cirino et al., 2014; Gu et al., 2003; Knohl & Baldocchi, 2008; Mercado et al., 2009) and nutrient deposition (Magnani et al., 2007; Mahowald et al., 2011; Wang et al., 2017). These processes are currently absent but will be soon included in future ORCHIDEE versions to give more accurate estimations on aerosol impacts. It should also be noted that the impacts of aerosols estimated here might be somewhat different from using actual coupled simulations. This is because the LSM used here is not the ones imbedded in the CMIP5 ESMs (the ORCHIDEE LSM used here is an updated version from the one in IPSL-CM5A-LR). Also, the bias correction treatment applied and described in this study could result in different feedback terms from the CMIP5 simulations. Furthermore, the CMIP5*hist*experiment is not fully coupled. It omitted the carbon-climate feedback due to the use of atmospheric CO_2 concentration other than CO_2 emissions as forcing.

5. Conclusions

In this study we investigated the impacts of aerosol-induced climate change on land Cfluxes during the period 1860–2005 using a set of offline simulations on ORCHIDEE LSM, driven by climate under CMIP5*hist* and*NoAA/No*Ascenarios simulated by IPSL, CSIRO, and GISS ESMs.

At the global scale, we estimated a 11.6-to 41.8-PgC NBP increase due to aerosols during the study period. Without aerosol-induced climate change, the results from the ESM used in ORCHIDEE indicate that land ecosystems would be a small cumulative source of carbon, instead of a small sink since 1860. All our simulations agree that the increased C sink occurred mainly in the tropics and north midlatitudes, while the NBP at high latitudes decreases in response to aerosols. Using a set of no land use change experiments, we show that the aerosol-induced C sink is mainly due to a change in the natural sink rather than in the land use emissions.

Using Cflux sensitivities to different climate factors, we investigated the mechanisms of how aerosols affect NBP. We found that aerosol-caused cooling is responsible for most of the NBP changes. At high latitudes, GPP decrease due to aerosol cooling triggered NBP decline. At midlatitudes, cooling triggered stronger decrease in TER than in GPP, resulting in NBP increase. At low latitudes, cooling enhanced both GPP and NBP. However, this enhancement can be easily canceled when aerosols also decrease precipitation. Due to the large divergence in tropical precipitation modeling, simulations using climate from different ESMs showed uncertainty in the aerosol-caused NBP change, highlighting the need to improve precipitation modeling in ESMs.

Acknowledgments
This work was supported by the European Research Council Synergy grant ERC-2013-SyG-610028 IMBALANCE-P. We thank the ORCHIDEE group for the code and help with the ORCHIDEE model. We also thank Chris D. Jones for his constructive comments, which have helped improve this manuscript. Data used in this study can be accessed through https://esgf-node.ipsl.upmc.fr/projects/esgf-ipsl/, https://www.esrl.noaa.gov/gmd/ccgg/trends/ and https://vesg.ipsl.upmc.fr/thredds/catalog/store/p529viov/cruncep/V72_1901_2016/catalog.html.

References

Ahlström, A., Canadell, J. G., Schurgers, G., Wu, M., Berry, J. A., Guan, K., & Jackson, R. B. (2017). Hydrologic resilience and Amazon productivity.*Nature Communications*,*8*(1), 387. https://doi.org/10.1038/s41467-017-00306-z

Andrews, T., Forster, P. M., Boucher, O., Bellouin, N., & Jones, A. (2010). Precipitation, radiative forcing and global temperature change. *Geophysical Research Letters*,*37*, L14701. https://doi.org/10.1029/2010GL043991

Bellouin, N., Rae, J., Jones, A., Johnson, C., Haywood, J., & Boucher, O. (2011). Aerosol forcing in the Climate Model Intercomparison Project (CMIP5) simulations by HadGEM2-ES and the role of ammonium nitrate.*Journal of Geophysical Research*,*116*, D20206. https://doi.org/10.1029/2011JD016074

Boucher, O. (2015).*Atmospheric aerosols: Properties and climate impacts*. Netherlands: Springer.

Boucher, O., Randall, D., Artaxo, P., Bretherton, C., Feingold, G., Forster, P., et al. (2013). Clouds and aerosols. In*Climate change 2013: The physical science basis. Contribution of Working Group I to the Fifth Assessment Report of the Intergovernmental Panel on Climate Change* (pp. 571–657). Cambridge, UK and New York: Cambridge University Press.

Bowman, W. D., Cleveland, C. C., Halada,Ľ., Hreško, J., & Baron, J. S. (2008). Negative impact of nitrogen deposition on soil buffering capacity.*Nature Geoscience*,*1*(11), 767–770. https://doi.org/10.1038/ngeo339

Ciais, P., Reichstein, M., Viovy, N., Granier, A., Ogée, J., Allard, V., et al. (2005). Europe-wide reduction in primary productivity caused by the heat and drought in 2003.*Nature*,*437*(7058), 529–533. https://doi.org/10.1038/nature03972

Ciais, P., Sabine, C., Bala, G., Bopp, L., Brovkin, V., Canadell, J., et al. (2013). Carbon and other biogeochemical cycles. In*Climate change 2013: The physical science basis. Contribution of Working Group I to the Fifth Assessment Report of the Intergovernmental Panel on Climate Change*(pp. 465–570). Cambridge, UK and New York: Cambridge University Press.

Cirino, G., Souza, R., Adams, D., & Artaxo, P. (2014). The effect of atmospheric aerosol particles and clouds on net ecosystem exchange in the Amazon.*Atmospheric Chemistry and Physics*,*14*(13), 6523–6543. https://doi.org/10.5194/acp-14-6523-2014

Cox, P. M., Pearson, D., Booth, B. B., Friedlingstein, P., Huntingford, C., Jones, C. D., & Luke, C. M. (2013). Sensitivity of tropical carbon to climate change constrained by carbon dioxide variability.*Nature*,*494*(7437), 341–344. https://doi.org/10.1038/nature11882

De Rosnay, P., & Polcher, J. (1998). Modelling root water uptake in a complex land surface scheme coupled to a GCM.*Hydrology and Earth System Sciences Discussions*,*2*(2/3), 239–255. https://doi.org/10.5194/hess-2-239-1998

Ducoudré, N. I., Laval, K., & Perrier, A. (1993). SECHIBA, a new set of parameterizations of the hydrologic exchanges at the land-atmosphere interface within the LMD atmospheric general circulation model.*Journal of Climate*,*6*(2), 248–273. https://doi.org/10.1175/1520-0442(1993)006<0248:SANSOP>2.0.CO;2

Dufresne, J.-L., Foujols, M.-A., Denvil, S., Caubel, A., Marti, O., Aumont, O., et al. (2013). Climate change projections using the IPSL-CM5 Earth system model: From CMIP3 to CMIP5.*Climate Dynamics*,*40*(9–10), 2123–2165. https://doi.org/10.1007/s00382-012-1636-1

Eliseev, A. V. (2015). Impact of tropospheric sulphate aerosols on the terrestrial carbon cycle.*Global and Planetary Change*,*124* , 30–40. https://doi.org/10.1016/j.gloplacha.2014.11.005

Erb, K.-H., Kastner, T., Plutzar, C., Bais, A. L. S., Carvalhais, N., Fetzel, T., et al. (2018). Unexpectedly large impact of forest management and grazing on global vegetation biomass.*Nature*,*553*(7686), 73–76. https://doi.org/10.1038/nature25138

Flato, G., Marotzke, J., Abiodun, B., Braconnot, P., Chou, S. C., Collins, W. J., et al. (2013). Evaluation of climate models. In*Climate change 2013: The physical science basis. Contribution of Working Group I to the Fifth Assessment Report of the Intergovernmental Panel on Climate Change, Climate Change 2013*,*5*(pp. 741–866). Cambridge, UK and New York: Cambridge University Press.

Gasser, T., & Ciais, P. (2013). A theoretical framework for the net land-to-atmosphere CO_2 flux and its implications in the definition of "emissions from land-use change".*Earth System Dynamics*,*4*(1), 171–186. https://doi.org/10.5194/esd-4-171-2013

Gu, L., Baldocchi, D. D., Wofsy, S. C., Munger, J. W., Michalsky, J. J., Urbanski, S. P., & Boden, T. A. (2003). Response of a deciduous forest to the Mount Pinatubo eruption: Enhanced photosynthesis.*Science*,*299*(5615), 2035–2038. https://doi.org/10.1126/science.1078366

Haywood, J., & Boucher, O. (2000). Estimates of the direct and indirect radiative forcing due to tropospheric aerosols: A review.*Reviews of Geophysics*,*38*(4), 513–543. https://doi.org/10.1029/1999RG000078

Huete, A. R., Didan, K., Shimabukuro, Y. E., Ratana, P., Saleska, S. R., Hutyra, L. R., et al. (2006). Amazon rainforests green-up with sunlight in dry season.*Geophysical Research Letters*,*33*, L06405. https://doi.org/10.1029/2005GL025583

Hurtt, G. C., Chini, L. P., Frolking, S., Betts, R., Feddema, J., Fischer, G., et al. (2011). Harmonization of land-use scenarios for the period 1500–2100: 600 years of global gridded annual land-use transitions, wood harvest, and resulting secondary lands.*Climatic Change*, *109*(1–2), 117–161. https://doi.org/10.1007/s10584-011-0153-2

Jeffrey, S., Rotstayn, L., Collier, M., Dravitzki, S., Hamalainen, C., Moeseneder, C., et al. (2013). Australia's CMIP5 submission using the CSIRO Mk3. 6 model.*Australian Meteorological and Oceanographic Journal*,*63*(1), 1–14. https://doi.org/10.22499/2.6301.001

Jones, C. D., Cox, P. M., Essery, R. L., Roberts, D. L., & Woodage, M. J. (2003). Strong carbon cycle feedbacks in a climate model with interactive CO_2 and sulphate aerosols.*Geophysical Research Letters*,*30*(9), 1479. https://doi.org/10.1029/2003GL016867

Jung, M., Reichstein, M., Schwalm, C. R., Huntingford, C., Sitch, S., Ahlström, A., et al. (2017). Compensatory water effects link yearly global land CO_2 sink changes to temperature.*Nature*,*541*(7638), 516–520. https://doi.org/10.1038/nature20780

Knohl, A., & Baldocchi, D. D. (2008). Effects of diffuse radiation on canopy gas exchange processes in a forest ecosystem.*Journal of Geophysical Research*,*113*, G02023. https://doi.org/10.1029/2007JG000663

Koven, C. D., Chambers, J. Q., Georgiou, K., Knox, R., Negron-Juarez, R., Riley, W. J., et al. (2015). Controls on terrestrial carbon feedbacks by productivity versus turnover in the CMIP5 Earth system models.*Biogeosciences*,*12*(17), 5211–5228. https://doi.org/10.5194/bg-12-5211-2015

Krinner, G., Viovy, N., De Noblet-Ducoudré, N., Ogée, J., Polcher, J., Friedlingstein, P., et al. (2005). A dynamic global vegetation model for studies of the coupled atmosphere-biosphere system.*Global Biogeochemical Cycles*,*19*, GB1015. https://doi.org/10.1029/2003GB002199

Le Quéré, C., Andrew, R. M., Friedlingstein, P., Sitch, S., Pongratz, J., Manning, A. C., et al. (2017). Global carbon budget 2017.*Earth System Science Data Discussions*, 1–79. https://doi.org/10.5194/essd-2017-123

Luo, Y., Su, B., Currie, W. S., Dukes, J. S., Finzi, A., Hartwig, U., et al. (2004). Progressive nitrogen limitation of ecosystem responses to rising atmospheric carbon dioxide.*AIBS Bulletin*,*54*(8), 731–739.

Magnani, F., Mencuccini, M., Borghetti, M., Berbigier, P., Berninger, F., Delzon, S., et al. (2007). The human footprint in the carbon cycle of temperate and boreal forests.*Nature*,*447*(7146), 849–851. https://doi.org/10.1038/nature05847

Mahowald, N. (2011). Aerosol indirect effect on biogeochemical cycles and climate.*Science*,*334*(6057), 794–796. https://doi.org/10.1126/science.1207374

Mahowald, N., Lindsay, K., Rothenberg, D., Doney, S. C., Moore, J. K., Thornton, P., & Jones, C. (2011). Desert dust and anthropogenic aerosol interactions in the Community Climate System Model coupled-carbon-climate model.*Biogeosciences*,*8*(2), 387–414. https://doi.org/10.5194/bg-8-387-2011

Mahowald, N. M., Scanza, R., Brahney, J., Goodale, C. L., Hess, P. G., Moore, J. K., & Neff, J. (2017). Aerosol deposition impacts on land and ocean carbon cycles.*Current Climate Change Reports*,*3*(1), 16–31. https://doi.org/10.1007/s40641-017-0056-z

Mehran, A., AghaKouchak, A., & Phillips, T. J. (2014). Evaluation of CMIP5 continental precipitation simulations relative to satellite-based gauge-adjusted observations.*Journal of Geophysical Research: Atmospheres*,*119*, 1695–1707. https://doi.org/10.1002/2013JD021152

Mercado, L. M., Bellouin, N., Sitch, S., Boucher, O., Huntingford, C., Wild, M., & Cox, P. M. (2009). Impact of changes in diffuse radiation on the global land carbon sink.*Nature*,*458*(7241), 1014–1017. https://doi.org/10.1038/nature07949

Miller, R. L., Schmidt, G. A., Nazarenko, L. S., Tausnev, N., Bauer, S. E., DelGenio, A. D., et al. (2014). CMIP5 historical simulations (1850–2012) with GISS ModelE2.*Journal of Advances in Modeling Earth Systems ,6*, 441–478. https://doi.org/10.1002/2013MS000266

Nemani, R. R., Keeling, C. D., Hashimoto, H., Jolly, W. M., Piper, S. C., Tucker, C. J., et al. (2003). Climate-driven increases in global terrestrial net primary production from 1982 to 1999.*Science*,*300*(5625), 1560–1563. https://doi.org/10.1126/science.1082750

Norby, R. J., Warren, J. M., Iversen, C. M., Medlyn, B. E., & McMurtrie, R. E. (2010). CO_2 enhancement of forest productivity constrained by limited nitrogen availability.*Proceedings of the National Academy of Sciences*,*107*(45), 19,368–19,373. https://doi.org/10.1073/pnas.1006463107

Parker, D., Wilson, H., Jones, P. D., Christy, J., & Folland, C. K. (1996). The impact of Mount Pinatubo on world-wide temperatures. *International Journal of Climatology*,*16*(5), 487–497. https://doi.org/10.1002/(SICI)1097-0088(199605)16:5<487::AID-JOC39>3.0.CO;2-J

Piao, S., Ciais, P., Friedlingstein, P., De Noblet-Ducoudré, N., Cadule, P., Viovy, N., & Wang, T. (2009). Spatiotemporal patterns of terrestrial carbon cycle during the 20th century.*Global Biogeochemical Cycles*,*23*, GB4026. https://doi.org/10.1029/2008GB003339

Piao, S., Fang, J., Ciais, P., Peylin, P., Huang, Y., Sitch, S., & Wang, T. (2009). The carbon balance of terrestrial ecosystems in China.*Nature*, *458*(7241), 1009–1013. https://doi.org/10.1038/nature07944

Piao, S., Sitch, S., Ciais, P., Friedlingstein, P., Peylin, P., Wang, X., et al. (2013). Evaluation of terrestrial carbon cycle models for their response to climate variability and to CO_2 trends.*Global Change Biology*,*19*(7), 2117–2132. https://doi.org/10.1111/gcb.12187

Piao, S. L., Friedlingstein, P., Ciais, P., Zhou, L. M., & Chen, A. P. (2006). Effect of climate and CO_2 changes on the greening of the Northern Hemisphere over the past two decades.*Geophysical Research Letters*,*33*, L23402. https://doi.org/10.1029/2006GL028205

Poulter, B., MacBean, N., Hartley, A., Khlystova, I., Arino, O., Betts, R., et al. (2015). Plant functional type classification for Earth system models: Results from the European Space Agency's Land Cover Climate Change Initiative.*Geoscientific Model Development*,*8*(7), 2315–2328. https://doi.org/10.5194/gmd-8-2315-2015

Reichstein, M., Ciais, P., Papale, D., Valentini, R., Running, S., Viovy, N., et al. (2007). Reduction of ecosystem productivity and respiration during the European summer 2003 climate anomaly: A jointflux tower, remote sensing and modelling analysis.*Global Change Biology*, *13*(3), 634–651. https://doi.org/10.1111/j.1365-2486.2006.01224.x

Rotstayn, L., Jeffrey, S., Collier, M., Dravitzki, S., Hirst, A., Syktus, J., & Wong, K. (2012). Aerosol-and greenhouse gas-induced changes in summer rainfall and circulation in the Australasian region: A study using single-forcing climate simulations.*Atmospheric Chemistry and Physics*,*12*(14), 6377–6404. https://doi.org/10.5194/acp-12-6377-2012

Samset, B., Myhre, G., Forster, P., Hodnebrog, Ø., Andrews, T., et al. (2016). Fast and slow precipitation responses to individual climate forcers: A PDRMIP multimodel study.*Geophysical Research Letters*,*43*, 2782–2791. https://doi.org/10.1002/2016GL068064

Schmidt, G. A., Kelley, M., Nazarenko, L., Ruedy, R., Russell, G. L., Aleinov, I., et al. (2014). Configuration and assessment of the GISS ModelE2 contributions to the CMIP5 archive.*Journal of Advances in Modeling Earth Systems*,*6*, 141–184. https://doi.org/10.1002/2013MS000265

Schwartz, R. D. (2005). Global dimming: Clear-sky atmospheric transmission from astronomical extinction measurements.*Journal of Geophysical Research*,*110*, D14210. https://doi.org/10.1029/2005JD005882

Scott, C., Arnold, S., Monks, S., Asmi, A., Paasonen, P., & Spracklen, D. (2018). Substantial large-scale feedbacks between natural aerosols and climate.*Nature Geoscience*,*11*(1), 44–48. https://doi.org/10.1038/s41561-017-0020-5

Sitch, S., Cox, P., Collins, W., & Huntingford, C. (2007). Indirect radiative forcing of climate change through ozone effects on the land-carbon sink.*Nature*,*448*(7155), 791–794. https://doi.org/10.1038/nature06059

Sitch, S., Huntingford, C., Gedney, N., Levy, P., Lomas, M., Piao, S., et al. (2008). Evaluation of the terrestrial carbon cycle, future plant geography and climate-carbon cycle feedbacks usingfive dynamic global vegetation models (DGVMs).*Global Change Biology*,*14*(9), 2015–2039. https://doi.org/10.1111/j.1365-2486.2008.01626.x

Sitch, S., Smith, B., Prentice, I. C., Arneth, A., Bondeau, A., Cramer, W., et al. (2003). Evaluation of ecosystem dynamics, plant geography and terrestrial carbon cycling in the LPJ dynamic global vegetation model.*Global Change Biology*,*9*(2), 161–185. https://doi.org/10.1046/j.1365-2486.2003.00569.x

Stine, A., & Huybers, P. (2014). Arctic tree rings as recorders of variations in light availability.*Nature Communications*,*5*(1), 3836. https://doi.org/10.1038/ncomms4836

Taylor, K. E., Stouffer, R. J., & Meehl, G. A. (2012). An overview of CMIP5 and the experiment design.*Bulletin of the American Meteorological Society*,*93*(4), 485–498. https://doi.org/10.1175/BAMS-D-11-00094.1

Thornthwaite, C. W. (1948). An approach toward a rational classification of climate.*Geographical Review*,*38*(1), 55–94. https://doi.org/10.2307/210739

Traore, A. K., Ciais, P., Vuichard, N., Poulter, B., Viovy, N., Guimberteau, M., et al. (2014). Evaluation of the ORCHIDEE ecosystem model over Africa against 25 years of satellite-based water and carbon measurements.*Journal of Geophysical Research:Biogeosciences*,*119*, 1554–1575. https://doi.org/10.1002/2014JG002638

Wang, R., Goll, D., Balkanski, Y., Hauglustaine, D., Boucher, O., Ciais, P., et al. (2017). Global forest carbon uptake due to nitrogen and phosphorus deposition from 1850 to 2100.*Global Change Biology*.,*23*(11), 4854–4872. https://doi.org/10.1111/gcb.13766

Wang, W., Ciais, P., Nemani, R. R., Canadell, J. G., Piao, S., Sitch, S., et al. (2013). Variations in atmospheric CO_2 growth rates coupled with tropical temperature.*Proceedings of the National Academy of Sciences*,*110*(32), 13,061–13,066. https://doi.org/10.1073/pnas.1219683110

Wang, X., Piao, S., Ciais, P., Friedlingstein, P., Myneni, R. B., Cox, P., et al. (2014). A two-fold increase of carbon cycle sensitivity to tropical temperature variations.*Nature*,*506*(7487), 212.

Wu, P., Christidis, N., & Stott, P. (2013). Anthropogenic impact on Earth's hydrological cycle.*Nature Climate Change*,*3*(9), 807–810. https://doi.org/10.1038/nclimate1932

Xing, J., Wang, J., Mathur, R., Wang, S., Sarwar, G., Pleim, J., et al. (2017). Impacts of aerosol direct effects on tropospheric ozone through changes in atmospheric dynamics and photolysis rates.*Atmospheric Chemistry and Physics*,*17*(16), 9869–9883. https://doi.org/10.5194/acp-17-9869-2017

Zhang, Y., Zhu, Z., Liu, Z., Zeng, Z., Ciais, P., Huang, M., et al. (2016). Seasonal and interannual changes in vegetation activity of tropical forests in Southeast Asia.*Agricultural and Forest Meteorology*,*224* , 1–10. https://doi.org/10.1016/j.agrformet.2016.04.009

Global Biogeochemical Cycles

Supporting Information for

Increased global land carbon sink due to aerosol-induced cooling

Yuan ZHANG[1, 2], GOLL Daniel[1 *], BASTOS Ana[1 *], BALKANSKI Yves[1], BOUCHER Olivier[2], CESCATTI Alessandro[3], COLLIER Mark[4], GASSER Thomas[5], GHATTAS Josefine[2], LI Laurent[2], PIAO Shilong[6], VIOVY Nicolas[1], ZHU Dan[1], CIAIS Philippe[1]

[1] Laboratoire des Sciences du Climat et de l'Environnement, LSCE/IPSL - CEA-CNRS-UVQS, Gif sur Yvette, France

[2] Laboratoire de Météorologie Dynamique, IPSL, Sorbonne Universités, UPMC Univ Paris 06, CNRS, 75252, Paris, France

[3] European Commission - DG Joint Research Centre, Institute for Environment and Sustainability, Climate Change Unit, 21020 Ispra, Italy

[4] CSIRO Oceans and Atmosphere, Aspendale, Victoria, Australia

[5] International Institute for Applied Systems Analysis, Laxenburg, Austria

[6] Sino-French Institute for Earth System Science, College of Urban and Environmental Sciences, Peking University, Beijing, China

* Contributed equally to this work

Corresponding author: Yuan ZHANG (yuan.zhang@lmd.jussieu.fr)

Contents of this file

Figures S1 to S9
Table S1

Figure S1. The initial C pools for each (a) IPSL, (b) CSIRO and (c) GISS simulations. The name of each experiment is indicated in Table S1.

Figure S2. Mean bias corrected annual temperature under *hist* (blue) and *NoAA*/*NoA* (red) scenarios in different latitudes. 5-year moving average was applied.

Figure S3. Same as Figure S2 but for precipitation.

Figure S4. Same as Figure S2 but for incoming shortwave radiation

Figure S5. Same as Figure 7 but for IPSL *NoAA* simulations.

Figure S6. Same as Figure 7 but for CSIRO *hist* simulations.

Figure S7. Same as Figure 7 but for CSIRO *NoAA* simulations.

Figure S8. Same as Figure 7 but for GISS *hist* simulations.

Figure S9. Same as Figure 7 but for GISS *NoA* simulations.

Figure S1.

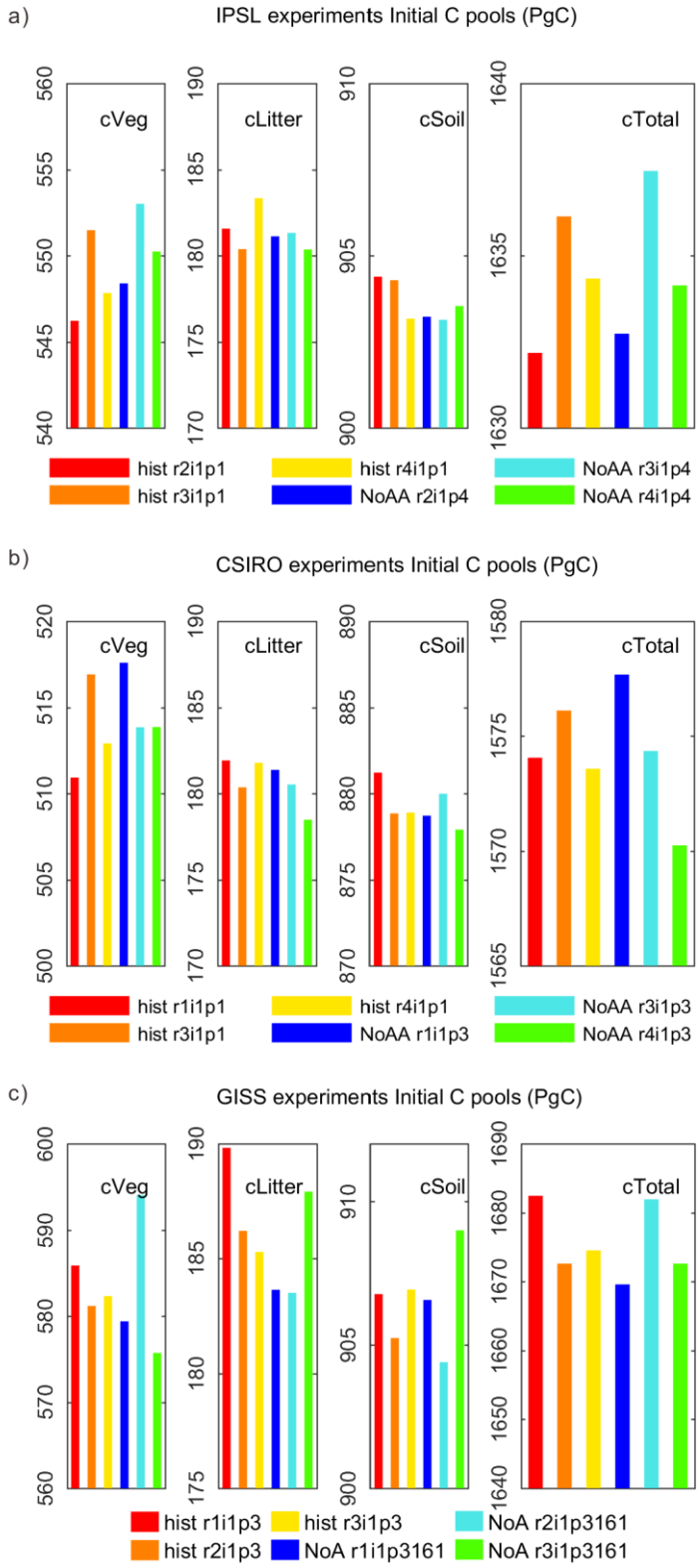
a)
IPSL experiments Initial C pools (PgC)
cVeg
cLitter
cSoil
cTotal
hist r2i1p1
hist r3i1p1
hist r4i1p1
NoAA r2i1p4
NoAA r3i1p4
NoAA r4i1p4
b)
CSIRO experiments Initial C pools (PgC)
cVeg
cLitter
cSoil
cTotal
hist r1i1p1
hist r3i1p1
hist r4i1p1
NoAA r1i1p3
NoAA r3i1p3
NoAA r4i1p3
c)
GISS experiments Initial C pools (PgC)
cVeg
cLitter
cSoil
cTotal
hist r1i1p3
hist r2i1p3
hist r3i1p3
NoA r1i1p3161
NoA r2i1p3161
NoA r3i1p3161

Figure S2.

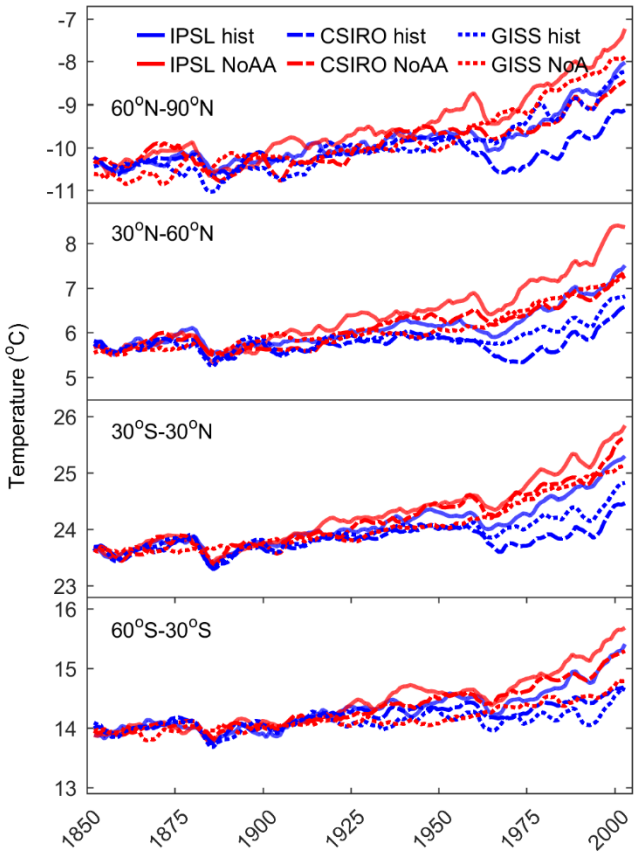
IPSL hist
CSIRO hist
GISS hist
IPSL NoAA
CSIRO NoAA
GISS NoA
60°N-90°N
30°N-60°N
30°S-30°N
60°S-30°S
Temperature (°C)
-7
-8
-9
-10
-11
8
7
6
5
26
25
24
23
16
15
14
13
1850
1875
1900
1925
1950
1975
2000

Figure S3.

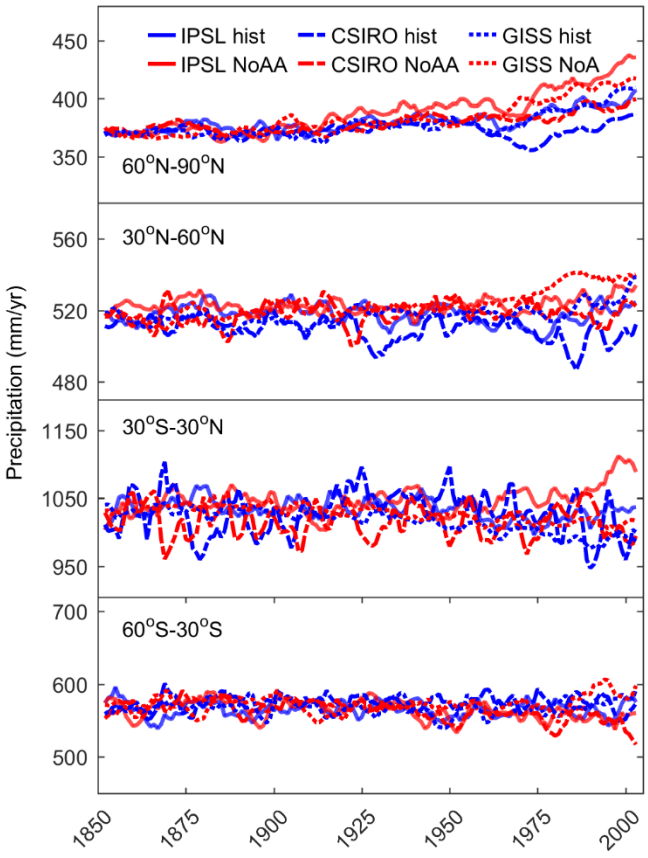
IPSL hist
CSIRO hist
GISS hist
IPSL NoAA
CSIRO NoAA
GISS NoA
Precipitation (mm/yr)
60°N-90°N
30°N-60°N
30°S-30°N
60°S-30°S
450
400
350
560
520
480
1150
1050
950
700
600
500
1850
1875
1900
1925
1950
1975
2000

Figure S4.

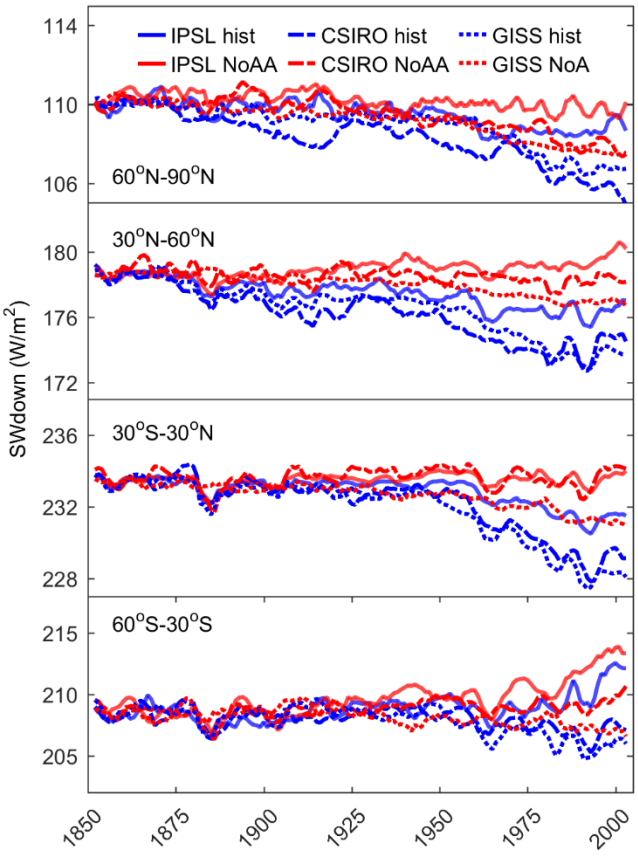
IPSL hist
CSIRO hist
GISS hist
IPSL NoAA
CSIRO NoAA
GISS NoA
60°N-90°N
30°N-60°N
30°S-30°N
60°S-30°S
SWdown (W/m2)
114
110
106
180
176
172
236
232
228
215
210
205
1850
1875
1900
1925
1950
1975
2000

Figure S5.

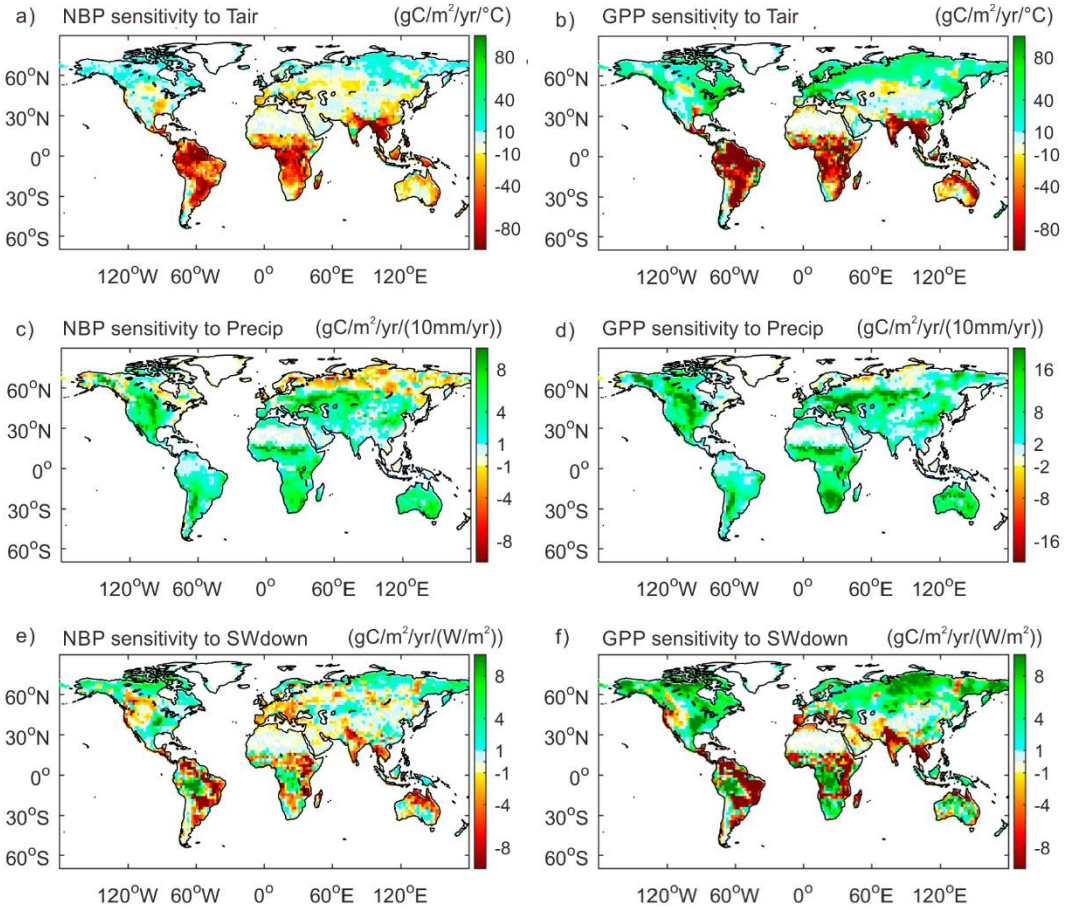
a) NBP sensitivity to Tair (gC/m²/yr/°C)
b) GPP sensitivity to Tair (gC/m²/yr/°C)
c) NBP sensitivity to Precip (gC/m²/yr/(10mm/yr))
d) GPP sensitivity to Precip (gC/m²/yr/(10mm/yr))
e) NBP sensitivity to SWdown (gC/m²/yr/(W/m²))
f) GPP sensitivity to SWdown (gC/m²/yr/(W/m²))
60°N
30°N
0°
30°S
60°S
120°W 60°W 0° 60°E 120°E
80 40 10 -10 -40 -80
16 8 2 -2 -8 -16
8 4 1 -1 -4 -8

Figure S6.

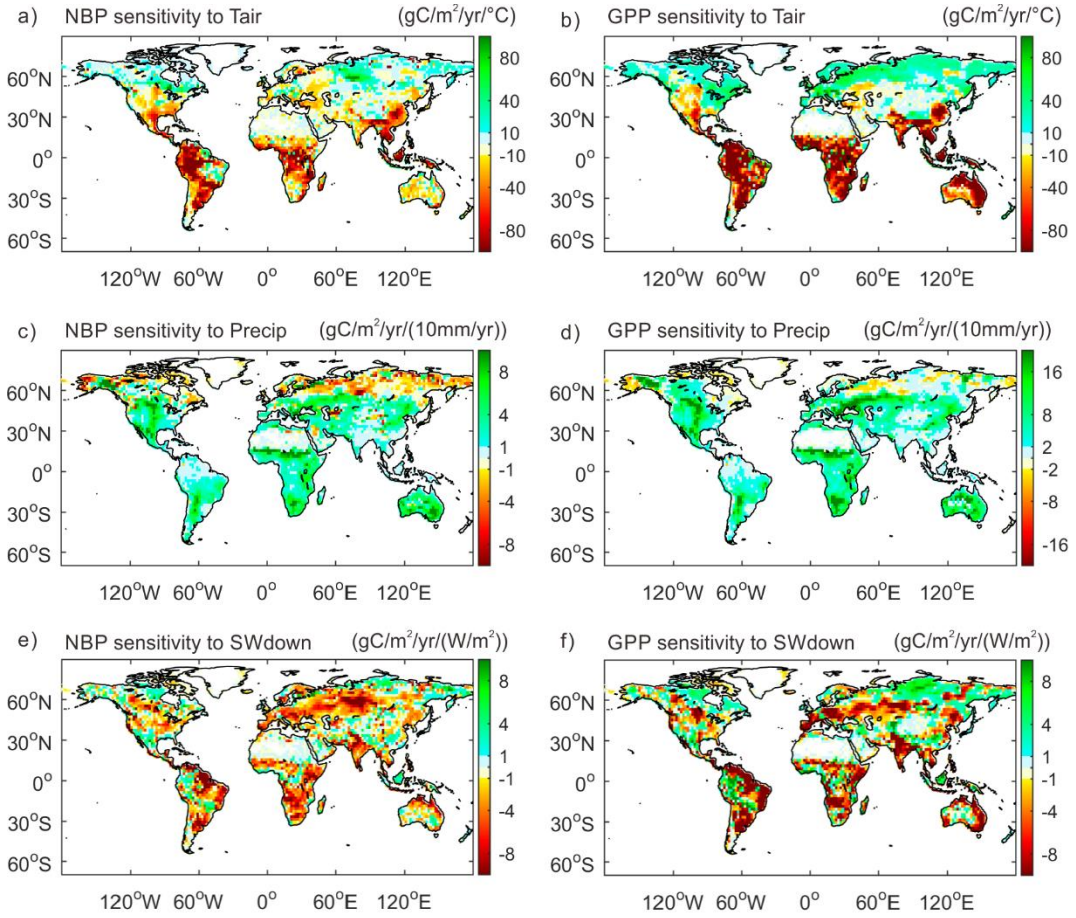
a) NBP sensitivity to Tair (gC/m²/yr/°C)
b) GPP sensitivity to Tair (gC/m²/yr/°C)
c) NBP sensitivity to Precip (gC/m²/yr/(10mm/yr))
d) GPP sensitivity to Precip (gC/m²/yr/(10mm/yr))
e) NBP sensitivity to SWdown (gC/m²/yr/(W/m²))
f) GPP sensitivity to SWdown (gC/m²/yr/(W/m²))
60°N
30°N
0°
30°S
60°S
120°W 60°W 0° 60°E 120°E
80 40 10 -10 -40 -80
16 8 2 -2 -8 -16
8 4 1 -1 -4 -8

Figure S7.

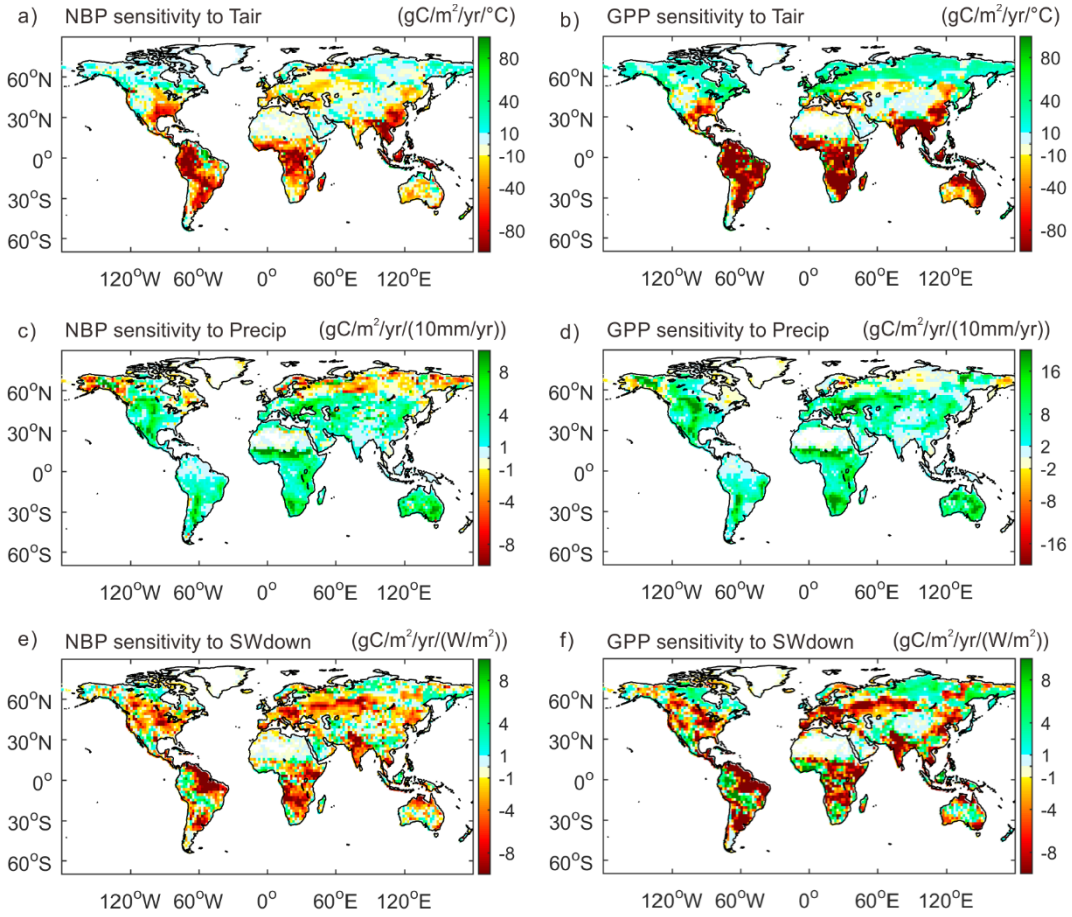
a) NBP sensitivity to Tair (gC/m²/yr/°C)
b) GPP sensitivity to Tair (gC/m²/yr/°C)
c) NBP sensitivity to Precip (gC/m²/yr/(10mm/yr))
d) GPP sensitivity to Precip (gC/m²/yr/(10mm/yr))
e) NBP sensitivity to SWdown (gC/m²/yr/(W/m²))
f) GPP sensitivity to SWdown (gC/m²/yr/(W/m²))
60°N
30°N
0°
30°S
60°S
120°W 60°W 0° 60°E 120°E
80 40 10 -10 -40 -80
8 4 1 -1 -4 -8
16 8 2 -2 -8 -16

Figure S8.

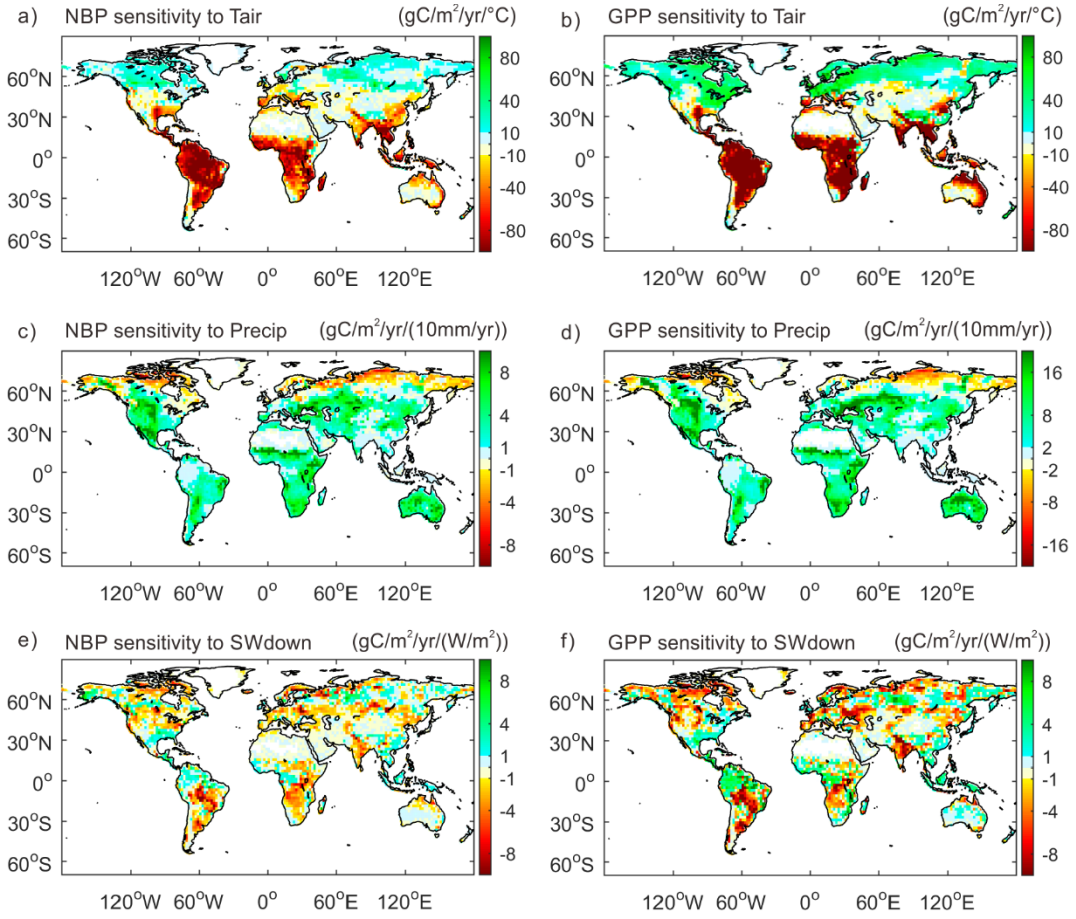
a) NBP sensitivity to Tair (gC/m²/yr/°C)
b) GPP sensitivity to Tair (gC/m²/yr/°C)
c) NBP sensitivity to Precip (gC/m²/yr/(10mm/yr))
d) GPP sensitivity to Precip (gC/m²/yr/(10mm/yr))
e) NBP sensitivity to SWdown (gC/m²/yr/(W/m²))
f) GPP sensitivity to SWdown (gC/m²/yr/(W/m²))
60°N
30°N
0°
30°S
60°S
120°W 60°W 0° 60°E 120°E
80 40 10 -10 -40 -80
8 4 1 -1 -4 -8
16 8 2 -2 -8 -16

Figure S9.

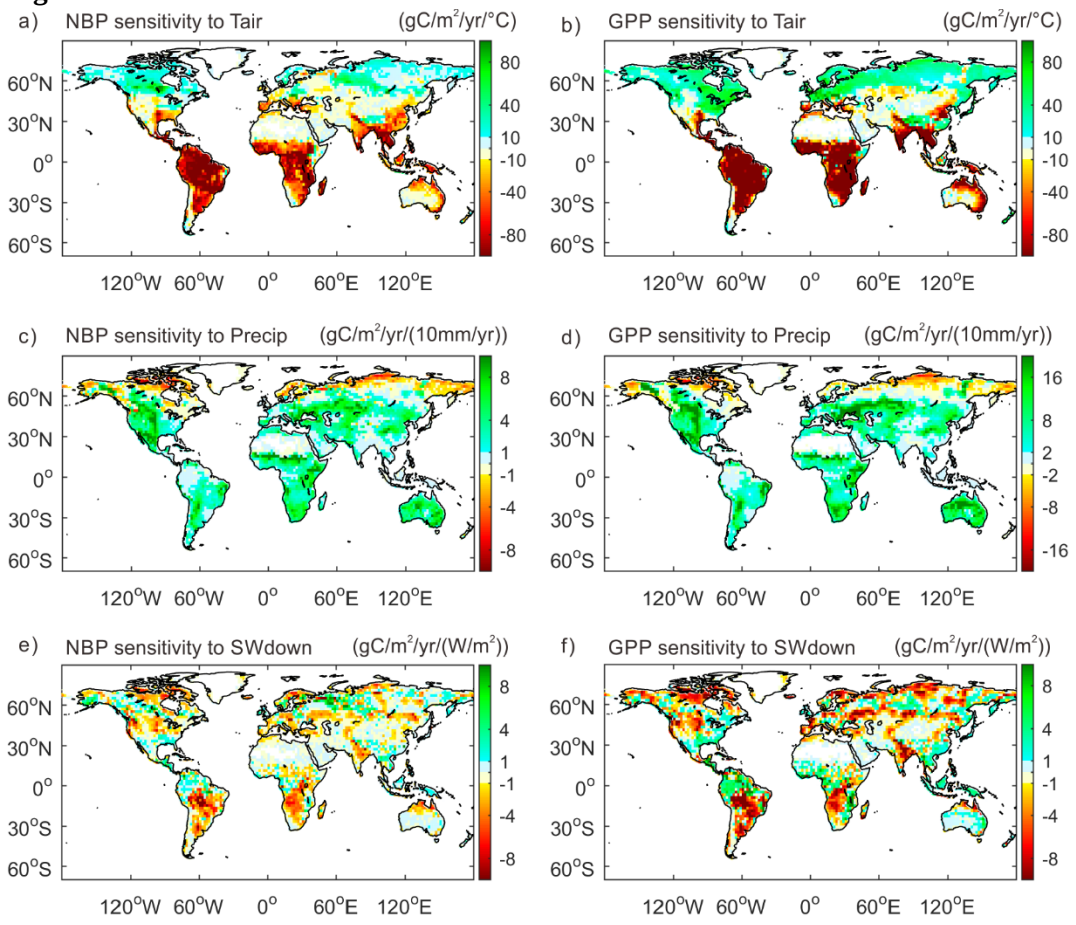
a) NBP sensitivity to Tair (gC/m²/yr/°C)
b) GPP sensitivity to Tair (gC/m²/yr/°C)
c) NBP sensitivity to Precip (gC/m²/yr/(10mm/yr))
d) GPP sensitivity to Precip (gC/m²/yr/(10mm/yr))
e) NBP sensitivity to SWdown (gC/m²/yr/(W/m²))
f) GPP sensitivity to SWdown (gC/m²/yr/(W/m²))
60°N
30°N
0°
30°S
60°S
120°W 60°W 0° 60°E 120°E
80 40 10 -10 -40 -80
8 4 1 -1 -4 -8
16 8 2 -2 -8 -16

Table S1. The CMIP5 climate simulations used in this study

scenario	CMIP5 ESM name	CMIP5 experiment name
IPSL historical	IPSL-CM5A-LR	r2i1p1, r3i1p1, r4i1p1
IPSL historicalNoAA	IPSL-CM5A-LR	r2i1p4, r3i1p4, r4i1p4
CSIRO historical	CSIRO-Mk3.6.0	r1i1p1, r3i1p1, r4i1p1
CSIRO historicalNoAA	CSIRO-Mk3.6.0	r1i1p3, r3i1p3, r4i1p3
GISS historical	GISS-E2-R	r1i1p3, r2i1p3, r3i1p3
GISS historicalNoA	GISS-E2-R	r1i1p3161, r2i1p3161, r3i1p3161

Chapter 3. Modelling the impacts of diffuse light fraction on photosynthesis

Summary

Aerosol and cloud-induced changes in diffuse light have important impacts on the global land carbon cycle by changing light distribution and photosynthesis in vegetation canopies. However, this effect remains poorly represented in current land surface models. Here we add a light partition module and a new canopy light transmission module to the ORCHIDEE land surface model (trunk version, v5453) to estimate the fraction of diffuse light and its effect on gross primary production (GPP) in a multi-layer canopy. We evaluate the new parametrizations (ORCHIDEE_DF) using flux observations from 159 eddy covariance sites over the globe. Our results show that compared to the original model, ORCHIDEE_DF improves the GPP simulation under sunny conditions and captures the observed higher photosynthesis under cloudier conditions in most plant functional types (PFTs). Our results also indicate that the larger GPP under cloudy conditions compared to sunny conditions is mainly driven by increased diffuse light in the morning and in the afternoon, and by the decreased water vapor pressure deficit (VPD) and air temperature at midday. The strongest positive effects of diffuse light on photosynthesis are found in the range 5-20 °C and VPD<1 kPa. This effect is found to decrease when VPD becomes too large, or temperature falls outside that range likely because stomatal conductance takes control of photosynthesis. ORCHIDEE_DF underestimates the diffuse light effect at low temperature in all PFTs and overestimates this effect at high temperature and high VPD in grasslands and croplands. This bias is likely due to the parameterization in the original model. The new model has the potential to better investigate the impact of large-scale aerosol changes on the terrestrial carbon budget, both in the historical period and in the context of future air quality policies and/or climate engineering. This chapter will be submitted as Zhang *et al.* The impacts of diffuse light fraction on photosynthesis in observations and a global land surface model.

3.1 Introduction

Process-based Land Surface Models (LSMs), which simulate the water and energy balance, and biogeochemical processes on land, have been widely used to attribute past changes in carbon (C) fluxes (Piao *et al.*, 2009; Sitch *et al.*, 2013) and to project the future land C budget (Ciais *et al.*, 2013). Despite being useful and widely applied tools, large uncertainties are a limitation of LSMs (Sitch *et al.*, 2008). One of the sources of the uncertainties is the omission or oversimplification of important processes that affect primary production. For instance, the impacts of light quality on photosynthesis is not currently represented in most LSMs, limiting the possibility to predict the variability of the carbon budget driven by changes in the atmospheric aerosol load which may be triggered by volcanic eruptions or variation in air pollution levels

It has been found by in situ observations that under the same light level, the increase of diffuse light fraction can enhance light use efficiency and ultimately photosynthesis, or gross primary production (GPP) (Gu *et al.*, 2003; Niyogi *et al.*, 2004; Mission *et al.*, 2005; Alton, 2007a; Knohl and Baldocchi, 2008; Mercado *et al.* 2009; Oliphant *et al.*, 2011; Kanniah *et al.*, 2013; Williams *et al.*, 2014; Cheng *et al.*, 2015; Wang *et al.*, 2018). Several mechanisms explaining this GPP enhancement have been proposed and tested. First, the more isotropic nature of diffuse light means that it penetrates deeper into the canopy to become available for the photosynthesis of lower canopy leaves, which would otherwise be shaded and light limited (Roderick *et al.*, 2001; Urban *et al.*, 2012). Second, the multi-directionality of diffuse light produces a more homogeneous distribution of radiation between sunlit and shaded leaves, enhancing the photosynthesis of upper canopy shaded leaves and limiting the waste of energy in light-saturated sunlit leaves (Li *et al.*, 2014; Williams *et al.*, 2014). Third, higher diffuse light fraction is often accompanied with less stressing temperature and vapor pressure deficit (VPD) for photosynthesis. The covariance of these environmental factors may also cause the GPP to increase under cloudier conditions, although not being a direct effect of diffuse light (Gu *et al.*, 2002; Cheng *et al.*, 2015; Li *et al.*, 2014). Finally, plant LAI (leaf area index, the area of leaves per unit land area) maximum may get acclimated to the cloudier seasons, which also contributes to higher GPP (Williams *et al.*, 2016).

Currently, most process-based LSMs simulate leaf photosynthesis using equations

and parameterizations derived from Farquhar *et al.* (1980) with different formulations of stomatal conductance, usually with stomatal closure under high VPD or low relative humidity (Ball *et al.*, 1987; Yin *et al.*, 2009; Medlyn *et al.*, 2011). These parameterizations calculate photosynthesis per unit LAI considering the stress from temperature, VPD and soil water, and then integrate it over the entire canopy volume. Therefore, the effects of temperature and VPD change under cloudier conditions have been usually implicitly considered in current LSMs (e.g. Zhang *et al.*, 2019). However, for the sake of simplicity and computational efficiency and for the lack of diffuse light fraction data, most global LSMs assumed a single extinction coefficient for both direct and diffuse light (Sellers *et al.*, 1997; Sitch *et al.*, 2008). These LSMs are therefore incapable to investigate the effect of diffuse light fraction changes on photosynthesis. This limit of LSMs is thought to cause considerable underestimation of land C sink after the eruption of Mount Pinatubo (Le Quere *et al.*, 2018).

There a few studies which have addressed the influence of light quality on GPP. Dai *et al.* (2004) introduced a two-big-leaf canopy model to simulate the effects of diffuse and direct radiation in the Common Land Model (CLM 2L). However, this model assumes a single-layer canopy and can therefore not simulate the vertical profile of leaf irradiance. A multilayer canopy model is more suitable to represent the vertical heterogeneity of leaf traits and radiation transfer (Alton *et al.*, 2007b; Bonan *et al.*, 2012). Differentiating sunlit and shaded leaves in a multilayer canopy LSM was firstly considered in the Joint UK Land Environment Simulator (JULES) LSM (Alton *et al.* 2007a; Mercado *et al.*, 2009). Using this version of JULES, Mercado *et al.* (2009) investigated the diffuse light effect and suggested that diffuse light fraction change enhanced by about a quarter the global land C sink during the 1960-1999 period. However, Mercado *et al.* (2009)'s model was only tested at two forest sites which cannot represent well global terrestrial ecosystems. Thus, there remains need to obtain well-evaluated LSMs that distinguish diffuse and direct light to test the results of Mercado *et al.* (2009) and to further investigate the diffuse radiation effect of aerosols.

Here we introduce a modified version of the LSM ORCHIDEE (Organizing Carbon and Hydrology In Dynamic Ecosystems, Krinner *et al.*, 2005), referred to as ORCHIDEE_DF, which uses a semi-empirical method to calculate the fraction of diffuse light, and a process-based multilayer canopy light transmission model to simulate the effects of diffuse light fraction on photosynthesis. We evaluated the GPP

simulated by ORCHIDEE_DF and the same version of the ORCHIDEE code without diffuse light (trunk version, v5453) using observations collected from 159 eddy covariance flux sites over 11 plant functional types (PFT) (Baldocchi *et al.*, 2001). Using both model simulations and observations at the flux sites, we also investigated the interactions between diffuse light fraction and biotic and abiotic factors on GPP, for the objective of understanding when and how much does light quality affect photosynthesis.

3.2 Data and method

3.2.1 Model description

3.2.1.1 Canopy light transmission and photosynthesis in the ORCHIDEE trunk

The ORCHIDEE_DF model is based on ORCHIDEE trunk revision 5453 (updated in September 2018). A general description of the physical processes related to energy and water balance, vegetation dynamics and biogeochemical processes in ORCHIDEE can be found in Krinner *et al.* (2005). The ORCHIDEE trunk version 5453 (hereafter referred to as trunk for simplicity) brings a number of improvements and photosynthesis parameters were recently re-calibrated against FLUXNET data (Baldocchi *et al.*, 2001) and atmospheric CO_2 observations for the IPSL Earth System Model (IPSL-CM6) and the CMIP6 simulations.

The leaf-scale photosynthesis calculation in the ORCHIDEE trunk version is based on the scheme of Yin and Struik (2009). This scheme is an adaptation of the biophysical model of Farquhar *et al.* (1980) with a specific parameterization of stomatal conductance. The Farquhar *et al.* model calculates assimilation (A) as the minimum of the Rubisco-limited rate of CO_2 assimilation (Ac) and the electron transport-limited rate of CO_2 assimilation (Aj):

$$A = \min\{Ac, Aj\} \quad \text{Eq. 3.1}$$

Here Ac is mainly affected by the maximum carboxylation capacity of Rubisco ($Vcmax$), which is temperature dependent (Yin and Struik., 2009), and the CO_2 concentration at the carboxylation site (Cc):

$$Ac = \frac{(Cc-\Gamma^*)Vcmax}{Cc+KmC(1 + O/KmO)} - Rd \quad \text{Eq. 3.2}$$

where Γ^* is the CO_2 compensation point in the absence of dark respiration (*Rd*). *KmC* and *KmO* are the Michaelis constants for CO_2 and O_2, *O* is the O_2 concentration at the carboxylation site.

Aj is calculated as a function of *Cc* and electron transport rate (*J*):

$$Aj = \frac{J(Cc-\Gamma^*)}{4.5Cc+10.5\Gamma^*} - Rd \quad \text{Eq. 3.3}$$

Here *J* is determined by a temperature-dependent maximum electron transport rate (*Jmax*) and the photosynthetic photons absorbed by leaves, calculated following Yin and Struik. (2009). Due to the uneven distribution of photosynthetically active radiation (PAR) in the canopy, *J* varies in the canopy. In addition, to account for the distribution of light and maximize the assimilation, plants tend to allocate nitrogen unevenly in the canopy profile (Niinemets *et al.*, 1997; Meir *et al.*, 2002), resulting in a vertical gradient in enzyme concentration and consequently in *Vcmax* and *Jmax*. The vertical heterogeneity of canopy photosynthetic properties highlights the need to represent the canopy in a multilayer way.

In order to simulate the vertical transmission and absorption of light within the canopy, ORCHIDEE trunk uses a multilayer canopy with a big leaf approximation in each layer. The canopy is geometrically divided into up to a maximum number of 20 layers depending on the leaf area index (LAI, in the unit of m^2m^{-2}). The discretization is represented in Figure 3.1a and the LAI at the interface of the layers are given by:

$$LAI\_c_i = 12 \times \frac{e^{0.15\times(i-1)}-1}{e^{0.15\times 20}-1} \quad \text{Eq. 3.4}$$

where LAI_c_i is the cumulative LAI above layer *i*, ($1 \leq i \leq 20$) and the layers are numbered from top to bottom. It should be noted that 20 layers are only for canopy with total LAI larger than 12. The number of layers decreases with total LAI accordingly. For instance, if the LAI is 2, only the first 10 layers are used to calculate the light distribution and photosynthesis (Figure 3.1a).

Light transmission in the multilayer canopy is calculated using the Beer-Lambert law (Monsi and Saeki, 1953) without distinguishing direct and diffuse light. The downward shortwave radiation arriving at the top of canopy (TOC) layer *i* (I_i) is:

$$I_i = I_0 e^{-k\times LAI\_c_i} \quad \text{Eq. 3.5}$$

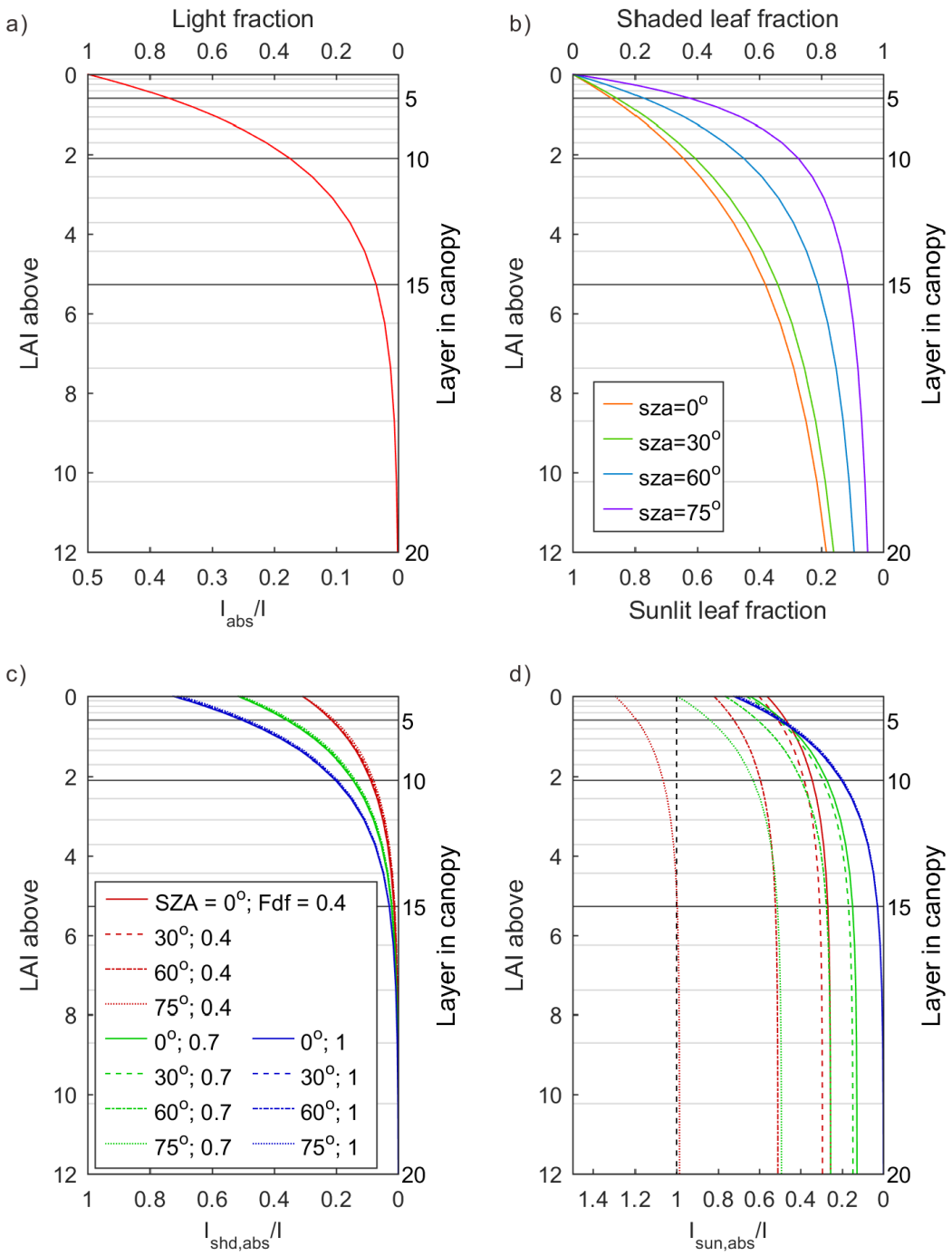

Figure 3.1 The distribution of light and leaves in canopy. (a) light distribution in ORCHIDEE trunk. (b) distribution of sunlit and shaded leaves in canopy in ORCHIDEE_DF. (c) light absorbed by shaded leaves in each canopy layer under different solar zenith angle (SZA) and fraction of diffuse light (*Fdf*) in ORCHIDEE_DF. (d) Same as (c) but for sunlit leaves. I, downward PPFD at the top of the canopy; I_{abs}, PPFD absorption per leaf area in ORCHIDEE trunk; $I_{shd,abs}$, PPFD absorption per leaf area in shaded leaves; $I_{sun,abs}$, PPFD absorption per leaf area in sunlit leaves.

where *k* is the light extinction coefficient, taken equal to 0.5. I_0 is the TOC downward shortwave radiation (W m^{-2}).

Because the radiation attenuation between one layer and the one just below is assumed to be due to leaf absorption, the absorbed radiation per leaf area at the top of layer *i* ($Iabs_i$) can be estimated as in Saeki (1960):

$$Iabs_i = \frac{-dI}{dLAI\_c}|LAI\_c_i = \ kI_0 e^{-kLAI\_c_i} \quad \text{Eq. 3.6}$$

Here we assume that all canopy layers are thin enough to neglect the difference in light absorption within each canopy layer. Then the absorbed radiation per leaf area in canopy layer *i* should equal to that at the top of the layer *i*, i.e. $Iabs_i$.

It should be noted that the radiation considered to calculate the *J* term in Eq. 3.3 is not shortwave radiation in W.m^{-2} but photosynthetic photon flux density (PPFD) in μmol $m^{-2}s^{-1}$. A translation from $Iabs_i$ to the absorbed PPFD per leaf area in canopy layer *i* ($PPFDabs_i$) is thus needed. Currently, there is no standard definition of the wavelength range for shortwave radiation (e.g. Howell *et al.*, 1982; Zhang *et al.*, 2004; Chen *et al.*, 2012). In ORCHIDEE trunk, shortwave radiation in W m^{-2} is multiplied by a factor of 0.5 to calculate photosynthetically active radiation (PAR) in W m^{-2}, and then a quanta-to-energy ratio of 4.6 mmol J^{-1} is used to convert PAR into PPFD in μmol $m^{-2}s^{-1}$.

ORCHIDEE accounts for a vertical gradient in enzyme concentration in canopy. Vcmax and Jmax are assumed in the model to be linearly related to photosynthetically active leaf nitrogen concentration (per leaf area) (Kattge *et al.* 2007). Meir *et al.* (2002) found an increasing leaf nitrogen concentration, as well as *Vcmax* and *Jmax* with increasing height in different ecosystems, suggesting an acclimation of plants to maximize photosynthesis in a canopy with unevenly distributed radiation. ORCHIDEE trunk lacks an explicit model of dynamic N allocation to leaves in the canopy, instead, it uses an empirical relationship to represent the impact of leaf nitrogen concentration on *Vcmax* and *Jmax* using the vertical profile of radiation (Zaehle *et al.*, 2010):

$$Vcmax_i = Vcmax_0(1 - 0.7 \times \left(1 - \frac{I_i}{I_0}\right)) \quad \text{Eq. 3.7}$$

$$Jmax_i = Jmax_0(1 - 0.7 \times \left(1 - \frac{I_i}{I_0}\right)) \quad \text{Eq. 3.8}$$

It should be noted that in ORCHIDEE trunk, the leaf-scale assimilation variables (e.g. $Vcmax$) are also affected by the instantaneous air temperature and the temperature of the last month which plants have adapted to. The calculation of *Cc* depends on VPD and also on whether the vegetation follows the C3 or C4 photosynthesis pathway (Yin and Struik, 2009). For simplicity, the near surface air temperature and humidity are used for the calculation of assimilation in all canopy layers. Furthermore, there are 13 PFTs in ORCHIDEE (Table S3.1) and *Vcmax* and *Jmax* are PFT-dependent.

3.2.1.2 Light partitioning in ORCHIDEE_DF

The lack of light quality (diffuse light fraction) information in most forcing datasets is one of the main difficulties when simulating the diffuse light effect. Here we partition the half-hourly downward PAR, which can be derived from the shortwave radiation, into diffuse and direct components following the Weiss and Norman (1985) empirical equation. Compared with another empirical method (Spitters *et al.*, 1986), we found that this method reproduces better the observed diffuse light fraction at the flux sites used in this study (see results and Figure S3.1). The diffuse PAR fraction (Fdf_{PAR}) above the canopy is estimated as:

$$Fdf_{PAR} = 1 - \frac{PAR_{p,dr}}{PAR_p}\left(1 - \left(\frac{a-R}{b}\right)^{\frac{2}{3}}\right) \quad \text{Eq. 3.9}$$

where PAR_p and $PAR_{p,dr}$ are the potential total and direct PAR, i.e. the total and direct PAR which would arrive at land surface under clear sky conditions. a and b are parameters, which take values of 0.9 and 0.7, and R is the ratio between actual (observed) and potential total downward shortwave radiation (SW_{obs} and SW_p) reaching the top of the canopy:

$$R = \frac{SW_{obs}}{SW_p} \quad \text{Eq. 3.10}$$

It should be noted that the potential downward shortwave radiation consists of potential downward PAR (visible, range 0.4-0.7μm) and potential downward near-infrared radiation (NIR, range 0.7-5μm). Also the potential PAR and NIR are the sum of direct ($PAR_{p,dr}$, $NIR_{p,dr}$) and diffuse ($PAR_{p,df}$, $NIR_{p,df}$) components, given by:

$$SW_p = PAR_p + NIR_p = PAR_{p,dr} + PAR_{p,df} + NIR_{p,dr} + NIR_{p,df} \quad \text{Eq. 3.11}$$

A simple atmospheric light transfer model modified from Weiss and Norman (1985) is used to estimate potential radiation. The potential direct PAR, $PAR_{p,dr}$ is calculated as:

$$PAR_{p,dr} = PAR_{TOA}\ e^{-0.185(p/p_0)m}\cos\theta \quad \text{Eq. 3.12}$$

where PAR_{TOA} is the PAR at top of atmosphere (TOA), *p* and *p0* indicate the local and standard sea level air pressure, *m* is the optical air mass, calculated using the solar zenith angle θ:

$$m = (\cos\theta)^{-1} \quad \text{Eq. 3.13}$$

The potential diffuse TOC PAR, $PAR_{p,df}$ is assessed as:

$$PAR_{p,df} = 0.4(PAR_{TOA}\cos\theta - PAR_{p,dr}) \quad \text{Eq. 3.14}$$

which expresses that 40% of the PAR flux that is extinguished in the atmosphere through scattering and absorption is available as diffuse PAR at the surface. Similarly, the potential direct and diffuse NIR at the top of the canopy ($NIR_{p,dr}$ and $NIR_{p,df}$ respectively), can be estimated as:

$$NIR_{p,dr} = (NIR_{TOA}e^{-0.06(p/p_0)m} - \omega)\cos\theta \quad \text{Eq. 3.15}$$

$$NIR_{p,df} = 0.6(NIR_{TOA}\cos\theta - NIR_{p,dr} - \omega\cos\theta) \quad \text{Eq. 3.16}$$

where ω is a flux term accounting for atmospheric water vapor absorption, calculated as a function of the solar constant (*SC*, in Wm^{-2}) and *m*:

$$\omega = SC \times 10^{(-1.195+0.4459\log_{10}m-0.0345(\log_{10}m)^2)} \quad \text{Eq. 3.17}$$

Using the results from Eqs. 12, 14, 15 and 16, we are able to calculate the SW_p to obtain the value of *R* in Eq 10.

It should be noted that the quanta-to-energy ratio (in mmol J^{-1}) is different under different sky conditions, because atmospheric scattering varies spectrally with the air mass and the cloud amount (Dye, 2004). For this consideration, the PPFD calculation from PAR uses the observation-oriented empirical equations from Dye (2004):

$$\beta_t = 4.576 - 0.03314Fdf_{PAR} \quad \text{Eq. 3.18}$$

$$\beta_{df} = \frac{4.5886Fdf_{PAR}}{0.010773+Fdf_{PAR}} \quad \text{Eq. 3.19}$$

where the β_t is the quanta-to-energy ratio for the total PAR (PAR_t) at the top of the canopy, while β_{df} is for its diffuse component (PAR_{df}):

$$PPFD_t = \beta_t PAR_t \quad \text{Eq. 3.20}$$

$$PPFD_{df} = \beta_{df} PAR_{df} \quad \text{Eq. 3.21}$$

The diffuse PPFD fraction (Fdf_{PPFD}) can thus be calculated as:

$$Fdf_{PPFD} = \frac{PPFD_{df}}{PPFD_t} = \frac{\beta_{df}}{\beta_t} Fdf_{PAR} \quad \text{Eq. 3.22}$$

3.2.1.3 Canopy light transmission in ORCHIDEE_DF

In ORCHIDEE_DF, we use the same stratification of canopy as in the trunk version (Eq. 3.4). But for the light transmission, we use a two-stream radiative transfer model following Spitters (1986). For convenience, we use radiation and *I* in this section to refer to the PPFD derived from the light partitioning step.

An assumption of the model is that leaves are bi-Lambertian surfaces for radiation, i.e. the reflection and transmission are isotropic. This reflection and transmission are together referred to as leaf scattering. This assumption implies that once direct radiation encounters a leaf, it gets either absorbed or scattered as diffuse light. While for diffuse radiation, the scattered light remains diffuse. The scattering coefficient, σ, is assumed equal to 0.2 following Spitters (1986), meaning 20% of the light encountering a leaf is scattered (80% is absorbed).

Based on this assumption, the radiation penetrating the canopy can be divided into three components (Figure 3.2): the direct light which has not been intercepted by leaves ($I_{dr,dr}$), the diffuse light generated by leaf scattering of intercepted direct light ($I_{dr,df}$), and the diffuse light in the canopy provided by the TOC diffuse radiation (I_{df}). It should be noted that the diffuse light generated by multiple times of scattering of the direct light is grouped into $I_{dr,df}$, while those from the scattering of TOC diffuse radiation belong to I_{df} (Figure 3.2). The sum of $I_{dr,dr}$ and $I_{dr,df}$ hereafter noted as I_{dr} represents the total radiation in each canopy later derived from the TOC direct radiation, hereafter $I_{dr,0}$.

If we also consider direct radiation as parallel beams, only the first leaves on the way of direct light can absorb $I_{dr,dr}$. These leaves are referred to as sunlit leaves. The

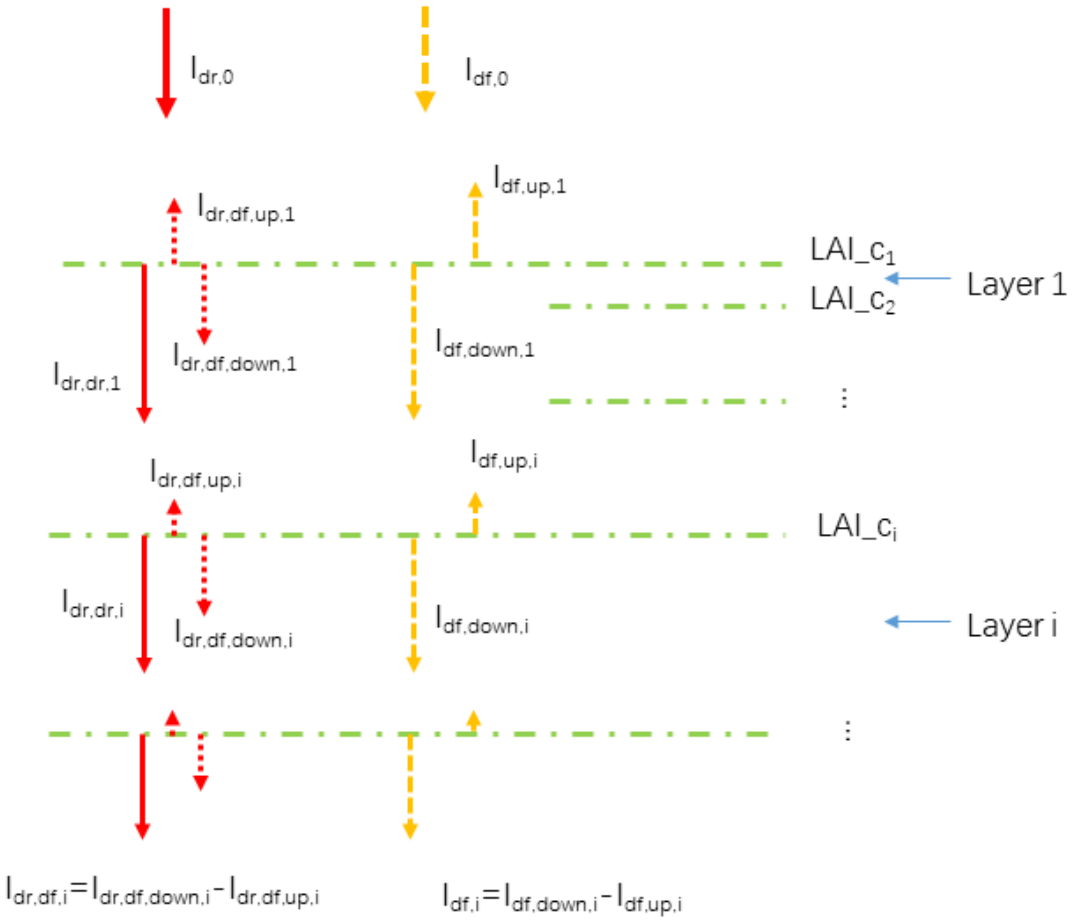

Figure 3.2 The diagram of the canopy light transmission in ORCHIDEE_DF. $I_{dr,0}$, downward direct PPFD at the top of the canopy; $I_{df,0}$, downward diffuse PPFD at the top of the canopy; LAI_c_i, cumulative LAI above canopy layer *i*; $I_{dr,dr,i}$, downward direct PPFD at the top of canopy layer *i*; $I_{dr,df,i}$, net diffuse PPFD derived from the scattering of $I_{dr,0}$ at the top of canopy layer *i*, equal to the difference of its downward ($I_{dr,df,down,i}$) and upward ($I_{dr,df,up,i}$) components; $I_{df,i}$, net diffuse PPFD derived from $I_{df,0}$ at the top of canopy layer *i*, equal to the difference of its downward ($I_{df,down,i}$) and upward ($I_{df,up,i}$) components.

fraction of sunlit leaves in each canopy layer can be calculated by applying Beer-Lambert law using an extinction coefficient for opaque, non-reflective "black" leaves (Figure 3.1b):

$$LAIf_{sun,i} = e^{-k_b LAI\_c_i} \qquad \text{Eq. 3.23}$$

where $LAIf_{sun,i}$ is the fraction of sunlit LAI in canopy layer i. LAI_c_i is the cumulative LAI in Eq. 3.4. k_b is the extinction coefficient if the leaves are assumed "black". A

function of θ, leaf angle distribution index (LA) and leaf clumping index (LC) is used to represent the geometry between the direct radiation and leaves:

$$k_b = \frac{LA*LC}{\cos\theta} \quad \text{Eq. 3.24}$$

For spherically distributed leaves, LA equals 0.5 (Goudriaan, 1977; Bodin and Franklin, 2012). LC is defined as in Myneni *et al.* (1989) and Baldocchi and Wilson (2001), varying between 0 and 1. Here we use the value 0.85 instead of 0.84 as recommended by an observationally-based study (Baldocchi and Wilson, 2001).

The leaves which cannot absorb $I_{dr,dr}$ are referred to as shaded leaves. The fraction of shaded LAI in canopy layer *i* ($LAIf_{shd,i}$) is thus the complement of $LAIf_{sun,i}$:

$$LAIf_{shd,i} = 1 - LAIf_{sun,i} \quad \text{Eq. 3.25}$$

Because $I_{dr,dr}$ is assumed not to be transmitted as direct radiation through leaves, $I_{dr,dr,i}$, which represents $I_{dr,dr}$ at layer *i* can be calculated similarly as in Eq. 3.23 using the downward direct radiation at the top of the canopy ($I_{dr,0}$):

$$I_{dr,dr,i} = I_{dr,0}e^{-k_b LAI\_c_i} \quad \text{Eq. 3.26}$$

The transmission of $I_{dr,df}$ is difficult to estimate directly. Here we calculate it as the difference between I_{dr} and $I_{dr,dr}$ in each layer:

$$I_{dr,df,i} = I_{dr,i} - I_{dr,dr,i} \quad \text{Eq. 3.27}$$

where $I_{dr,df,i}$ and $I_{dr,i}$ represent net (downward minus upward) $I_{dr,df}$ and net I_{dr} at layer *i*, respectively.

The calculation of $I_{dr,i}$ is based on Goudriaan (1982) and Hikosaka *et al.* (2016) under the assumptions that there is no difference in optical traits between leaves from different the canopy layers and that the canopy is deep enough to neglect the reflection of the soil:

$$I_{dr,i} = (1-\rho)I_{dr,0}e^{-\sqrt{1-\sigma}k_b LAI\_c_i} \quad \text{Eq. 3.28}$$

where ρ indicates the canopy reflection coefficient (i.e. the ratio between the TOC downward and upward radiation), calculated as:

$$\rho = \left(\frac{1-\sqrt{1-\sigma}}{1+\sqrt{1-\sigma}}\right)\left(\frac{2}{1+1.6cos\theta}\right) \quad \text{Eq. 3.29}$$

In contrast to the direct light transmission, the diffuse light will not change its directional characteristics when scattered by leaves. Similar to Eq. 3.5, net I_{df} at canopy layer *i* ($I_{df,i}$) can be estimated using TOC downward diffuse radiation ($I_{df,0}$) in a Beer-Lambert equation:

$$I_{df,i} = (1-\rho) I_{df,0} e^{-k_d LAI\_c_i} \quad \text{Eq. 3.30}$$

where k_d is the light extinction coefficient for diffuse light, calculated following Spitters (1986) as:

$$k_d = 0.8\sqrt{1-\sigma} \quad \text{Eq. 3.31}$$

Similar to Eq. 3.6, the flux of light that is absorbed per canopy leaf area in layer *i* from I_{df} ($Iabs_{df,i}$), I_{dr} ($Iabs_{dr,i}$), and $I_{dr,dr}$ ($Iabs_{dr,dr,i}$) can be written respectively as:

$$Iabs_{df,i} = \frac{-dI_{df}}{dLAI\_c} | LAI\_c_i = k_d I_{df,i} \quad \text{Eq. 3.32}$$

$$Iabs_{dr,i} = \frac{-dI_{dr}}{dLAI\_c} | LAI\_c_i = \sqrt{1-\sigma} k_b I_{dr,i} \quad \text{Eq. 3.33}$$

$$Iabs_{dr,dr,i} = \frac{-dI_{dr,dr}}{dLAI\_c} | LAI\_c_i = k_b I_{dr,dr,i} \quad \text{Eq. 3.34}$$

The $I_{dr,df}$ absorbed per canopy leaf area by layer *i* ($Iabs_{dr,df,i}$) is:

$$Iabs_{dr,df,i} = Iabs_{dr,i} - Iabs_{dr,dr,i} \quad \text{Eq. 3.35}$$

It should be noted that all leaves can absorb diffuse radiation. Therefore Eq. 3.32 and Eq. 3.35 also represent the absorption of I_{df} and $I_{dr,df}$ at the leaf scale. However, $I_{dr,dr}$ is only absorbed by sunlit leaves, thus the absorption of $I_{dr,dr}$ per sunlit leaf area does not equal to $Iabs_{dr,dr,i}$, which is the average at canopy scale. Instead, because $I_{dr,dr}$ does not change its intensity, the absorption of $I_{dr,dr}$ per sunlit leaf area can be written as:

$$Iabs_{dr,dr,i,sun} = (1-\sigma) k_b I_{dr,0} \quad \text{Eq. 3.36}$$

We have assumed that shaded leaves can only absorb diffuse light. Then, the radiation absorbed (per leaf area) by shaded leaves layer *i* ($I_{shd,i,abs}$) is:

$$Iabs_{shd,i} = Iabs_{df,i} + Iabs_{dr,df,i} \quad \text{Eq. 3.37}$$

The sunlit leaves also absorb the direct light besides diffuse light. The radiation received by sunlit leaves can thus calculated as:

$$Iabs_{sun,i} = Iabs_{shd,i} + Iabs_{dr,dr,i,sun} \quad \text{Eq. 3.38}$$

Apart from light transmission, all other parameters (e.g. *Vcmax*, *Jmax*) in ORCHIDEE_DF are kept the same as in ORCHIDEE trunk.

3.2.2 Flux data and site level simulations

To evaluate ORCHIDEE_DF, we collected flux site measurements from the La Thuile dataset, which includes 965 site-year observations from in total 252 sites. Because our ORCHIDEE simulations assumes that the ecosystems are in equilibrium and do not experience disturbances (e.g. logging, fire), we selected flux sites without strong disturbances during the last 10 years. For sites that also provided growing season LAI information, we also removed forests site with LAI<2, which may be considered as sparse forests with understory vegetation. In the end, observations of 655 site-years from 159 sites were retained (Table S3.2). The annual climate of the sites spans from −9 to 27 ºC in temperature, and from 67 mm yr^{-1} to over 3000 mm yr^{-1} in precipitation (Figure S3.2), which is representative to most of the climate conditions over the globe. The dataset provides in situ meteorology, net ecosystem exchange (NEE), gross primary productivity (GPP), and data quality information at 30-min time steps. The GPP provided by this dataset is partitioned from NEE and gap filled using the method of Reichstein *et al.* (2005). Specifically, 64 of the 159 sites provided measurements of both total and diffuse PPFD, which allows us to evaluate the light partitioning parametrization (Eqs 9-20). The gaps and missing variables in meteorology are filled using the approach from Vuichard and Papale (2015) to meet the model input requirements.

Because ORCHIDEE has different photosynthesis parameters for different PFTs, we classified the vegetation at each site into the 13 ORCHIDEE PFTs (Table S3.1) according to the IGBP land cover types specified on the website of FluxNet (www.fluxdata.org). If the IGBP land cover type is not specified or may match more than one ORCHIDEE PFTs (e.g. shrublands, savannas and wetlands), the PFT is determined according to the dominant plant species described in related references. Specifically, the mixed forests (MF) type exists in the IGBP classification but not in the

ORCHIDEE PFTs. Because MF sites are mostly located in temperate regions, we assume that they are composed of 50% temperate broadleaf deciduous forests and 50% temperature evergreen needle-leaf forests. Detailed information of flux sites is found in Table S3.2.

To evaluate the model, spinup simulations of 30 years are firstly conducted on ORCHIDEE_DF at each site to equilibrate the leaf area index with site conditions. Then the simulations with 30 min output are conducted with ORCHIDEE trunk and ORCHIDE_DF, using the full span of the Fluxnet la Thille series respectively at each site. It should be noted that we use the same spinup for ORCHIDEE trunk and ORCHIDEE_DF to ensure the same initial states of the two simulations. A test has shown that different spinup simulations do not affect the simulation of GPP on the following years (not shown).

3.2.3 Analyses

When evaluating the modeled GPP response to diffuse light we have not used all the 30-min data points due to several concerns. First, all night time data points were excluded from the analyses given that GPP is zero at night. Second, all data points flagged with poor quality in the FLUXNET archive have been removed. Third, ORCHIDEE might be not perfect in capturing the seasonality of leaf flushing and shedding. In order to minimize the uncertainty from phenology, we used only data from the growing season at each site, which is defined as months when:

$$GPP_m > GPP_{m,min} + (GPP_{m,max} - GPP_{m,min})/4 \quad \text{Eq. 3.39}$$

where GPP_m is the observed monthly GPP, $GPP_{m,min}$ and $GPP_{m,max}$ are the observed minimum and maximum monthly GPP at corresponding site.

To assess the effect of variable diffuse light fraction on both GPP and light use efficiency (LUE, the ratio between GPP and incoming shortwave radiation), we look at the difference in GPP and LUE during sunny and cloudy conditions. We define sunny and cloudy conditions as those when the fraction of diffuse PPFD at the top of the canopy (Fdf_{PPFD}) is smaller than 0.4 and greater than 0.8, respectively, and calculate the average sunny and cloudy GPP and LUE at each site. It should be noted that to ensure that the comparison between sunny and cloudy conditions are at the same PPFD level, the sunny time steps with PPFD larger than the maximum PPFD under cloudy

conditions are removed from the average, and vice versa. In addition, to make sure that the difference in GPP between sunny and cloudy is not an artifact of different LAI, sites with average modelled LAI under cloudy and sunny cognitions differing over 0.3 are excluded.

Table 3.1 Variables in this study

variable	meaning
A	Net photosynthesis rate
Ac	Rubisco activity limited net photosynthesis rate
Aj	Electron transport limited net photosynthesis rate
Cc	Chloroplast CO_2 partial pressure
Fdf_{PAR}	The fraction of diffuse PAR in total PAR
Fdf_{PPFD}	The fraction of diffuse PPFD in total PPFD
I	Leaf layer in canopy, for the top layer, i = 1
I_0	Downward shortwave radiation at the top of the canopy
$Iabs_{df,i}$	Average absorption of I_{df} per unit leaf area in canopy layer i
$Iabs_{dr,df,i}$	Average absorption of $I_{dr,df}$ per unit leaf area in canopy layer i
$Iabs_{dr,dr,i}$	Average absorption of $I_{dr,dr}$ per unit leaf area in canopy layer i
$Iabs_{dr,dr,i,sun}$	Absorption of $I_{dr,dr}$ per sunlit unit leaf area in canopy layer i
$Iabs_{dr,i}$	Average absorption of I_{dr} per unit leaf area in canopy layer i
$Iabs_i$	Average radiation absorption per unit leaf area in canopy layer i
$Iabs_{shd,i}$	PPFD absorbed by shaded leaves per unit leaf area in canopy layer i
$Iabs_{sun,i}$	PPFD absorbed by sunlit leaves per unit leaf area in canopy layer i
$I_{df,0}$	Diffuse downward PPFD at the top of the canopy
$I_{df,i}$	Net PPFD derived from $I_{df,0}$ at the top of canopy layer i
$I_{dr,0}$	Direct downward PPFD at the top of the canopy
$I_{dr,df,i}$	Net diffuse PPFD derived from the scattering of $I_{dr,0}$ at the top of canopy layer i
$I_{dr,dr,i}$	Downward direct PPFD at the top of canopy layer i
$I_{dr,i}$	Net PPFD derived from $I_{dr,0}$ at the top of canopy layer i, the sum of $I_{dr,dr,i}$ and $I_{dr,df,i}$
I_i	Downward shortwave radiation arriving at canopy layer i
J	Rate of electron transport
$Jmax$	Maximum value of J under saturated light, depending on temperature
$Jmax_0$	$Jmax$ at the top of the canopy
$Jmax_i$	$Jmax$ at the canopy layer i
k	Light extinction coefficient in ORCHIDEE trunk
k_b	Light extinction coefficient when leaves are assumed black
k_d	Light extinction coefficient for diffuse PPFD
KmC	Michaelis constants for CO_2, depending on temperature
KmO	Michaelis constants for O_2, depending on temperature

LAI_c_i	Cumulative LAI above canopy layer *i*
$LAIf_{shd,i}$	Fraction of shaded leaf area in total leaf area in canopy layer *i*
$LAIf_{sun,i}$	Fraction of sunlit leaf area in total leaf area in canopy layer *i*
m	Optical air mass
NIR_p	Potential total downward near infrared radiation at the top of the canopy
$NIR_{p,df}$	Potential diffuse downward near infrared radiation at the top of the canopy
$NIR_{p,dr}$	Potential direct downward near infrared radiation at the top of the canopy
NIR_{TOA}	Downward near infrared radiation at the top of the atmosphere
O	Chloroplast O_2 partial pressure
p	Air pressure near surface
$p0$	Standard sea level air pressure
PAR_p	Potential total downward photosynthetically active radiation at the top of the canopy
$PAR_{p,df}$	Potential diffuse downward photosynthetically active radiation at the top of the canopy
$PAR_{p,dr}$	Potential direct downward photosynthetically active radiation at the top of the canopy
PAR_{TOA}	Downward photosynthetically active radiation at the top of the atmosphere
$PPFDabs_i$	Average photosynthetic photon flux density absorption per unit leaf area in canopy layer *i*
$PPFD_{df}$, $I_{df,0}$	Diffuse downward photosynthetic photon flux density above canopy
$PPFD_t$	Total downward photosynthetic photon flux density above canopy
R	Ratio between actual and potential downward shortwave radiation at the top of the canopy
Rd	Dark respiration
SW_{obs}	Actual (observed) downward shortwave radiation at the top of the canopy
SW_p	Potential (under clearsky conditions without clouds and aerosols) downward shortwave radiation at the top of the canopy
$Vcmax$	Maximum rate of Rubisco activity-limited carboxylation, depending on temperature
$Vcmax_0$	*Vcmax* at the top of the canopy
$Vcmax_i$	*Vcmax* at the canopy layer *i*
β_{df}	Quanta-to-energy ratio for diffuse PAR
β_t	Quanta-to-energy ratio for total PAR
Γ^*	CO_2 compensation point in the absence of *Rd*
θ	Solar zenith angle
ρ	The reflection coefficient of the canopy, i.e. the ratio between the downward and upward radiation at the top of the canopy
ω	Term accounting for atmospheric water vapor absorption

3.3 Results

3.3.1 Diffuse light fraction

Figure 3.3 shows the relationship between 30-min modeled and measured Fdf_{PPFD} at flux sites (64 sites). The data points are generally distributed along the 1:1 line, indicating an unbiased estimation of our diffuse light model. In total, our simple model explains over 51% of the variance in observed diffuse PPFD fraction. Although this model is imperfect, we currently have no better way to reproduce the diffuse PPFD at the flux site scale.

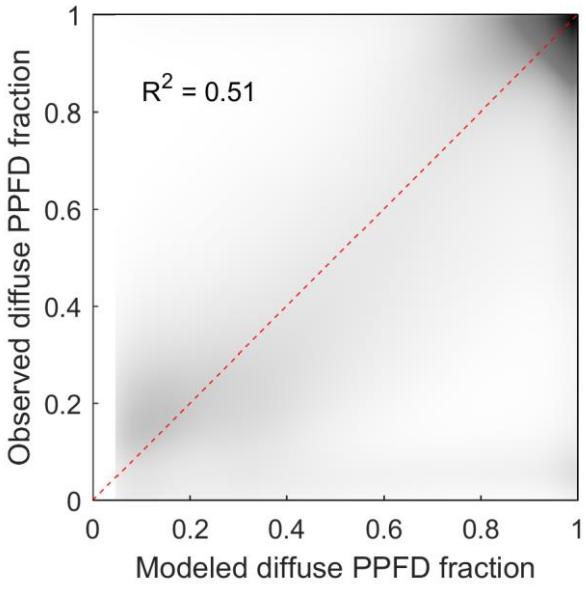

Figure 3.3 Modeled and observed diffuse PPFD fraction. The dark area indicates high data density, while light area indicates low data density.

3.3.2 General model performance

The performance of both ORCHIDEE trunk and ORCHIDEE_DF for 30-min GPP from each PFT (all sites) is presented in Figure 3.4. Generally, ORCHIDEE trunk

underestimated the standard deviation (STD) of GPP at 30-min time-step compared with observations, and across all PFTs except Boreal evergreen needleleaf forests and C4 Croplands (Figure 3.4a). The correlation coefficients between trunk GPP and observations are generally between 0.5 and 0.7 among PFTs (Figure 3.4b). In tropical broadleaf forests, this correlation coefficient is about 0.2, which is much smaller than in other PFTs and likely due to the limited seasonality of primary production in the tropics. The GPP simulated by ORCHIDEE_DF shows comparable performance with ORCHIDEE trunk, but with slightly smaller STD (Figure 3.4a).

Similar evaluations on the GPP from the two models are performed under cloudy and sunny conditions respectively (Figure 3.4c-f). Under cloudy conditions, ORCHIDEE trunk and ORCHIDEE_DF both underestimated GPP STD. The correlation coefficients to observations are generally between 0.5 and 0.8 (Figure 3.4d). Compared with ORCHIDEE trunk, ORCHIDEE_DF shows slightly worse correlation coefficients but improves STD for most of the PFTs except Tropical broad-leaved evergreen forests (TrEBF) and Temperate needleleaf evergreen forests (TeENF) (Figure 3.4c).

Compared with cloudy conditions, the GPP simulated by the two models under sunny conditions show weaker correlation to observations. The correlation coefficients generally vary between 0.3 and 0.6 among PFTs. However, it should be noted that ORCHIDEE_DF better reproduced GPP variation under sunny conditions compared with ORCHIDEE trunk in most PFTs except TeDBF and C4Cro (Figure 3.4f). The GPP STD derived from ORCHIDEE trunk simulations under sunny conditions show larger variability among PFTs than under cloudy conditions. While for ORCHIDEE_DF, the GPP STD under sunny and cloudy conditions show similar bias compared with observations (Figure 3.4e).

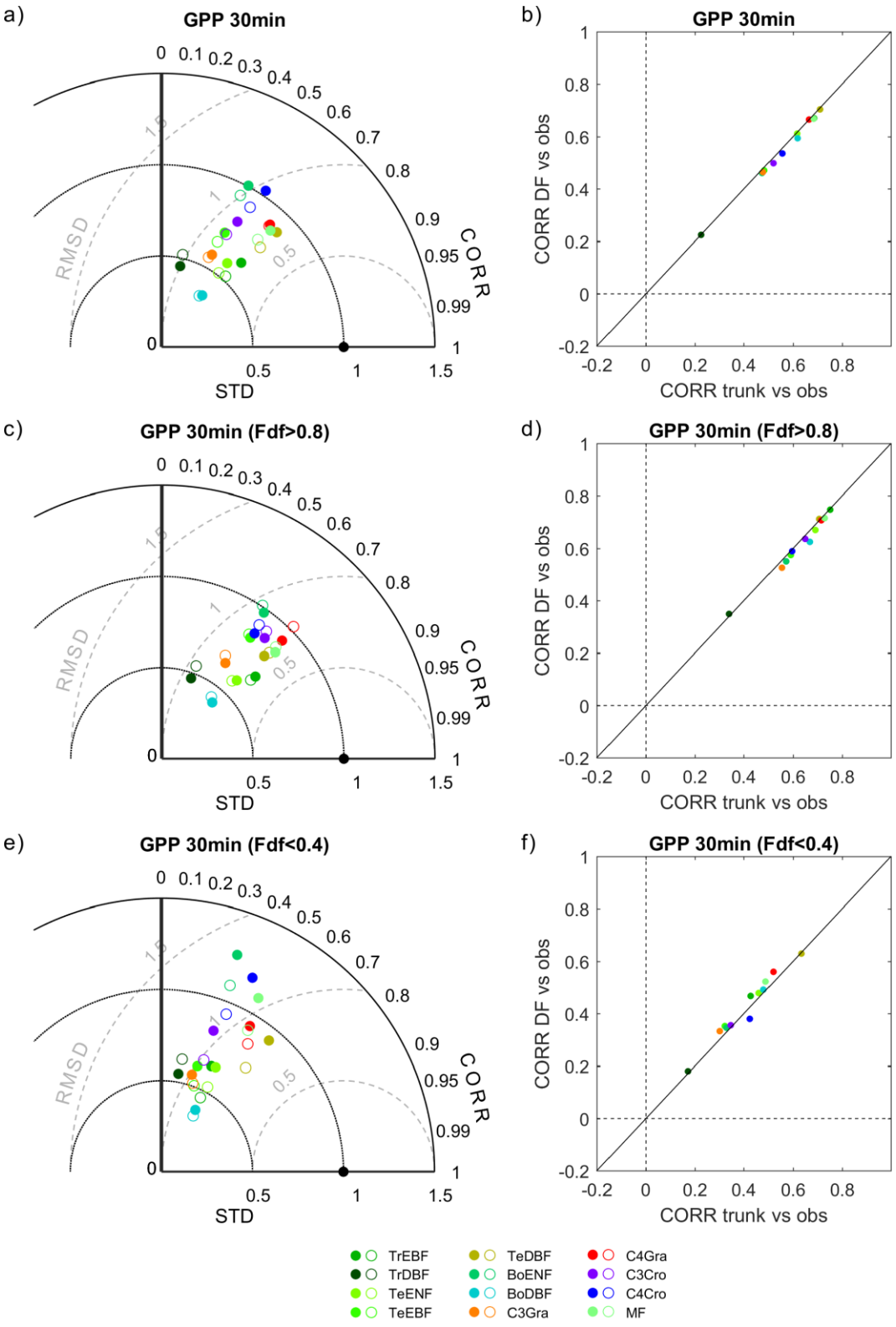

Figure 3.4 Performance of ORCHIDEE trunk and ORCHIDEE_DF at different PFTs. (a) the Taylor plot of GPP, all valid 30min observations are used as reference, the filled circles indicate ORCHIDEE trunk, opened circles indicate ORCHIDEE_DF. (b) comparison of the correlation coefficients between the two models and observations. (c) and (e) same as (a) but for cloudy (diffuse light fraction >0.8) and sunny (diffuse light fraction<0.4) conditions only. (d) and (f) same as (b) but for cloudy and sunny conditions only.

3.3.3 Effects of diffuse light on GPP and LUE

Because the modification of ORCHIDEE_DF was limited to light transmission, the pertinent process-oriented evaluation of the two models should focus on their ability to capture the observed GPP differences between cloudy and sunny conditions (hereafter ΔGPP), rather than on correlations or RMSE with observations, that may result from different structural and parametric errors of the model, not related to diffuse light.

Figure 3.5 shows the observed and modeled GPP under sunny and cloudy conditions at different PPFD levels at flux sites with relatively long time series of observations from each PFT. For all the sites selected, the observed GPP under cloudy conditions is larger than under sunny conditions. However, the GPP simulated by ORCHIDEE trunk shows no or small difference between cloudy and sunny conditions at most sites. In contrast, ORCHIDEE_DF reproduces this GPP difference in most PFTs except TrDBF, BoDBF and C4Gra. However, there is only one TrDBF site and very few C4Gra sites in our dataset. Furthermore, at most C4Gra sites, we are not able to find PPFD levels where sunny and cloudy conditions co-exist. Therefore, we are not able to make further evaluation of cloudy-minus-sunny GPP differences for TrDBF and C4Gra. At three of the four BoDBF sites, the modeled GPP difference under cloudy and sunny conditions is relatively small (not shown). This might be because the model overestimated the limit of low temperature on photosynthesis at the BoDBF sites (mean annual temperature<3 ^{o}C). In total, observations from about 70% of the sites show remarkable higher GPP under cloudy than sunny conditions. This percentage is only 30% in ORCHIDEE trunk simulations but 60% in ORCHIDEE_DF simulations.

To summarize the site level results, we investigated the distribution of GPP difference between cloudy and sunny conditions (here after refer to as ΔGPP) (Figure 3.6a). Observations and ORCHIDEE_DF show a positive bias in ΔGPP, with ΔGPP values between 0-3×10^{-4} gC m^{-2} s^{-1} at most sites. However, for ORCHIDEE trunk, ΔGPP is near zero at most sites. This result confirms that ORCHIDEE_DF performs much better than ORCHIDEE trunk in simulating differences in GPP under different light conditions.

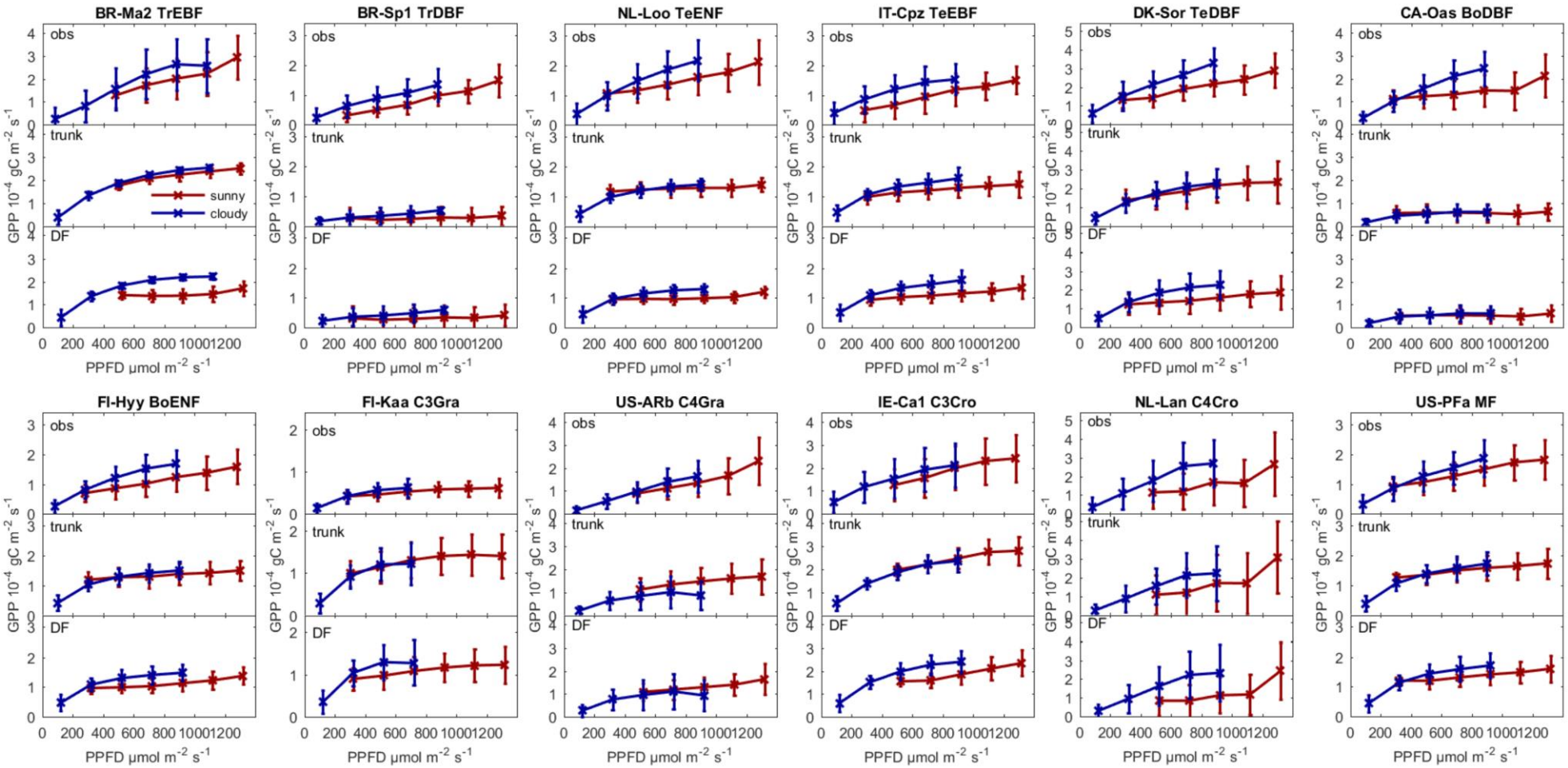

Figure 3.5 Observed GPP and GPP modeled by ORCHIDEE trunk and ORCHIDEE_DF under cloudy (diffuse light fraction >0.8) and sunny (diffuse light fraction<0.4) conditions at selected sites (with relatively long time series) from each PFT.

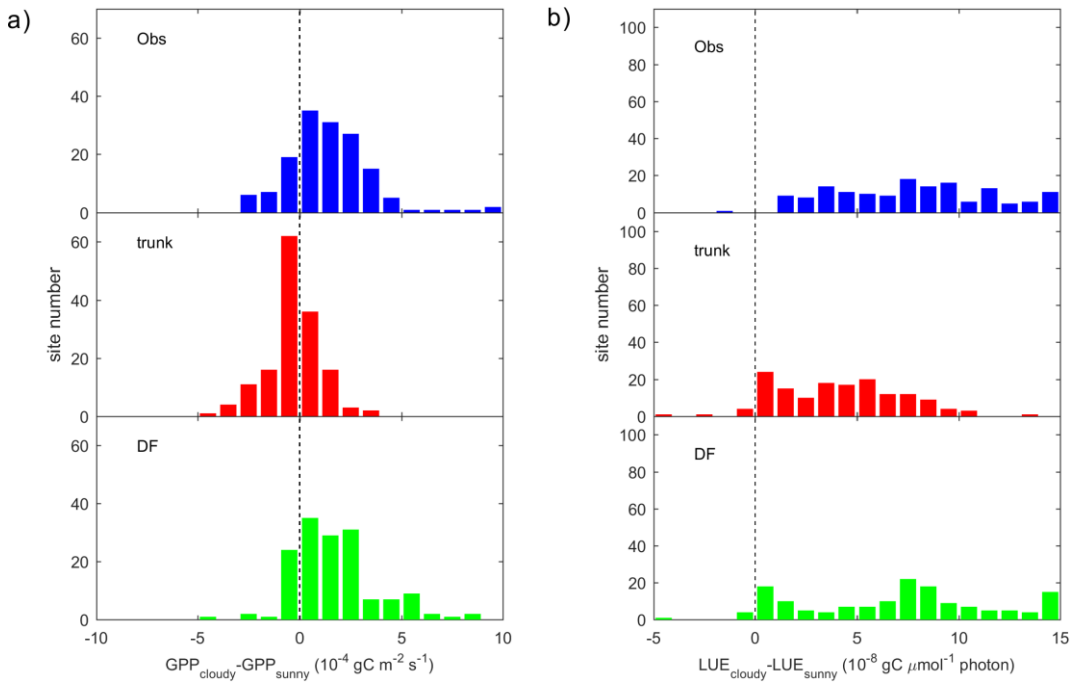

Figure 3.6 Site distribution of (a) the GPP difference between cloudy (diffuse light fraction >0.8) and sunny (diffuse light fraction<0.4) conditions. (b) same as (a) but for LUE. It should be noted that the light level is controlled the same for sunny and cloudy conditions at each site.

It should be noted that ΔGPP can be affected by PPFD. At sites where sunny and cloudy conditions only coexist at a relatively low PPFD level, the ΔGPP should be also small. To remove the effect of PPFD level on ΔGPP, we analyzed the difference in LUE, i.e. ΔLUE, between the two conditions (Figure 3.6b). Compared with ΔGPP, positive ΔLUE values are more evenly distributed around 0-15×10^{-8} gC μmol^{-1} photon for observation and ORCHIDEE_DF simulation. For ORCHIDEE trunk, the ΔLUE has the range of 0-8 ×10^{-8} gC μmol^{-1} photon, with the upper range smaller than in the observations and ORCHIDEE_DF.

We further refined this analysis to investigate if the effects of diffuse light differ at different times of the day (Figure 3.7). Results for three different periods in the day show that in the morning and afternoon, cloudy conditions result in higher GPP of 0-5×10^{-4} gC m^{-2} s^{-1} than sunny conditions at most sites, which is generally captured by ORCHIDEE_DF but missed by ORCHIDEE trunk in the morning (Figure 3.6a, c). At midday, due to the dependence of Fdf on PPFD (Eq. 3.9, 3.10), we fail at many sites to

find PPFD levels where sunny and cloudy conditions coexist. Nevertheless, the result generally indicates larger mid-day ΔGPP than those in the morning and afternoon. It should be noted that this large difference is captured by both ORCHIDEE_DF and ORCHIDEE trunk (Figure 3.7b). Because the diffuse and direct lights are treated indifferently in ORCHIDEE trunk, this midday ΔGPP should be mainly contributed by other environmental factors other than diffuse light fraction. The ΔLUE derived by ORCHIDEE_DF also shows a largely similar distribution as in observations, but ORCHIDEE trunk underestimates the morning and afternoon ΔLUE (Figure 3.7d-f).

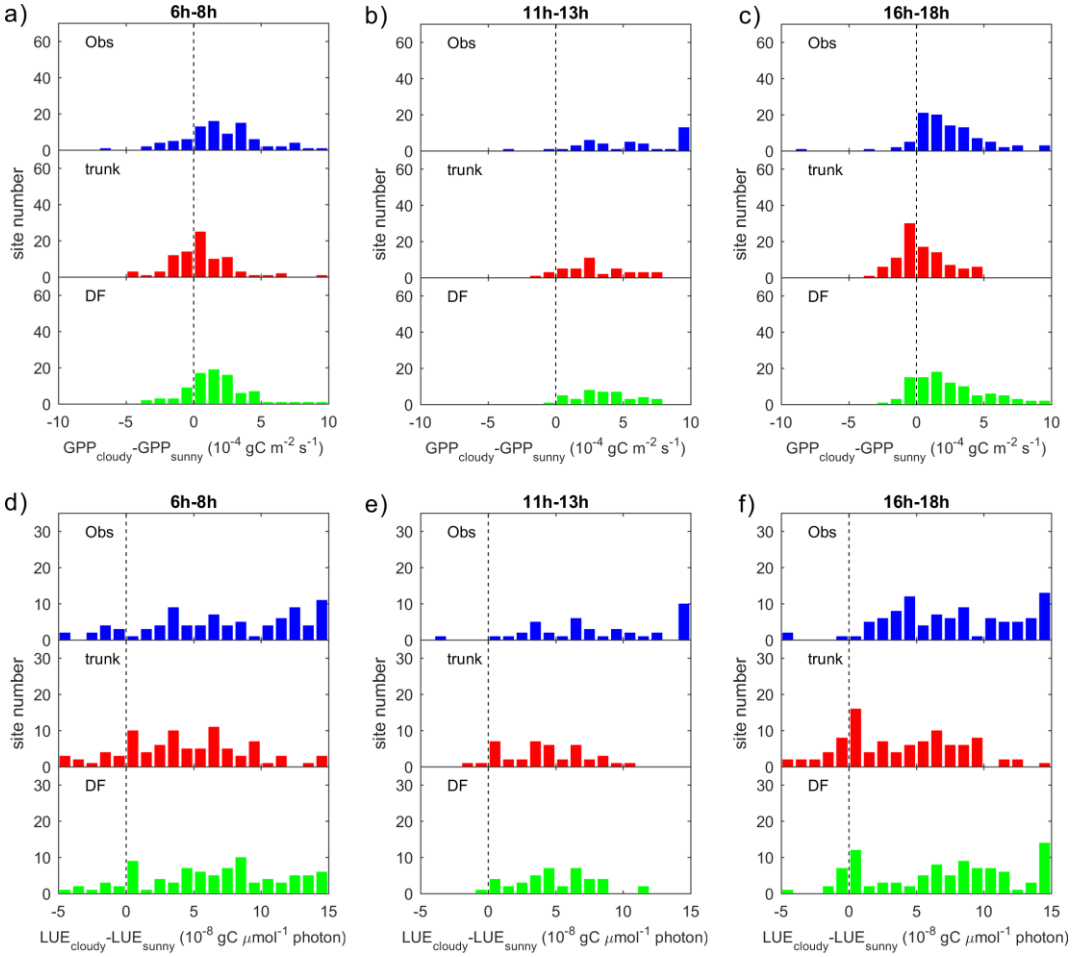

Figure 3.7 Same as Figure 3.6 but for different time of the day.

3.3.4 Interactions between diffuse light and environmental factors

As implied by figure 3.7, the diffuse light fraction is not the only factor causing ΔGPP. Other possible factors include temperature and VPD (Gu *et al.*, 2002; Cheng *et al.*, 2015; Li *et al.*, 2014). Here, we thus investigate the diffuse light effect along

temperature and VPD gradients in Figure 3.8. To remove the effect of PPFD level, we only show ΔLUE.

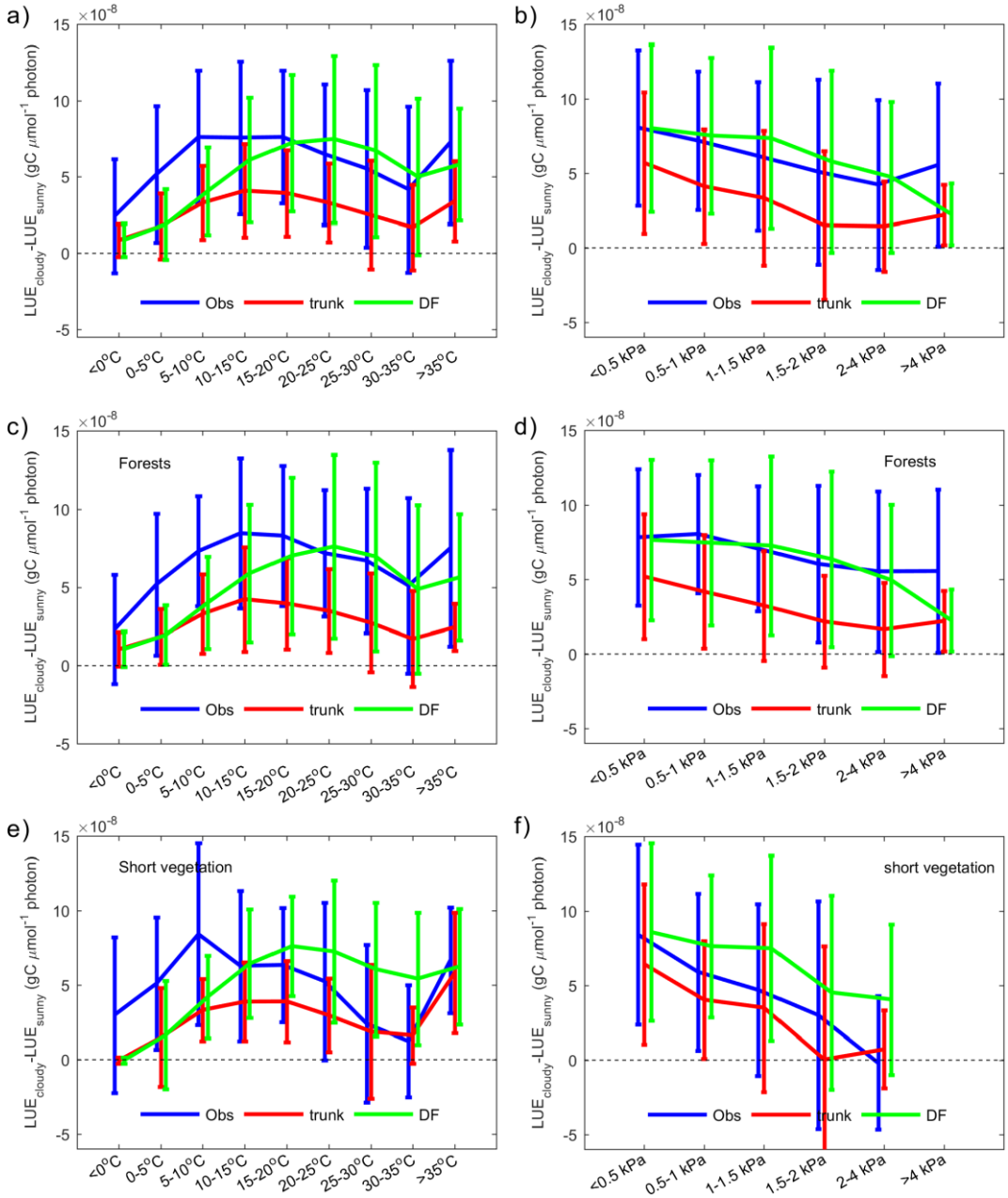

Figure 3.8 The dependence of LUE difference between cloudy and sunny conditions on climate factors. In observation (blue), ORCHIDEE trunk (red) and ORCHIDEE_DF (green), the average and error bars indicate statistics of site level means (a) dependence of LUE difference on temperature, (b) dependence of LUE difference on VPD. (c) and (e) the same as (a) but for only forest sites and short vegetation (grasslands and croplands) sites. (d) and (f) the same as (b) but for forest sites and short vegetation sites

ΔLUE shows a unimodal curve along the temperature gradient for observation and the two models (Figure 3.8a). At low temperature, both models indicate a very low ΔLUE of 1 gC μmol^{-1} photon, which is about 1/3 of the ΔLUE derived from observations. With increasing temperature, the observed ΔLUE shows a maximum at 10-20 °C, with a magnitude of ~8×10^{-8} gC μmol^{-1} photon and declines slightly at higher temperatures. The peak of ΔLUE simulated by ORCHIDEE_DF has a magnitude comparable to that of observations, but at higher temperature (20-25 °C) than in observations. The ΔLUE simulated by ORCHIDEE trunk is much smaller, with a peak of ~4×10^{-8} gC μmol^{-1} photon at 10-15 °C.

The effect of VPD on ΔLUE is shown in Figure 3.8b. For observations and both model simulations, a monotonic decreasing trend of ΔLUE along the VPD gradient is found. The ΔLUE from observations and ORCHIDEE_DF show a comparable magnitude, from 8×10^{-8} gC μmol^{-1} photon at VPD<0.5 kPa to 5×10^{-8} gC μmol^{-1} photon at 2-4 kPa VPD level. The ΔLUE simulated by ORCHIDEE trunk is smaller than observations.

Apart from environmental factors, the effects of diffuse light may also differ among PFTs because different PFTs have different canopy structures and photosynthetic parameters (e.g. Vcmax). Here we analyzed the ΔLUE in forests and short vegetation (grasslands and croplands) separately (Figure 3.8c-f). In forests (Figure 3.8c, d), ORCHIDEE_DF underestimates ΔLUE at temperatures lower than 20 °C. It also largely captures the observed ΔLUE trend with VPD, while ORCHIDEE trunk underestimates ΔLUE at all cases. Compared with forests, in short vegetation (Figure 3.8e, f), observations show a stronger decline of ΔLUE at high temperatures (>25 °C) and high VPD conditions (>0.5 kPa). However, for ORCHIDEE_DF, the short vegetation ΔLUE remains as high as for forests.

Figure 3.9 shows the distribution of ΔLUE in the T-VPD dimensions. Observations indicate that the largest ΔLUE is reached under conditions when temperature is in the range 5-20 °C and VPD <1 kPa (Figure 3.9a). The ΔLUE under such conditions is usually over 7×10^{-8} gC μmol^{-1} photon. When the temperature is lower than 5 °C or higher than 20 °C, or VPD becomes larger than 1 kPa, ΔLUE tends to decline. Compared with observations, the ΔLUE simulated by ORCHIDEE_DF shows a similar decreasing trend with VPD at all temperature levels (Figure 3.9c), however, no obvious

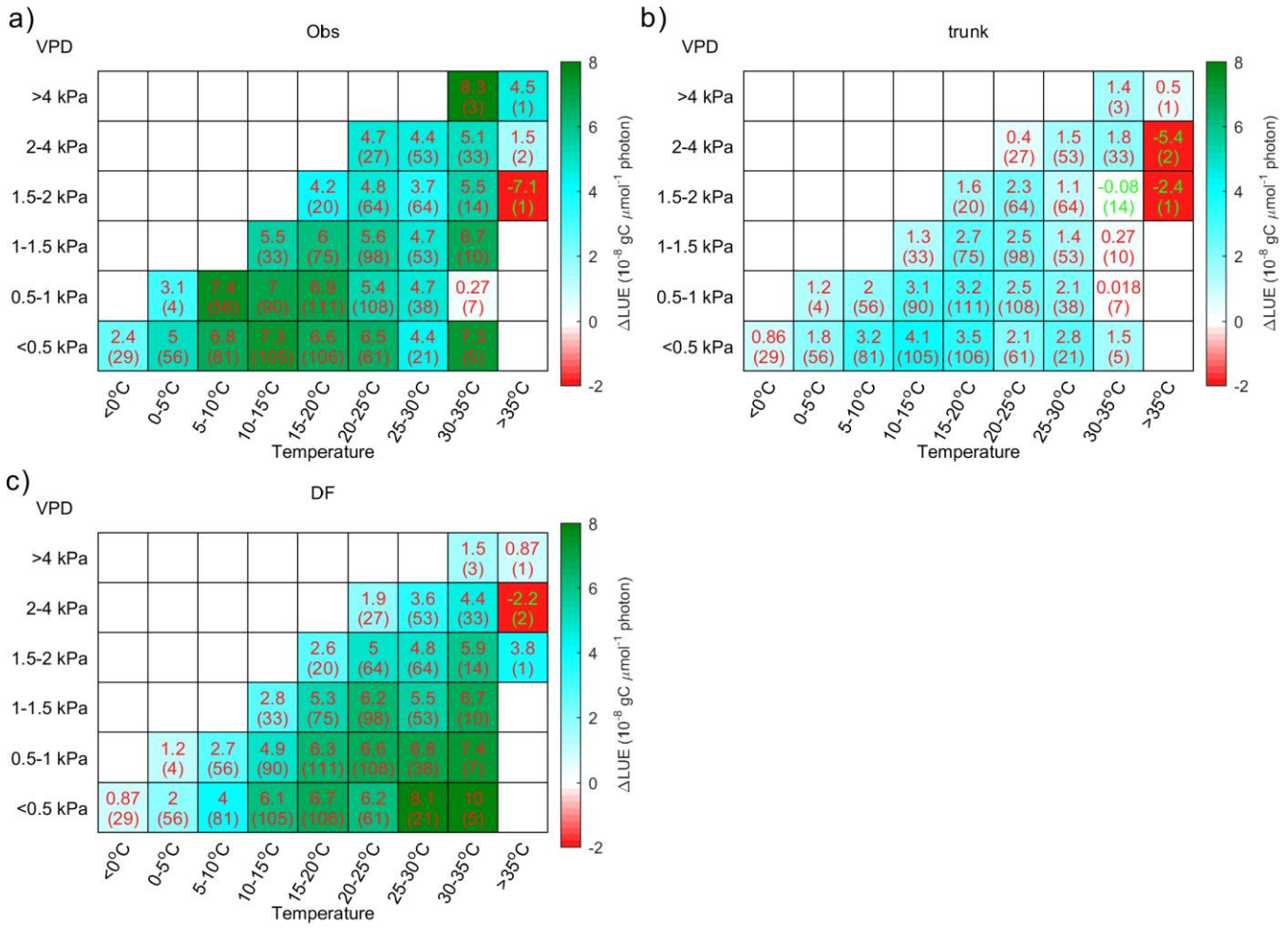

Figure 3.9 The distribution of LUE difference between cloudy and sunny conditions (ΔLUE) in temperature-VPD field. The upper numbers in each grid indicate the average of site level ΔLUE, while numbers in brackets indicate the number of sites with valid data. (a) the ΔLUE based on observations, (b) the ΔLUE based on ORCHIDEE trunk, (c) the ΔLUE based on ORCHIDEE_DF

decline of ΔLUE is found at high temperatures. The ΔLUE simulated by ORCHIDEE trunk is much smaller compared with observations (Figure 3.9b).

The ΔLUE from forests and short vegetation are shown separately in Figure 3.10. Based on site level observations (Figure 3.10a), both vegetation types show a larger ΔLUE at lower VPD between 5-20 °C. In forests, there is also large ΔLUE at high temperature conditions, which mainly occurs in tropical forests (Figure S3.3). Nevertheless, ORCHIDEE_DF still overestimates the ΔLUE at high temperatures (Figure 3.10e), which is mainly due to the overestimation of ΔLUE at high temperatures for temperate forests (Figure S3.3).

Compared with forests, the short vegetation shows a much stronger decline of ΔLUE at higher VPD level (Figure 3.10b), however, it is not well captured by ORCHIDEE_DF (Figure 3.10f). In most cases, ORCHIDEE trunk tend to strongly underestimate ΔLUE unless the observed ΔLUE is small or negative (e.g. VPD > 2kPa for short vegetation).

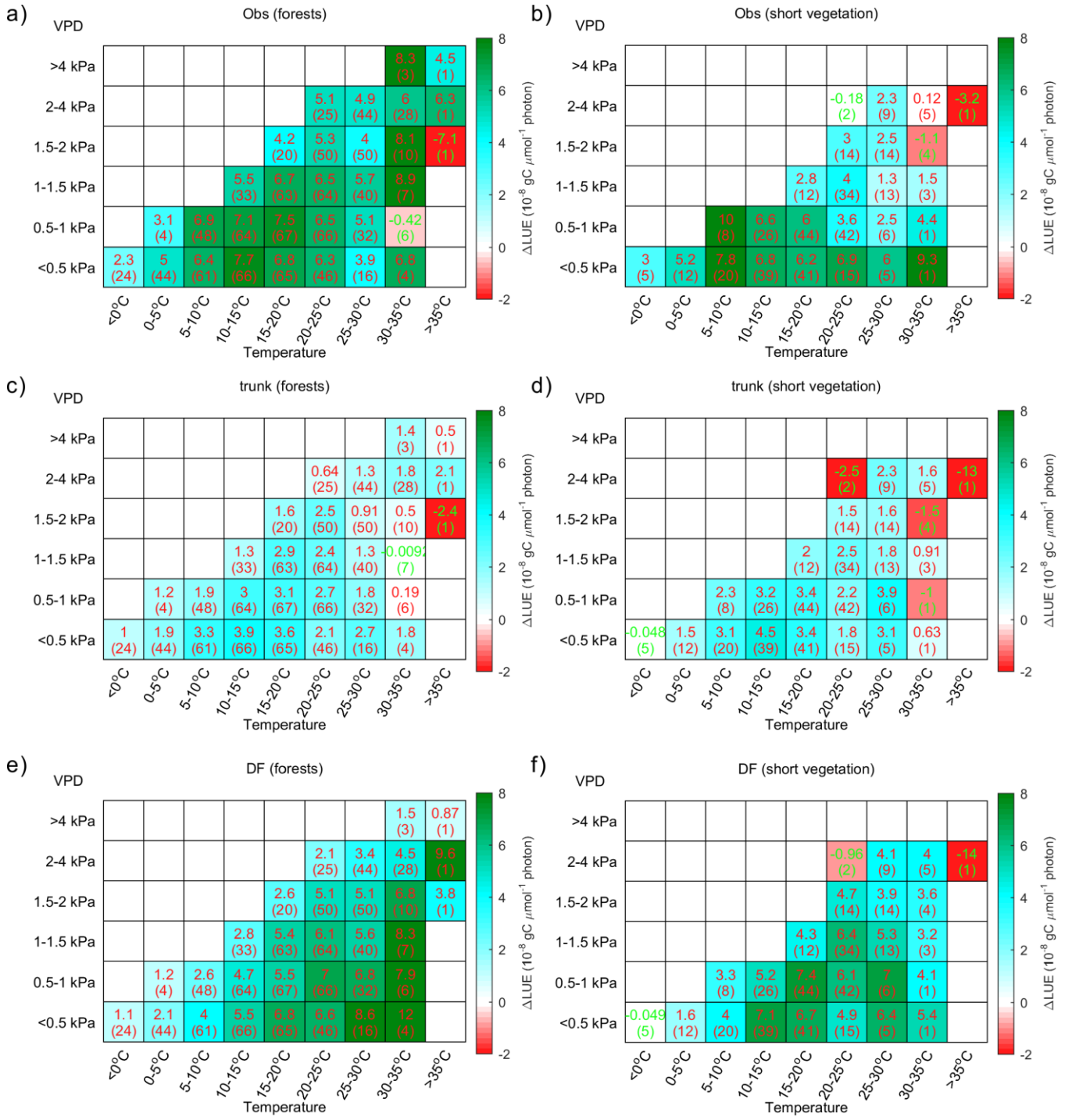

Figure 3.10 same as Figure 3.9 but for forests (a, c, e) and for short vegetation (b, d, f).

3.4 Discussion

3.4.1 Improvement of ORCHIDEE_DF

The role of diffuse light on photosynthesis has been found and modeled in different vegetation types (Gu *et al.*, 2003; Niyogi *et al.*, 2004; Mission *et al.*, 2005; Alton *et al.*, 2007; Knohl and Baldocchi, 2008; Mercado *et al.* 2009; Oliphant *et al.*, 2011; Kanniah *et al.*, 2013; Williams *et al.*, 2014; Cheng *et al.*, 2015; Wang *et al.*, 2018). However, very few studies attempt to account for the diffuse light effect in a global land surface model, and fewer studies have used large FLUXNET datasets for evaluation. Here, by using flux observations from 159 sites over the globe, we show that by separating the direct and diffuse light, ORCHIDEE_DF improves the simulation of GPP under sunny conditions and, more important, reproduced the observed impacts of diffuse light on GPP and LUE for most of the PFTs (Figures 3.4-3.6). Under cloudy conditions, ORCHIDEE_DF seems to perform slightly worse compared with ORCHIDEE trunk (Figure 3.4). However, it should be noted that ORCHIDEE_DF has not been recalibrated and all parameters are those from ORCHIDEE trunk despite the substantial changes in the code. On the contrary, the GPP simulated by ORCHIDEE trunk shows different GPP STD biases under sunny and cloudy conditions, while ORCHIDEE_DF gives a more systematically underestimated GPP STD, which should be more easily corrected in a future calibration. The site level comparison (Figure 3.5) also explains how ORCHIDEE_DF reproduces the GPP increase compared to ORCHIDEE trunk. At most sites, the GPP simulated by the two models show similar magnitude under cloudy conditions. While under sunny conditions, the GPP simulated by ORCHIDEE_DF is significantly smaller. This is because in the one-stream canopy light transmission model in ORCHIDEE trunk, all light is considered as diffuse light and evenly distributed in each leaf layer. This simplified approach to the modelling of light distribution leads to larger GPP under sunny conditions because the effect of light saturation on sunlit lit is ignored. Since ORCHIDEE trunk was calibrated using both sunny and cloudy data, but ORCHIDEE_DF corrected the overestimation under sunny conditions, ORCHIDEE_DF may give an overall underestimation using current parameters.

3.4.2 Factors affecting diffuse light effect on GPP

Although diffuse light can increase photosynthesis of shaded leaves, the GPP increase under cloudy conditions is not contributed only by this effect. A recent field study suggested that photosynthesis from part of the canopy (especially sunlit leaves) benefits from the lower VPD rather than higher diffuse light fraction under cloudier conditions (Wang *et al.*, 2018). Our results show that in the morning and the afternoon, higher diffuse PAR fraction is the main factor causing the larger GPP under cloudy conditions compared with sunny conditions, as only ORCHIDEE_DF reproduced the observed positive ΔGPP during the two period (Figure 3.7). While at midday, the larger GPP under cloudy conditions should be mainly due to lower T or VPD other than to diffuse light because ORCHIDEE trunk, which does not simulate the diffuse light effect, also reproduces this effect (Figure 3.7). A similar effect is also reported by Cheng *et al.* (2015), who found in croplands that midday GPP increase under cloudier conditions is mainly caused by lower temperature and lower VPD rather than by diffuse light. Photosynthesis is often considered as limited by either carboxylation or electron transportation (Farquhar *et al.*, 1980). It is when the shaded leaf photosynthesis is limited by light that diffuse light can increase GPP. At midday, large VPD may cause a stomatal closure, leading to a carboxylation-limited photosynthesis. Our results imply that it might be important to consider the diurnal cycle of environmental factors to better understand the effect of diffuse light.

It should be noted that the covariation of environmental factors with more diffuse light under cloudier conditions does not always benefit to photosynthesis. For instance, if the vegetation is cold stressed, the decrease of temperature under cloudier condition may strengthen this stress and offset the effect of diffuse light. Our analyses indicate that under most stressed conditions, the effect of diffuse light on photosynthesis is weakened (Figures 3.9, 3.10).

Another important factor is the light itself. When there is no light saturation of shaded leaves, under the same diffuse light fraction, stronger light levels are likely to benefit the shaded leaves more (Figure 3.5), resulting in higher ΔGPP. Nevertheless, in this study we investigated LUE apart from GPP, which has removed this effect.

Besides environmental factors, the canopy structure is also very important.

Theoretically, thicker canopies with large LAI tend to be more sensitive to diffuse light because a larger fraction of shaded leaves, that are light limited, are distributed in deep canopies (Figure 3.1). Existing LAI observations at flux sites suggested a very weak positive effect of LAI on ΔLUE (Figure S3.4). However, the LAI observations are not well defined (maximum or average) and remain very limited in the current FLUXNET dataset (less than 10 in each LAI interval), more LAI observations are needed to test this effect. In our study, LAI simulated by ORCHIDEE trunk and ORCHIDEE_DF are very similar (not shown), thus it should not be the reason causing the difference in ΔGPP and ΔLUE in the two models.

3.4.3 Uncertainties and Limitations

Many empirical methods have been proposed to partition solar radiation into diffuse and direct light (e.g. Spitters *et al.*, 1986; Weiss and Norman, 1985; Erbs *et al.*, 1982). Although these methods have been more or less proven useful, biases remain in the predicted diffuse light fraction under all aerosol and cloud conditions, which inevitably introduces some uncertainties to our analyses. However, such methods are currently the most feasible approach at flux site level. A more systematic measurement of direct and diffuse surface radiation is desirable.

Another source of uncertainty is from the light transmission model. In ORCHIDEE_DF, we used a two-stream radiative transfer approximation. In this model, the canopy traits parameters such as leaf scattering, leaf orientation and leaf clumping factors are assumed the same for all PFTs, however real canopies are very diverse (Smith *et al.*, 2004). In situ observations are required to obtain better parameters. Furthermore, the validity of the light transmission model in ORCHIDEE_DF depends on the several assumptions described in the model description section. These assumptions are not always valid in reality. For example, because direct solar beams are not exact parallels, leaves in canopies are not always sunlit or shaded, they may also fall in penumbra regions, (i.e. regions where only part of the incoming direct solar beams are blocked, Cescatti and Niinemets, 2005). These more complex processes should be considered in future model development. Nevertheless, our simplified light transmission already succeeds reproducing the observed diffuse light impact.

There are other sources of uncertainties in complex land surface models. Although

ORCHIDEE_DF reproduces the magnitude of the diffuse light effect, it fails to reproduce the response of ΔLUE to temperature. For all PFTs, ORCHIDEE_DF underestimates the ΔLUE at low temperatures, and overestimates ΔLUE at high temperatures (Figure 3.8). The low temperature underestimation is also found in ORCHIDEE trunk, indicating that the models may have underestimated the tolerance of plants to low temperatures. While at high temperatures, ORCHIDEE_DF tends to underestimate the impact of heat stress. This bias might due to parameterization of temperature acclimation which is based on observation mainly from a narrow temperature range (11-29 ^{o}C) (Kattge *et al.*, 2007). In short vegetation, the introduction of diffuse light into the model results in an increase of ΔLUE at high temperatures and high VPD (Figure 3.8, 3.10), indicating the vegetation simulated by ORCHIDEE trunk remains light limited under such conditions. However, the strong decrease trend of observed ΔLUE along temperature and VPD gradients indicates a heat and VPD stress. This implies that parameters in current ORCHIDEE version may have underestimated the response of grassland and cropland photosynthesis to heat and dry stress.

3.5 Conclusion

In this study, we added to the ORCHIDEE trunk a module to partition the downward surface solar radiation into diffuse and direct components, and a new canopy radiative transfer model, which separates the existing multilayer canopy into sunlit and shaded leaves. The resulting new land surface model, ORCHIDEE_DF, is evaluated using the La Thuile flux dataset over 159 sites over 11 PFTs. Compared with ORCHIDEE trunk, ORCHIDEE_DF improves the GPP simulation under sunny conditions. This improvement successfully reproduces the observed enhancement of GPP under cloudier conditions at most of the sites.

Using observed and modeled GPP, we found an increase of GPP under cloudier conditions at all time of a day, however, the mechanisms causing this effect are different at midday from morning and afternoon. In morning and afternoon, the increase in GPP is mainly contributed by increased diffuse light fraction, while at midday, the GPP increase is mainly due to weaker stress from temperature and VPD.

Observations indicate that under cloudy and sunny conditions for the same light level, the maximum LUE difference can be over 7×10^{-8} gC μmol^{-1} photon. The

maximum LUE is found at temperatures between 5 and 20 °C with VPD < 1 kPa. With increasing VPD, or under lower or higher temperatures, the LUE may decrease. Compared with observations, ORCHIDEE_DF underestimates the diffuse light effect at low temperature and overestimates it at high temperatures, possibly due to imperfect temperature acclimation parameterization in the current ORCHIDEE model. In grasslands and croplands, ORCHIDEE_DF overestimates the diffuse light effect on LUE, which might be due to an overestimation of their tolerance to dry conditions.

As ORCHIDEE_DF is a land surface model which is able to capture the effect of diffuse light over a large number of sites over the globe, we are confident that, with this improved model framework, we can investigate the effect of aerosols on global biogeochemical cycles, and assess the impact of aerosol emission policies and aerosol related climate engineering on such cycles.

Supporting Information for Chapter 3

Contents of this file

Figures S3.1 to S3.4
Table S3.1 and S3.2

Figure S3.1 Same as Figure 3.3 but diffuse PPFD fraction calculated using method from Spitters (1986).

Figure S3.2 Mean annual climate of at the sites used in this study. The colors indicate different PFTs. Color codes are shown in Figure 3.4

Figure S3.3 Same as Figure 3.10 but for tropical forests (a, d, g), temperate forests (b, e, h) and boreal forests (c, f, i) respectively

Figure S3.4 Same as Figure 3.8a, but for LAI

Table S3.1 Plant functional types (PFT) in ORCHIDEE

Table S3.2 The information of the flux sites used in this study

Figure S3.1

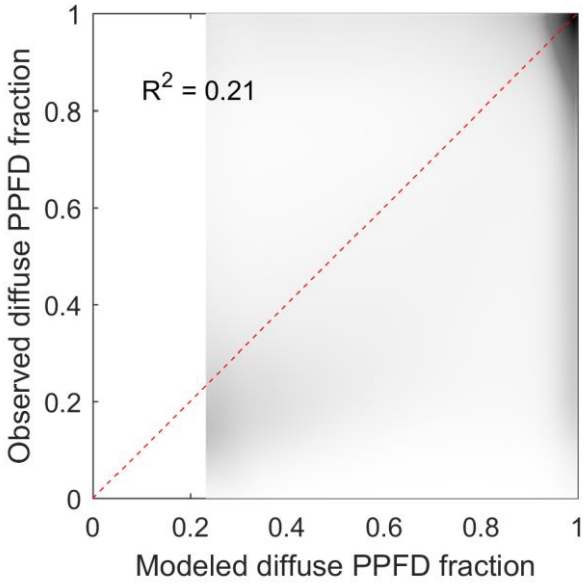

Figure S3.2

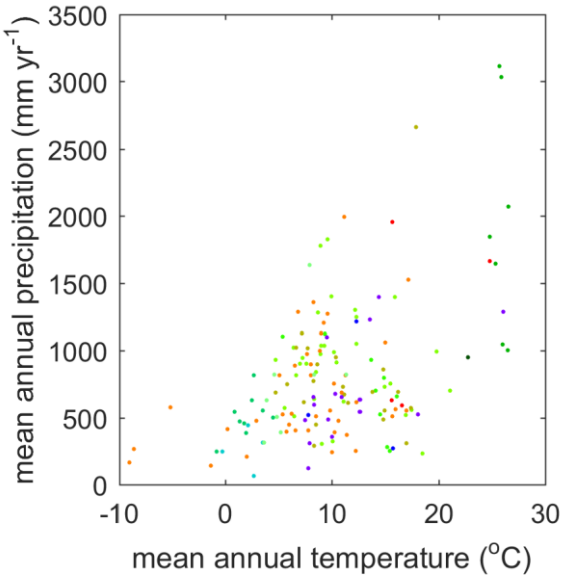

Figure S3.3

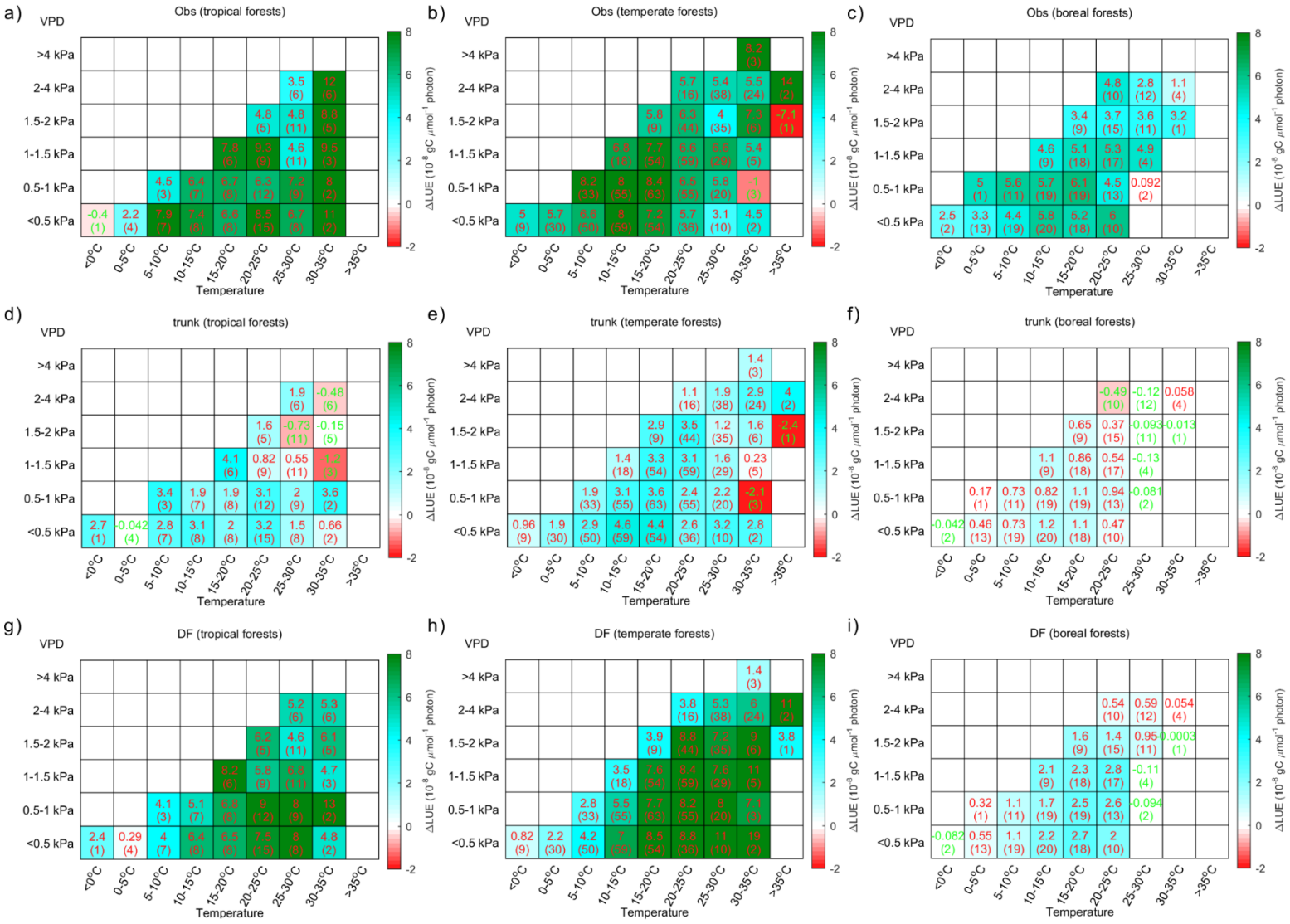
a)
Obs (tropical forests)
b)
Obs (temperate forests)
c)
Obs (boreal forests)
d)
trunk (tropical forests)
e)
trunk (temperate forests)
f)
trunk (boreal forests)
g)
DF (tropical forests)
h)
DF (temperate forests)
i)
DF (boreal forests)
VPD
>4 kPa
2-4 kPa
1.5-2 kPa
1-1.5 kPa
0.5-1 kPa
<0.5 kPa
<0°C
0-5°C
5-10°C
10-15°C
15-20°C
20-25°C
25-30°C
30-35°C
>35°C
Temperature
ΔLUE (10⁻⁸ gC μmol⁻¹ photon)

Figure S3.4

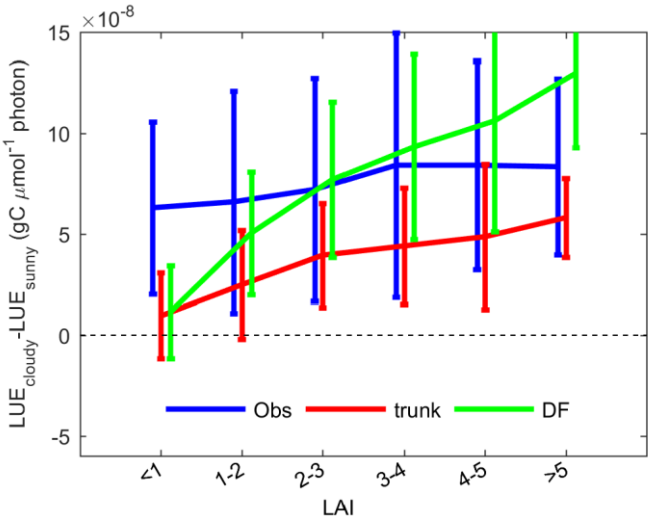

Table S3.1 Plant functional types (PFT) in ORCHIDEE

PFT number	PFT abbreviation	PFT name
1		Bare soil
2	TrEBF	Tropical broad-leaved evergreen forests
3	TrDBF	Tropical broad-leaved raingreen forests
4	TeENF	Temperate needleleaf evergreen forests
5	TeEBF	Temperate broad-leaved evergreen forests
6	TeDBF	Temperate broad-leaved summergreen forests
7	BoENF	Boreal needleleaf evergreen forests
8	BoDBF	Boreal broad-leaved summergreen forests
9	BoDNF	Boreal needleleaf summergreen forests
10	C3Gra	C3 grasslands
11	C4Gra	C4 grasslands
12	C3Cro	C3 croplands
13	C4Cro	C4 croplands

Table S3.2 The information of the flux sites used in this study

Site name	Latitude	Longitude	PFT_ORCHIDEE	time
AT-Neu	47.12	11.32	GraC3	2002-2006
AU-Tum	-35.66	148.15	TeEBF	2001-2006
AU-Wac	-37.43	145.19	TeEBF	2005-2007
BE-Bra	51.31	4.52	MF*	1997-2006
BE-Jal	50.56	6.07	MF	2006
BE-Lon	50.55	4.74	CroC3	2004-2006
BE-Vie	50.31	6	MF	1996-2006
BR-Ban	-9.82	-50.16	TrEBF	2003-2006
BR-Ji1	-10.76	-62.36	GraC4	1999
BR-Ji2	-10.08	-61.93	TrEBF	2000-2002
BR-Ma2	-2.61	-60.21	TrEBF	1999-2006
BR-Sa2	-3.01	-54.54	CroC3	2001-2002
BR-Sa3	-3.02	-54.97	TrEBF	2000-2003
BR-Sp1	-21.62	-47.65	TrDBF	2001-2002
CA-Ca1	49.87	-125.33	TeENF	1997-2005
CA-Ca3	49.53	-124.9	TeENF	2001-2005
CA-Gro	48.22	-82.16	MF	2003-2005
CA-Oas	53.63	-106.2	BoDBF	1997-2005
CA-Obs	53.99	-105.12	BoENF	1999-2005
CA-Ojp	53.92	-104.69	BoENF	1999-2005
CA-Qfo	49.69	-74.34	BoENF	2003-2006
CA-SF1	54.49	-105.82	BoENF	2003-2005
CA-SJ3	53.88	-104.65	BoENF	2004-2005
CA-TP2	42.77	-80.46	TeENF	2003-2005
CA-TP3	42.71	-80.35	TeENF	2003-2005
CA-TP4	42.71	-80.36	TeENF	2003-2005
CA-WP1	54.95	-112.47	MF	2003-2005
CA-WP2	55.54	-112.33	GraC3	2004
CA-WP3	54.47	-113.32	GraC3	2004
CH-Oe1	47.29	7.73	GraC3	2002-2006
CH-Oe2	47.29	7.73	CroC3	2005
CN-Anh	33	117	TeDBF	2005-2006
CN-Bed	39.53	116.25	TeEBF	2005-2006
CN-Cha	42.4	128.1	MF	2003
CN-Do1	31.52	121.96	GraC4	2005
CN-Du1	42.05	116.67	CroC3	2005-2006
CN-Du2	42.05	116.28	GraC3	2006
CN-HaM	37.37	101.18	GraC3	2002-2004
CN-Xfs	44.13	116.33	GraC3	2004-2006
CN-Xi1	43.55	116.68	GraC3	2006
CN-Xi2	43.55	116.67	GraC3	2006
CZ-BK1	49.5	18.54	TeENF	2000-2006

CZ-BK2	49.5	18.54	GraC3	2004-2006
CZ-wet	49.03	14.77	GraC3	2006
DE-Bay	50.14	11.87	TeENF	1996-1999
DE-Geb	51.1	10.91	CroC3	2004-2006
DE-Gri	50.95	13.51	GraC3	2005-2006
DE-Hai	51.08	10.45	TeDBF	2000-2006
DE-Har	47.93	7.6	TeENF	2005-2006
DE-Kli	50.89	13.52	CroC3	2004-2006
DE-Tha	50.96	13.57	TeENF	1996-2006
DE-Wet	50.45	11.46	TeENF	2002-2006
DK-Fou	56.48	9.59	CroC3	2005
DK-Lva	55.68	12.08	GraC3	2005-2006
DK-Ris	55.53	12.1	CroC3	2004-2005
DK-Sor	55.49	11.65	TeDBF	1996-2006
ES-ES1	39.35	-0.32	TeENF	1999-2006
ES-ES2	39.28	-0.32	CroC3	2004-2006
ES-LMa	39.94	-5.77	TeDBF	2004-2006
ES-VDA	42.15	1.45	GraC3	2004-2006
FI-Hyy	61.85	24.29	BoENF	1996-2006
FI-Kaa	69.14	27.3	GraC3	2000-2006
FI-Sii	61.83	24.19	GraC3	2004-2005
FR-Aur	43.55	1.11	CroC3	2005
FR-Fon	48.48	2.78	TeDBF	2005-2006
FR-Hes	48.67	7.06	TeDBF	1997-2006
FR-Lam	43.49	1.24	CroC4	2005
FR-Lq1	45.64	2.74	GraC3	2004-2006
FR-Lq2	45.64	2.74	GraC3	2004-2006
FR-Pue	43.74	3.6	TeEBF	2000-2006
GF-Guy	5.28	-52.93	TrEBF	2004-2006
HU-Bug	46.69	19.6	GraC3	2002-2006
HU-Mat	47.85	19.73	GraC3	2004-2006
ID-Pag	2.35	114.04	TrEBF	2002-2003
IE-Ca1	52.86	-6.92	CroC3	2004-2006
IE-Dri	51.99	-8.75	GraC3	2003-2005
IL-Yat	31.35	35.05	TeENF	2001-2006
IT-Amp	41.9	13.61	GraC3	2002-2006
IT-Be2	46	13.03	CroC4	2006
IT-Bon	39.48	16.53	TeENF	2006
IT-Col	41.85	13.59	TeDBF	1996-2006
IT-Cpz	41.71	12.38	TeEBF	1997-2006
IT-Lav	45.96	11.28	TeENF	2000-2006
IT-Lec	43.3	11.27	TeEBF	2005-2006
IT-LMa	45.58	7.15	TeDBF	2003-2006
IT-Mal	46.12	11.7	GraC3	2003-2006

IT-MBo	46.02	11.05	GraC3	2003-2006
IT-Noe	40.61	8.15	TeENF	2004-2006
IT-Pia	42.58	10.08	TeENF	2002-2005
IT-Ren	46.59	11.43	TeENF	1999-2006
IT-Ro2	42.39	11.92	TeDBF	2002-2006
IT-SRo	43.73	10.28	TeENF	1999-2006
JP-Mas	36.05	140.03	CroC3	2002-2003
JP-Tak	36.15	137.42	TeDBF	1999-2004
KR-Hnm	34.55	126.57	CroC3	2004-2006
NL-Ca1	51.97	4.93	GraC3	2003-2006
NL-Haa	52	4.81	GraC3	2003-2004
NL-Lan	51.95	4.9	CroC4	2005-2006
NL-Loo	52.17	5.74	TeENF	1996-2006
NL-Lut	53.4	6.36	CroC3	2006
NL-Mol	51.65	4.64	CroC3	2005-2006
PL-wet	52.76	16.31	GraC3	2004-2005
PT-Esp	38.64	-8.6	TeEBF	2002-2006
PT-Mi2	38.48	-8.02	GraC3	2004-2006
RU-Cok	70.62	147.88	BoDBF	2003-2005
SE-Abi	68.36	18.79	BoDBF	2005
SE-Deg	64.18	19.55	GraC3	2001-2005
SE-Fla	64.11	19.46	BoENF	1996-2002
SE-Nor	60.09	17.48	TeENF	1996-2005
SE-Sk2	60.13	17.84	TeENF	2004-2005
UK-AMo	55.79	-3.24	GraC3	2005
UK-EBu	55.87	-3.21	GraC3	2004-2006
UK-ESa	55.91	-2.86	CroC3	2003-2005
UK-Gri	56.61	-3.8	TeENF	1997-2006
UK-Ham	51.12	-0.86	TeDBF	2004-2005
UK-PL3	51.45	-1.27	TeDBF	2005-2006
UK-Tad	51.21	-2.83	GraC3	2001
US-ARb	35.55	-98.04	GraC4	2005-2006
US-ARc	35.54	-98.04	GraC4	2005-2006
US-ARM	36.61	-97.49	CroC3	2003-2006
US-Atq	70.47	-157.41	GraC3	1999-2006
US-Bar	44.06	-71.29	TeDBF	2004-2005
US-Blo	38.9	-120.63	TeENF	1997-2006
US-Bn1	63.92	-145.38	BoENF	2003
US-Bn2	63.92	-145.38	BoDBF	2003
US-Brw	71.32	-156.63	GraC3	1998-2002
US-CaV	39.06	-79.42	GraC3	2004-2005
US-Dk1	35.97	-79.09	GraC3	2001-2005
US-FPe	48.31	-105.1	GraC3	2000-2006
US-Fuf	35.09	-111.76	TeENF	2005-2006

US-Fwf	35.45	-111.77	GraC3	2005-2006
US-Goo	34.25	-89.97	GraC3	2002-2006
US-Ho1	45.2	-68.74	TeENF	1996-2004
US-IB2	41.84	-88.24	GraC3	2004-2007
US-Ivo	68.49	-155.75	GraC3	2003-2006
US-Los	46.08	-89.98	TeDBF	2001-2005
US-Me3	44.32	-121.61	TeENF	2004-2005
US-Me4	44.5	-121.62	TeENF	1996-2000
US-MMS	39.32	-86.41	TeDBF	1999-2005
US-MOz	38.74	-92.2	TeDBF	2004-2006
US-NC2	35.8	-76.67	TeENF	2005-2006
US-NR1	40.03	-105.55	BoENF	1999-2003
US-Oho	41.55	-83.84	TeDBF	2004-2005
US-PFa	45.95	-90.27	MF	1996-2003
US-SO2	33.37	-116.62	TeDBF	1997-2006
US-SO4	33.38	-116.64	TeDBF	2004-2006
US-SP1	29.74	-82.22	TeENF	2000-2005
US-SP3	29.75	-82.16	TeENF	1999-2004
US-Syv	46.24	-89.35	MF	2002-2006
US-Ton	38.43	-120.97	TeDBF	2001-2006
US-UMB	45.56	-84.71	TeDBF	1999-2003
US-Var	38.41	-120.95	GraC3	2001-2006
US-WBW	35.96	-84.29	TeDBF	1995-1999
US-WCr	45.81	-90.08	TeDBF	1999-2006
US-Wi1	46.73	-91.23	TeDBF	2003
US-Wi2	46.69	-91.15	TeENF	2003
US-Wi4	46.74	-91.17	TeENF	2002-2005
US-Wrc	45.82	-121.95	TeENF	1998-2006
VU-Coc	-15.44	167.19	TrEBF	2001-2004

* Mix forests, treated as 50% TeDBF and 50% TeENF

Chapter 4. Aerosol impacts on the land carbon cycle through changing diffuse radiation

Summary

Chapter 3 described a land surface model, ORCHIDEE_DF, which is able to simulate the impacts of diffuse radiation on photosynthesis. In this chapter, we set up two sets of simulations with empirically tuned ORCHIDEE_DF, respectively using observation-based climate dataset CRUJRA, and the climate from IPSL-CM6A-LR simulations to systematically investigate the impacts of aerosol-induced changes in diffuse radiation and other factors. The two sets of simulations find an enhanced cumulative land C sink of 6.8 PgC (CRUJRA climate) and 15.9 PgC (IPSL-CM6A-LR climate) in response to the anthropogenic aerosol-caused diffuse radiation fraction changes during the historical period and this enhancement mainly occurs after the 1950s. Based on a series of factorial simulations driven by IPSL-CM6A-LR climate, we found that globally, the anthropogenic aerosol-induced land C sink increase is mainly due to the diffuse light fertilization effect but also contributed by the cooling effect of aerosols. We also compared different ways reconstructing diffuse radiation under no anthropogenic aerosol scenario and found that correctly considering the variability of diffuse radiation fraction is essential to obtain unbiased carbon fluxes.

4.1 Introduction

Anthropogenic aerosols are receiving more and more attention during the last decades in climate change studies as they significantly affect the climate system through aerosol-radiation and aerosol-cloud interactions (Boucher *et al.*, 2013). Besides these well-known (but not well-understood) physical processes in the atmosphere, which alter the land surface radiation budget directly, atmospheric aerosols also have an indirect impact on the C cycle, especially its terrestrial component (Chapter 2; Mercado *et al.*, 2009), which consequently affects the global climate through the

climate-carbon feedback (Friedlingstein *et al.*, 2006). However, the relevant processes remain poorly known and it is uncertain how much anthropogenic aerosols perturb the land C cycle.

One of the main mechanisms by which aerosols affect the land C cycle is through changing the quantity and quality of radiation received by vegetation, with an impact on photosynthesis. On the one hand, the absorption and scattering of solar radiation due to atmospheric aerosols decrease the amount of incoming solar radiation at the top of the vegetation canopy. In situ observations have shown negative relationships between aerosol optical depth (AOD) and incoming solar radiation at the land surface (Kanniah *et al.*, 2010). This decrease may cause a decrease in photosynthesis, especially in ecosystems which are light-limited, such as tropical forests (Nemani *et al.*, 2003). On the other hand, aerosols alter the angular distribution of incoming light. The scattering of radiation by aerosols can significantly increase the fraction of diffuse light, which is able to penetrate deeper and distribute more evenly in the canopy (Roderick *et al.*, 2001). Since sunlit leaves are often light saturated while shaded leaves are not, an increase in diffuse radiation may benefit the photosynthesis of the entire canopy. In situ observations show that diffuse radiation increases the light use efficiency of plants in various ecosystem types such as forests, grasslands and croplands (Choudhury, 2001; Gu *et al.*, 2002; Alton *et al.*, 2007a; Alton *et al.*, 2008).

It has been investigated at different sites whether the increase in light use efficiency (LUE) due to diffuse radiation increase can compensate for the gross primary production (GPP) loss due to total radiation decline in the presence of aerosols and clouds (Hollinger *et al.* 1994; Kanniah *et al.*, 2010; Alton *et al.*, 2007a). However, there is no consensus on which process is more important. One of the reasons is because field studies were performed in various ecosystems under different environmental conditions, highlighting the importance to understand this question at a larger scale. Another reason is because the role of decreased light versus increased diffuse light fraction depends on the amount of aerosols in the atmospheric column, their optical properties and the relative occurrences of clear sky and cloudy weather.

At larger scales, the aerosol impacts are generally investigated using atmospheric and land surface models (LSM) (Jones *et al.*, 2003; Mahowald *et al.*, 2011; Chapter 2). The effect of decreasing radiation can be explicitly considered, as total incoming

radiation is an important factor driving photosynthesis in process-based LSMs (e.g., Chapter 2). However, the fertilization effect of diffuse radiation is often ignored in LSMs as most of them still do not distinguish direct and diffuse radiation in the canopy. Using the Joint UK Land Environment Simulator (JULES) model, Alton *et al.* (2007b) and Mercado *et al.* (2009) modified the light transmission in the canopy to represent the absorption of diffuse radiation and estimated its impacts on global C fluxes. The work by Alton *et al.* (2007) was based on the comparison between two different versions of a model, which could not address the question of the aerosol impact because the difference in C fluxes might be due to the difference in model structure. Mercado *et al.* (2009) set up their simulations simply using different configurations of the fraction of diffuse radiation without changing the total radiation and without isolating the effect of climate change due to aerosols. Thus their results strictly presented the fertilization effect of diffuse radiation. But as shown in Chapter 2, aerosol-caused climate change also has a considerable impact on the land C budget. The need to investigate the full impacts of anthropogenic aerosols on the land C budget at the global scale thus remains.

In Chapter 3, I presented the development of ORCHIDEE_DF, a modified version of the ORCHIDEE LSM which distinguishes direct and diffuse radiation. Using this LSM, we are now able to investigate the full impacts of aerosols on the global land C cycle and identify the role of each mechanism (e.g., changes in temperature, precipitation, as well as in light quantity and quality). Here, we set up two sets of simulations driven by the latest climate data from the CRUJRA dataset and the IPSL-CM6A-LR simulations (hereafter referred to as the CRUJRA and IPSL) to (1) quantify the impacts of aerosol-induced changes of diffuse radiation and climate change on the land C budget during the historical period; (2) determine whether the fertilization by diffuse radiation compensates for the reduction of incoming radiation due to anthropogenic aerosols globally; (3) understand how aerosol-induced changes in radiation, temperature and precipitation individually affect land C cycle.

4.2 Data and Methods

4.2.1 ORCHIDEE_DF model

In this study we performed simulations with ORCHIDEE_DF, a new development of ORCHIDEE trunk (v5453) (Krinner *et al.*, 2005). Compared with ORCHIDEE trunk, which uses a one-stream canopy radiative transfer calculation (i.e. all radiation treated as diffuse), ORCHIDEE_DF uses a two-stream canopy radiative transfer module which distinguishes direct and diffuse radiation and considers the differential light absorption of sunlit and shaded leaves. A detailed description of canopy light transmission in ORCHIDEE_DF is found in Chapter 3.

In this study the empirical equations calculating the fraction of diffuse radiation (Fdf) (Eqs. 9 and 10 in Chapter 3) are not used. Instead, along with the CRUJRA dataset, a new global Fdf field based on atmospheric radiative transfer calculations is provided as an additional input in order to investigate the impact of diffuse radiation (see the data section). Since the Fdf calculated from the atmospheric radiative transfer model is considered more accurate than the empirical model used in Chapter 3, we adapted ORCHIDEE_DF to accept and interpolate the Fdf field along with other input climate fields for the CRUJRA simulations.

Compared with the CRUJRA dataset, the output of IPSL-CM6A-LR simulations provide more detailed cloud and aerosol information, which allows a more realistic representation of the diffuse light in the model. In large-scale simulations, the forcing data are meant to be representative of a large area (a gridbox) rather than a point or small area like usually observed at flux sites. Therefore, radiation and Fdf can differ dramatically within a gridbox due to the heterogeneous cloud distribution. As the response of photosynthesis to Fdf is not linear, it is crucial to calculate photosynthesis separately in the clear and cloudy subgrid area. To consider this effect, ORCHIDEE_DF used for the simulations using IPSL-CM6A-LR climate field is modified to calculate photosynthesis separately in clear and cloudy subgrid area (Figure 4.1). At each time step, each gridbox is firstly divided into a clear and a cloudy area according to the total cloud fraction (clt) of this gridbox. In the clear sky subgrid area, the incoming direct ($SWdown_{clear,dir}$) and diffuse ($SWdown_{clear,dif}$) shortwave radiation at the surface are obtained considering tropospheric and stratospheric aerosol optical depth at 550 nm, as well as solar zenith angle from a look up table. The look up table is built with an atmospheric radiative transfer model named Streamer (Mercado *et al.*, 2009; Key *et al.*, 1998). Using $SWdown_{clear,dir}$ and $SWdown_{clear,dif}$ we are able to calculate the sum of their counterparts in the cloudy subgrid area ($SWdown_{cloudy,dir}$ + $SWdown_{cloudy,dif}$) from

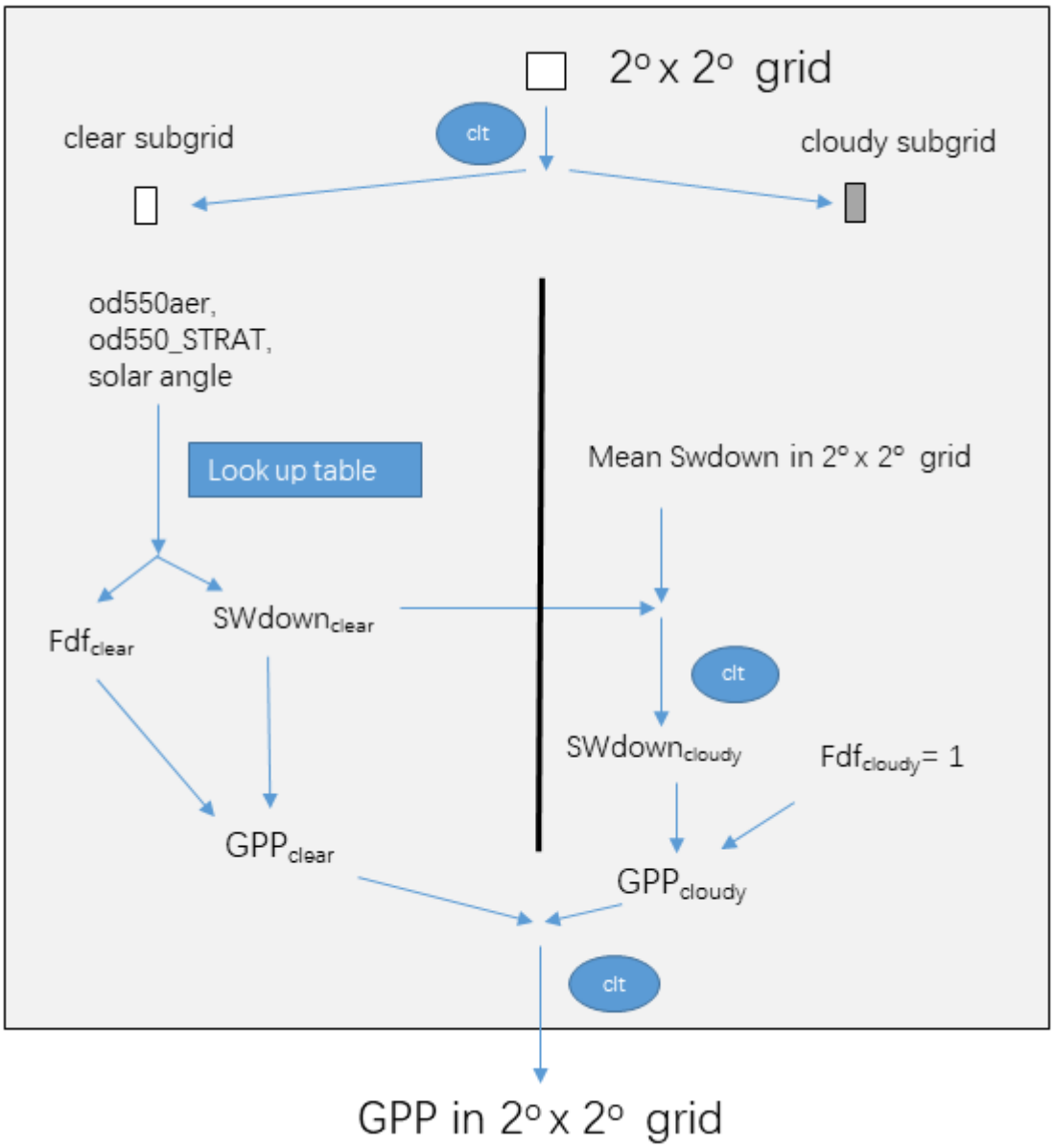

Figure 4.1 The GPP calculation in the IPSL simulations. clt: cloud fraction; Fdf: fraction of diffuse shortwave radiation; SWdown: downward shortwave radiation at land surface; od550aer: tropospheric AOD at 550nm; od550_STRAT: stratospheric AOD at 550nm.

the average incoming downward shortwave radiation field (SWdown) provided in the IPSL-CM6A-LR output:

$$SWdown = (SWdown_{clear,dir} + SWdown_{clear,dif}) \times (1 - clt) + (SWdown_{cloudy,dir} + SWdown_{cloudy,dif}) \times clt \quad \text{Eq. 4.1}$$

where $SWdown_{cloudy,dir}$ and $SWdown_{cloudy,dif}$ represent the direct and diffuse radiation of the cloudy subgrid area. Here we assume $SWdown_{cloudy,dir}$ to be zero following Mercado *et al.* (2009). This is a good assumption because the optical depth of clouds is generally

larger than a few units except for thin high-level clouds. The $SW_{cloudy,dif}$ can then be estimated as:

$$SWdown_{cloudy,dif} = (SWdown - (SWdown_{clear,dir} + SWdown_{clear,dif}) \times (1 - clt)) / clt \quad \text{Eq. 4.2}$$

where SWdown and clt come from the IPSL-CM6A-LR model simulations while $SWdown_{clear,dir}$ and $SWdown_{clear,dif}$ come from the look up table. It should be noted that as ORCHIDEE_DF has a time step of 30 minutes but the forcing fields have coarser temporal resolution, we have to interpolate all forcing data into 30 minutes in ORCHIDEE_DF. Furthermore, IPSL-CM6A-LR and the look up table use different radiative transfer scheme and the IPSL-CM6A-LR radiation scheme relies on the full 3D structure of clouds. This causes unavoidable mismatch between the different terms of Eq. 4.2, which may occasionally lead to unreasonable negative $SWdown_{cloudy,dif}$ or larger $SWdown_{cloudy,dif}$ than $SWdown_{clear,dir}$ + $SWdown_{clear,dif}$. In the first case, the $SWdown_{cloudy,dif}$ is set as zero and $SWdown_{clear,dir}$ and $SWdown_{clear,dif}$ are linearly scaled to keep the total SWdown conserved. In the second case, $SWdown_{cloudy,dif}$ is capped to $SWdown_{clear,dir}$ + $SWdown_{clear,dif}$ and then $SWdown_{clear,dir}$ and $SWdown_{clear,dif}$ are linearly scaled to equilibrate Eq. 4.1.

After this light partitioning, light transmission and photosynthesis in the vegetation canopy can be calculated in each of the clear and cloudy area of the gridbox. The photosynthesis in the two fractions of the gridbox can then be combined into a gridbox average (Figure 4.1).

Due to the lack of time as well as the lack of cloud cover information at flux sites, we did not perform a systematic calibration of ORCHIDEE_DF using the large amount of existing flux site observations collected in Chapter 3. Instead, because the TRENDY simulations must match the observation-based global carbon budget for the decade of the 1990s, we used the TRENDY v7 S3 simulation using ORCHIDEE trunk in the 1900s as the reference and empirically tuned photosynthesis-related parameters (Vcmax, specific leaf area, leaf age) in our two versions of ORCHIDEE_DF to get similar global GPP for each plant functional type (results not shown).

4.2.2 Forcing data and Experimental design

4.2.2.1 CRUJRA simulations

The first set of simulations performed in this chapter is driven by the CRUJRA v1.1 dataset (Harris *et al.*, 2014; Harris, 2019; Kobayashi *et al.*, 2015). CRUJRA v1.1 dataset was generated by adjusting the Japanese Reanalysis data (JRA) produced by the Japanese Meteorological Agency (JMA) with the observation-based monthly Climatic Research Unit (CRU) TS 3.26 data. As the replacement of CRUNCEP dataset used in Chapter 2, CRUJRA v1.1 provides 6-hourly meteorological variables at 0.5×0.5 degree including 2-metre air temperature (Tair), total precipitation (Precip), downward shortwave radiation (SWdown), downward longwave radiation (LWdown), 2-meter specific humidity (Qair), air pressure (Psurf) and the zonal and meridional components of 10-m wind (Wind_E and Wind_N). For the sake of investigating the effect of diffuse radiation with a framework consistent with the TRENDY simulations, a new Fdf field is provided along with the abovementioned climate variables at the same spatial and temporal resolutions. The Fdf field is based on atmospheric radiative transfer calculations using global aerosol and cloud cover fields, including tropospheric aerosol optical depth from a HadGEM2-ES historical simulation (Bellouin *et al.* 2011) bias-corrected by the CAMS reanalysis of atmospheric composition (Inness *et al.* 2019), the updated climatology of stratospheric aerosol optical depth by Sato *et al.* (1993), and the JRA cloud fraction (Kobayashi *et al.*, 2015) itself bias-corrected by the observationally-based CRU TS v4.03 monthly data.

The climate fields (except for the diffuse radiation fraction) of CRUJRA dataset have been used in TRENDY v7 simulations using the ORCHIDEE trunk (v5375) model version. ORCHIDEE_DF has the same parameters as this ORCHIDEE trunk version (except abovementioned photosynthesis-related parameters) and the two models just differ in their representation of the canopy radiative transfer. Because of the lack of time, we did not attempt to run a long spinup as the TRENDY v7 simulations had done. Instead, a 50-year fast spin-up recycling climate from 1901 and 1910 was run for ORCHIDEE_DF directly after the mandatory 1701-1900 transient simulation on ORCHIDEE trunk, in order to re-equilibrate the photosynthesis-related carbon pools (e.g., leaf biomass) with the new radiative transfer scheme. Then, experiments for historical and historical-no aerosol scenarios were set up. The detailed information for these CRUJRA simulations can be found in Table 4.1. The historical simulation (*Dfv*, or varying diffuse light fraction) was driven by climate fields (including Fdf) and land use map varying with time. In contrast, for the historical-no aerosol simulations, the

Table 4.1 Experimental design for the CRUJRA simulations.

Name	Forcing	
	Climate and land use map	Diffuse SWdown fraction
Dfv	All variables varying	Varying during 1901-2014
Df_clim	All variables varying	Repeat the 6-hour average of 1901, 1904-1906, 1909, 1911, 1915-1920, with diurnal and seasonal variations maintained
Df_1901[*]	All variables varying	Repeat the 6-hour 1901 values
Df_1905	All variables varying	Repeat the 6-hour 1905 values
Df_1916	All variables varying	Repeat the 6-hour 1916 values
Df_cons	All variables varying	Repeat the average of 1901, 1904-1906, 1909, 1911, 1915-1920 over all time steps (i.e., no diurnal and seasonal variations considered)

[*] the average of the output of *Df_1901*, *Df_1905*, *Df_1916* is named *Df_ens* for simplicity

Fdf field was kept at its pre-industrial level but the other forcing fields vary normally with time (same as *Dfv*). It should be noted that it is difficult to define the preindustrial Fdf level as there is no direct observations. Mercado *et al.* (2009) averaged the Fdf from 1901-1910 for each gridbox and month to represent the pre-industrial level. However, this method also removed the diurnal cycle of Fdf. Both in situ observations and modelling show that Fdf has a strong diurnal variation, with values typically ranging between 0.4 and 0.9 at different times of the day in clear-sky conditions (e.g. Iziomon and Aro, 1998). Given the strong nonlinearities in the system, it is important to keep the diurnal cycle of Fdf. To this effect we first tentatively constructed a pre-industrial climatological Fdf by averaging Fdf from volcano-free years during the 1901-1920 period (1901, 1904-1906, 1909, 1911, 1915-1920) at each gridbox and at each 6-hour time steps across years. Although this method retains the diurnal cycle of Fdf, it still smooths out the Fdf values by averaging Fdf across multiple years. As shown in Figure 4.2, such a volcano-free climatological Fdf has much smaller number of gridboxes with very sunny (Fdf<0.3) and completely cloudy (Fdf=1) conditions and a larger number of gridboxes with intermediate conditions. To circumvent this problem, we selected three years (1901, 1905 and 1916) whose global mean Fdf is close to that of the climatological reconstruction and we repeated the Fdf during the entire historical period for each of the three selected years in order to provide a realistic pre-industrial Fdf field

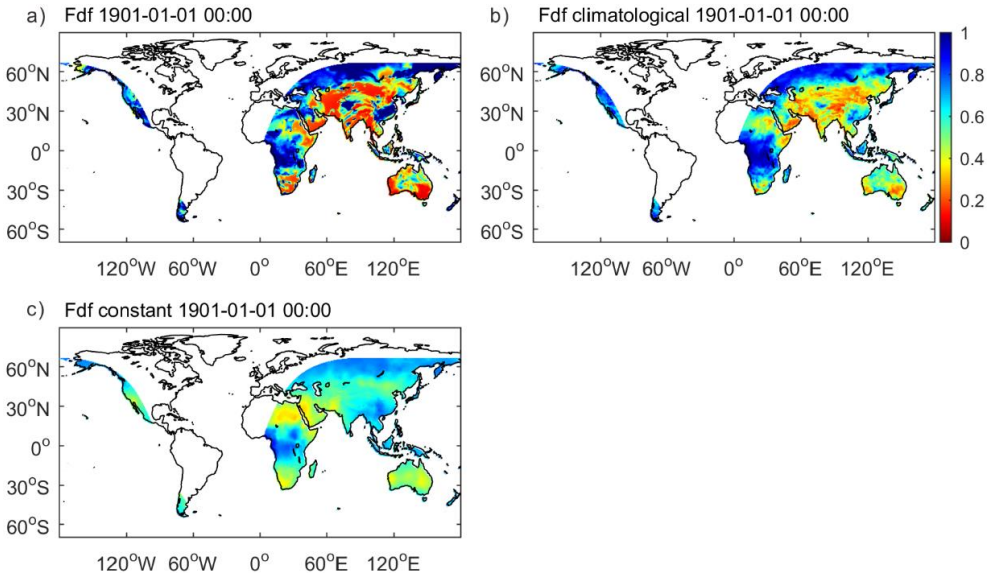

Figure 4.2 Comparison between Fdf processed with different methods at a selected time step. (a) original Fdf, (b) Fdf climatology *Df_clim*, from averaging each 6-hour value over 1901-1920 volcano-free years, (c) Fdf for *Df_cons*, averaged over all time steps over 1901-1920 volcano-free years (night time pixels masked on the plot for comparison)

for no aerosol simulations. To investigate the impact of smoothing the Fdf diurnal cycle, we also set up a simulation with Fdf averaged over all time steps.

4.2.2.2 IPSL simulations

IPSL-CM6A-LR is an Earth system model which consists of an atmospheric model LMDZ (v3554), an ocean model NEMO (v9455), a land surface model ORCHIDEE (trunk v5661) and a coupler (OASIS). As a model participating to the Coupled Model Intercomparison Project Phase 6 (CMIP6, Eyring *et al.*, 2016), IPSL-CM6A-LR ran a preindustrial control simulation (*piControl*) driven by constant external forcing representative of year 1850, after a long spin up. The historical climate fields are taken from the IPSL-CM6A-LR r1i1p1f1 (*historical)* simulation, which is one of the simulations performed for the 1850-2014 period driven by all natural and anthropogenic forcings and initialized from the 01-01-1910 state of the *piControl* simulation. From the same initial conditions of the *piControl* simulation, another simulation r1i1p1f2 (*histNoAA*) was performed by prescribing all the forcing terms the same as in r1i1p1f1 but keeping the anthropogenic aerosols at their pre-industrial level (1850).

The two simulations provide daily climate surface or near-surface variables including 2-meter maximum (Tmax) and minimum (Tmin) air temperature, Precip, SWdown, LWdown, Qair, Psurf, Wind_E and Wind_N. A similar method as described in Chapter 2 was used to correct the model biases in the above climate variables. Instead of using the CRUNCEP dataset as in Chapter 2, we used the CRUJRA v1.1 dataset as the reference. The aerosol information was obtained from the monthly tropospheric aerosol optical depth at 550 nm (od550aer) and monthly stratospheric aerosol optical depth at 550 nm (od550_STRAT) as used in the IPSL-CM6A-LR model. Because clouds change on short (sub-diurnal) timescales and have a strong impact on diffuse radiation, 3-hourly clt data is used. Due to the lack of observations of preindustrial aerosol and cloud properties and amounts, we did not perform the same bias-correction on aerosol and cloud fraction variables. All these variables which were originally provided on a 144×143 global grid were firstly re-gridded into a 2°×2° grid as model input, and interpolated to 30-min time steps in ORCHIDEE_DF.

For the IPSL simulations, to get equilibrated C pools, a spin-up simulation using the 1850-1859 bias-corrected climate from the historical climate (hereafter all IPSL climate refer to the bias-corrected climate if not specialized) was firstly performed for 400 years using the spin-up analytic mode of ORCHIDEE (Lardy *et al.*, 2011), which accelerates the spin-up procedure for slow soil carbon pools. After the spin-up, a set of experiments separating the impacts of anthropogenic aerosols were set up. The detailed information about the experimental design can be found in Table 4.2.

The *hist* and *NoAA* simulations were respectively driven by the full set of climate variables from the two CMIP6 simulations described above. The difference between the two simulations corresponds to the full impact of anthropogenic aerosols due to both their effects on climate and diffuse light fraction. As radiation, precipitation and temperature are the three most important factors controlling land carbon fluxes (Nemani *et al.*, 2003), we performed *NoAASW*, *NoAAprecip* and *NoAATair* simulations, which use *historical* climate but replace SWdown, precipitation and Tair fields, respectively, by that from the *histNoAA* scenario. These factorial simulations aim to investigate the relative contributions of the various aerosol effects originating from each one of these climate variables. It should be noted here that the difference between *hist* and *NoAASW* simulations represents the impacts of the aerosol-induced full change in solar radiation, including both quality and quantity. Beside these experiments, we also set up the

NoAARqlt simulation which used the same forcing as the *hist* simulation but recalculated the diffuse light fraction of the clear area of each grid box using the tropospheric AOD from the *histNoAA* simulation. This simulation is used to investigate the impacts of the Fdf change caused by anthropogenic aerosols alone. In the end, a simulation without volcanic aerosols (*NoVA*) was performed to investigate the volcanic impacts alone. It should be noted that the difference between *hist* and *NoVA* simulations includes only the impacts of the Fdf change from volcanoes but not the full climate impact caused by volcanic aerosols. All the simulations use the land use map updated every year from ESA-LUH2v2 dataset.

Table 4.2 Experimental design for the IPSL simulations.

Name	Forcing source							
	Tair	precip	SWdown	Tropospheric AOD (partition SW between clear and cloudy subgrid area)	clt	Tropospheric AOD (used to calculate diffuse SWdown in clear subgrid area)	Stratospheric AOD (almost same for *hist* and *NoAA*)	Other variables
hist	*hist*[1]	*hist*	*hist*	*hist*	*hist*	*Hist*	*hist*	*hist*
NoAA	*NoAA*[2]	*NoAA*	*NoAA*	*NoAA*	*NoAA*	*NoAA*	*hist*	*NoAA*
NoAASW	*hist*	*hist*	*NoAA*	*NoAA*	*NoAA*	*NoAA*	*hist*	*hist*
NoAAprecip	*hist*	*NoAA*	*hist*	*hist*	*hist*	*hist*	*hist*	*hist*
NoAATair	*NoAA*	*hist*	*hist*	*hist*	*hist*	*hist*	*hist*	*hist*
NoAARqlt	*hist*	*hist*	*hist*	*hist*	*hist*	*NoAA*	*hist*	*hist*
NoVA	*hist*	*hist*	*hist*	*hist*	*hist*	*hist*	*0 all the time*[*]	*hist*

* the stratospheric AOD values under most volcano-free cases are grouped into the same category as 0 in the look up table

1, 2 *hist* and *NoAA* in the forcing field of the table indicate *historical* (r1i1p1f1) and *histNoAA* (r1i1p1f2) on IPSL-CM6A-LR

4.3 Results

4.3.1 CRUJRA simulations

4.3.1.1 Diffuse radiation change

The evolution of historical Fdf derived from CRUJRA dataset (see data and method) is displayed in Figure 4.3. Generally, the global mean Fdf has three phases during the entire period covered by the dataset (Figure 4.3a). Before 1950, the mean Fdf varies around 0.62. During 1950-1980, the mean Fdf increases from 0.62 to 0.64 mainly in response to increasing anthropogenic aerosol emissions. After 1980s, the mean Fdf stays around 0.64. This stop of Fdf increase should be the total effect of decreasing aerosol emissions in Europe and the increasing aerosol emissions in East and South Asia (Figure 4.7). In addition to the three phases, notable spikes of Fdf of 0.02-0.04 above the baseline are found in years with strong volcanic eruptions, e.g. Santa Maria in 1902-1903, El Chichón in 1982, Mount Pinatubo in 1991. The spatial distribution of the Fdf difference between 1960-2010 and pre-industrial level is shown in Figure 4.3b. Generally, the higher aerosol emissions after mid-20th century cause a global increase in Fdf. The strongest Fdf increase is over 0.05, found in East Asia, South Europe, western Central Africa, West Amazon, East and West Australia. It should be noted that the strongest change in Fdf is not always found in regions where there are intense pollutions (e.g. Africa and Amazon have strong Fdf increase despite low anthropogenic aerosol emissions), nor the most polluted regions always have the strongest Fdf increase (e.g. East US). This might be due to the different distribution of

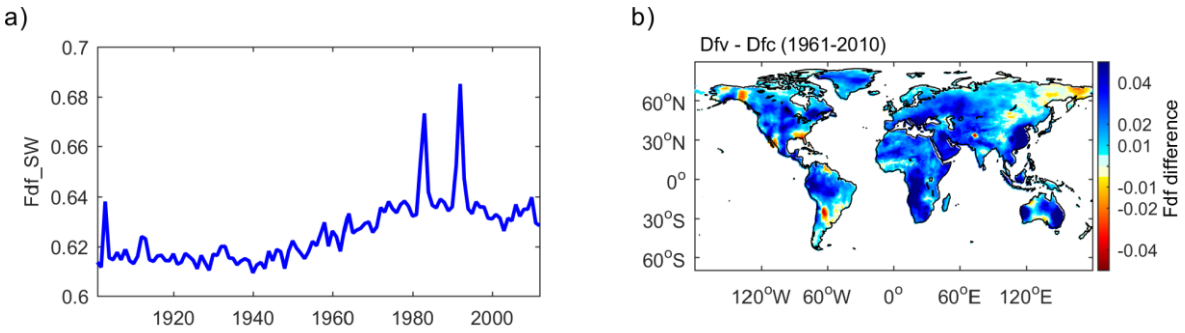

Figure 4.3 The diffuse SWdown fraction for CRUJRA simulations. (a) the evolution of global mean diffuse SWdown fraction; (b) the spatial distribution of diffuse SWdown fraction difference between *Dfv* and the reconstructed no aerosol (*Dfc*) scenarios (D*f_clim*, *Df_ens* and *Df_cons* share the similar mean Fdf) during 1961-2010.

cloud fraction between 1960-2010 and the preindustrial period.

4.3.1.2 Response of C fluxes

Figure 4.4 shows the global land GPP changes in response to changes in diffuse radiation fraction. Since the *Df_1901*, *Df_1905* and *Df_1916* simulations have very similar C fluxes, we use the average of the three simulations (*Df_ens*) for the analyses. Using Fdf reconstructed with different methods, we obtained a global mean GPP with similar interannual variation but dramatically different baselines (Figure 4.4). Compared with the *Dfv* simulation, the *Df_ens* generally shows a slightly smaller GPP (-0.7-0 PgC yr^{-1}) before 1950s. After 1950s, the *Df_ens* GPP surpasses the *Dfv* GPP and the difference between the two stays around 1-2 PgC yr^{-1} during the rest of the study period. The GPP difference between *Dfv* and *Df_clim* is generally 2 PgC yr^{-1} smaller than the difference between *Dfv* and *Df_ens*, while the difference between *Dfv* and *Df_cons* is even larger, with its value being around −14 PgC yr^{-1}. The large differences among *Df_ens*, *Df_clim* and *Df_cons* indicate a crucial impact of Fdf variations on GPP. Because of this difference in GPP, the *Df_clim* and *Df_cons* simulations respectively show 30 and 150 PgC higher cumulative net biome production (NBP) compared with *Df_ens* during the entire study period (not shown). As all the three simulations have similar mean Fdf as *Dfv* during 1901-1920, but only *Df_ens* has GPP not strongly biased from *Dfv*, we consider the *Df_ens* as the best simulation to

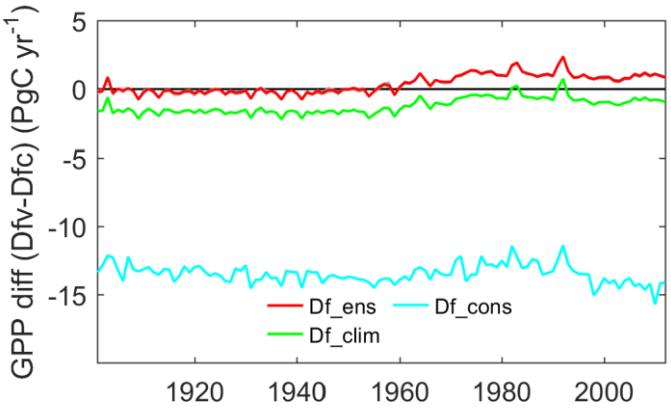

Figure 4.4 GPP difference between CRUJRA *Dfv* and different *Dfc* (no aerosol) simulations. The grey area behind the red line indicates the range of *Df_1901, Df_1905, Df_1916* simulations

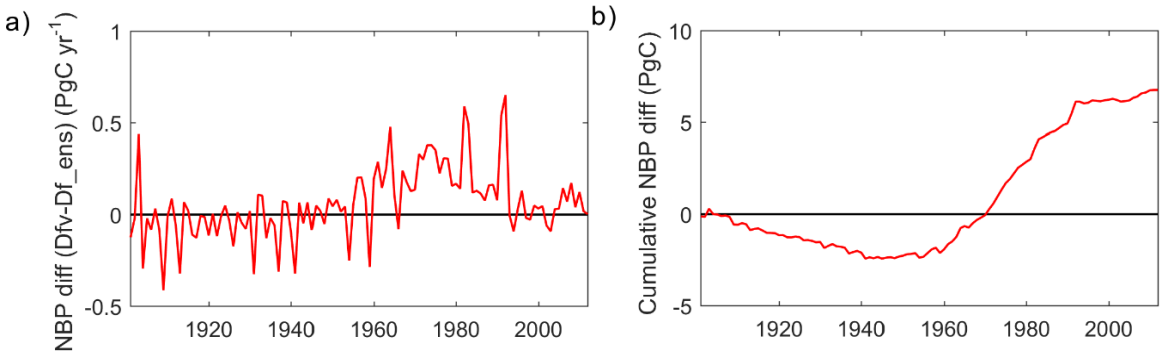

Figure 4.5 NBP difference between CRUJRA *Dfv* and *Df_ens*. (a) mean annual land NBP; (b) cumulative NBP since 1901

represent the preindustrial Fdf conditions and use the C flux from this simulation for further analyses.

The global NBP response to Fdf changes are shown in Figure 4.5. Similar to GPP, Fdf changes cause a small NBP decline (−0.05 PgC yr^{-1} on average) before the 1950s (Figure 4.5a). After the 1950s, the NBP response to Fdf changes becomes positive (stronger sink) and increases rapidly to about 0.4 PgC yr^{-1} in 1970s then declines to around 0 after 2000s. Cumulatively, the Fdf changes enhanced the global land C sink

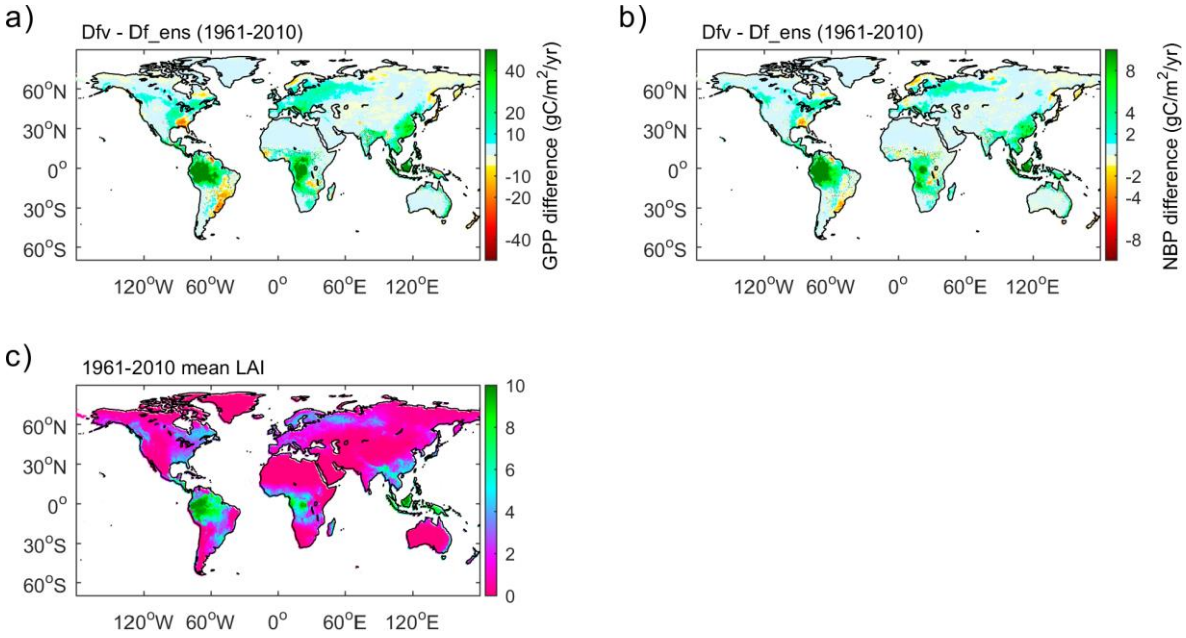

Figure 4.6 (a) the spatial distribution of Fdf change-caused GPP change during 1961-2010; (b) same as a but for NBP; (c) mean simulated LAI during 1961-2010

by 6.8 PgC during 1901-2012 (Figure 4.5b), accounting for 5% of the cumulative NBP during the same period.

The spatial distribution of the Fdf change-induced GPP and NBP changes are shown in Figure 4.6a, b. The signs of GPP changes generally match the pattern of Fdf difference between 1961-2010 and the pre-industrial period (Figure 4.3b ,4.6a), with most regions showing positive GPP responses to Fdf, except for Southeast US, Argentina and East Russia, where 1961-2010 Fdf is lower than the pre-industrial level. Despite this consistency in signs, a large Fdf increase does not always lead to strong GPP increase. For instance, regions with GPP enhanced by over 10 PgC yr^{-1} are mostly distributed in East and Southeast Asia, Europe, regions around the Great Lakes, Central Africa and West Amazon (Figure 4.6a), where Fdf increases by over 0.03 (Figure 4.3b). However, in West Asia, and East and West Australia, Fdf shows a comparable increase, while GPP shows only very small increase (Figure 4.6a). The NBP response to Fdf changes show a similar pattern as GPP (Figure 4.6b).

As the fertilization of diffuse radiation is considered to be through increasing the light received by the shaded leaves, the response of photosynthesis to Fdf changes should be also affected by the amount of shaded leaves. Since more shaded leaves are expected in deeper canopies (i.e. canopies with larger LAI), we investigated the distribution of LAI in Figure 4.6c. The regions with mean LAI larger than 4 are mainly found in East and Southeast Asia, Europe, eastern North America, Central Africa and Amazon, which happens to be the regions with strong GPP increase (Figure 4.6a). The regions with low LAI generally correspond to low GPP responses to Fdf changes.

Since East Asia, Europe and eastern North America are the most industrialized regions with intense aerosol emissions, we additionally investigated the evolution of Fdf and the GPP response in these regions (Figure 4.7). In East Asia, Fdf shows an increase from 0.62 to 0.64 after 1960s. In response, the Fdf-caused GPP change shows an increasing trend during the same period. The Fdf in Europe is on average higher than in East Asia due to the larger occurrence of large solar zenith angles at higher latitudes (Figure 4.7b). Apart from this difference, the European Fdf shows an increase during 1950-1980 and then a strong decline after 1980s. At the end of the study period, the average Fdf generally drops to the 1900s level. As a result, the Fdf-induced GPP change returns to zero after an increase of 0.15 PgC yr^{-1} during the period 1950-1980.

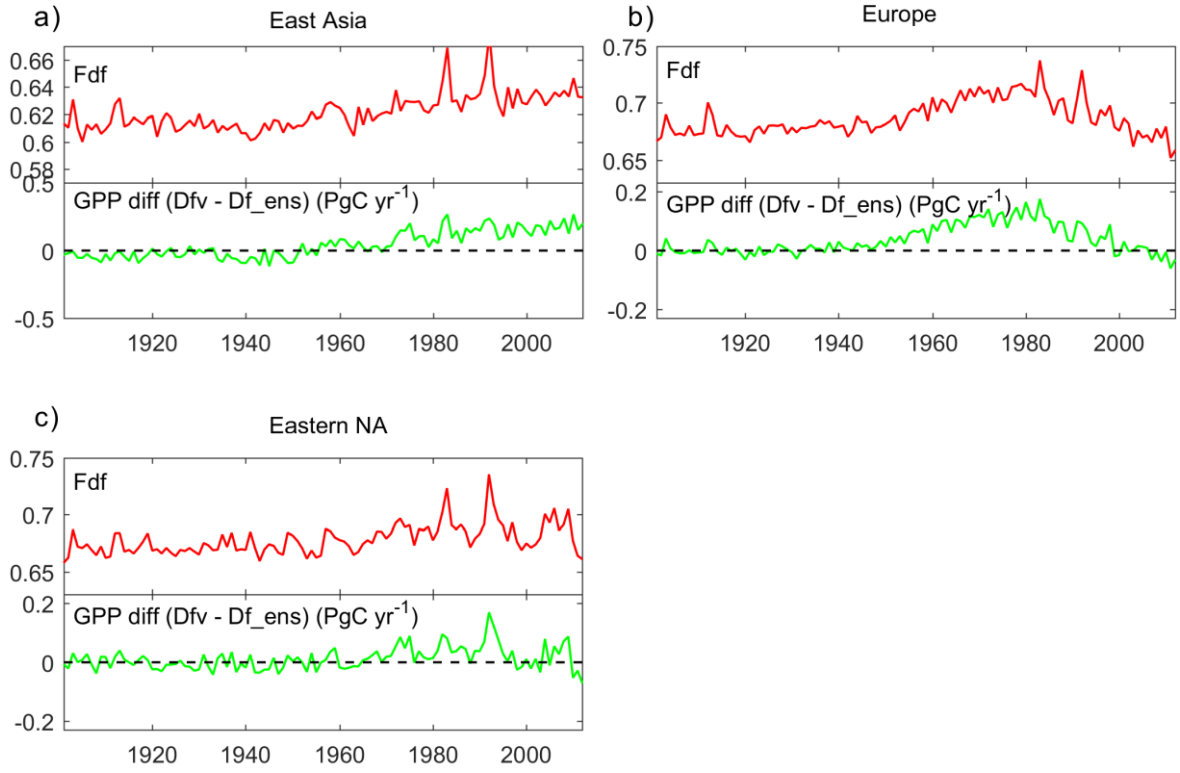

Figure 4.7 The evolution of Fdf for CRUJRA simulations and GPP response at main industrialized regions. (a) East Asia; (b) Europe; (c) Eastern North America

Compared with Europe and East Asia, the Fdf and GPP changes in Eastern North America are not very significant, probably due to its lower aerosol concentrations (Skeie *et al.*, 2011). Nevertheless, both Fdf and GPP changes are generally positive after 1970s (Figure 4.7c).

4.3.2 IPSL simulations

4.3.2.1 Aerosol-induced climate change

The variation of bias-corrected global land yearly mean climate from the IPSL-CM6A-LR *historical* and *histNoAA* experiments is shown in Figure 4.8. As the emission of anthropogenic greenhouse gases and aerosols did not significantly increase before the early part of the 20th century, during this period, the climate remains relatively stable and the two scenarios show no substantial difference. For both scenarios, the land mean temperature, precipitation and SWdown generally varies around 13°C, 800 mm yr^{-1} and 196 W m^{-2} respectively. The global tropospheric AOD

average over land stays around 0.1 before 1940, while cloud cover is around 51-52%. After 1950, as a result of the increased aerosol emissions (Figure 4.8d), the climate under the two scenarios starts to diverge. For Tair (Figure 4.8a), both *historical* and *histNoAA* Tair show an increase after 1950s. However, the Tair under *NoAA* scenario increases faster, resulting in 0.6 °C warmer climate during the last 2 decades compared with the *hist* scenario. This aerosol cooling effect is comparable to the one from IPSL-CM5A-LR simulations in Chapter 2. In terms of SWdown, a dimming effect is found along with the cooling from anthropogenic aerosols (Figure 4.8c). The *historical* SWdown decreases by about 3 W m^{-2} since 1950s, while the *histNoAA* SWdown shows no significant decrease during the same period. Compared with Tair and SWdown, no substantial differences are found on precipitation and cloud fraction between *historical*

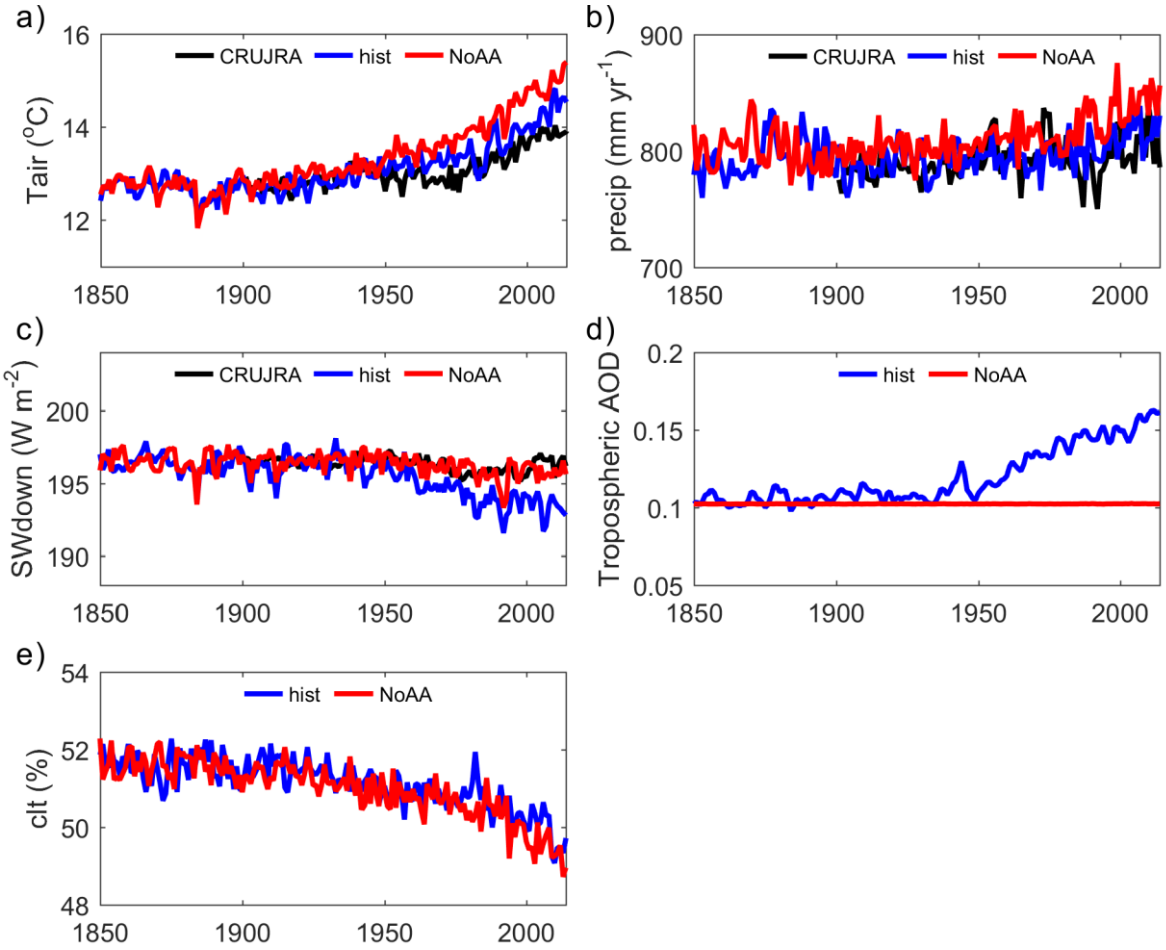

Figure 4.8 The bias-corrected climate over terrestrial regions from IPSL-CM6A-LR r1i1p1f1 (*historical*, blue lines) and r1i1p1f2 (*histNoAA*, red lines) simulations. The black lines show the reference from CRUJRA dataset. (a) air temperature; (b) precipitation; (c) downward shortwave radiation; (d) tropospheric AOD; (e) cloud fraction

and *histNoAA* scenarios.

The spatial distributions of the aerosol-induced climate changes are shown in Figure 4.9. For the consideration that *hist* and *NoAA* scenarios differ significantly only after 1950s regarding tropospheric AOD (Figure 4.8d), we take the period 1961-2010 to investigate the aerosol impact. The Tair from IPSL-CM6A-LR indicates a widespread cooling effect of anthropogenic aerosols over the land regions (Figure 4.9a) except western North America, where the mean Tair are not significantly different between the two scenarios. In contrast to the ubiquitously decreasing Tair, changes in aridity index (precipitation-potential evapotranspiration, P-PET, used in Chapter 2) is more heterogeneous (Figure 4.9a). A slight to medium drying effect of aerosols is found in Sahel, India, South China and eastern US. While in Argentina and the regions around Mediterranean, anthropogenic aerosols are found to decrease the aridity index. Compared with the IPSL-CM5A-LR climate in Chapter 2 (Figure 5b in Chapter 2), the IPSL-CM6A-LR climate does not show a strong drying effect due to aerosols in Amazonia.

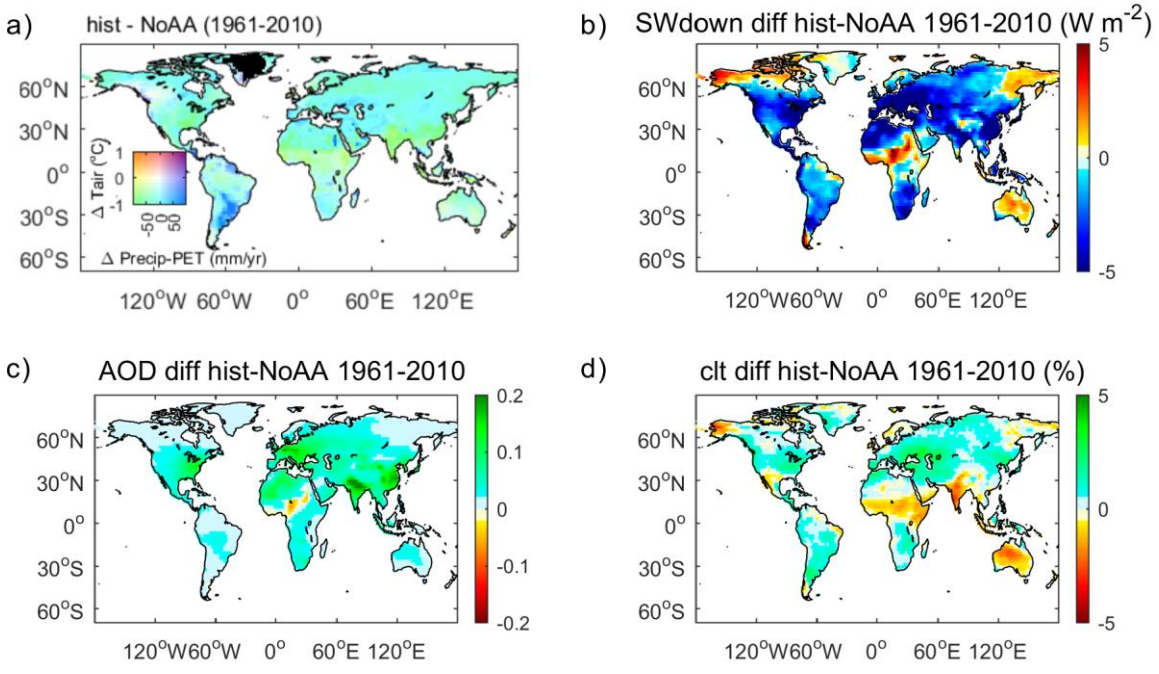

Figure 4.9 The spatial distribution of anthropogenic aerosol-induced climate changes (from IPSL-CM6A-LR) during 1961-2010. (a) changes in Tair and precipitation-PET; (b) changes in SWdown; (c) changes in tropospheric AOD; (d) changes in cloud fraction.

In terms of SWdown changes (Figure 4.9b), a dimming effect of anthropogenic aerosols is found in 78% of the global land regions. The magnitude of the dimming is generally 0-5 W m^{-2} except East Asia, Europe and East US, where the dimming is over 5 W m^{-2}. A 0-3 W m^{-2} brightening are found in North Canada, East Russian, Central Africa, India and Australia, corresponding to the regions where aerosol is causing a decrease in cloud fraction (Figure 4.9d).

As expected, the emission of anthropogenic aerosols causes an increase of tropospheric aerosol optical depth, with the largest increase found in the most polluted regions (East Asia, India, Europe and eastern US) (Figure 4.9c). It should be noted that the emissions of anthropogenic aerosols do not always increase tropospheric AOD. For instance, a higher tropospheric AOD is found in Central Africa under the *hist* scenario compared with the *NoAA* scenario (Figure 4.9c). This might be due to an altered aerosol distribution in response to the anthropogenic aerosol-induced atmospheric circulation changes.

4.3.2.2 Response of land C fluxes to aerosols at global scale

The evolution of GPP and total ecosystem respiration (TER) from different IPSL experiments are shown in Figure 4.10. All the experiments show a GPP increase from 123 PgC yr^{-1} in 1850 to about 164-168 PgC yr^{-1} in 2014 (Figure 4.10a). This GPP increase is most probably due to the fertilization effect of rising atmospheric CO_2 concentration. Despite this consistent trend, differences among simulations remain significant. Compared with the *NoAA* simulation, the *hist* simulation has lower GPP in most of the years before 1950, but higher GPP afterwards (Figure 4.10c), indicating that the response of GPP to changing anthropogenic aerosols has changed by the 1950s, when aerosol emissions became important (Figure 4.8). Before 1950, the GPP difference between *hist* and *NoAA* simulations is very similar to the impacts of only Tair (*hist-NoAATair*) (Figure 4.10c), while only changes in SWdown or precipitation from aerosols (*NoAASW* and *NoAAprecip* compared with *hist*) has small impacts on global GPP. This result indicates that the aerosol impact is dominated by temperature changes before 1950s, which is in line with the findings from Chapter 2. However, after the 1960s, the full aerosol impact (*hist-NoAA*) on GPP starts to deviate from the temperature-alone induced changes (*hist-NoAATair*) and becomes positive. This change should be related to the increasing impact of aerosol-induced SWdown changes, as the

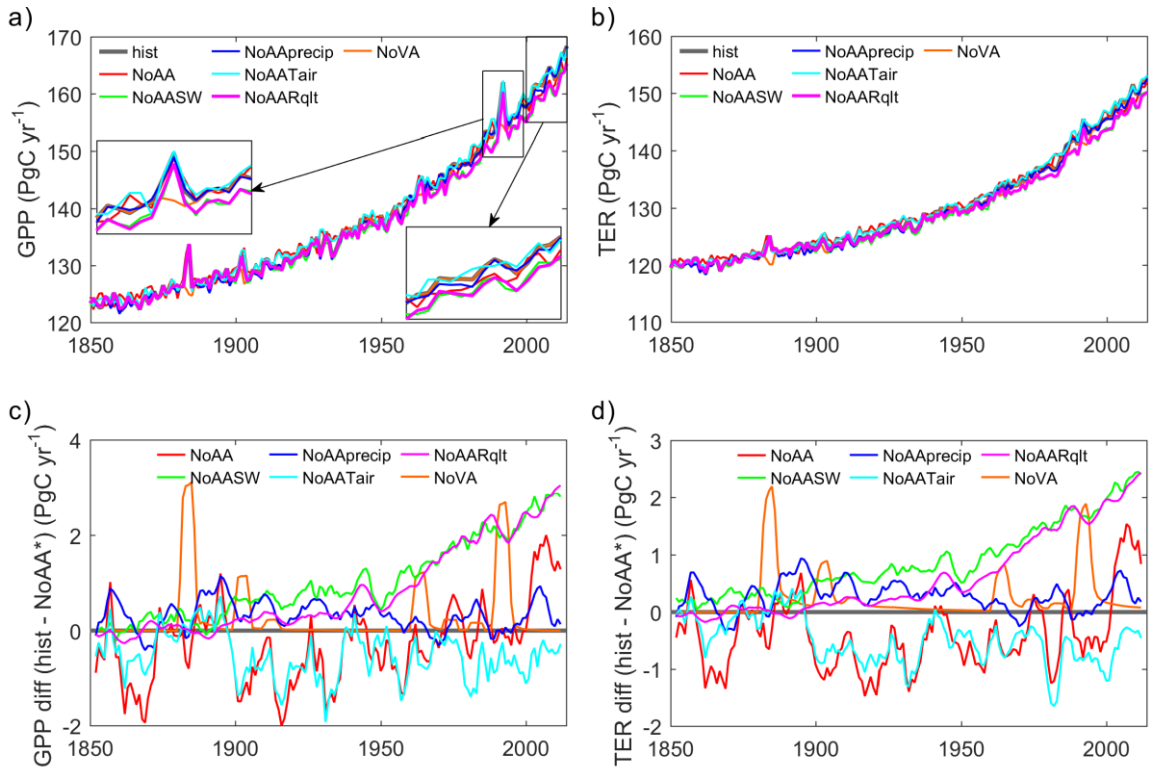

Figure 4.10 The evolution of total land GPP and TER from IPSL simulations. (a) GPP; (b) TER; (c) GPP difference between *hist* and different factorial simulations (NoAA*); (d) same as (c) but for TER. The differences (c and d) have been smoothed using 5-year windows to decrease the noise.

impact from aerosol-induced precipitation changes remains small but the GPP difference between *hist* and *NoAASW* simulation increases dramatically from <1 to 3 PgC yr^{-1} during this period. In addition, the *NoAARqlt* simulation shows very similar GPP than the *NoAASW* simulation, implying that the GPP change is more attributable to the change in radiation quality (diffuse radiation fraction) rather than quantity (dimming). By comparing GPP from *NoVA* and *hist* simulations, we are able to better understand the impact of the Fdf change caused by volcanic aerosols alone. For the years with strong volcanic eruptions, GPP increases of 5-10 PgC yr^{-1} can be found in all simulations except in *NoVA* (Figure 4.10a). This difference is generally larger than the slow varying and weaker impacts of anthropogenic aerosols, however, it lasts for a short time. The stratospheric AOD can increase by over 0.15 after large eruptions, which is larger than tropospheric AOD increase caused by anthropogenic aerosols. For years without volcanic eruptions, the *hist* and *NoVA* GPP are generally identical, as expected.

In terms of the TER, the global averages show similar increasing trend of TER among the factorial simulations (Figure 4.10b). From 1850 to 2014, the global TER increases from 120 to 150 PgC yr^{-1}. This increase should be a result of the increase in GPP, which provides more organic matter for respiration, and the increase in temperature, which accelerates the turnover of C pools. The difference in TER between *hist* and the other experiments shows very similar patterns as the difference in GPP (Figure 4.10c, 4.10d). Before the 1950s, anthropogenic aerosols cause a 0-1 PgC yr^{-1} decrease in TER mainly through their impact on temperature (cooling, causing a reduced GPP). While after the 1960s, a positive impact of aerosol-caused SWdown changes on TER is found and the total TER response to aerosols finally becomes positive after the 2000s. It should be noted that the impacts of volcanic aerosols on TER are smaller but last much longer than GPP. After each eruption, following a sudden increase, a gradual decline of TER can be found during the following 3-4 decades or until the next volcano eruption (Figure 4.10d).

The cumulative net biome production (NBP) since 1850 is investigated in Figure

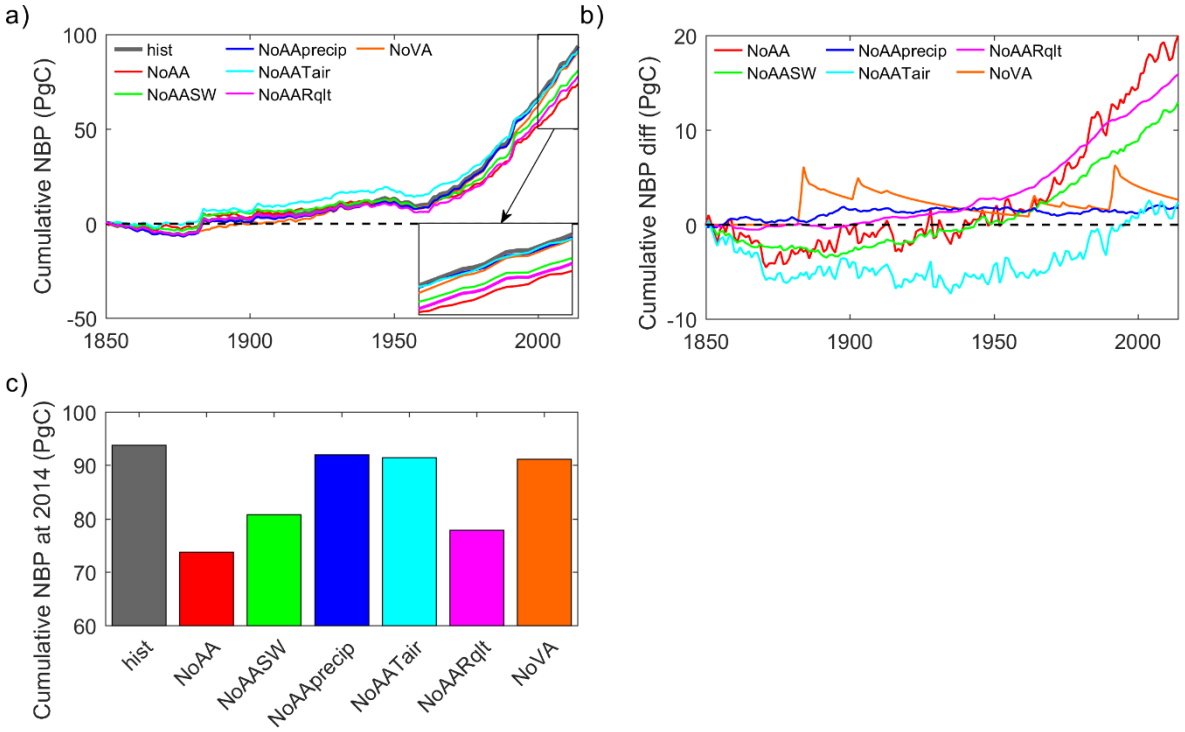

Figure 4.11 The cumulative land NBP from IPSL simulations. (a) cumulative NBP since 1850; (b) cumulative NBP difference between *hist* and different factorial simulations; (c) cumulative NBP at the end (2014) of each simulation.

4.11. All the simulations show a slight decline of cumulative NBP before 1880s. Then a slow increase in cumulative NBP is found between the 1880s to the 1950s. After the 1950s, the global land cumulative NBP increases rapidly from 10 to 70-90 PgC in 2014 (Figure 4.11a, 4.11c). This value is close to the trendy v7 S3 (historical) simulation performed with ORCHIDEE trunk (v5375) (not shown) and the historical simulation on JULES (Mercado *et al.*, 2009), but much larger than the simulations performed with the older version of ORCHIDEE trunk in Chapter 2 (v4220) (Figure 3 in Chapter 2), which generally showed a neutral cumulative NBP at the end of the simulation, more consistent with observational constraints of the land carbon budget (Khatiwala *et al.*, 2009). This large difference could result from the difference in parameters between the old (Chapter 2) and new model versions (this chapter) (Peylin *et al.*, in prep). In addition, the new versions of ORCHIDEE trunk and ORCHIDEE_DF use 15-PFT instead of 13-PFT maps as they separate C3 grasslands into tropical, temperate and boreal types. The difference in PFT maps may also contribute to the NBP difference.

Despite the large difference of cumulative NBP between the two versions of ORCHIDEE, the anthropogenic aerosol-induced NBP change (*hist-NoAA*) found in this chapter is similar to what we found in Chapter 2. At the end of the study period (2014), the *hist* simulation shows a 20.0 PgC higher cumulative NBP than the *NoAA* simulation (Figure 4.11c), indicating a net positive impact of anthropogenic aerosols on land C sink.

Besides the full impact of anthropogenic aerosols, we also investigated the impact of each environmental factor on cumulative NBP in Figure 4.11 by comparing the *hist* simulation and each factorial simulation. Compared with *hist*, the cumulative NBP from *NoAATair* simulation decreases before 1880s and stays around −6 PgC until 1950s (Figure 4.11b), indicating an aerosol-induced inhibition of land C sink during this period. After the 1950s, the impact of aerosol-induced Tair changes reversed and the difference in cumulative NBP increased to 2.3 PgC at 2014. This reversed unimodal curve implies that the impact of aerosol-induced temperature changes can be different during different periods, although it has overall enhanced the land C sink during the entire period.

Compared with the impacts of Tair, the impacts of precipitation on cumulative NBP (*hist-NoAAprecip*) show much smaller variations within 0-2 PgC during the entire study period (Figure 4.11b), indicating limited impacts of aerosol-induced precipitation

changes. In terms of radiation, the cumulative NBP differences between *hist* and *NoAASW* and between *hist* and *NoAARqlt* simulations show similar trends during the entire study period (Figure 4.11b). Before the 1950s, both the two factorial simulations have the cumulative NBP close to the *hist* simulation, indicating limited impacts of aerosol-induced radiation changes during this period. This small impact of radiation changes is not surprising as the anthropogenic aerosol-induced changes in light quantity and quality remain small (Figure 4.8c-e). After 1950s, along with the increasing aerosol emissions, dramatic increases in cumulative NBP difference between *hist* and both the *NoAASW* and *NoAARqlt* simulations are found (Figure 4.11b). Until 2014, aerosol-induced total radiation changes (*hist-NoAASW*) and diffuse light fraction changes (*hist-NoAARqlt*) enhance global land C sink by 12.9 PgC and 15.9 PgC, respectively. As the total radiation changes include changes in light quantity (value of SWdown), cloud fraction and diffuse light fraction, the aerosol-induced changes in light quantity and cloud fraction should have inhibited the land C sink by 3.0 PgC. Considering the full impacts of anthropogenic aerosols of 20.0 PgC, the changes in diffuse light fraction alone contribute to about 80% of the increase in land C sink.

Unlike anthropogenic aerosols, volcanic aerosols are emitted sporadically during years with large eruptions. In response, the immediate land C sink can surge by over 6 PgC depending on the intensity of the eruption (Figure 4.11b). It should be noted that these pulses do not disappear right after the periods during which the stratosphere is influenced by the volcanic eruptions. Instead, the cumulative NBP difference between *hist* and *NoVA* simulation retains some memory and relaxes slowly towards its pre-volcanic state during the following decades, at least until the next eruption takes place. In 2014, the diffuse radiation changes caused by volcanic aerosols cumulatively increased the land C sink by 2.7 PgC.

4.3.2.3 Response of land C fluxes to aerosols at different latitudes

As concluded in Chapter 2, different environmental factors may have different impacts on C fluxes in different latitudes. Here we investigate the regional difference in cumulative NBP between *hist* simulation and each factorial simulation in Figure 4.12. Similar to Chapter 2, anthropogenic aerosols on average increased the land C sink at low to mid latitudes, while decreased the C sink at high latitudes. These impacts are mainly contributed by the decades after the 1960s (Figure 4.12a, c, e, g).

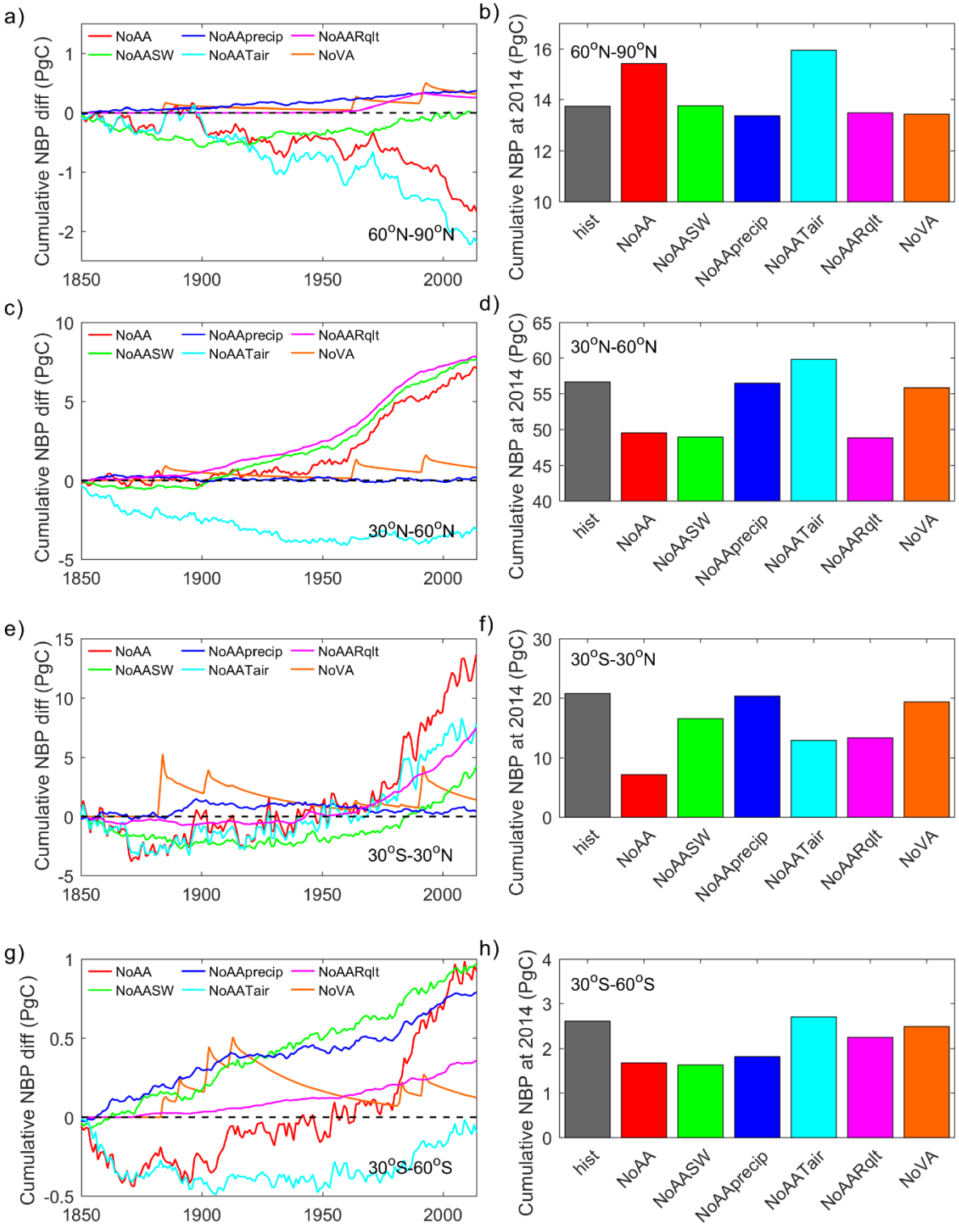

Figure 4.12 The cumulative land NBP from IPSL simulations in different latitudes. (a) differences in cumulative NBP between *hist* and each factorial simulations in 60°N-90°N; (b) cumulative NBP at the end (2014) of each simulation in 60°N-90°N; (c), (e) and (g) same as (a) but for 30°N-60°N, 30°S-30°N and 30°S-60°S respectively; (d), (f) and (h) same as (b) but for 30°N-60°N, 30°S-30°N and 30°S-60°S respectively

At the northern high latitudes, all factorial simulations except *NoAATair* show small cumulative NBP difference (<0.6 PgC) compared with *hist* simulation (Figure 4.12a, b), indicating small impacts of aerosol-induced radiation and precipitation changes in this region. In contrast, the temperature-alone changes from anthropogenic aerosols cause a remarkable decline in cumulative NBP (*hist-NoAATair*) over those temperature-limited ecosystems during the entire study period. This decline is small before the 1950s but becomes more pronounced afterwards, resulting in a 2.2 PgC lower cumulative C sink in the *hist* than the *NoAATair* simulation by 2014. The full impact of anthropogenic aerosols (*hist-NoAA*) shows very similar trend and interannual variation compared with the impact of aerosol induced temperature changes (*hist-NoAATair*), implying that anthropogenic aerosols are mainly causing a decline in C sink through their cooling effect in this region.

In contrast to the high latitudes, the northern mid latitudes show a positive impact of anthropogenic aerosols (*hist-NoAA*) on cumulative NBP (Figure 4.12c, d), despite the fact that those biomes are also limited by temperature, so that a cooling from aerosols alone decreases the NBP (*hist-NoAATair*). The positive impact of aerosols (*hist-NoAA*) is generally in line with the impacts exerted by SWdown (*hist-NoAASW*) or by only diffuse radiation fraction (*hist-NoAARqlt*), but slightly offset by the negative impact of aerosol-induced Tair changes (*hist-NoAATair*), indicating that the impact of aerosols in this region is mainly through the changes in light quality offsetting the effect of cooling. The difference between *hist* and *NoAAprecip* simulations remains small in this region. Until the end of the study period 2014, anthropogenic aerosols cumulatively increased NBP in this regions by 7.1 PgC. SWdown, Fdf and Tair respectively increased NBP by 7.7 PgC, 7.8 PgC and decreased NBP by 3.2 PgC.

Unlike the northern mid and high latitudes, where aerosol induced NBP changes are dominated by a single environmental factor, no single factor is found to explain the full impacts of anthropogenic aerosols at low latitudes (Figure 4.12e, f). In this region, the cumulative NBP differences between *hist* and each of *NoAA*, *NoAATair*, *NoAASW* and *NoAARqlt* simulations decrease in the first half of the study period and increase rapidly after the 1950s. Until 2014, the overall effect of anthropogenic aerosols increases the cumulative C sink in this region by 13.7 PgC, with changes in Tair, Fdf and SWdown explaining 7.8, 7.4 and 4.4 PgC, respectively. Note that in the tropics, cooling induced by aerosols has a positive effect on NBP as it reduced the evaporation

demand and allows more photosynthesis, unlike in the mid and high latitudes where biomes are mainly temperature limited. Compared with other variables, the impacts of aerosol-induced precipitation changes are small.

The impacts of aerosols in southern mid latitudes is smaller than in other latitudes as the land area in this region is relatively small (Figure 4.12g, h). Until the end of the study period, the anthropogenic aerosols enhanced the C sink by 0.9 PgC (*hist-NoAA*), which is close to the single impact of aerosol-induced SWdown changes (*hist-NoAASW,* 1.0 PgC) and precipitation changes (*hist-NoAAprecip,* 0.8 PgC). The changes in Tair cause a very small decline of cumulative NBP (0.5 PgC) before 1900 and an increase of C sink after 1960s. At the end of the period, the *hist* and *NoAATair* only has −0.1 PgC difference in cumulative NBP. It should be noted that unlike the other latitudes where the impact of radiation quality changes is larger than the full impacts of radiation changes, in this region, the cumulative NBP difference between *hist* and *NoAARqlt* is much smaller than that between *hist* and *NoAASW*. This is reasonable because the anthropogenic aerosol emissions are small in this region and have little impact on tropospheric AOD and thus diffuse radiation fraction (Figure 4.9c). In addition, the SWdown increased in a considerable proportion of the land area in this region in response to anthropogenic aerosol-induced cloud fraction changes (Figure 4.9b, d), this brightening may be responsible to the large difference in radiation impacts between this region and the other latitudes.

4.2.3.4 Spatial distribution of the aerosol impacts

Since the aerosol-induced fluxes changes mainly occur after 1950s, to further understand how it happens, we examine the detailed regional spatial patterns of GPP and NBP differences between *hist* and each factorial simulation during 1961-2010 in Figures 4.13 and 4.14.

The full impacts of anthropogenic aerosols on GPP generally show a latitudinal pattern (Figure 4.13a), with most regions in low latitudes experiencing a positive impact of anthropogenic aerosols and most mid to high latitude regions a negative impact, except for East Asia, eastern US and Europe, where the most pronounced tropospheric AOD increases in response to anthropogenic aerosol emissions are found (Figure 4.9). The strongest negative GPP decrease in response to aerosols are found in central and western US and northern Russia, with a magnitude < −50 gC m^{-2} yr^{-1}.

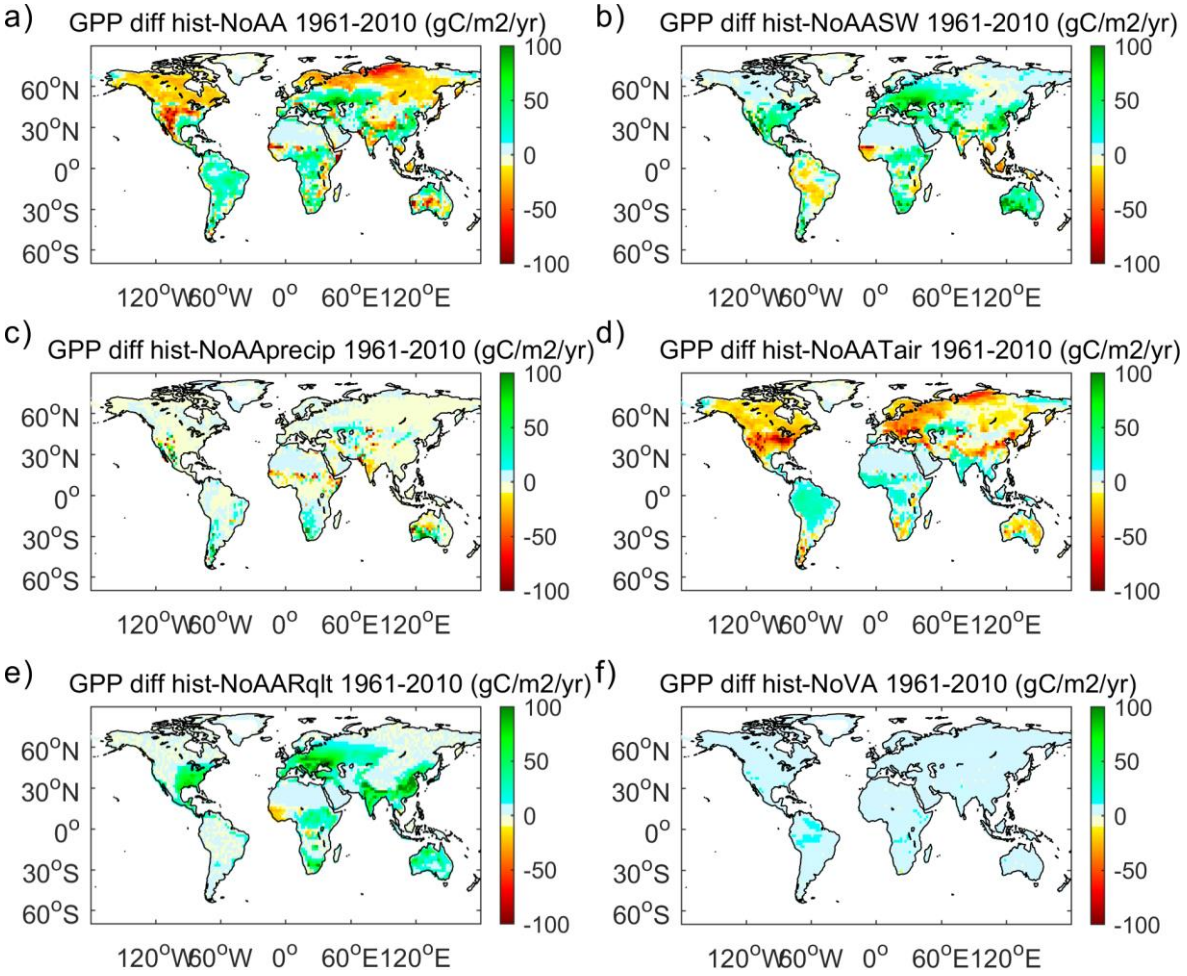

Figure 4.13 The spatial distribution of GPP difference between IPSL *hist* and each factorial simulations during 1961-2010.

The impacts of aerosol-induced Tair changes show a similar latitudinal pattern as the full aerosol impacts (Figure 4.13d), i.e. a decreased GPP at mid to high latitudes and an increased GPP at low latitudes. In contrast to the full impacts of anthropogenic aerosols, the Tair changes alone from aerosols generally decreased GPP in East Asia, eastern US and Europe. In contrast to Tair, aerosol-caused precipitation changes have relatively small impacts on GPP in most regions (Figure 4.13c). In over 85% of the land area, the precipitation changes cause less than 10 gC m^{-2} yr^{-1} changes (generally <1%) in GPP. Nevertheless, in dry regions like the Sahel and Central India, GPP decreases significantly in response to aerosol-induced precipitation changes (Figure 4.13c), which partly explains the total aerosol-induced GPP decline in these regions (Figure 4.13a). The impact of radiation (Figure 4.13b, e) changes translates into a spatial pattern strongly related to the aerosol emissions (Figure 4.9c). Both *NoAASW* and *NoAARqlt*

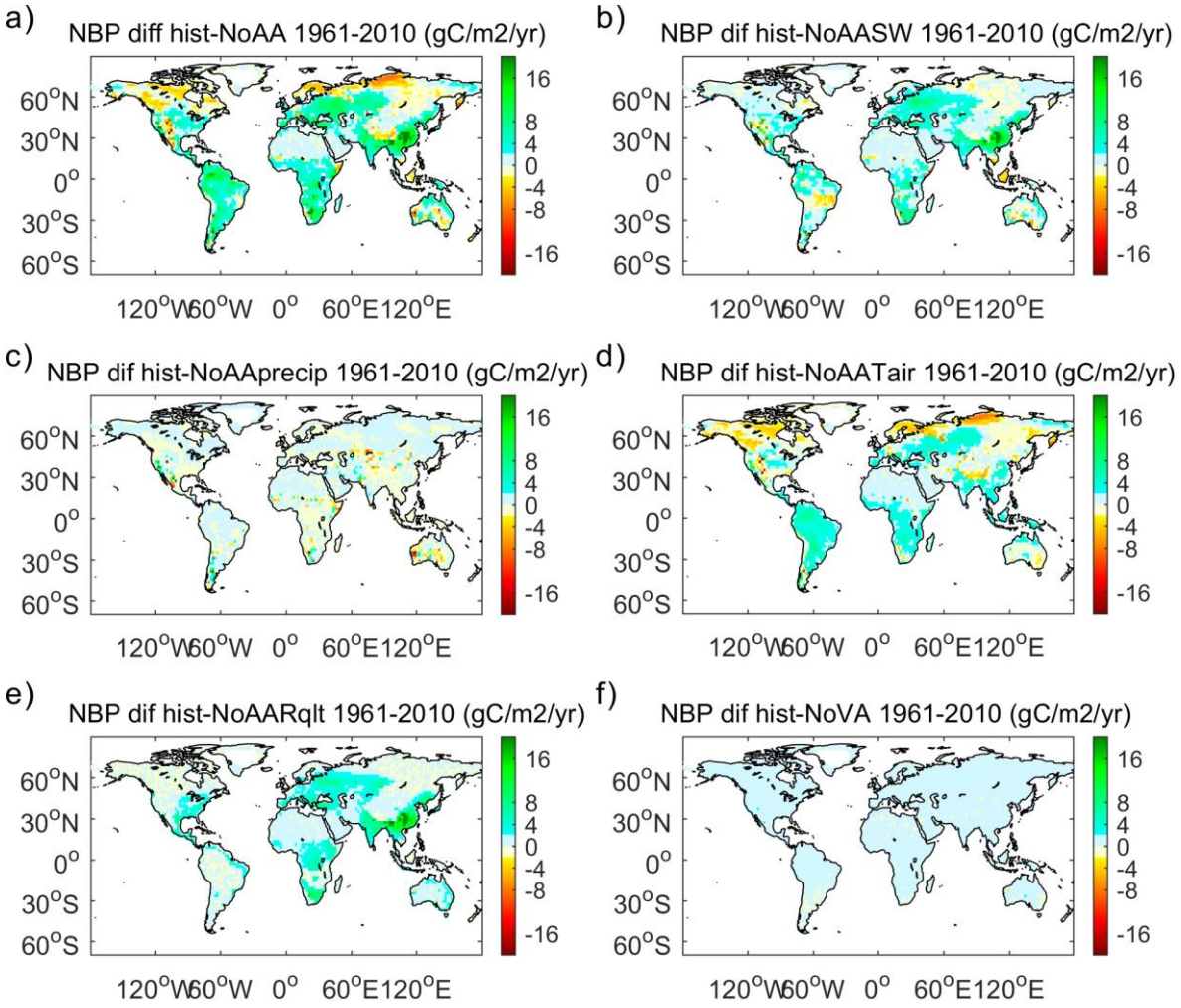

Figure 4.14 Same as Figure 4.13 but for NBP.

have over 50 gC m^{-2} yr^{-1} higher GPP than *hist* in the most polluted regions, i.e. East Asia, eastern US and Europe. Despite of this similarity, only light quality changes caused by anthropogenic aerosols result in an increase of GPP in India and Southeast Asia, and no significant GPP changes in Amazon (Figure 4.13e), while when additionally considering the changes in light quantity (mainly dimming) and cloud fraction, GPP in these regions shows a decreasing response (Figure 4.13b). This difference implies that many low-latitude ecosystems are light-limited as suggested by Nemani *et al.* (2003). In these regions, aerosol induced radiation quantity change may play a more important role than the diffuse radiation fraction increase. Compared with anthropogenic aerosols, volcanic aerosols have limited impacts on GPP on longer time scales (Figure 4.13f).

The NBP response to anthropogenic aerosols generally shows a similar pattern as

that of GPP, with a positive response in low latitudes and a negative response in high latitudes (Figure 4.14a). Compared to GPP, the area of NBP decrease in mid and high latitudes is much smaller. Large regions in North America and in Russia show negative impacts of anthropogenic aerosols on GPP but positive impacts on NBP (Figures 4.13a, 4.14a). These patterns are in line with the Tair change-induced C flux changes (Figures 4.13d, 4.14d), leading to the same finding as in Chapter 2, i.e. at the mid latitudes, aerosol-induced cooling enhances the regional land C sink by decreasing more respiration than photosynthesis. In contrast to temperature, that has strong impacts on heterotrophic respiration, the aerosol-induced radiation changes do not directly alter respiration. Not surprisingly, the spatial pattern of radiation change-induced GPP and NBP changes are similar (Figures 4.13b, e, 4.14b, e). NBP is found significantly increased in response to the radiation changes in forested regions with high aerosol emissions such as East and South Asia, eastern US and Europe. The responses of NBP to aerosol-induced precipitation changes and volcanic aerosols are small on the 50-year time scale (Figure 4.14c, f). At shorter time scales, the large pulses of sink induced by volcanoes are more distributed in tropics (Figure 4.12).

4.4 Discussion

4.4.1 Fdf response to anthropogenic aerosols

It has been widely accepted that increasing anthropogenic aerosol emissions can cause an increase in Fdf, as the result of the scattering of aerosols. This effect is generally confirmed in this study by the CRUJRA-based Fdf dataset (Figure 4.3). In the lookup table used for the Fdf calculation using IPSL-CM6A-LR data, Fdf also highly depends on aerosol optical depth. However, it should be noted that Fdf depends not only on anthropogenic aerosols but also on natural aerosols and clouds, which might be affected by the climate changes attributable to anthropogenic aerosols. For instance, although the global average clt is not very different between IPSL-CM6A-LR *historical* and *histNoAA* scenario, the IPSL-CM6A-LR *historical* clt is significantly lower than the *histNoAA* clt in tropical Africa, South Asia and Australia, and higher in mid latitudes (Figures 4.8e, 4.9d). This difference might be due to a wider *historical* Hadley circulation than *histNoAA* as the *historical* climate is warmer (Hu *et al.*, 2018). Nevertheless, our understanding of how climate and aerosols influence local and global

cloud cover is very poor. And the uncertainty in clouds remains one of the greatest uncertainties in current climate model (Stocker *et al.*, 2013). Better understanding of cloud physics and greater ensembles of earth system models would help to reduce this uncertainty.

4.4.2 Methods to reconstruct NoAA Fdf

One of the major difficulties in understanding the global impacts of anthropogenic aerosols on C cycle is the absence of observations under *NoAA* conditions. In the CRUJRA simulations, we omitted the evolution of cloud fraction and assumed that the *NoAA* scenario retains the preindustrial Fdf level. We used three methods to reconstruct the Fdf field. Although the three methods share similar mean Fdf at each pixel, their different variabilities result in totally different C fluxes (Figure 4.4). In natural conditions, Fdf is strongly affected by solar zenith angle as different solar positions correspond to different atmospheric optical paths. Generally, the Fdf is higher in the morning and afternoon, and lower at midday (e.g. Iziomon and Aro, 1998). The average over time steps longer than one day dampens this diurnal cycle, causing an underestimation of Fdf in the morning and afternoon and an overestimation at midday. Since Fdf has different impacts on photosynthesis at different times in the day and at different SWdown levels (Chapter 3), the smoothing of Fdf will strongly bias the C fluxes (*Df_cons* in Figure 4.4).

In contrast to the *Df_cons* reconstruction, the *Df_clim* forcing conserves the diurnal and seasonal variations of Fdf. However, it still results in a biased GPP. In general, due to the concurrence of aerosol/cloud scattering and absorption to solar radiation, the Fdf is negatively related to SWdown (Spitters *et al.*, 1986; Weiss and Norman, 1986). When we use average Fdf values to calculate the *Df_clim*, we artificially cause a non-physical unrealistic mismatch between Fdf and SWdown, i.e. increase the sunny Fdf and decrease the cloudy Fdf. This mismatch further causes mismatches between Fdf and other environmental factors such as temperature and water vapor pressure deficit.

For the reason given above, the mismatch between Fdf and SWdown is unavoidable if one of them is controlled. Nevertheless, it seems that if no smoothing is applied for the Fdf data (*Df_ens*), the GPP will not be too strongly biased. To address

this concern, we recommend to use ensemble simulations with unsmoothed Fdf from different years, rather than an averaged climatological Fdf to represent a constant-emission scenario when Fdf observations are absent. In a previous study, Mercado *et al.* (2009) estimated that the aerosol-induced diffuse light enhanced the global land NBP by a quarter between 1960 and 1999. This result should be treated with caution as their simulation used monthly smoothed Fdf.

4.4.3 Global impacts of diffuse radiation on C fluxes

The impact of anthropogenic aerosol-induced Fdf changes have been explored using two sets of simulations in this study. Globally, both the CRUJRA and IPSL simulations show enhanced GPP (1-2 PgC yr^{-1} and 1-3 PgC yr^{-1}, respectively, in late 20th century) in response to the Fdf changes (*Dfv-Df_ens*, *hist-NoAARqlt*). Although these increases in GPP are only 1-3% of the global total GPP, they result in enhanced land C sink (NBP) of 6.8 PgC since 1901 for CRUJRA and of 15.9 PgC since 1850 for IPSL. These NBP increases are significant as they account for about 5% (CRUJRA) and 17% (IPSL) the cumulative global land C sink during the same period. The enhanced land C sink indicates that the diffuse radiation fertilization effect reported at flux sites (Gu *et al.*, 2003; Niyogi *et al.*, 2004; Mission *et al.*, 2005; Alton, 2007a; Knohl and Baldocchi, 2008; Oliphant *et al.*, 2011; Kanniah *et al.*, 2013; Williams *et al.*, 2014; Cheng *et al.*, 2015) has considerable global impacts under a scenario with intense aerosol emissions. Mercado *et al.* (2009) used JULES to investigate the impacts of Fdf changes on land C sink and reported an increase of C sink of 0.44 PgC yr^{-1} during 1960-1980 and 0.3 PgC yr^{-1} during 1980-1999. Compared with their estimation, our simulations give near half of their NBP enhancement due to Fdf changes during the same period (0.24 and 0.17 PgC yr^{-1} for CRUJRA, 0.23 and 0.21 PgC yr^{-1} for IPSL). As climate field of both studies are generally observationally-based or bias-corrected with observations, this difference of Fdf impacts between JULES and ORCHIDEE_DF may be due to different parameterizations of the two land surface models, but also to different ways used for constructing *NoAA* Fdf series as discussed above.

4.4.4 The impacts of Radiation quality vs Radiation quantity

One of the key questions on the aerosol impacts is whether the effect of increased

diffuse radiation offsets the effect of decreasing total radiation (dimming). By investigating the C fluxes at different AOD levels, Niyogi *et al.* (2004) found that higher AOD increases C sink at forest and cropland sites but decreases C sink at grassland sites. This might be explained by the different canopy architecture of different ecosystems as more leaves are shaded in canopies with larger LAI (e.g. forests, croplands). As a result, a higher diffuse radiation can cause a larger increase in photosynthesis rate in these ecosystems. In contrast, grasslands often have smaller LAI and the fertilization effect from diffuse radiation increase is thus much weaker. In an extreme case, imagine a canopy with only one layer of leaves, all leaves should be sunlit and increase diffuse radiation will give no benefits to GPP. However, in all these cases the dimming effect of aerosols will always inhibit photosynthesis. In this study we also found that large C sink increase are only found in regions with large LAI (Figure 4.6).

Apart from LAI, the total radiation impacts (quality and quantity) is suggested to also depend on whether the diffuse radiation is from the scattering of aerosols or clouds, as the later media is thought to be less conservative regarding total downward shortwave radiation (Alton *et al.*, 2008). This effect is implicitly considered in the IPSL simulations where photosynthesis was calculated in subgrid fractions with and without clouds.

Using *NoAASW* and *NoAARqlt* we are able to separate the effect of changes in light quantity and light quality. Our results show that globally, the fertilization from aerosol-induced diffuse radiation increase is stronger than its dimming effect and dominates the radiation change-caused C flux changes. Some exceptions are found in tropical forests where the amounts of anthropogenic aerosols are relatively small (Figure 4.9) and the forests are light limited, therefore the dimming-caused GPP decline dominates.

4.4.5 The main factors causing C flux changes

In Chapter 2 we found that the increase of the land C sink in response to anthropogenic aerosols is mainly due to their cooling effect, which enhances tropical GPP and causes a stronger decline in TER than in GPP in mid latitudes. In this study, although the increased global land C sink due to aerosol-induced cooling is much smaller than in Chapter 2, the latitudinal pattern of cooling-caused C flux changes are

similar in the late part of the 20th century (Figures 4.13, 4.14) compared with Chapter 2. Before the 1950s, the aerosol-induced cooling is small in tropics but much larger at mid to high latitudes (Figure 4.15), which explains the decrease in global land C sink during that period. The similar impacts of cooling on GPP and NBP further confirmed the validity of the statistical method used in Chapter 2 to attribute aerosol impacts to different factors.

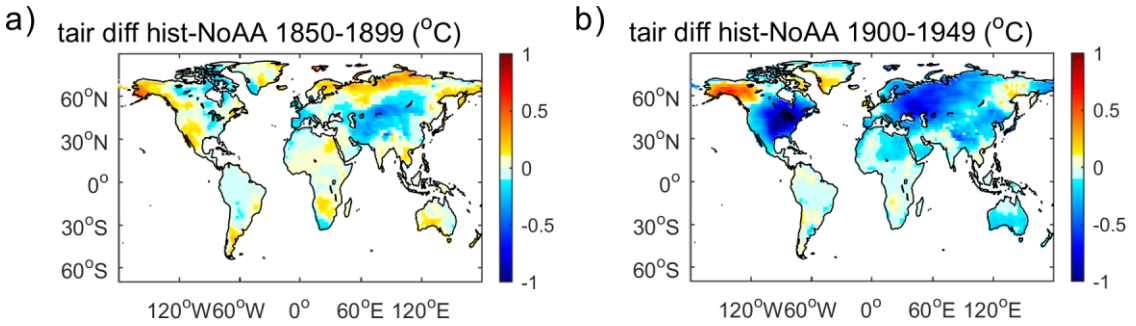

Figure 4.15 The impacts of aerosol-caused Tair changes during (a) 1850-1899 and (b) 1900-1949.

Compared with temperature, the impacts from changing precipitation (Figures 4.13, 4.14) are generally small. However, as shown in Chapter 2, if anthropogenic aerosols have strong drying effect in very productive tropical regions, it can strongly affect regional C budget. In IPSL-CM6A-LR climate, aerosol-induced drying is mainly found in the Sahel region and in South Asia. In response, the GPP in these regions is smaller in *hist* than *NoAAprecip* simulation. This regional change has limited impact on the total C fluxes. Nevertheless, the modeled precipitation impacts should be always treated with caution because the response of precipitation to aerosols remains very uncertain in current earth system models (see Chapter 2).

According to Chapter 2, the aerosol-induced dimming has limited direct impacts on land C fluxes as most land ecosystems are temperature or precipitation limited rather than radiation limited (Nemani *et al.*, 2003; Piao *et al.*, 2009). Our results in this chapter indicate a larger contribution of aerosol-induced radiation changes than temperature to global NBP changes (Figure 4.11), which seems to contradict the conclusion in Chapter 2. However, if we further decompose the overall radiation change into quality and quantity changes, we found that the large NBP increase from radiation changes of this chapter is mainly attributed to aerosol-induced light quality changes (increased diffuse

light) (Figure 4.11). The aerosol-induced light quantity changes (dimming), which is generally equivalent to the radiation changes investigated in Chapter 2, are still found to slightly decrease the GPP and NBP in intensely polluted regions (Figure 4.16). However, this dimming-induced decrease is not comparable in magnitude to neither the impacts of light quality changes, nor to those of temperature changes (Figure 4.13, 4.14).

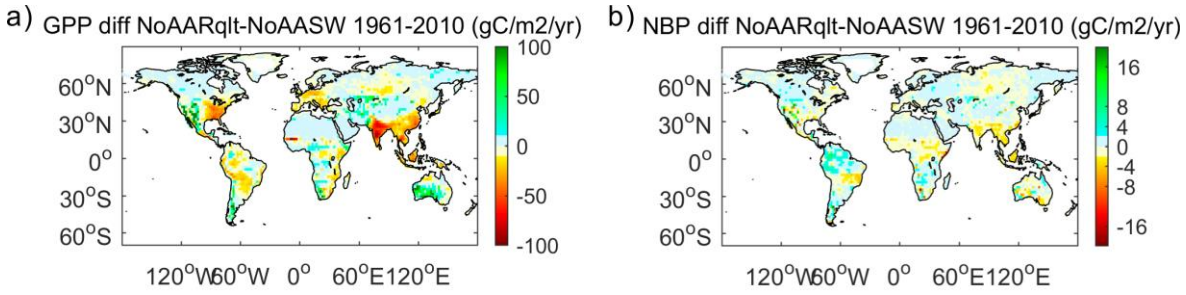

Figure 4.16 The impacts of aerosol-caused light quantity changes (dimming) during 1961-2010 on (a) GPP and (b) NBP.

4.4.6 The impacts of volcanoes

Volcanoes are a very important source of atmospheric aerosols and they have been reported to significantly enhance GPP at the site level due to their impact on Fdf (Gu *et al.*, 2003). However, at the global scale, there remain no reliable observations available to investigate the impacts of volcanic aerosols. The eruption of Mount Pinatubo is covered by several atmospheric inversion C flux datasets (e.g. Rödenbeck *et al.*, 2003), but it is difficult to separate the aerosol impacts from the impacts of climate variations, especially when an El Nino event occurred right after the eruption. Based on models, the eruption of Mount Pinatubo is estimated to have induced an increase in land C sink of 1-2.5 PgC yr^{-1} in the 1-2 years right after the eruption, which is suggested to be strongly contributed by the Fdf changes caused by the volcanic aerosols (Roderick *et al.*, 2001; Mercado *et al.*, 2009). In this study, our CRUJRA simulations show an enhanced NBP of 0.6 PgC yr^{-1} in response to Mount Pinatubo eruption and about 0.5 PgC yr^{-1} in low latitudes in response to other large eruptions (Santa María and El Chichón). The IPSL simulations show a sudden increase of global land NBP of 3.2 PgC yr^{-1} in response to the aerosols emitted by Mount Pinatubo and about 1.2 PgC yr^{-1} in response to Santa María and El Chichón. This volcanic aerosol impacts from IPSL simulations partly explained the observed drop of atmospheric CO_2 growth rate after

the eruption and are generally in line with the previous estimations (Roderick *et al.*, 2001; Mercado *et al.*, 2009). The smaller impacts detected in the CRUJRA simulations is probably due to a mismatch between climate and the directly-used preindustrial Fdf. It should be noted that in both CRUJRA and IPSL simulations we only considered the change in diffuse radiation fraction in response to volcanic aerosols, but did not included the cooling and dimming caused by volcano eruptions.

Because volcanic aerosols have a strong cooling effect on global land surface temperature through reducing the solar radiation, stratospheric aerosol injection technique, which mimics the eruption of volcanoes, has been proposed as a possible geoengineering technique to mitigate global warming (Boucher *et al.*, 2013). Proposed strategies often keep injecting aerosols to keep the stratospheric aerosols at a high level (i.e. Tjinputra *et al.* 2016), in order to keep a low surface temperature. In this study, we found that the impact of such a sudden change in stratospheric aerosols have persistent impacts on land C budget after 3-5 decades (Figure 4.11), implying that the stratospheric aerosol injection technique may have a long-term atmospheric carbon dioxide removal consequence. This effect needs to be considered when evaluating current geoengineering strategies.

4.4.7 Uncertainties

In this study we obtained consistent results that aerosol-induced diffuse radiation changes enhances the land C sinks using two sets of simulations. However, each of the simulation set has their own limitations.

For CRUJRA simulation, we investigated different methods to construct the Fdf under *NoAA* scenarios and found a very large bias if the Fdf is smoothed (Figure 4.4). To avoid this error, an ensemble with three members that can represent the preindustrial level Fdf was used. Nevertheless, there remains uncertainty because the Fdf for *Df_ens* simulations do not match well the climate, especially SWdown, in years other than 1901, 1905, 1916. The impact of this mismatch is still difficult to estimate.

In contrast to CRUJRA simulations, the IPSL simulations used consistent climate and Fdf-related variables from the *histNoAA* coupled simulation. Therefore, there should not be large errors from the mismatch between Fdf and radiation. Nevertheless, due to the lack of aerosol type information to well match the look-up table, we have to

assume a single type of aerosol in each region, which might introduce some uncertainty in the Fdf. Apart from this uncertainty, as shown in Chapter 2, the uncertainty in aerosol-induced climate changes, especially precipitation changes, can also potentially cause large uncertainty in the C fluxes. However, the *histNoAA* is not a mandatory experiment in CMIP6, few models have performed it. Also, not all CMIP6 data have been archived currently. It remains difficult to quantify the uncertainty in this effect from a multi-model perspective at this moment.

Besides the forcing field, uncertainties may also come from the land surface model. In this study we used ORCHIDEE_DF to investigate the Fdf and climate effects. Although the climate impacts detected here have similar spatial pattern as those discussed in Chapter 2, the magnitude of C flux response to the aerosol-caused cooling is different. This implies that the use of multiple models to assess the impacts of aerosols on the carbon cycle is needed. Furthermore, the ORCHIDEE_DF model includes no nutrient limitation on vegetation growth, which means that the nutrients deposition along with the deposition of aerosols are not possibly considered in our simulations. It has been suggested that N deposition can be a main factor causing land C sink in some ecosystems (e.g. Magnani *et al.*, 2007). Understanding how this effect interacts with aerosol-induced climate and Fdf still require land surface models with more complex processes.

4.5 Conclusion

In this study we used two sets of simulations with ORCHIDEE_DF using CRUJRA and IPSL-CM6A-LR climates to investigate the impact of anthropogenic aerosols-induced Fdf and climate changes on terrestrial C fluxes. The two sets of simulations find an enhanced cumulative land C sink of 6.8 PgC and 15.9 PgC in response to the anthropogenic aerosol-caused Fdf changes during the historical period and this enhancement mainly occurs after the 1950s. The spatial distribution of the magnitude of Fdf fertilization depends on both the aerosol emissions and the canopy structure of the vegetation.

According to the factorial simulations driven by IPSL climate, we conclude that globally, the anthropogenic aerosol-induced Fdf changes cause a stronger enhancement of photosynthesis than the reduction due to aerosol-caused dimming, leading to an

overall positive impact of aerosol caused radiation changes (quality and quantity). The aerosol-caused diffuse radiation changes, along with the temperature changes (cooling), explain most of global C sink increase. The cooling impact detected in this study generally follows the same spatial pattern detected in Chapter 2. i.e. decreased GPP and NBP at high latitudes and increased GPP and NBP at low latitudes. At mid latitudes, cooling causes a decline in both GPP and TER, but its impact on NBP depends on region and time.

Apart from these results, we also found that the different methods to reconstruct the Fdf series under no aerosol scenario have dramatic impacts on the results. To avoid the error, we suggest to use methods that keep the natural variability of Fdf to investigate the diffuse light impact at large scale.

Chapter 5. Conclusion and perspectives

In summary, from the starting point that the current understanding of the impacts of anthropogenic aerosols on the carbon cycle is poorly understood, which hinders a reliable projection of future climate and makes it difficult to evaluate the full climate impacts of possible aerosol emission policies, this thesis includes a series of studies quantifying and attributing the impacts of anthropogenic aerosols on the terrestrial carbon budget during the historical period. Meanwhile, we have also spent a significant amount of time to improve and evaluate the ORCHIDEE modeling tools for a better understanding of the aerosol impacts on photosynthesis. The main conclusions are given as follows.

Firstly, we used a set of simulations using ORCHIDEE trunk driven by CMIP5 climate fields to investigate the impacts of anthropogenic aerosols on the land C cycle through their impacts on climate. Our results indicate an increased cumulative land C sink of 11.6-41.8 PgC during 1850-2005 due to anthropogenic aerosols. The increase in net biome production (NBP) mainly occurs in the tropics and northern mid latitudes where aerosol-induced cooling has a beneficial effect on carbon storage. In contrast, at high latitudes, aerosol-induced cooling caused a stronger decrease in gross primary production (GPP) than in total ecosystem respiration (TER), leading to lower NBP, that is, aerosols reduce the net land C storage. At mid latitudes, cooling-induced decrease in TER is stronger than for GPP, resulting in a net NBP increase. At low latitudes, NBP was also enhanced due to the cooling-induced GPP increase, but regional precipitation decline in response to anthropogenic aerosol emissions may negate the effect of temperature. As Earth system models (ESMs) currently disagree on how aerosol emissions affect tropical precipitation, the precipitation change in response to aerosols becomes the main source of uncertainty in aerosol-caused C flux changes. Our results suggest that better understanding and simulation of how anthropogenic aerosols affect precipitation in ESMs is required for a more accurate attribution of aerosol effects on the terrestrial carbon cycle.

Secondly, we added to the ORCHIDEE trunk a new module to partition the downward surface solar radiation into diffuse and direct components, and a new canopy radiative transfer model, which separates the existing multilayer canopy into sunlit and

shaded leaves. The new model, named ORCHIDEE_DF, was evaluated in details using GPP observations collected from 159 flux sites over most of the PFTs around the world. Our results indicate that compared with ORCHIDEE trunk, ORCHIDEE_DF improved the GPP simulation under sunny conditions. This improvement successfully reproduces the observed enhancement of GPP under cloudy as compared to sunny conditions at most of the flux sites. By comparing the observed and simulated GPP differences between sunny and cloudy conditions at different times in the day, a key metrics to assess the effect of diffuse light, we found that the mechanisms about how different sky conditions affect GPP are different at midday and at other times of day. In the morning and afternoon, the enhancement of GPP under cloudy conditions is mainly due to a higher diffuse light fraction. Whereas at midday, the simultaneous changes in environmental conditions (e.g., lower temperature and lower VPD) are also responsible for the higher cloudy GPP, irrespective of a higher diffuse fraction. Flux towers observations indicate that under cloudy and sunny conditions for the same light level, the maximum light use efficiency (LUE) difference can be over 7×10^{-8} gC μmol^{-1} photon. This maximum LUE difference is found at temperatures between 5 and 20 °C with VPD < 1 kPa. With increasing VPD, or under lower or higher temperatures, the LUE difference may decrease. Compared with observations, ORCHIDEE_DF underestimates the diffuse light effect at low temperature and overestimates it at high temperatures, possibly due to imperfect temperature acclimation parameterization in the model. In grasslands and croplands, ORCHIDEE_DF overestimates the diffuse light effect on LUE, which might be due to an overestimation of their tolerance to dry conditions. Despite this bias inherited from ORCHIDEE trunk, ORCHIDEE_DF is proved to be able to capture the diffuse light fertilization effect in various vegetation types. For this reason, we have confidence that this new model has the potential to be used in investigating the effect of aerosol-induced diffuse light changes.

Thirdly, two sets of simulations respectively driven by CRUJRA climate and IPSL-CM6A-LR climate fields under *historical* and *histNoAA* scenarios were conducted after empirically tuning ORCHIDEE_DF in order to quantify the impact of aerosol-induced diffuse radiation changes on the historical land C budget. The two sets of simulations indicate an increase in global cumulative land C sink of 6.8 and 15.9 PgC, respectively, in response to aerosol-induced diffuse radiation changes during the historical period (1901-2012 for CRUJRA; 1850-2014 for IPSL) and mainly occurring

after the 1950s. Together with aerosol-induced climate change, the aerosols enchance land C sink by 20.0 PgC during 1850-2014 (IPSL). The spatial distribution of the Fdf fertilization effect depends on both the aerosol emissions and the canopy structure of the vegetation. According to the factorial simulations driven by IPSL climate, we found that globally, the anthropogenic aerosol-induced Fdf changes cause an enhancement of photosynthesis that offsets the aerosols' dimming impacts, leading to a net positive impact of aerosol-caused overall radiation changes (quality and quantity). The aerosol-caused diffuse radiation changes, along with the temperature changes (cooling), explain most of global C sink increase in response to aerosols. Despite the smaller magnitude at the global scale, the cooling impact detected in this study generally follows the same spatial patterns that was discussed in Chapter 2. i.e. a decrease GPP and NBP at high and mid latitudes and an increase in GPP and NBP in low latitudes. At mid latitudes, cooling causes a decline in both GPP and TER, but its impact on NBP depends on region and time. By comparing different methods processing Fdf data, we also found that different methods to construct the Fdf series under no aerosol scenario have dramatic impacts on the results. To avoid biasing the results, we suggest to use methods that conserve the natural variability of Fdf to investigate the diffuse light impact at large scale.

Previous studies on anthropogenic aerosol impacts at the global scale either ignored the diffuse radiation impacts and considered only the overall aerosol-induced climate changes (Jones *et al.*, 2003; Mahowald *et al.*, 2011), or investigated only aerosol-caused diffuse radiation changes (Mercado *et al.*, 2009). This thesis for the first time systematically investigated the aerosol impacts through different pathways, quantified the impacts of anthropogenic aerosols, illustrated the most important factors affecting the terrestrial C cycle and pointed out the source of the large uncertainties in current estimations of aerosol impacts. The understandings gained from this thesis will contribute to more reliable future climate projections and help to make better aerosol emission policies and geoengineering strategies.

Nevertheless, there remain unsolved problems. Firstly, current land surface models remain unable to perfectly simulate the aerosol impacts. As mentioned in Chapter 1, nutrients can be the key factor limiting GPP and the net C sinks in some ecosystems. For instance, Magnani *et al.* (2007) suggested that the C sinks in European temperate and boreal forest are mainly driven by anthropogenic nitrogen deposition. Apart from

the impact on climate and diffuse light fraction, anthropogenic aerosols are thought to be responsible of most of the N deposition on natural ecosystems over the world. Currently, more and more land surface models start to include nutrient limitations in terrestrial ecosystems (e.g., Goll *et al.*, 2017). Merging our canopy transmission module to such land surface models will provide the opportunity to simulate more complete impacts of aerosols. In terms of soil acidification and aerosol-originated toxic chemicals (Figure 1.5), due to the limit understandings on these processes, it remains difficult to get reliable parameterization of these processes. For this reason, most processes related to soil acidification and toxic chemicals are still absent in land surface models (except ozone, which is considered in a few models e.g. Sitch *et al.*, 2007; Chen, 2013). To understand the complete impact of aerosols, better understandings on such processes are needed.

Apart from the missing processes, current land surface models also get biased by their poorly-tuned parameters. As many processes are parameterized using empirically relationships in current land surface models, the accuracy of the parameters in these relationships is crucial for correctly simulate the C fluxes. To get the parameters well calibrated, large amount of observations from various ecosystems at different scales are needed. The development of the flux observation network provided a good chance to do the calibration (Baldocchi *et al.*, 2001). Unfortunately, there remains ecosystem types which are poorly covered by the network or whose data is not shared (e.g. tropical forests, deciduous needle-leaf forests). Furthermore, not all the important variables needed for evaluation and calibration of land surface models including aerosol-related processes are obtained. For instance, a large proportion of the flux sites provides no LAI observations, and very few of the sites record LAI time series. Because diffuse radiation impacts are strongly affected by LAI, the lack of LAI observations lead to difficulties calibrating the canopy light transmission model. The satellite LAI products (e.g. Zhu *et al.*, 2013) might be help solving this problem. However, the mismatch between the large gridbox of satellite data and small footprint of in situ observations, as well as the uncertainties in the algorisms obtaining LAI from the canopy reflectance signal can both result in large uncertainties in the calibration.

Secondly, our current estimations of aerosol impacts are all based on offline simulations, which is unable to fully include the feedbacks in the system. The Earth system is a highly coupled system. Any changes in land C budget will result in changes

in atmospheric CO_2 concentration. The climate-carbon feedback was reported to cause up to 1.5 ºC difference in climate around 2100 (Friedlingstein *et al.*, 2006). In this thesis, the climate data are from CMIP5 and CMIP6 coupled simulations. However, the CMIP5 and CMIP6 models are not able to simulate the full feedback from the aerosol-induced C budget changes due to the lack of processes such as diffuse radiation fertilization. Therefore, the climate fields to drive our *NoAA* simulations should be different from a real *NoAA* scenario. To avoid this problem, a fully coupled simulation on an Earth system model with aerosol-related processes included is needed.

In addition to the climate, there exists another feedback regarding aerosols. Apart from anthropogenic aerosols, a large fraction of the atmospheric aerosols is of biogenic origin. These aerosols may change in response to vegetation changes (Kulmala *et al.*, 2004). A recent assessment indicates that the feedback from natural aerosols may cause a radiative impact comparable to those from other biogeochemical feedbacks (Scott *et al.*, 2017), highlighting the importance of natural aerosols. As shown in this thesis, anthropogenic aerosols can affect vegetation through various pathways, it can in turn cause changes in biogenic aerosol emissions, and consequently affect vegetation and climate similarly to anthropogenic aerosols. This effect is potentially important as the optical depth of natural aerosols is comparable to anthropogenic aerosols (Boucher *et al.*, 2013; Carslaw *et al.*, 2017). Furthermore, the natural aerosols are more distributed in productive tropical regions, where ecosystems have much larger contribution to the total terrestrial C budget (Chapter 2). This feedback is not considered in current Earth system models but is expected to be included in future models.

Finally, for now, we have investigated the aerosol impacts during the historical period in details, but have not yet looked at the aerosol impacts in the future. One of the main target of Earth system models is to make reliable projections on future climate. To reach this target, besides the well-developed models described above, future aerosol emissions information is also needed. Fortunately, the Scenario Model Intercomparison Project (ScenarioMIP) have provided a set of Shared Socioeconomic Pathway-Representative Concentration Pathway (SSP-RCP) scenarios by considering possible emissions (including greenhouse gases, aerosols, etc.) under different socioeconomic scenarios and their corresponding climate impacts (O'Neill *et al.*, 2016). Using forcing from different SSP-RCP scenarios, we are able to evaluate the possible impacts of aerosols in the future and make better policies to balance economic development and

climate change mitigation.

References

Ainsworth, E. A., and Long, S. P. (2005), What have we learned from 15 years of free-air CO_2 enrichment (FACE)? A meta-analytic review of the responses of photosynthesis, canopy properties and plant production to rising CO_2, *New Phytologist*, *165*(2), 351-372.

Alton, P. (2008), Reduced carbon sequestration in terrestrial ecosystems under overcast skies compared to clear skies, *Agricultural and Forest Meteorology*, *148*(10), 1641-1653.

Alton, P., North, P., & Los, S. (2007), The impact of diffuse sunlight on canopy light-use efficiency, gross photosynthetic product and net ecosystem exchange in three forest biomes, *Global Change Biology*, *13*(4), 776-787.

Alton, P., Ellis, R., Los, S., & North, P. (2007), Improved global simulations of gross primary product based on a separate and explicit treatment of diffuse and direct sunlight, *Journal of Geophysical Research: Atmospheres*, *112*, D07203, doi:10.1029/2006JD008022.1.

Andrews, T., Forster, P. M., Boucher, O., Bellouin, N., & Jones, A. (2010). Precipitation, radiative forcing and global temperature change. *Geophysical Research Letters*, *37*, L14701. https://doi.org/10.1029/2010GL043991

Baldocchi, D. D., and Wilson, K. B. (2001), Modeling CO_2 and water vapor exchange of a temperate broadleaved forest across hourly to decadal time scales, *Ecological Modelling*, *142*(1-2), 155-184.

Baldocchi, D., Falge, E., Gu, L., Olson, R., Hollinger, D., Running, S., *et al.* (2001), FLUXNET: A new tool to study the temporal and spatial variability of ecosystem-scale carbon dioxide, water vapor, and energy flux densities, *Bulletin of the American Meteorological Society*, *82*(11), 2415-2434.

Barr, A., Griffis, T., Black, T., Lee, X., Staebler, R., Fuentes, J., *et al.* (2002),

Comparing the carbon budgets of boreal and temperate deciduous forest stands, *Canadian Journal of Forest Research, 32*(5), 813-822.

Beer, C., Reichstein, M., Tomelleri, E., Ciais, P., Jung, M., Carvalhais, N., *et al.* (2010), Terrestrial gross carbon dioxide uptake: global distribution and covariation with climate, *Science*, *329*(5993), 834-838.

Bellouin, N., Rae, J., Jones, A., Johnson, C., Haywood, J., & Boucher, O. (2011), Aerosol forcing in the Climate Model Intercomparison Project (CMIP5) simulations by HadGEM2-ES and the role of ammonium nitrate, *Journal of Geophysical Research: Atmospheres, 116*, D20206, doi:10.1029/2011JD016074.1.

Berry, J., & Bjorkman, O. (1980), Photosynthetic response and adaptation to temperature in higher plants, *Annual Review of Plant Physiology*, *31*(1), 491-543.

Bodin, P., & Franklin, O. (2012), Efficient modeling of sun/shade canopy radiation dynamics explicitly accounting for scattering, *Geoscientific Model Development*, *5*(2), 535-541.

Bonan, G. B., Oleson, K. W., Fisher, R. A., Lasslop, G., & Reichstein, M. (2012), Reconciling leaf physiological traits and canopy flux data: Use of the TRY and FLUXNET databases in the Community Land Model version 4, *Journal of Geophysical Research: Biogeosciences*, *117*, G02026, doi:10.1029/2011JG001913.1.

Boucher, O. (2015), *Atmospheric aerosols: Properties and climate impacts*, Springer.

Boucher, O., Randall, D., Artaxo, P., Bretherton, C., Feingold, G., Forster, P., *et al.* (2013), Clouds and aerosols, in *Climate change 2013: the physical science basis. Contribution of Working Group I to the Fifth Assessment Report of the Intergovernmental Panel on Climate Change*, pp. 571-657, Cambridge: Cambridge University Press.

Bowman, W. D., Cleveland, C. C., Halada, Ľ., Hreško, J., & Baron, J. S. (2008), Negative impact of nitrogen deposition on soil buffering capacity, *Nature Geoscience*, *1*(11), 767-770.

Brando, P. M., Balch, J. K., Nepstad, D. C., Morton, D. C., Putz, F. E., Coe, M. T., *et al.* (2014), Abrupt increases in Amazonian tree mortality due to drought–fire interactions, *Proceedings of the National Academy of Sciences*, *111*(17), 6347-6352.

Carslaw, K. S., Gordon, H., Hamilton, D. S., Johnson, J. S., Regayre, L. A., Yoshioka, M., & Pringle, K. J. (2017), Aerosols in the pre-industrial atmosphere, *Current Climate Change Reports*, *3*(1), 1-15.

Chen, M. (2013), *Evaluation of atmospheric aerosol and tropospheric ozone effects on global terrestrial ecosystem carbon dynamics* (Doctoral dissertation), Purdue University.

Chen, L., Yan, G., Wang, T., Ren, H., Calbó, J., Zhao, J., & McKenzie, R. (2012), Estimation of surface shortwave radiation components under all sky conditions: Modeling and sensitivity analysis, *Remote Sensing of Environment*, *123*, 457-469.

Cheng, S. J., Bohrer, G., Steiner, A. L., Hollinger, D. Y., Suyker, A., Phillips, R. P., & Nadelhoffer, K. J. (2015), Variations in the influence of diffuse light on gross primary productivity in temperate ecosystems, *Agricultural and Forest Feteorology*, *201*, 98-110.

Choudhury, B. J. (2001), Estimating gross photosynthesis using satellite and ancillary data: Approach and preliminary results, *Remote Sensing of Environment*, *75*(1), 1-21.

Ciais, P., Reichstein, M., Viovy, N., Granier, A., Ogée, J., Allard, V., *et al.* (2005), Europe-wide reduction in primary productivity caused by the heat and drought in 2003, *Nature*, *437*(7058), 529-533.

Ciais, P., Sabine, C., Bala, G., Bopp, L., Brovkin, V., Canadell, J., *et al.* (2013), Carbon and other biogeochemical cycles, in *Climate change 2013: the physical science basis. Contribution of Working Group I to the Fifth Assessment Report of the Intergovernmental Panel on Climate Change*, pp. 465-570, Cambridge: Cambridge University Press.

Cirino, G., Souza, R., Adams, D., & Artaxo, P. (2014), The effect of atmospheric aerosol particles and clouds on net ecosystem exchange in the Amazon, *Atmospheric Chemistry and Physics*, *14*(13), 6523-6543.

Cox, P. M., Betts, R. A., Jones, C. D., Spall, S. A., & Totterdell, I. J. (2000), Acceleration of global warming due to carbon-cycle feedbacks in a coupled climate model, *Nature*, *408*(6809), 184-187.

Cox, P. M., Pearson, D., Booth, B. B., Friedlingstein, P., Huntingford, C., Jones, C. D., & Luke, C. M. (2013), Sensitivity of tropical carbon to climate change constrained by carbon dioxide variability, *Nature*, *494*(7437), 341-344.

Cramer, W., Kicklighter, D. W., Bondeau, A., Iii, B. M., Churkina, G., Nemry, B., *et al.* (1999), Comparing global models of terrestrial net primary productivity (NPP): overview and key results, *Global Change Biology*, *5*(S1), 1-15.

Dai, Y., Dickinson, R. E., & Wang, Y.-P. (2004), A two-big-leaf model for canopy temperature, photosynthesis, and stomatal conductance, *Journal of Climate*, *17*(12), 2281-2299.

Davidson, E. A., Belk, E., & Boone, R. D. (1998), Soil water content and temperature as independent or confounded factors controlling soil respiration in a temperate mixed hardwood forest, *Global Change Biology*, *4*(2), 217-227.

de Rosnay, P., & Polcher, J. (1998), Modelling root water uptake in a complex land surface scheme coupled to a GCM, *Hydrology and Earth System Sciences*, *2*(2-3), 239–255, https://doi.org/10.5194/hess-2-239-1998.

Ducoudré, N. I., Laval, K., & Perrier, A. (1993), SECHIBA, a new set of

parameterizations of the hydrologic exchanges at the land-atmosphere interface within the LMD atmospheric general circulation model, *Journal of Climate*, *6*(2), 248-273.

Dufresne, J.-L., Foujols, M.-A., Denvil, S., Caubel, A., Marti, O., Aumont, O., *et al.* (2013), Climate change projections using the IPSL-CM5 Earth System Model: from CMIP3 to CMIP5, *Climate Dynamics*, *40*(9-10), 2123-2165.

Dye, D. G. (2004), Spectral composition and quanta-to-energy ratio of diffuse photosynthetically active radiation under diverse cloud conditions, *Journal of Geophysical Research: Atmospheres*, *109*, D10203, doi:10.1029/2003JD004251.

Eliseev, A. V. (2015), Impact of tropospheric sulphate aerosols on the terrestrial carbon cycle, *Global and Planetary Change*, *124*, 30-40.

Erb, K.-H., Kastner, T., Plutzar, C., Bais, A. L. S., Carvalhais, N., Fetzel, T., *et al.* (2018), Unexpectedly large impact of forest management and grazing on global vegetation biomass, *Nature*, *553*(7686), 73.

Erbs, D., Klein, S., & Duffie, J. (1982), Estimation of the diffuse radiation fraction for hourly, daily and monthly-average global radiation, *Solar Energy*, *28*(4), 293-302.

Eyring, V., Bony, S., Meehl, G. A., Senior, C. A., Stevens, B., Stouffer, R. J., & Taylor, K. E. (2016), Overview of the Coupled Model Intercomparison Project Phase 6 (CMIP6) experimental design and organization, *Geoscientific Model Development*, *9*, 1937–1958, https://doi.org/10.5194/gmd-9-1937-2016

Farquhar, G. D., von Caemmerer, S., & Berry, J. A. (1980), A biochemical model of photosynthetic CO_2 assimilation in leaves of C_3 species, *Planta*, *149*(1), 78-90.

Flato, G., Marotzke, J., Abiodun, B., Braconnot, P., Chou, S. C., Collins, W. J., *et al.* (2013), Evaluation of climate models. In *Climate change 2013: the physical science basis. Contribution of Working Group I to the Fifth Assessment Report of the Intergovernmental Panel on Climate Change*, pp. 741-866, Cambridge:

Cambridge University Press.

Friedlingstein, P., Meinshausen, M., Arora, V. K., Jones, C. D., Anav, A., Liddicoat, S. K., & Knutti, R. (2014), Uncertainties in CMIP5 climate projections due to carbon cycle feedbacks, *Journal of Climate*, *27*(2), 511-526.

Friedlingstein, P., Cox, P., Betts, R., Bopp, L., von Bloh, W., Brovkin, V., *et al.* (2006), Climate–carbon cycle feedback analysis: results from the C4MIP model intercomparison, *Journal of Climate*, *19*(14), 3337-3353.

Friedlingstein, P., Jones, M., O'Sullivan, M., Andrew, R., Hauck, J., Peters, G., *et al.* (2019), Global carbon budget 2019, *Earth System Science Data*, *11*(4), 1783-1838.

Goll, D., Vuichard, N., Maignan, F., Jornet-Puig, A., Sardans, J., Violette, A., *et al.* (2017), A representation of the phosphorus cycle for ORCHIDEE (revision 4520), *Geoscientific Model Development*, *10*, 3745–3770, https://doi.org/10.5194/gmd-10-3745-2017, 2017.

Goudriaan, J. (1977), *Crop micrometeorology: A simulation study*. Wagenigen: Pudoc.

Goudriaan, J. (1982), Potential production processes, in *Simulation of plant growth and crop production*, pp. 98-113, Wageningen: Pudoc.

Graham, E. A., Mulkey, S. S., Kitajima, K., Phillips, N. G., & Wright, S. J. (2003), Cloud cover limits net CO_2 uptake and growth of a rainforest tree during tropical rainy seasons, *Proceedings of the National Academy of Sciences*, *100*(2), 572-576.

Gu, L., Fuentes, J. D., Shugart, H. H., Staebler, R. M., & Black, T. A. (1999), Responses of net ecosystem exchanges of carbon dioxide to changes in cloudiness: Results from two North American deciduous forests, *Journal of Geophysical Research: Atmospheres*, *104*(D24), 31421-31434.

Gu, L., Baldocchi, D., Verma, S. B., Black, T., Vesala, T., Falge, E. M., and Dowty,

P. R. (2002), Advantages of diffuse radiation for terrestrial ecosystem productivity, *Journal of Geophysical Research: Atmospheres*, *107*(D6), ACL 2-1-ACL 2-23.

Gu, L., Baldocchi, D. D., Wofsy, S. C., Munger, J. W., Michalsky, J. J., Urbanski, S. P., & Boden, T. A. (2003), Response of a deciduous forest to the Mount Pinatubo eruption: Enhanced photosynthesis, *Science*, *299*(5615), 2035-2038.

Guan, K., Pan, M., Li, H., Wolf, A., Wu, J., Medvigy, D., *et al.* (2015), Photosynthetic seasonality of global tropical forests constrained by hydroclimate, *Nature Geoscience*, *8*(4), 284-289.

Harris, I. (2019), CRU JRA v1.1: A forcings dataset of gridded land surface blend of Climatic Research Unit (CRU) and Japanese reanalysis (JRA) data; Jan.1901 - Dec.2017. Centre for Environmental Data Analysis, 25 February 2019. doi:10.5285/13f3635174794bb98cf8ac4b0ee8f4ed.

Harris, I., Jones, P. D., Osborn, T. J., & Lister, D. H. (2014), Updated high-resolution grids of monthly climatic observations–the CRU TS3. 10 Dataset, *International Journal of Climatology*, *34*(3), 623-642.

Haywood, J., and Boucher, O. (2000), Estimates of the direct and indirect radiative forcing due to tropospheric aerosols: A review, *Reviews of Geophysics*, *38*(4), 513-543.

Holland, E. A., Braswell, B., Lamarque, J. F., Townsend, A., Sulzman, J., Müller, J. F., *et al.* (1997), Variations in the predicted spatial distribution of atmospheric nitrogen deposition and their impact on carbon uptake by terrestrial ecosystems, *Journal of Geophysical Research: Atmospheres*, *102*(D13), 15849-15866.

Hollinger, D., Kelliher, F., Byers, J., Hunt, J., McSeveny, T., & Weir, P. (1994), Carbon dioxide exchange between an undisturbed old-growth temperate forest and the atmosphere, *Ecology*, *75*(1), 134-150.

Howell, T., Meek, D., and Hatfield, J. (1983), Relationship of photosynthetically

active radiation to shortwave radiation in the San Joaquin Valley, *Agricultural Meteorology*, *28*(2), 157-175.

Hu, Y., Huang, H., and Zhou, C. (2018), Widening and weakening of the Hadley circulation under global warming, *Science Bulletin*, *63*(10), 640-644.

Huang, M., Piao, S., Ciais, P., Peñuelas, J., Wang, X., Keenan, T. F., *et al.* (2019), Air temperature optima of vegetation productivity across global biomes, *Nature Ecology & Evolution*, *3*(5), 772-779.

Huete, A. R., Didan, K., Shimabukuro, Y. E., Ratana, P., Saleska, S. R., Hutyra, L. R., *et al.* (2006), Amazon rainforests green-up with sunlight in dry season, *Geophysical Research Letters*, *33*, L06405, doi:10.1029/2005GL025583

Hurtt, G. C., Chini, L. P., Frolking, S., Betts, R., Feddema, J., Fischer, G., *et al.* (2011), Harmonization of land-use scenarios for the period 1500–2100: 600 years of global gridded annual land-use transitions, wood harvest, and resulting secondary lands, *Climatic Change*, *109*(1-2), 117-161, doi 10.1007/s10584-011-0153-2.

Inness, A., Ades, M., Agusti-Panareda, A., Barré, J., Benedictow, A., Blechschmidt, A.-M., *et al.* (2019), The CAMS reanalysis of atmospheric composition, *Atmospheric Chemistry and Physics*, *19*(6), 3515-3556.

Iziomon, M., & Aro, T. (1998), The Diffuse Fraction of Global Solar Irradiance at a Tropical Location, *Theoretical and Applied Climatology*, *61*(1-2), 77-84.

Janssens, I., Dieleman, W., Luyssaert, S., Subke, J.-A., Reichstein, M., Ceulemans, R., *et al.* (2010), Reduction of forest soil respiration in response to nitrogen deposition, *Nature Geoscience*, *3*(5), 315-322.

Jeffrey, S., Rotstayn, L., Collier, M., Dravitzki, S., Hamalainen, C., Moeseneder, C., *et al.* (2013), Australia's CMIP5 submission using the CSIRO Mk3. 6 model, *Australian Meteorological and Oceanographic Journal*, *63*, 1-13.

Jones, C. D., Cox, P. M., Essery, R. L., Roberts, D. L., & Woodage, M. J. (2003),

Strong carbon cycle feedbacks in a climate model with interactive CO_2 and sulphate aerosols, *Geophysical Research Letters*, *30*(9), 1479, doi:10.1029/2003GL016867, 2003..

Jones, C. D., Arora, V., Friedlingstein, P., Bopp, L., Brovkin, V., Dunne, J., *et al.* (2016), C4MIP–The Coupled Climate–Carbon Cycle Model Intercomparison Project: experimental protocol for CMIP6, *Geoscientific Model Development*, *9*(8), 2853-2880.

Jung, M., Reichstein, M., Margolis, H. A., Cescatti, A., Richardson, A. D., Arain, M. A., *et al.* (2011), Global patterns of land-atmosphere fluxes of carbon dioxide, latent heat, and sensible heat derived from eddy covariance, satellite, and meteorological observations, *Journal of Geophysical Research: Biogeosciences*, *116*, G00J07, doi:10.1029/2010JG001566.

Jung, M., Reichstein, M., Schwalm, C. R., Huntingford, C., Sitch, S., Ahlström, A., *et al.* (2017), Compensatory water effects link yearly global land CO_2 sink changes to temperature, *Nature*, *541*(7638), 516-520.

Kanniah, K. D., Beringer, J., & Hutley, L. (2013), Exploring the link between clouds, radiation, and canopy productivity of tropical savannas, *Agricultural and Forest Meteorology*, *182*, 304-313.

Kanniah, K. D., Beringer, J., Tapper, N. J., & Long, C. N. (2010), Aerosols and their influence on radiation partitioning and savanna productivity in northern Australia, *Theoretical and Applied Climatology*, *100*(3-4), 423-438.

Kattge, J., & Knorr, W. (2007), Temperature acclimation in a biochemical model of photosynthesis: a reanalysis of data from 36 species, *Plant, Cell & Environment*, *30*(9), 1176-1190.

Key, J. R., & Schweiger, A. J. (1998), Tools for atmospheric radiative transfer: Streamer and FluxNet, *Computers & Geosciences*, *24*(5), 443-451.

Knohl, A., & Baldocchi, D. D. (2008), Effects of diffuse radiation on canopy gas

exchange processes in a forest ecosystem, *Journal of Geophysical Research: Biogeosciences*, *113*, G02023, doi:10.1029/2007JG000663.

Kobayashi, S., Ota, Y., Harada, Y., Ebita, A., Moriya, M., Onoda, H., *et al.* (2015), The JRA-55 reanalysis: General specifications and basic characteristics, *Journal of the Meteorological Society of Japan. Ser. II*, *93*(1), 5-48.

Koven, C., Chambers, J., Georgiou, K., Knox, R., Negron-Juarez, R., Riley, W., *et al.* (2015), Controls on terrestrial carbon feedbacks by productivity versus turnover in the CMIP5 Earth System Models, *Biogeosciences*, *12*, 5211–5228, https://doi.org/10.5194/bg-12-5211-2015.

Krinner, G., Viovy, N., de Noblet-Ducoudré, N., Ogée, J., Polcher, J., Friedlingstein, P., *et al.* (2005), A dynamic global vegetation model for studies of the coupled atmosphere-biosphere system, *Global Biogeochemical Cycles*, *19*(1), GB1015, doi:10.1029/2003GB002199

Kulmala, M., Suni, T., Lehtinen, K., Dal Maso, M., Boy, M., Reissell, A., *et al.* (2004), A new feedback mechanism linking forests, aerosols, and climate. *Atmospheric Chemistry and Physics*, *4*, 557–562

Kuniyal, J. C., & Guleria, R. P. (2019), The current state of aerosol-radiation interactions: A mini review, *Journal of Aerosol Science*, *130*, 45-54.

Lardy, R., Bellocchi, G., and Soussana, J.-F. (2011), A new method to determine soil organic carbon equilibrium, *Environmental Modelling & Software*, *26*(12), 1759-1763.

Le Qu ér é, C., Andrew, R. M., Friedlingstein, P., Sitch, S., Pongratz, J., Manning, A. C., *et al.* (2017), Global carbon budget 2017, *Earth System Science Data*, *10*, 405–448, https://doi.org/10.5194/essd-10-405-2018.

LeBauer, D. S., & Treseder, K. K. (2008), Nitrogen limitation of net primary productivity in terrestrial ecosystems is globally distributed, *Ecology*, *89*(2), 371-379.

Li, T., Heuvelink, E., Dueck, T., Janse, J., Gort, G., & Marcelis, L. (2014), Enhancement of crop photosynthesis by diffuse light: quantifying the contributing factors, *Annals of Botany*, *114*(1), 145-156.

Liu, L., & Greaver, T. L. (2009), A review of nitrogen enrichment effects on three biogenic GHGs: the CO_2 sink may be largely offset by stimulated N_2O and CH_4 emission, *Ecology Letters*, *12*(10), 1103-1117.

Lloyd, J., & Taylor, J. (1994), On the temperature dependence of soil respiration, *Functional Ecology*, *8*, 315-323.

Luo, Y., Su, B., Currie, W. S., Dukes, J. S., Finzi, A., Hartwig, U., *et al.* (2004), Progressive nitrogen limitation of ecosystem responses to rising atmospheric carbon dioxide, *AIBS Bulletin*, *54*(8), 731-739.

Magnani, F., Mencuccini, M., Borghetti, M., Berbigier, P., Berninger, F., Delzon, S., *et al.* (2007), The human footprint in the carbon cycle of temperate and boreal forests, *Nature*, *447*(7146), 849-851.

Mahowald, N. (2011), Aerosol indirect effect on biogeochemical cycles and climate, *Science*, *334*(6057), 794-796.

Mahowald, N., Lindsay, K., Rothenberg, D., Doney, S. C., Moore, J. K., Thornton, P., & Jones, C. (2011), Desert dust and anthropogenic aerosol interactions in the Community Climate System Model coupled-carbon-climate model, *Biogeosciences*, *8*(2), 387-414.

Mahowald, N. M., Scanza, R., Brahney, J., Goodale, C. L., Hess, P. G., Moore, J. K., & Neff, J. (2017), Aerosol deposition impacts on land and ocean carbon cycles, *Current Climate Change Reports*, *3*(1), 16-31.

Mehran, A., AghaKouchak, A., & Phillips, T. J. (2014), Evaluation of CMIP5 continental precipitation simulations relative to satellite-based gauge-adjusted observations, *Journal of Geophysical Research: Atmospheres*, *119*(4), 1695-1707.

Meir, P., Kruijt, B., Broadmeadow, M., Barbosa, E., Kull, O., Carswell, F., *et al.* (2002), Acclimation of photosynthetic capacity to irradiance in tree canopies in relation to leaf nitrogen concentration and leaf mass per unit area, *Plant, Cell & Environment*, *25*(3), 343-357.

Mencuccini, M., Minunno, F., Salmon, Y., Martínez-Vilalta, J., & Hölttä, T. (2015), Coordination of physiological traits involved in drought-induced mortality of woody plants, *New Phytologist*, *208*(2), 396-409.

Mercado, L. M., Bellouin, N., Sitch, S., Boucher, O., Huntingford, C., Wild, M., & Cox, P. M. (2009), Impact of changes in diffuse radiation on the global land carbon sink, *Nature*, *458*(7241), 1014-1017.

Mercado, L. M., Medlyn, B. E., Huntingford, C., Oliver, R. J., Clark, D. B., Sitch, S., *et al.* (2018), Large sensitivity in land carbon storage due to geographical and temporal variation in the thermal response of photosynthetic capacity, *New Phytologist*, *218*(4), 1462-1477.

Miller, R. L., Schmidt, G. A., Nazarenko, L. S., Tausnev, N., Bauer, S. E., DelGenio, A. D., *et al.* (2014), CMIP5 historical simulations (1850–2012) with GISS ModelE2, *Journal of Advances in Modeling Earth Systems*, *6*(2), 441-478.

Misson, L., Lunden, M., McKay, M., & Goldstein, A. H. (2005), Atmospheric aerosol light scattering and surface wetness influence the diurnal pattern of net ecosystem exchange in a semi-arid ponderosa pine plantation, *Agricultural and Forest Meteorology*, *129*(1-2), 69-83.

Monsi, M., & Saeki, T. (2005), On the factor light in plant communities and its importance for matter production, *Annals of Botany*, *95*(3), 549-567.

Myneni, R. B., Ross, J., & Asrar, G. (1989), A review on the theory of photon transport in leaf canopies, *Agricultural and Forest Meteorology*, *45*(1-2), 1-153.

Nemani, R. R., Keeling, C. D., Hashimoto, H., Jolly, W. M., Piper, S. C., Tucker, C. J., *et al.* (2003), Climate-driven increases in global terrestrial net primary

production from 1982 to 1999, *Science*, *300*(5625), 1560-1563.

Niemand, C., Köstner, B., Prasse, H., Grünwald, T., & Bernhofer, C. (2005), Relating tree phenology with annual carbon fluxes at Tharandt forest, *Meteorologische Zeitschrift*, *14*(2), 197-202.

Niinemets, U., Kull, O., & Tenhunen, J. D. (1998), An analysis of light effects on foliar morphology, physiology, and light interception in temperate deciduous woody species of contrasting shade tolerance, *Tree Physiology*, *18*(10), 681-696.

Niyogi, D., Chang, H. I., Saxena, V., Holt, T., Alapaty, K., Booker, F., *et al.* (2004), Direct observations of the effects of aerosol loading on net ecosystem CO_2 exchanges over different landscapes, *Geophysical Research Letters*, *31*, L20506, doi:10.1029/2004GL020915.

Norby, R. J., Warren, J. M., Iversen, C. M., Medlyn, B. E., and McMurtrie, R. E. (2010), CO_2 enhancement of forest productivity constrained by limited nitrogen availability, *Proceedings of the National Academy of Sciences*, *107*(45), 19368-19373.

Norby, R. J., DeLucia, E. H., Gielen, B., Calfapietra, C., Giardina, C. P., King, J. S., *et al.* (2005), Forest response to elevated CO_2 is conserved across a broad range of productivity, *Proceedings of the National Academy of Sciences*, *102*(50), 18052-18056.

Nowak, R. S., Ellsworth, D. S., & Smith, S. D. (2004), Functional responses of plants to elevated atmospheric CO_2–do photosynthetic and productivity data from FACE experiments support early predictions?, *New Phytologist*, *162*(2), 253-280.

Oliphant, A., Dragoni, D., Deng, B., Grimmond, C., Schmid, H.-P., & Scott, S. (2011), The role of sky conditions on gross primary production in a mixed deciduous forest, *Agricultural and Forest Meteorology*, *151*(7), 781-791.

O'Neill, B. C., Tebaldi, C., Van Vuuren, D. P., Eyring, V., Friedlingstein, P., Hurtt,

G., *et al.* (2016), The scenario model intercomparison project (ScenarioMIP) for CMIP6, *Geoscientific Model Development*, *9*, 3461–3482, https://doi.org/10.5194/gmd-9-3461-2016

Parker, D., Wilson, H., Jones, P. D., Christy, J., & Folland, C. K. (1996), The impact of Mount Pinatubo on world-wide temperatures, *International Journal of Climatology*, *16*(5), 487-497.

Peng, S., Piao, S., Wang, T., Sun, J., & Shen, Z. (2009), Temperature sensitivity of soil respiration in different ecosystems in China, *Soil Biology and Biochemistry*, *41*(5), 1008-1014.

Phillips, O. L., Aragão, L. E., Lewis, S. L., Fisher, J. B., Lloyd, J., López-González, G., *et al.* (2009), Drought sensitivity of the Amazon rainforest, *Science*, *323*(5919), 1344-1347.

Piao, S., Ciais, P., Friedlingstein, P., de Noblet-Ducoudré, N., Cadule, P., Viovy, N., & Wang, T. (2009), Spatiotemporal patterns of terrestrial carbon cycle during the 20th century, *Global Biogeochemical Cycles*, *23*, GB4026, doi:10.1029/2008GB003339.

Piao, S., Fang, J., Ciais, P., Peylin, P., Huang, Y., Sitch, S., & Wang, T. (2009), The carbon balance of terrestrial ecosystems in China, *Nature*, *458*(7241), 1009-1013.

Piao, S., Sitch, S., Ciais, P., Friedlingstein, P., Peylin, P., Wang, X., *et al.* (2013), Evaluation of terrestrial carbon cycle models for their response to climate variability and to CO_2 trends, *Global Change Biology*, *19*(7), 2117-2132.

Piao, S., Liu, Q., Chen, A., Janssens, I. A., Fu, Y., Dai, J., *et al.* (2019), Plant phenology and global climate change: Current progresses and challenges, *Global Change Biology*, *25*(6), 1922-1940.

Poulter, B., MacBean, N., Hartley, A., Khlystova, I., Arino, O., Betts, R., *et al.* (2015), Plant functional type classification for earth system models: results from

the European Space Agency's Land Cover Climate Change Initiative, *Geoscientific Model Development*, *8*, 2315–2328.

Reichstein, M., Falge, E., Baldocchi, D., Papale, D., Aubinet, M., Berbigier, P., *et al.* (2005), On the separation of net ecosystem exchange into assimilation and ecosystem respiration: review and improved algorithm, *Global Change Biology*, *11*(9), 1424-1439.

Reichstein, M., Ciais, P., Papale, D., Valentini, R., Running, S., Viovy, N., *et al.* (2007), Reduction of ecosystem productivity and respiration during the European summer 2003 climate anomaly: a joint flux tower, remote sensing and modelling analysis, *Global Change Biology*, *13*(3), 634-651.

Ripullone, F., Grassi, G., Lauteri, M., & Borghetti, M. (2003), Photosynthesis–nitrogen relationships: interpretation of different patterns between Pseudotsuga menziesii and Populus × euroamericana in a mini-stand experiment, *Tree Physiology*, *23*(2), 137-144.

Rödenbeck, C., Houweling, S., Gloor, M., & Heimann, M. (2003), CO_2 flux history 1982-2001 inferred from atmospheric data using a global inversion of atmospheric transport, Atmospheric Chemistry and Physics, 3, 1919–1964, https://doi.org/10.5194/acp-3-1919-2003.

Roderick, M. L., Farquhar, G. D., Berry, S. L., & Noble, I. R. (2001), On the direct effect of clouds and atmospheric particles on the productivity and structure of vegetation, *Oecologia*, *129*(1), 21-30.

Rodhe, H., Dentener, F., & Schulz, M. (2002), The global distribution of acidifying wet deposition, *Environmental Science & Technology*, *36*(20), 4382-4388.

Saeki, T. (1960), Interrelationships between leaf amount, light distribution and total photosynthesis in a plant community, *Botanical Magazine (Tokyo)*, *73*(860), 55-63.

Saleska, S. R., Miller, S. D., Matross, D. M., Goulden, M. L., Wofsy, S. C., Da

Rocha, H. R., *et al.* (2003), Carbon in Amazon forests: unexpected seasonal fluxes and disturbance-induced losses, *Science*, *302*(5650), 1554-1557.

Samset, B., Myhre, G., Forster, P., Hodnebrog, Ø., Andrews, T., Faluvegi, G., *et al.* (2016), Fast and slow precipitation responses to individual climate forcers: A PDRMIP multimodel study, *Geophysical Research Letters*, *43*(6), 2782-2791.

Sato, M., Hansen, J. E., McCormick, M. P., & Pollack, J. B. (1993), Stratospheric aerosol optical depths, 1850-1990, *Journal of Geophysical Research: Atmospheres*, *98*(D12), 22987-22994.

Schindler, D., & Bayley, S. (1993), The biosphere as an increasing sink for atmospheric carbon: estimates from increased nitrogen depostion, *Global Biogeochemical Cycles*, *7*(4), 717-733.

Schippers, P., Sterck, F., Vlam, M., & Zuidema, P. A. (2015), Tree growth variation in the tropical forest: understanding effects of temperature, rainfall and CO_2, *Global Change Biology*, *21*(7), 2749-2761.

Schmidt, G. A., Kelley, M., Nazarenko, L., Ruedy, R., Russell, G. L., Aleinov, I., *et al.* (2014), Configuration and assessment of the GISS ModelE2 contributions to the CMIP5 archive, *Journal of Advances in Modeling Earth Systems*, *6*(1), 141-184.

Schulz, M., Textor, C., Kinne, S., Balkanski, Y., Bauer, S., Berntsen, T., *et al.* (2006), Radiative forcing by aerosols as derived from the AeroCom present-day and pre-industrial simulations, *Atmospheric Chemistry and Physics*, *6*(12), 5225-5246.

Schwartz, R. D. (2005), Global dimming: Clear-sky atmospheric transmission from astronomical extinction measurements, *Journal of Geophysical Research: Atmospheres*, *110*, D14210, doi:10.1029/2005JD005882.

Scott, C., Arnold, S., Monks, S., Asmi, A., Paasonen, P., & Spracklen, D. (2018), Substantial large-scale feedbacks between natural aerosols and climate, *Nature Geoscience*, *11*(1), 44-48.

Sellers, P., Dickinson, R., Randall, D., Betts, A., Hall, F., Berry, J., *et al.* (1997), Modeling the exchanges of energy, water, and carbon between continents and the atmosphere, *Science*, *275*(5299), 502-509.

Sitch, S., Cox, P., Collins, W., & Huntingford, C. (2007), Indirect radiative forcing of climate change through ozone effects on the land-carbon sink, *Nature*, *448*(7155), 791-794.

Sitch, S., Smith, B., Prentice, I. C., Arneth, A., Bondeau, A., Cramer, W., *et al.* (2003), Evaluation of ecosystem dynamics, plant geography and terrestrial carbon cycling in the LPJ dynamic global vegetation model, *Global Change Biology*, *9*(2), 161-185.

Sitch, S., Huntingford, C., Gedney, N., Levy, P., Lomas, M., Piao, S., *et al.* (2008), Evaluation of the terrestrial carbon cycle, future plant geography and climate-carbon cycle feedbacks using five Dynamic Global Vegetation Models (DGVMs), *Global Change Biology*, *14*(9), 2015-2039.

Smith, N. G., & Dukes, J. S. (2013), Plant respiration and photosynthesis in global-scale models: incorporating acclimation to temperature and CO_2, *Global Change Biology*, *19*(1), 45-63.

Smith, N. G., & Dukes, J. S. (2017), Short-term acclimation to warmer temperatures accelerates leaf carbon exchange processes across plant types, *Global Change Biology*, *23*(11), 4840-4853.

Smith, W. K., Vogelmann, T. C., & Critchley, C. (2010), *Photosynthetic adaptation: chloroplast to landscape*, Springer Science & Business Media.

Spitters, C. (1986), Separating the diffuse and direct component of global radiation and its implications for modeling canopy photosynthesis Part II. Calculation of canopy photosynthesis, *Agricultural and Forest Meteorology*, *38*(1-3), 231-242.

Spitters, C., Toussaint, H., & Goudriaan, J. (1986), Separating the diffuse and direct component of global radiation and its implications for modeling canopy

photosynthesis Part I. Components of incoming radiation, *Agricultural and Forest Meteorology*, *38*(1-3), 217-229.

Stark, J. M., and Firestone, M. K. (1995), Mechanisms for soil moisture effects on activity of nitrifying bacteria, *Applied and Environmental Microbiology*, *61*(1), 218-221.

Stocker, T. F., Qin, D., Plattner, G.-K., Tignor, M., Allen, S. K., Boschung, J., *et al.* (2013), Climate change 2013: The physical science basis, *Contribution of working group I to the fifth assessment report of the intergovernmental panel on climate change*, Cambridge: Cambridge University Press.

Sun, Z., Liu, L., Ma, Y., Yin, G., Zhao, C., Zhang, Y., & Piao, S. (2014), The effect of nitrogen addition on soil respiration from a nitrogen-limited forest soil, *Agricultural and forest meteorology*, *197*, 103-110.

Sun, Y., Peng, S., Goll, D. S., Ciais, P., Guenet, B., Guimberteau, M., *et al.* (2017), Diagnosing phosphorus limitations in natural terrestrial ecosystems in carbon cycle models, *Earth's Future*, *5*(7), 730-749.

Suseela, V., Conant, R. T., Wallenstein, M. D., & Dukes, J. S. (2012), Effects of soil moisture on the temperature sensitivity of heterotrophic respiration vary seasonally in an old-field climate change experiment, *Global Change Biology*, *18*(1), 336-348.

Taylor, K. E., Stouffer, R. J., and Meehl, G. A. (2012), An overview of CMIP5 and the experiment design, *Bulletin of the American Meteorological Society*, *93*(4), 485-498.

Tjiputra, J., Grini, A., and Lee, H. (2016), Impact of idealized future stratospheric aerosol injection on the large-scale ocean and land carbon cycles, *Journal of Geophysical Research: Biogeosciences*, *121*(1), 2-27.

Townsend, A., Braswell, B., Holland, E., & Penner, J. (1996), Spatial and temporal patterns in terrestrial carbon storage due to deposition of fossil fuel nitrogen,

Ecological Applications, *6*(3), 806-814.

Urban, O., Klem, K., Ač, A., Havránková, K., Holišová, P., Navrátil, M., *et al.* (2012), Impact of clear and cloudy sky conditions on the vertical distribution of photosynthetic CO_2 uptake within a spruce canopy, *Functional Ecology*, *26*(1), 46-55.

van't Hoff, J. H. (1898), *Lectures on theoretical and physical chemistry*: Part I. Chemical Dynamics (translated by R. A. Lehfeldt), 224-229. London: Edward Arnold

Vuichard, N., & Papale, D. (2015), Filling the gaps in meteorological continuous data measured at FLUXNET sites with ERA-Interim reanalysis, *Earth System Science Data*, *7*(2), 157-171.

Wang, Y., Law, R., & Pak, B. (2010), A global model of carbon, nitrogen and phosphorus cycles for the terrestrial biosphere, *Biogeosciences*, *7*(7), 2261-2282.

Wang, W., Ciais, P., Nemani, R. R., Canadell, J. G., Piao, S., Sitch, S., *et al.* (2013), Variations in atmospheric CO_2 growth rates coupled with tropical temperature, *Proceedings of the National Academy of Sciences*, *110*(32), 13061-13066.

Wang, R., Goll, D., Balkanski, Y., Hauglustaine, D., Boucher, O., Ciais, P., *et al.* (2017), Global forest carbon uptake due to nitrogen and phosphorus deposition from 1850 to 2100, *Global Change Biology*, *23*, 4854–4872

Wang, X., Wu, J., Chen, M., Xu, X., Wang, Z., Wang, B., *et al.* (2018), Field evidences for the positive effects of aerosols on tree growth, *Global Change Biology*, *24*(10), 4983-4992.

Wang, Y., Ciais, P., Goll, D., Huang, Y., Luo, Y., Wang, Y.-P., *et al.* (2018), GOLUM-CNP v1. 0: a data-driven modeling of carbon, nitrogen and phosphorus cycles in major terrestrial biomes, *Geoscientific Model Development*, *11*(9), 3903-3928.

Weiss, A., & Norman, J. (1985), Partitioning solar radiation into direct and diffuse,

visible and near-infrared components, *Agricultural and forest meteorology*, *34*(2-3), 205-213.

Welp, L. R., Keeling, R. F., Meijer, H. A., Bollenbacher, A. F., Piper, S. C., Yoshimura, K., *et al.* (2011), Interannual variability in the oxygen isotopes of atmospheric CO_2 driven by El Niño, *Nature*, *477*(7366), 579–582.

Williams, M., Rastetter, E. B., Van der Pol, L., & Shaver, G. R. (2014), Arctic canopy photosynthetic efficiency enhanced under diffuse light, linked to a reduction in the fraction of the canopy in deep shade, *New Phytologist*, *202*(4), 1267-1276.

Wu, P., Christidis, N., and Stott, P. (2013), Anthropogenic impact on Earth's hydrological cycle, *Nature Climate Change*, *3*(9), 807-810.

Xing, J., Wang, J., Mathur, R., Wang, S., Sarwar, G., Pleim, J., *et al.* (2017), Impacts of aerosol direct effects on tropospheric ozone through changes in atmospheric dynamics and photolysis rates, *Atmospheric Chemistry and Physics*, *17*(16), 9869-9883.

Yamori, W., Hikosaka, K., & Way, D. A. (2014), Temperature response of photosynthesis in C_3, C_4, and CAM plants: temperature acclimation and temperature adaptation, *Photosynthesis Research*, *119*(1-2), 101-117.

Yin, X., & Struik, P. (2009), C_3 and C_4 photosynthesis models: an overview from the perspective of crop modelling, *NJAS-Wageningen Journal of Life Sciences*, *57*(1), 27-38.

Yu, H., Luedeling, E., & Xu, J. (2010), Winter and spring warming result in delayed spring phenology on the Tibetan Plateau, *Proceedings of the National Academy of Sciences*, *107*(51), 22151-22156.

Yu, T., Sun, R., Xiao, Z., Zhang, Q., Liu, G., Cui, T., & Wang, J. (2018), Estimation of global vegetation productivity from global land surface satellite data, *Remote Sensing*, *10*(2), 327.

Yuste, J. C., Janssens, I., Carrara, A., Meiresonne, L., & Ceulemans, R. (2003),

Interactive effects of temperature and precipitation on soil respiration in a temperate maritime pine forest, *Tree Physiology*, *23*(18), 1263-1270.

Zaehle, S., & Dalmonech, D. (2011), Carbon–nitrogen interactions on land at global scales: current understanding in modelling climate biosphere feedbacks, *Current Opinion in Environmental Sustainability*, *3*(5), 311-320.

Zhang, Y., Rossow, W. B., Lacis, A. A., Oinas, V., & Mishchenko, M. I. (2004), Calculation of radiative fluxes from the surface to top of atmosphere based on ISCCP and other global data sets: Refinements of the radiative transfer model and the input data, *Journal of Geophysical Research: Atmospheres*, *109*, D19105, doi:10.1029/2003JD004457.

Zhang, Y., Zhu, Z., Liu, Z., Zeng, Z., Ciais, P., Huang, M., *et al.* (2016), Seasonal and interannual changes in vegetation activity of tropical forests in Southeast Asia, *Agricultural and Forest Meteorology*, *224*, 1-10.

Zhao, M., Heinsch, F. A., Nemani, R. R., & Running, S. W. (2005), Improvements of the MODIS terrestrial gross and net primary production global data set, *Remote Sensing of Environment*, *95*(2), 164-176.

Zhu, Z., Bi, J., Pan, Y., Ganguly, S., Anav, A., Xu, L., *et al.* (2013), Global data sets of vegetation leaf area index (LAI) 3g and fraction of photosynthetically active radiation (FPAR) 3g derived from global inventory modeling and mapping studies (GIMMS) normalized difference vegetation index (NDVI3g) for the period 1981 to 2011, *Remote Sensing*, *5*(2), 927-948.